Theoretical modeling of paramagnetic chemical shifts in actinide complexes

Mohammad Ashraful Islam

Université Fédérale
Toulouse Midi-Pyrénées

THÈSE

En vue de l'obtention du
DOCTORAT DE L'UNIVERSITÉ DE TOULOUSE

Délivré par l'Université Toulouse 3 - Paul Sabatier

Présentée et soutenue par

MOHAMMAD ASHRAFUL ISLAM

Le 24 novembre 2021

Theoretical modeling of paramagnetic chemical shifts in actinide complexes

---

Ecole doctorale : **SDM - SCIENCES DE LA MATIERE - Toulouse**

Spécialité : **Physico-Chimie Théorique**

Unité de recherche :
LCPQ-IRSAMC - Laboratoire de Chimie et Physique Quantiques

Thèse dirigée par
Hélène BOLVIN et Nicolas SUAUD

Jury

M. Jochen Autschbach, Rapporteur
M. Boris Le Guennic, Rapporteur
M. Laurent Maron, Examinateur
M. Nicholas Chilton, Examinateur
Mme Hélène BOLVIN, Directrice de thèse
M. Alessandro Soncini, Invité
M. Claude Berthon, Invité

Acknowledgement

First and foremost I would like to express my deepest gratitude and sincere thanks to my esteemed supervisor, Dr. Hélène Bolvin for her invaluable supervision, erudite suggestions, generous and friendly nature, constant encouragement, critical evaluation, and counsel during the whole course of this work. Her diligence and deep understanding of the subject were a source of inspiration. I must confess that I have been benefited immensely by working under a distinguished thinker like her.

Besides my supervisor, I would like to thanks the rest of my thesis committee: Prof. Jochen Autschbach, Dr. Boris Le Guennic, Dr. Nicholas F. Chilton, Prof. Laurent Maron, Prof. Alessandro Soncini, and Dr. Claude Berthon for serving on the peer review of my thesis.

The illuminating lectures of Dr. Jean-Paul Malrieu and Dr. Trond Saue certainly added extra dimensions to my understanding by imparting knowledge on quantum chemistry and 'its' behavior at the speed of light to make further troubles for students. It gives me great pleasure to offer my profound thanks to our SEM group, as well as other LCPQ members, for their constructive discussion, valuable suggestion, and timely assistance and collaboration. I am grateful to the technicians, David and Eric for providing technical support and sharing their technical expertise. I would like to also thank to our experimental colleagues Matthieu, Claude, Laura for their fruitful collaborations throughout these years. I would also like to thank Julie Jung for her theoretical contributions. I also thank Stanislav Komorovsky for sharing the ReSpect code with us and a week–long discussion in Bratislava.

There are no words to express my gratitude to Prof. Gopalan Rajaraman of IIT Bombay. I am grateful to you, 'Sir', for allowing me to work in your group and for allowing me to complete my master's project. I would like to take this time to thank all of my other professors from both my undergraduate and graduate program and all of my teachers in school life, without whom I would not have arrived at this point.

I thank my fellow lab-mates; Maen, Martin, Miguel, Gabriele, Linjie, Mohammed, Clément, Fernand and all, for their unconditional support and for a cherished time spent together in the lab, Upsidum, outside and in social settings. They provided stimulating discussions as well as happy distractions to rest my mind outside of my research. Their

companionship has helped me to forget the pain of being away from home. I would like to express my deepest gratitude to all of my Indian friends whom I met in Toulouse. All of your presence around me and kind cooperation in different situations, helped me to fix several things and made me feel comfortable. I would like to express my warm appreciation and sense of gratitude to all of my friends specially my childhood friends for always being there and for your true, unwavering support and love. I thank all of my classmates from schools and college for their warm company. I want to express my gratitude to Sourav da, Arup da, and Mursaleem at IIT Bombay for their continued assistance during the early days when I was having hard time adjusting to quantum chemistry.

I grab the golden opportunity to thank ANR for providing me funding as well as financial support for this work and bearing conference/summer-school expenses. I also thank CNRS for being constantly helpful to me in the administrative work. I am also grateful to the NEXT/NanoX funding for providing me financial support for the out-going training module in the US (in Jochen Autschbach's group) which unfortunately I could not use because of COVID.

I am and will always be indebted to my parents for their unconditional love, ultimate care, and commitment. I can not image being on this stage without their unrelenting, unwavering, and constant support. Words are insufficient to explain their kindness, devotion, and love for my efforts. I am also grateful to have such loving, caring, and supportive family members and relatives. Thank you for accepting me as I am and where I am at this time. Knowing how much I am genuinely loved gives me a great deal of comfort.

A sincere thank you to everyone!!

Abbreviations

AMFI	Atomic Mean Field Integrals
AILFT	*Ab Initio* Ligand Field Theory
AIS	Actinide Induced Shifts
ANO-RCC	Atomic Natural Orbitals Relativistically Core Correlated
C(R)ASSCF	Complete (Restricted) Active Space Self-Consistent Field
C(R)ASPT2	Complete (Restricted) Active Space Perturbation Theory at 2nd order
CFT	Crystal Field Theory
CFP	Crystal Field Parameter
DFT	Density Functional Theory
DKH	Douglas-Kroll-Hess
EPR	Electron Paramagnetic Resonance
HFC	HyperFine Coupling
ITO	Irreducible Tensor Operators
LIS	Lanthanide Induced Shifts
NEVPT2	N-Electron Valence state Perturbation Theory at 2nd order
(N)KD	(Non-) Kramers doublet
NO	Natural Orbital
pNMR	Paramagnetic Nuclear Magnetic Resonance
PAF	Principal Axes Frame
SOC	Spin-Orbit Coupling
SR	Scalar Relativistic
TIP	Temperature Independent Paramagnetism
ZORA	Zeroth Order Regular Approximation
ZFS	Zero-Field Splitting

Contents

General introduction

The early actinides utilize their valence electrons more readily than the lanthanides because of the small energy gaps between the $5f$, $6d$ and $7s$ subshells, so the outer electrons are easily excited, resulting in a greater multiplicity of oxidation states. In Table 1, the known oxidation states of the actinides are shown. The data are taken from the Book "Lanthanide and actinide chemistry" by S. Cotton [1]. However, beyond Pu, there is a break of periodicity and the later actinides are more stable in the +3 oxidation state like the lanthanides due to more stabilization of the $5f$ subshells. The heaviest naturally occurring element is uranium. Rest of the trans-uranium actinides are man-made, they are unstable and decay radioactively. Several studies have pointed out that in the actinide complexes, the metal ligand interactions resemble to those of d-orbitals' interactions in the transition metal complexes and the metal ligand bonding occurs through the aforementioned energetically close valence orbitals [2, 3, 4, 5]. So when it comes to chemistry, actinides can offer as rich chemistry as the transition metals and also exhibit the same potentiality as the lanthanides in terms of the promising magnetic properties [6, 7]. But for practical reasons, much of the studies of actinide chemistry is restricted to the early actinides and also little explored. While handling of radioactivity is a serious concern for many experimental techniques, the commonly used NMR methodology has been successively emerging as a probe to study their electronic and magnetic properties [8, 9, 10, 11].

Table 1: Known oxidation states of the actinides. The most stable states are shown in red.

Ac	Th	Pa	U	Np	Pu	Am	Cm	Bk	Cf	Es	Fm	Md	No	Lr
						2			2	2	2	2	2	
3			3	3	3	3	3	3	3	3	3	3	3	3
	4	4	4	4	4	4	4	4	4					
		5	5	5	5	5								
			6	6	6									
				7	7									

Since the very first use of lanthanide complexes as NMR shift reagents [12], several interests were put forward in the potential use of lanthanide induced shifts (LIS) in the struc-

ture determinations, especially for biomolecules such as proteins and steroids [13, 14]. The very useful information that the study of the metal induced chemical shifts can offer, relies on the separation of the contact and pseudocontact contributions. The contact contributions to the paramagnetic chemical (pNMR) shifts originate from the delocalization of the spin density from the paramagnetic center to the observed nuclei and the pseudocontact (or dipolar) shifts are essentially through-space magnetic dipolar interactions. The contact shifts are more prominent in the close vicinity of the paramagnetic center whereas the magnetic dipolar interactions effectively induce additional shifts for the nuclei farther from the metal. Theoretical methods had been proposed to separate these two contributions. The two contributions were early modeled in the 1950s by McConnel and Robertson in terms of the spin Hamiltonian parameters; those models are best realized to study the pNMR shifts in the transition metal complexes [15]. However, in the 1970s, many theoretical methods had been systematically developed those are relevant for the lanthanide and actinide complexes also. The pioneering work of Kurland and McGarvey provided a general formula for the evaluation of the pNMR shifts, the pseudocontact shifts are calculated from the anisotropic magnetic susceptibility and the contact shifts are in terms of the isotropic spin-only susceptibility and Fermi contact coupling constant [16]. Soon after, Bleaney described the origin of magnetic anisotropy responsible for the LIS based on crystal field theory (CFT) and deduced a dominant T^{-2} temperature dependence for the pNMR (pseudocontact) shifts [17, 18]. At the same time, the theoretical study of the ^{14}N and ^{17}O NMR shifts in lanthanide complexes by Golding *et al.* resulted in a T^{-1} dependence for the contact shifts [19]. These temperature dependent models became popular and widely explored by chemists for the separation of the contact and pseudocontact terms [20, 21, 22, 23]. Reilley had proposed a structure independent method that helps to separate the two contributions without the knowledge of the geometrical parameters of the observed nuclei and spin densities at their positions [24]. This facilitates the separation of the terms at a given temperature for a lanthanide series using the metal dependent constants provided by Bleaney or can be evaluated *ab initio* [25, 26]. Throughout the decades, numerous formulations of the pNMR shifts were proposed based on different approaches that bear the same conclusions as drawn by Kurland, Bleaney, Golding, *et al.* at the earlier stage of the pNMR shifts technique [27, 28, 29, 30]. Simultaneously, in the experimental field, the LIS method became increasingly popular for structure determination in solution and to probe the lanthanide ligand bonding [31, 32, 33, 34].

However, the actinide induced shifts (AIS) are not as studied as for the lanthanides probably due to the small community of actinide chemists around the world. Also, the potential applications of actinides in various fields are disputable because of the issues associated with radioactivity and safety measurements. Yet for purely academic purposes, the physicochemical properties of the actinides are as interesting as those of transition metals and lanthanides. The main goal of this thesis is not to present the actinides as the

alternative to lanthanides as NMR shift reagents, but using the pNMR shifts technique to probe the magnetic properties of the actinides and their interactions with the ligand field. In this thesis, the AIS in several actinide complexes are presented and the interpretations of the AIS are carried out with the help of *ab initio* calculations. Theoretical modeling of the actinide paramagnetism has been conducted to estimate the magnetic properties from the temperature dependent curves. Due to the lack of experimental data for the late actinides, throughout this thesis, we will deal with the complexes of lighter actinides in different oxidation states. Paramagnetic chemical shifts are collected from various chelating ligands such as dipicolinate DPA^{2-} (pyridine-2,6-dicarboxylate), $DOTA^{4-}$ (dodecane tetraacetate), TEDGA (tetraethyldiglycolamide) etc. The diamagnetic counterpart is the corresponding isostructural complex with a diamagnetic actinide ion. We will discuss their *ab initio* electronic structures, magnetic properties keeping in mind that most of the discussions will circulate unraveling the nature of the pNMR shifts in these complexes. In due course, we have also pointed out the differences in electronic structures between the lanthanides and actinides. Bleaney's theory has been surveyed for the considered actinide complexes and further considerations beyond the Bleaney's assumptions are highlighted. Additionally, the *ab initio* computed electronic structures of the isostructural Ln^{III} (Ln = Ce- Yb) and An^{IV} (An = U- Pu) complexes with the DPA ligands are discussed based on CFT and the associated parameters are compared along and in between the series to find out the trends of electron-electron repulsion, spin-orbit coupling (SOC), $J-J$ coupling, covalency etc.

The first two chapters in this thesis are dedicated to being familiar with the molecular magnetic properties and their modeling for a system, and the quantum chemical methodology to compute them *ab initio*. Then in the next two chapters, the analyses of the AIS collected for the different complexes are discussed and the chapters are divided according to the oxidation state of the actinide center. In the last chapter, we have discussed the trends of crystal field parameters (CFPs) extracted using the ITO (Irreducible Tensor Operators) and AILFT (*Ab Initio* Ligand Field Theory) methods for the two mentioned series.

Chapter 1

Introduction to the paramagnetic chemical shifts

1.1 The chemical shifts and the shielding constants

In the nuclear magnetic resonance (NMR) technique, a sample is placed in an external magnetic field and electromagnetic frequencies are provided to resonate the NMR active nuclei (with nuclear spin $I > 0$) and a detector collects the signal. The characteristic resonance frequency ν_K for the nuclear spin transition of a nucleus K is given by

$$\nu_K = \frac{\gamma_K B_0}{2\pi}(1-\sigma_K) \tag{1.1.1}$$

where B_0 is the applied magnetic field and σ_K is a proportionality constant. γ_K is the gyromagnetic constant of the nucleus. In a molecule, the nuclei are surrounded by electrons. The local electronic environment (in chemistry, often it is regarded as the chemical environment) effectively shields the nucleus from B_0 . The negative sign in Eq. 1.1.1 indicates an opposing magnetic field produced by the chemical environment which is proportional to the constant σ_K. That is why σ_K is called the shielding constant. Note that $\frac{\gamma_K B_0}{2\pi}$ is the transition frequency of the bare nucleus and proportional to the strength of the magnetic field generated by the spectrometer. So the so-called "spectrometer frequency" of the nucleus K is $\nu_{spec} = \frac{\gamma_K B_0}{2\pi}$. The chemical shift δ_K is defined as the observed transition frequency relative to the signal of a reference compound ν_{ref} as

$$\delta_K = \frac{\nu_K - \nu_{ref}}{\nu_{ref}} \tag{1.1.2}$$

δ_K is usually expressed in ppm and marks the chemically different nucleus. To standardize the measured resonance frequency from different spectrometers, ν_{ref} in the denominator is replaced by the spectrometer frequency. In the case of a diamagnetic system, circulation

of the paired electron around the nucleus generates a local opposing magnetic field which is very small in terms of strength. In case of a paramagnetic system, the unpaired electrons provide additional shielding by generating a strong magnetic field and this extra induced shielding is called the pNMR shielding σ_K^p and the additional shift is the pNMR shift δ_K^p of the nucleus. δ_K^p is given by

$$\delta_K^p = \delta_K - \delta_K^{dia} = \frac{\nu_K - \nu_K^{dia}}{\nu_{spec}} \tag{1.1.3}$$

$$= \sigma_K^{dia} - \sigma_K \tag{1.1.4}$$

where δ_K and δ_K^{dia} are the observed chemical shifts of nucleus K in the isostructural paramagnetic and diamagnetic complexes, respectively.

The pNMR shifts are the consequences of the presence of paramagnetic center(s) in the close vicinity and related to its (their) magnetic properties. So the study of the pNMR shifts can be useful to probe the magnetic properties and their anisotropies for a system. The magnetic resonance parameters, for example, the shielding constant σ_K obtained from the NMR or the electron paramagnetic resonance (EPR) parameters (g-values, hyperfine coupling constants) are related to spectra obtained in a magnetic field. So in the next few sections, we will introduce the effects of magnetic field on an unpaired-electrons' system and the magnetic properties which are defined from the response.

1.2 Hamiltonian in a magnetic field

The most renowned non-relativistic Hamiltonian of an electron in a magnetic field with an external potential energy V is the Schrödinger-Pauli Hamiltonian written as

$$H = \frac{(\boldsymbol{\sigma}\cdot\boldsymbol{\pi})(\boldsymbol{\sigma}\cdot\boldsymbol{\pi})}{2m} + V \tag{1.2.1}$$

where $\boldsymbol{\sigma}$ comprises the three Pauli spin matrices $\boldsymbol{\sigma}_x, \boldsymbol{\sigma}_y, \boldsymbol{\sigma}_z$; $\boldsymbol{\pi} = \boldsymbol{p} + e\boldsymbol{A}$ is the kinematic momentum in a vector potential $\boldsymbol{A}$. $\boldsymbol{p}$ is the momentum without the presence of magnetic field, and e and m are the charge and mass of an electron, respectively. Putting the form of $\boldsymbol{\pi}$ in Eq. 1.2.1 becomes

$$H = \frac{p^2}{2m} + V + \frac{e}{2m}(\boldsymbol{p}\cdot\boldsymbol{A} + \boldsymbol{A}\cdot\boldsymbol{p}) + \frac{e\hbar}{2m}\boldsymbol{\sigma}\cdot\boldsymbol{B} + \frac{e^2}{2m}A^2 \tag{1.2.2}$$

where $\boldsymbol{B} = \boldsymbol{\nabla}\times\boldsymbol{A}$. According to the Coulomb gauge theory, $\boldsymbol{\nabla}\cdot\boldsymbol{A} = 0$ and it can be shown that $\boldsymbol{p}\cdot\boldsymbol{A} + \boldsymbol{A}\cdot\boldsymbol{p} = 2\boldsymbol{A}\cdot\boldsymbol{p}$. So the Hamiltonian in Eq. 1.2.2 can be separated into three terms as follows

$$H = H^{(0)} + H^{(1)} + H^{(2)} \begin{cases} H^{(0)} = \frac{p^2}{2m} + V \\ H^{(1)} = \frac{e}{m}(\boldsymbol{A}\cdot\boldsymbol{p}) + \frac{e\hbar}{2m}\boldsymbol{\sigma}\cdot\boldsymbol{B} \\ H^{(2)} = \frac{e^2}{2m}A^2 \end{cases} \tag{1.2.3}$$

where $H^{(0)}$ is the Hamiltonian of an electron with a potential energy V. $H^{(1)}$ and $H^{(2)}$ are the first and second order responses to the magnetic field, respectively. Vector potential of a uniform magnetic field is given by $\boldsymbol{A} = \frac{1}{2}\boldsymbol{B}\times\boldsymbol{r}$ and putting this from into $H^{(1)}$ reduces to

$$\begin{aligned} H^{(1)} &= \frac{e}{2m}\boldsymbol{B}\times\boldsymbol{r}\cdot\boldsymbol{p} + \frac{e\hbar}{2m}2\boldsymbol{s}\cdot\boldsymbol{B} \\ &= \frac{e}{2m}\boldsymbol{B}\cdot\boldsymbol{r}\times\boldsymbol{p} + \frac{e\hbar}{2m}2\boldsymbol{s}\cdot\boldsymbol{B} \\ &= \frac{e\hbar}{2m}(\boldsymbol{B}\cdot\boldsymbol{l} + 2\boldsymbol{s}\cdot\boldsymbol{B}) \\ &= \mu_B(\boldsymbol{l}+2\boldsymbol{s})\cdot\boldsymbol{B} \end{aligned} \tag{1.2.4}$$

where $\boldsymbol{l} = \boldsymbol{r}\times\boldsymbol{p}$ is the angular momentum of an electron and $\boldsymbol{s}$ is its spin angular momentum. $H^{(1)}$ is called the Zeeman Hamiltonian $\left(H^Z\right)$, describes the splitting of the energy levels in a magnetic field. For a paramagnetic ion with N unpaired electrons, the Zeeman interaction is given by

$$\begin{aligned} H^Z &= \sum_{i=1}^{N}\mu_B(\boldsymbol{l}_i + g_e\boldsymbol{s}_i)\cdot\boldsymbol{B} \\ &= \mu_B(\boldsymbol{L}+g_e\boldsymbol{S})\cdot\boldsymbol{B} \end{aligned} \tag{1.2.5}$$

where $\boldsymbol{L}$ and $\boldsymbol{S}$ are the total orbital angular momentum and total spin angular momentum of the ion, respectively. g_e is the Landé g-factor of an electron and equals to 2.002319. From the Dirac equation of quantum mechanics, $g_e = 2$, but according to quantum electrodynamics g_e is slightly bigger than 2. The second order response Hamiltonian $H^{(2)}$ is the diamagnetic interaction term and always raises the energies of the electronic states.

1.3 Magnetic moments

The quantity $-\mu_B(\boldsymbol{L}+g_e\boldsymbol{S})$ in Eq. 1.2.5 is the total electronic magnetic moment $\boldsymbol{m}$ of the system,

$$\boldsymbol{m} = -\mu_B(\boldsymbol{L}+g_e\boldsymbol{S}) \tag{1.3.1}$$

$$= \boldsymbol{m}^L + \boldsymbol{m}^S \tag{1.3.2}$$

where $\boldsymbol{m}^L = -\mu_B \boldsymbol{L}$ is the total orbital magnetic moment and $\boldsymbol{m}^S = -g_e \mu_B \boldsymbol{S}$ is the total spin magnetic moment. In case of SOC[1], L and S are not good quantum numbers but $J = L+S$ is and according to Landé's theorem,

$$\mu_B \left(\boldsymbol{L} + g_e \boldsymbol{S}\right) \quad = \quad \mu_B g_J \boldsymbol{J} \tag{1.3.3}$$

where $g_J = 1 + \frac{J(J+1)+S(S+1)-L(L+1)}{2J(J+1)}$ is the Landé g-factor of a paramagnetic ion.
If a strong external magnetic field $\boldsymbol{B} = B_0 \boldsymbol{z}$ is given, the magnetic moments of all the paramagnetic centers will be along z direction and in that case $\boldsymbol{m} = -\mu_B g_J \boldsymbol{J}_z$. The induced magnetic moment $\langle m \rangle$ per particle is given by the expectation value,

$$\langle m \rangle \quad = \quad -\mu_B g_J \langle J_z \rangle \tag{1.3.4}$$

where

$$\langle J_z \rangle = \frac{\sum_{J,M_J} \left\langle J, M_J \left| \hat{J}_z \right| J, M_J \right\rangle \exp\left(-E_{J,M_J}/k_B T\right)}{\sum_{J,M_J} \exp\left(-E_{J,M_J}/k_B T\right)} \tag{1.3.5}$$

$|J, M_J\rangle$ are the eigenstates of $\hat{J}_z$ with the corresponding energies E_{J,M_J}. If the energy splitting of all the M_J states is less than the thermal energy $k_B T$ (k_B, the Boltzmann constant) i.e. $\mu_B g_J M_J B_0 \ll k_B T$, then one can consider $\exp\left(-E_{J,M_J}/k_B T\right) \approx \left(1 - \mu_B g_J M_J B_0/k_B T\right)$ and Eq. 1.3.5 becomes

$$\langle J_z \rangle \quad = \quad -\frac{\mu_B g_J B_0}{3 k_B T} J(J+1) \tag{1.3.6}$$

The induced magnetic moment per mol m_{ind} is given by

$$m_{ind} \quad = N_A \langle m \rangle = \quad \frac{N_A \mu_B^2 g_J^2 B_0}{3 k_B T} J(J+1) \tag{1.3.7}$$

1.4 Magnetization and magnetic susceptibility

The molar magnetization M is the induced magnetic moment per mole. The molar magnetic susceptibility χ_m $\left(\text{in } \text{m}^3\text{mol}^{-1}\right)$ is defined as

$$\chi_m \quad = \quad \frac{\mu_0 M}{B_0} = \frac{\mu_0 m_{ind}}{B_0} = \frac{\mu_0 N_A \langle m \rangle}{B_0} \tag{1.4.1}$$

Substituting Eq. 1.3.7 in Eq. 1.4.1 reduces to the Curie's law of magnetic susceptibility

$$\chi_m \quad = \quad \frac{N_A \mu_0 \mu_B^2 g_J^2}{3 k_B T} J(J+1) \tag{1.4.2}$$

[1]List of abbreviations is given at the beginning of the thesis.

Note that according to Curie's law, magnetic susceptibility behaves with temperature as a function of $1/T$.

1.5 Origin of magnetic anisotropy

In the lanthanide complexes, the anisotropic magnetic susceptibility originates from the crystal field splitting of the ground J manifold. The model Hamiltonian which describes the crystal field and Zeeman splittings of a J manifold is written as

$$\hat{H}^{mod} = \sum_{k=2,4,6} \alpha_J^k \sum_{q=-k}^{k} B_q^k \hat{O}_q^k(J) + \mu_B g_J \hat{\boldsymbol{J}} \cdot \boldsymbol{B}_0 \tag{1.5.1}$$

where $\hat{O}_q^k$ are the Stevens operators acting on the J manifold of the ion, B_q^k the CFPs (in Wybourne convention [35]), $\alpha_J^k = \langle J \| \alpha^k \| J \rangle$ the reduced matrix elements of the second ($k=2$), fourth ($k=4$), and sixth ($k=6$) orders and are determined by number of the f electrons N, L and J. α_J^k are tabulated in the book of Abragam and Bleaney [36]. In Stevens notation, each $\hat{O}_q^k$ is expressed by the Cartesian components $\hat{J}_x$, $\hat{J}_y$, $\hat{J}_z$ and their linearly independent multiplicative terms or in terms of the ladder operators $\hat{J}_\pm$ and their higher order forms. For example, $\hat{O}_0^2 = 3\hat{J}_z^2 - J(J+1)$, $\hat{O}_2^2 = \frac{1}{2}\left(\hat{J}_+^2 + \hat{J}_-^2\right) = \left(\hat{J}_x^2 - \hat{J}_y^2\right)$. According to Eq. 1.5.1, in principle, there are 27 CFPs for open shell f complexes. However, the number of parameters highly decreases with increasing the symmetry of the crystal environment. For example, in the cubic environment such as in O_h symmetry, only two independent parameters are required, in an axial symmetry only three parameters are left: B_0^2, B_0^4 and B_0^6. In the 1970s, Bleaney had derived the anisotropic magnetic susceptibility for the axial Ln complexes with considering the term of second order only, with the evaluation of the matrix element as

$$\left\langle J, M_J \left| \hat{H}^{mod} \right| J, M_J \right\rangle = \left\langle J, M_J \left| \sum_{k=2} \alpha_J^2 \sum_{q=-2}^{2} B_q^2 \hat{O}_q^2 + \mu_B g_J B_0 \hat{\boldsymbol{J}} \right| J, M_J \right\rangle \tag{1.5.2}$$

When the crystal field splitting is less than room temperature energy, the expressions of the magnetic susceptibilities obtained by Bleaney [17] are summarized as follows

$$\chi_{m,zz} = N_A \mu_0 \mu_B^2 g_J^2 \left[\frac{J(J+1)}{3k_B T} - \frac{B_0^2 \langle J \| \alpha \| J \rangle}{30 k_B^2 T^2} J(J+1)(2J-1)(2J+3) \right] \tag{1.5.3}$$

$$\chi_m = \frac{N_A \mu_0 \mu_B^2 g_J^2}{3k_B T} J(J+1) \tag{1.5.4}$$

B_0^2 is the 2nd order axial CPF. The anisotropic magnetic susceptibility defined as $\Delta\chi_{ax}^B = \chi_{m,zz} - \chi_m$ is given by

$$\Delta\chi_{ax}^B = -\frac{N_A \mu_0 \mu_B^2 B_0^2}{30 k_B^2 T^2} \langle J \| \alpha \| J \rangle g_J^2 J(J+1)(2J-1)(2J+3) \tag{1.5.5}$$

Note that according to Bleaney's theory within a given J manifold, χ_m is still a function of

$1/T$ i.e. reduces to Curie's law, but the crystal field splitting results in an anisotropic magnetic moments and in the case of axial symmetry, the anisotropic magnetic susceptibility follows $1/T^2$ dependency. Moreover, interaction with the excited manifolds might introduce additional terms (quite important for Sm^{III} complexes) as shown also by Bleaney and the CFPs of 4th and 6th order might be needed for a better description [37, 38, 39]. Additionally, Bleaney's theory is based on the cancellation of magnetic anisotropy of an individual state by the others due to the substantial population in all the states of a J manifold (quite true for Ln), but if the splitting is larger (such as for An) and high anisotropy in the effective g-factors will result in anisotropic magnetization.

1.6 The hyperfine interaction

The hyperfine interaction is the response of the unpaired electrons to the tiny magnetic field produced by nucleus K with the nuclear spin $I_K \neq 0$. The nuclear magnetic dipole moment of the nucleus, $\boldsymbol{\mu}_K = \mu_N g_K \boldsymbol{I}_K$ (g_K is the g-factor of the nucleus, μ_N the nuclear magneton) produces a magnetic field at position $\boldsymbol{r}$,

$$\boldsymbol{B}_K = -\frac{\mu_0}{4\pi r^3}\left(\boldsymbol{\mu}_K - 3\frac{\boldsymbol{r}\left(\boldsymbol{\mu}_K \cdot \boldsymbol{r}\right)}{r^2}\right) + \frac{2}{3}\mu_0 \boldsymbol{\mu}_K \delta\left(\boldsymbol{r}\right) \tag{1.6.1}$$

where $\delta\left(\boldsymbol{r}\right)$ is the Kronecker symbol i.e. vanishes everywhere except $r = 0$, at the position of the nucleus. The electronic magnetic moment of the paramagnetic center $\boldsymbol{m}$ interacts with the above magnetic field and this tiny interaction is solely responsible for the additional chemical shift in the NMR spectrum.

1.6.1 The dipolar interaction

We can place the paramagnetic center at the origin such that we can write Eq. 1.6.1 in terms of $\boldsymbol{r}_K$. In the point dipole approximation, the first term of $\boldsymbol{B}_K$ is responsible for the through-space classical magnetic dipole-dipole interaction,

$$E_K^{dip} = \boldsymbol{m} \cdot \frac{\mu_0}{4\pi r_K^3}\left(\boldsymbol{\mu}_K - 3\frac{\boldsymbol{r}_K\left(\boldsymbol{\mu}_K \cdot \boldsymbol{r}_K\right)}{r^2}\right) \tag{1.6.2}$$

$$= -\frac{\mu_0}{4\pi}\boldsymbol{m} \cdot \mathbf{T}_K \cdot \boldsymbol{\mu}_K \tag{1.6.3}$$

where $\mathbf{T}_K = r_K^{-5}\left(3\mathbf{r}_K \otimes \mathbf{r}_K - \mathbf{U}r_K^2\right)$ ($\otimes$ denotes Kronecker product) is the geometric tensor of nucleus K and $\mathbf{U}$ is the unit tensor. If the position vector of the nucleus $\boldsymbol{r}_K$ is expressed with the three Cartesian coordinates (x_K, y_K, z_K), then the geometric tensor $\mathbf{T}_K$ is the 3×3

matrix expressed as

$$T_K = r_K^{-5} \begin{pmatrix} 3x_K^2 - r_K^2 & 3x_K y_K & 3x_K z_K \\ 3y_K x_K & 3y_K^2 - r_K^2 & 3y_K z_K \\ 3z_K x_K & 3z_K y_K & 3z_K^2 - r_K^2 \end{pmatrix} \tag{1.6.4}$$

where $r_K = \sqrt{x_K^2 + y_K^2 + z_K^2}$ is the distance of the nucleus K to the paramagnetic center.

1.6.2 The contact interaction

The last term of $\boldsymbol{B}_K$ in Eq. 1.6.1 is giving rise to the contact interaction as this interaction is only possible when the unpaired electrons are in contact with the nucleus i.e. in quantum chemistry language if the spin population resides at the position of the nucleus. In a paramagnetic complex, spin population on the ligand atom K arises due to the through bond spin delocalization and for atoms farther from paramagnetic center, spin polarization plays the dominant role for introducing spin. If the spin population is in the s orbitals of the atom K, it has a finite probability to come in contact with the nucleus. One can then only focus on the spin magnetic moment $\boldsymbol{m}^S$ as the orbital angular momentum of an s orbital is zero. The contact interaction is given by,

$$E_K^c = -\boldsymbol{m}^S \cdot \frac{2}{3}\mu_0 \boldsymbol{\mu}_K \delta(\boldsymbol{r}_K) \tag{1.6.5}$$

$$= \frac{2}{3}\mu_0 \mu_B \mu_N g_e g_K \boldsymbol{I}_K \cdot \boldsymbol{S}\delta(\boldsymbol{r}_K) \tag{1.6.6}$$

Eq. 1.6.6 gives a non-zero interaction only at the position of the nucleus.

It is important to note that the hyperfine interaction discussed here is from a classical non-relativistic perspective. There is no term with a delta function in the minimally coupled four-component relativistic Dirac theory or non-relativsitic Lévy-Leblond theory [40] for an electron, hence there is no contact interaction. In fact, the first order interaction terms in the two-component theory derived from the four-component Dirac equation or the Lévy-Leblond equation naturally lead to the contact interaction [41]. Also, depending on how the four-component Dirac theory is reduced to the two-component method, the mathematical forms of hyperfine operators in the two-component methods vary from one to the other. The so called "picture change effects" of the hyperfine interaction can be found in Refs. [42, 43, 44]. Relativistic effects are minimal in the case of light atoms (AIS are discussed for light atoms throughout this thesis), so we can reasonably emphasis on the non-relativistic level of theory.

1.7 Tensor representation

In molecular physics, tensors are used to describe the anisotropic magnetic properties (i.e. the value changes with direction). A second rank tensor $\mathbf{P}$ can be a matrix whose elements are the products of the Cartesian components of two vectors $\boldsymbol{a}$ and $\boldsymbol{b}$ i.e. $\mathbf{P} = \boldsymbol{a} \otimes \boldsymbol{b} = \sum_{ij} p_{ij} \boldsymbol{i} \otimes \boldsymbol{j}$ and $p_{ij} = a_i b_j$; $i, j \in x, y, z$

$$\mathbf{P} = \begin{bmatrix} p_{xx} & p_{xy} & p_{xz} \\ p_{yx} & p_{yy} & p_{yz} \\ p_{zx} & p_{zy} & p_{zz} \end{bmatrix} \tag{1.7.1}$$

Any rotation in the spatial coordinates affects the matrix $\mathbf{P}$. So if $\mathbf{R}$ is the rotation matrix which transforms the spatial coordinates of the system, then in the new coordinates new matrix $\mathbf{P}^R$ is given by

$$\mathbf{P}^R = \mathbf{R}^T \mathbf{P} \mathbf{R} \tag{1.7.2}$$

where the superscript 'T' indicates a transpose operation. For any symmetric tensor, $p_{ij} = p_{ji}$ and it is possible to find a reference frame where $\mathbf{P}$ is diagonal i.e. it takes the form,

$$\begin{bmatrix} \tilde{p}_{11} & 0 & 0 \\ 0 & \tilde{p}_{22} & 0 \\ 0 & 0 & \tilde{p}_{33} \end{bmatrix} \tag{1.7.3}$$

This frame is called the principal axes frame (PAF), the main axes (which are the eigenvectors of $\mathbf{P}$) are the principal directions of the tensor and the diagonal values (which are the eigenvalues of $\mathbf{P}$) are the principal components of the tensor. In an anisotropic case, the properties are characterized by axiality and rhombicity. If one of the principal components are significantly larger/smaller than the other two, let's assume $\tilde{p}_{11} \leq \tilde{p}_{22} \ll \tilde{p}_{33}$, then the axiality is defined by $\Delta p_{ax} = \tilde{p}_{33} - \frac{\tilde{p}_{11}+\tilde{p}_{22}}{2}$, in this case the anisotropy is prolate, $\Delta p_{ax} > 0$. In the case, when $\tilde{p}_{33}$ is very small compared to others two, $\Delta p_{ax} < 0$, the anisotropy is oblate. The rhombicity is taken as $\delta p_{rh} = \tilde{p}_{22} - \tilde{p}_{11}$. In case of axial symmetry (with a rotational symmetry axis of order $n > 2$ such that x, y belong to the same irrep), axiality is assigned w.r.t. the symmetry axis (z axis). So for example, if the principal axis of $\tilde{p}_{33}$ is along the symmetry axis, $\tilde{p}_{33}$ is designated as $\tilde{p}_{\parallel}$ and $\tilde{p}_{\perp} = \frac{\tilde{p}_{11}+\tilde{p}_{22}}{2}$ and the anisotropic property of the tensor is given by $\Delta p_{ax} = \tilde{p}_{\parallel} - \tilde{p}_{\perp}$; if $\tilde{p}_{\parallel} > \tilde{p}_{\perp}$, $\Delta p_{ax} > 0$, the anisotropy is axial and if $\tilde{p}_{\parallel} < \tilde{p}_{\perp}$, $\Delta p_{ax} < 0$, it is planar.

1.8 Spin Hamiltonian formalism

In the domain of molecular magnetic properties, spin Hamiltonian (which is a model Hamiltonian) is routinely used to interpret the magnetic information of a molecule (or solid) that can be obtained from the paramagnetic resonance spectra or performing *ab initio* calculations. A typical EPR spectra of a molecule is rather complex and a model Hamiltonian is used to fit it. Since the model Hamiltonian uses spin operators only and hence the name, the matrix elements of the spin operators can be computed easily from a suitable spin manifold using the spin algebra. In quantum chemistry, the general purpose of introducing spin Hamiltonian or any model Hamiltonian is to project all the complicated details associated with the solutions of an "exact" Hamiltonian that are difficult to digest (to understand), into the few terms of the model Hamiltonian. The advantages of using such a model Hamiltonian are: 1) It can be system-specific and the same symmetry selection rules as for the crystal field applies and can be readily adopted. 2) A complete description (of course depends on up to which extent one desires) of the system is possible by means of few terms. 3) More specifically the parameters associated with the terms that effectively includes the underlying physics are easily comparable from one system to another. Crystal field Hamiltonian introduced previously (also in chapter 5, Eq. 5.1.1) is such a model Hamiltonian that effectively includes all the information associated to a ground J manifold into the CFPs.

Inspired by the terms of an actual Hamiltonian, the terms in the spin Hamiltonian are considered and there is always space to add necessary terms in a spin Hamiltonian for a meaningful projection of the information. Apart from those before-mentioned, perhaps the great advantage of using spin Hamiltonian to model the molecular magnetic properties is that the parameters associated are usually rank-2 tensors those best suit for the description of both the isotropic and anisotropic properties. The spin Hamiltonian parameters obtained from the experiment are used to compare with the values obtained from *ab initio* calculations. The parameters need to be comparable first and serve as a common ground for both the experimentalists and theoreticians to build up the critical discussions from each side. That is why, in the last two decades, with the advent of quantum chemistry methods, much interest in the molecular magnetic properties were put forward in the first principle computations of the spin Hamiltonian parameters [45].

It is to be noted here that the model space of a spin Hamiltonian has nothing to do with the real spin of a system. Usually to avoid confusion, the desired *ab initio* states are modeled by a pseudospin $\tilde{S}$. Thus, a set of $2\tilde{S}+1$ *ab initio* states $\{|\Psi_I\rangle\}$ of an actual Hamiltonian has the corresponding model space $\left\{\left|\tilde{S},M_{\tilde{S}}\right\rangle\right\}, M_{\tilde{S}} = -\tilde{S}, -\tilde{S}+1, .., +\tilde{S}$ in the spin Hamiltonian formalism. For example, a Kramers doublet (KD) of an odd number of unpaired-electrons' system is modeled by a pseudospin $\tilde{S} = 1/2$ and the model space of the KD is spanned by the pseudospin vectors $\{|1/2,+1/2\rangle, |1/2,-1/2\rangle\}$.

A set of triplet states is described by pseudospin $\tilde{S}=1$ and quartet states by $\tilde{S}=3/2$. When the zero-field splitting is too large, a quartet manifold breaks down into a problem with two KDs where each of the KD is described with pseudospin $\tilde{S}=1/2$. The most crucial step associated with spin Hamiltonian theory is to find out the one-to-one correspondence between the model states $\left|\tilde{S},M_{\tilde{S}}\right\rangle$ with the *ab initio* eigenstates $|\Psi_I\rangle$.

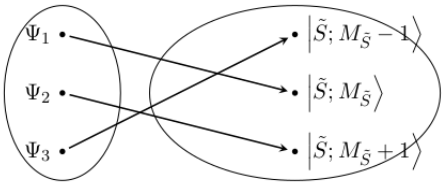

Figure 1.8.1: A graphical scheme is provided to show the one-to-one correspondences between the *ab initio* states and model states.

This is usually achieved by performing some transformations. As an example, it can be done by transforming the *ab initio* magnetic moment matrices $\mathbf{M}_z$, $\mathbf{M}_y$ and $\mathbf{M}_x$ in the set of the $\{|\Psi_I\rangle\}$ and correlating them with the magnetic moment matrices computed in the model space. In the model space $\left\{\left|\tilde{S},M_{\tilde{S}}\right\rangle\right\}$, $\mathbf{M}_z$ is diagonal, so after diagonalizing the *ab initio* $\mathbf{M}_z$, a one-to-one correspondence can be performed with the model $\mathbf{M}_z$; and the eigenvectors of the *ab initio* $\mathbf{M}_z$ are the *ab initio* counterparts $\left\{|\Psi_I\rangle^{AI}\right\}$ of the model states $\left\{\left|\tilde{S},M_{\tilde{S}}\right\rangle\right\}$. A phase factor must be assigned to $\left\{|\Psi_I\rangle^{AI}\right\}$ such that the off-diagonal elements of $\mathbf{M}_x$ and $\mathbf{M}_y$ become real and imaginary, respectively [39], as it is the case in the model space.

Now we want to be familiar with some of the terms considered in the spin Hamiltonian those are used to return all the interactions of the actual Hamiltonian. For example, a convenient way to handle the molecular Zeeman interaction in Eq. 1.2.5 is that of defining a tensor $\mathbf{g}$ which effectively includes the coupling of the electronic magnetic moment $\boldsymbol{m}$ with the external magnetic field $\boldsymbol{B}_0$. The corresponding Zeeman interaction term of Eq. 1.2.5 in the spin Hamiltonian formalism is given by

$$\hat{H}_s^Z = \mu_B \hat{\boldsymbol{S}}\cdot\mathbf{g}\cdot\boldsymbol{B}_0 \tag{1.8.1}$$

In case of a KD, the *ab initio* molecular wave functions $\left\{\Phi,\bar{\Phi}\right\}$ are modeled by pseudospin vectors $\{|1/2,+1/2\rangle,|1/2,-1/2\rangle\}$ and so the representation matrices of $\hat{\boldsymbol{S}}$ in Eq. 1.8.1 are the three Pauli spin matrices $\boldsymbol{\sigma}_l$, $l=x,y,z$. The $\mathbf{g}$ tensor of a KD can be obtained as

$$\frac{\delta}{\delta B_{0,k}}\begin{pmatrix}\langle\Phi|\hat{H}^Z|\Phi\rangle & \langle\Phi|\hat{H}^Z|\bar{\Phi}\rangle\\ \langle\bar{\Phi}|\hat{H}^Z|\Phi\rangle & \langle\bar{\Phi}|\hat{H}^Z|\bar{\Phi}\rangle\end{pmatrix}=\frac{1}{2}\mu_B\sum_l g_{lk}\boldsymbol{\sigma}_l \tag{1.8.2}$$

Likewise, the hyperfine interaction term is modeled by

$$\hat{H}_s^{Hyp} = \hat{\boldsymbol{S}}\cdot\mathbf{A}_K\cdot\boldsymbol{I}_K \tag{1.8.3}$$

and similarly for a KD, the hyperfine coupling tensor $\mathbf{A}_K$ can be obtained as

$$\frac{\delta}{\delta I_{K,k}}\begin{pmatrix} \left\langle \Phi \middle| \hat{H}_K^{Hyp} \middle| \Phi \right\rangle & \left\langle \Phi \middle| \hat{H}_K^{Hyp} \middle| \bar{\Phi} \right\rangle \\ \left\langle \bar{\Phi} \middle| \hat{H}_K^{Hyp} \middle| \Phi \right\rangle & \left\langle \bar{\Phi} \middle| \hat{H}_K^{Hyp} \middle| \bar{\Phi} \right\rangle \end{pmatrix} = \frac{1}{2}\sum_l A_{K,lk}\boldsymbol{\sigma}_l \tag{1.8.4}$$

where $\hat{H}_K^{Hyp}$ comprises both the dipolar and contact interaction terms (Eqs. 1.6.3, 1.6.6), $\hat{H}_K^{Hyp} = \hat{H}_K^{dip} + \hat{H}_K^{c}$. $\mathbf{A}_K$ can be further divided into the dipolar $\mathbf{A}_K^{dip}$ and the Fermi contact $\mathbf{A}_K^{c}$ contributions. Comparing with Eqs. 1.6.3, the dipolar hyperfine coupling tensor can be calculated as

$$\frac{\delta}{\delta I_{K,k}}\begin{pmatrix} \left\langle \Phi \middle| \hat{H}_K^{dip} \middle| \Phi \right\rangle & \left\langle \Phi \middle| \hat{H}_K^{dip} \middle| \bar{\Phi} \right\rangle \\ \left\langle \bar{\Phi} \middle| \hat{H}_K^{dip} \middle| \Phi \right\rangle & \left\langle \bar{\Phi} \middle| \hat{H}_K^{dip} \middle| \bar{\Phi} \right\rangle \end{pmatrix} = \frac{1}{2}\sum_l A_{K,lk}^{dip}\boldsymbol{\sigma}_l \tag{1.8.5}$$

$$-\frac{\mu_0 g_K \mu_N}{4\pi}\begin{pmatrix} \left\langle \Phi \middle| \sum_l \hat{m}_l T_{K,lk} \middle| \Phi \right\rangle & \left\langle \Phi \middle| \sum_l \hat{m}_l T_{K,lk} \middle| \bar{\Phi} \right\rangle \\ \left\langle \bar{\Phi} \middle| \sum_l \hat{m}_l T_{K,lk} \middle| \Phi \right\rangle & \left\langle \bar{\Phi} \middle| \sum_l \hat{m}_l T_{K,lk} \middle| \bar{\Phi} \right\rangle \end{pmatrix} = \frac{1}{2}\sum_l A_{K,lk}^{dip}\boldsymbol{\sigma}_l \tag{1.8.6}$$

and comparing with 1.6.6, the contact coupling parameters are calculated as

$$\frac{\delta}{\delta I_{K,k}}\begin{pmatrix} \left\langle \Phi \middle| \hat{H}_K^{c} \middle| \Phi \right\rangle & \left\langle \Phi \middle| \hat{H}_K^{c} \middle| \bar{\Phi} \right\rangle \\ \left\langle \bar{\Phi} \middle| \hat{H}_K^{c} \middle| \Phi \right\rangle & \left\langle \bar{\Phi} \middle| \hat{H}_K^{c} \middle| \bar{\Phi} \right\rangle \end{pmatrix} = \frac{1}{2}\sum_l A_{K,lk}^{c}\boldsymbol{\sigma}_l \tag{1.8.7}$$

$$\frac{2}{3}\mu_0\mu_B\mu_N g_e g_K \begin{pmatrix} \sum_i^{occ} \left\langle \phi_i \middle| \boldsymbol{\sigma}_k \delta\left(\boldsymbol{r}_K\right) \middle| \phi_i \right\rangle & \sum_i^{occ} \left\langle \phi_i \middle| \boldsymbol{\sigma}_k \delta\left(\boldsymbol{r}_K\right) \middle| \bar{\phi}_i \right\rangle \\ \sum_i^{occ} \left\langle \bar{\phi}_i \middle| \boldsymbol{\sigma}_k \delta\left(\boldsymbol{r}_K\right) \middle| \phi \right\rangle & \sum_i^{occ} \left\langle \bar{\phi}_i \middle| \boldsymbol{\sigma}_k \delta\left(\boldsymbol{r}_K\right) \middle| \bar{\phi}_i \right\rangle \end{pmatrix} = \sum_l A_{K,lk}^{c}\boldsymbol{\sigma}_l \tag{1.8.8}$$

In Eq. 1.8.7, Φ and $\bar{\Phi}$ are considered as single-determinants, ϕ_i the occupied two-component molecular spinors, $\phi_i = \begin{pmatrix} \phi_{i,a} \\ \phi_{i,b} \end{pmatrix}$. For $\boldsymbol{\sigma}_z$,

$$\sum_i^{occ} \left\langle \phi_i \middle| \boldsymbol{\sigma}_z \delta\left(\boldsymbol{r}_K\right) \middle| \phi_i \right\rangle = \sum_i^{occ} \left(\phi_{i,a}^* \phi_{i,a} \delta\left(\boldsymbol{r}_K\right) - \phi_{i,b}^* \phi_{i,b} \delta\left(\boldsymbol{r}_K\right) \right) \tag{1.8.9}$$

In the non-relativistic theory, $\phi_{i,a}$ and $\phi_{i,b}$ can be replaced by the spin orbitals ϕ_i^α and ϕ_i^β (α and β are the spin functions),

$$\sum_i^{occ} \left(\phi_i^{\alpha *} \phi_i^\alpha \delta\left(\boldsymbol{r}_K\right) - \phi_i^{\beta *} \phi_i^\beta \delta\left(\boldsymbol{r}_K\right) \right) = \sum_i^{occ} \left(\rho_i^\alpha\left(\boldsymbol{r}_K\right) - \rho_i^\beta\left(\boldsymbol{r}_K\right) \right) = \rho^s\left(\boldsymbol{r}_K\right) \tag{1.8.10}$$

where $\rho^s\left(\boldsymbol{r}_K\right)$ is the total spin density at the position of nucleus K. Pell *et al.* discussed that for a paramagnetic complex with multiple delocalized electrons, the Fermi hyperfine coupling constant should be divided with the number of unpaired electrons, $N = 2S$, in order to compare between different paramagnetic complexes i.e. the isotropic Fermi contact coupling constant per unpaired electron is given by

$$A_K^c = \frac{2}{3N}\mu_0\mu_B\mu_N g_e g_K \rho^s\left(\boldsymbol{r}_K\right) \tag{1.8.11}$$

Eq. 1.8.11 can be better used in a sense of comparing spin densities at nucleus K per

unpaired electron, $\frac{\rho^s(\boldsymbol{r}_K)}{N}$. The trend of spin delocalization in an isostructural series can be discussed in terms of the spin densities and can be used as a probe of covalency.

Chapter 2

Theoretical aspects and quantum chemical methodology

In the previous chapter, we have introduced the basic concepts of the magnetic properties and became familiar with the hyperfine interactions responsible for the pNMR shifts. In this chapter, we will deal with the theoretical aspects of pNMR shifts such as: a) first principle descriptions of the origin of the magnetic susceptibility and pNMR shifts, b) modeling of them in terms of spin Hamiltonian parameters, and c) the quantum chemical methods to calculate them *ab initio*. At this point, it is worthy to mention that the first principle description of the NMR shielding tensor was first developed by Ramsey in the 1950s for a system with a non-degenerate ground state [47]. His development can be fully realized for diamagnetic systems like the organic molecules or closed-shell main-group inorganic systems.

When an external magnetic field is applied, the electronic energy states undergo Zeeman splitting as developed in section 1.2, similarly nucleus K with nuclear spin $\boldsymbol{I}_K > 0$ shows nuclear Zeeman splitting. In the NMR technique, external electromagnetic frequencies are provided to resonate the nuclei and a detector collects the signal. From a theoretical point of view, interaction with a magnetic field adds additional energies (energy contributions from $H^{(1)}$ and $H^{(2)}$ in Eq. 1.2.3) to the non-perturbed electronic states of a system i.e. with the eigenvalues of $H^{(0)}$. It was Ramsey's genius idea to take the nuclear magnetic moment $\boldsymbol{\mu}_K$ and the external magnetic field $\boldsymbol{B}_0$ as perturbations, and ultimately expressing the additional energy terms with the help of perturbation theory. According to his theory, the electronic ground state energy of a non-degenerate system can be expanded as

$$E\left(\boldsymbol{\mu}_K, \boldsymbol{B}_0\right) = E_0 + \sum_{ij} \left.\frac{\partial^2 E}{\partial B_{0,i} \partial \mu_{K,j}}\right|_0 B_{0,i}\mu_{K,j} + \ldots \tag{2.0.1}$$

provided that both the perturbations $\boldsymbol{B}_0$ and $\boldsymbol{\mu}_K$ are quite small and $i, j \in x, y, z$. E_0 is the non-perturbed electronic ground state energy i.e. in the absence of any magnetic

field $(\boldsymbol{B}_0, \boldsymbol{\mu}_K)$. The coefficients of the above expansion are the components of the (3×3) shielding tensor $\boldsymbol{\sigma}_K$,

$$\sigma_{K,ij} = \left.\frac{\partial^2 E}{\partial B_{0,i} \partial \mu_{K,j}}\right|_0 \tag{2.0.2}$$

Thus the shielding tensor can be calculated as a second derivative of the energy. If there are more than one nucleus, the associated Taylor expansion terms can be added to the above ones and the shielding tensors are calculated in the same fashion.

2.1 Magnetic properties from the response terms

To include the effect of temperature on the pNMR shifts, Soncini and Van den Heuvel considered the Helmholtz free energy (F) of the system, $F = U - TS$, (U, internal energy and S, entropy of a system) instead of the electronic energy E as considered by Ramsey in Eq. 2.0.1 and the corresponding Taylor expansion becomes [29]

$$F(\boldsymbol{\mu}_K, \boldsymbol{B}_0) \quad = \quad F_0 + \sum_{ij} \left.\frac{\partial^2 F}{\partial B_{0,i} \partial \mu_{K,j}}\right|_0 B_{0,i} \mu_{K,j} + .. \tag{2.1.1}$$

The shielding tensor of a paramagnetic system is calculated as a second partial derivative of the Helmholtz free energy,

$$\sigma_{K,ij} = \left.\frac{\partial^2 F}{\partial B_{0,i} \partial \mu_{K,j}}\right|_0 \tag{2.1.2}$$

Soncini and Van den Heuvel concluded that the expansion terms w.r.t. the free energy have more promises, such as they can handle a paramagnetic system with degenerate energy states. The above kind of expansion w.r.t. F is more general in a sense that one can follow the line to define other magnetic properties such as magnetic susceptibility χ where the Taylor expansion is expressed with the components of the external magnetic field $\boldsymbol{B}_{0,i=x,y,z}$

$$F = F_0 + \sum_{ij} \left.\frac{\partial^2 F}{\partial B_{0,i} \partial B_{0,j}}\right|_0 B_{0,i} B_{0,j} + .. \tag{2.1.3}$$

and the expansion coefficients are the components of the susceptibility tensor, $\chi_{ij} = \left.\frac{\partial^2 F}{\partial B_{0,i} \partial B_{0,j}}\right|_0$. Similarly one can also define the nuclear magnetic resonance parameter $J_{KK'}$ (nuclear spin-spin coupling parameter) where one expands the additional energy terms as

$$F = F_0 + \sum_{ij} \left.\frac{\partial^2 F}{\partial \mu_{K,i} \partial \mu_{K',j}}\right|_0 \mu_{K,i} \mu_{K',j} + .. \tag{2.1.4}$$

where $J_{KK',ij} = \frac{\partial^2 F}{\partial \mu_{K,i} \partial \mu_{K',j}}\Big|_0$ are the components of the coupling tensor $\mathbf{J}_{KK'}$. Reminded that all the parameters mentioned above are essentially tensors and the isotropic value is one-third of the trace.

2.2 Sum-over-states formulations of the magnetic properties

Already we have seen that the magnetic properties are essentially the coefficients of the energy correction terms. One of the prescribed ways to calculate these second partial derivatives from the first principles is to express them as sum-over-states formulations. Soncini and Van den Heuvel brilliantly expressed the shielding tensors in a paramagnetic complex, and the final expression of their derivation is given below [29]

$$\begin{aligned}\sigma_{K,ij} &= \frac{1}{Q_0}\sum_n e^{-\beta E_n}\left[\sum_\nu \left\langle n\nu \left| D_{ij} \right| n\nu \right\rangle + \beta \sum_{\nu,\nu'} \left\langle n\nu|\hat{m}_i|n\nu' \right\rangle \left\langle n\nu'|\hat{F}_{K,j}|n\nu \right\rangle \right. \\ &\quad \left. +2\sum_{m\neq n}\sum_{\nu,\mu} \frac{\sum_{\nu,\nu'} \langle n\nu|\hat{m}_i|m\mu\rangle \langle m\mu|\hat{F}_{K,j}|n\nu\rangle}{E_m - E_n}\right] \qquad (2.2.1) \\ &= \sigma^{dia}_{K,ij} + \frac{1}{Q_0}\sum_n e^{-\beta E_n}\left[\beta \sum_{\nu,\nu'} \left\langle n\nu|\hat{m}_i|n\nu' \right\rangle \left\langle n\nu'|\hat{F}_{K,j}|n\nu \right\rangle \right. \\ &\quad \left. +2\sum_{m\neq n}\sum_{\nu,\mu} \frac{\sum_{\nu,\nu'} \langle n\nu|\hat{m}_i|m\mu\rangle \langle m\mu|\hat{F}_{K,j}|n\nu\rangle}{E_m - E_n}\right] \qquad (2.2.2)\end{aligned}$$

where Q_0 is the partition function in absence of the perturbations $(\boldsymbol{B}_0, \boldsymbol{\mu}_K)$, $\hat{\boldsymbol{m}}$ the electronic magnetic moment operator, $\hat{\boldsymbol{F}_K}$ related to the hyperfine coupling operator of nucleus K, $\hat{D}_{ij}$ gives the diamagnetic shielding contribution and $\beta = \frac{1}{k_B T}$. $|n\nu\rangle$, $|m\mu\rangle$ are the eigenstates of the non-perturbative Hamiltonian with eigenvalues E_n, E_m, respectively and ν, μ indicate their degenerate components. The diamagnetic shielding tensor in Eq. 2.2.2 is defined as $\sigma^{dia}_{K,ij} = \frac{1}{Q_0}\sum_n e^{-\beta E_n}\sum_\nu \left\langle n\nu \left| D_{ij} \right| n\nu \right\rangle$. The paramagnetic shielding as defined previously excludes the diamagnetic part from the total shielding, $\sigma^p_K = \sigma_K - \sigma^{dia}_K$ and each component of the paramagnetic shielding tensor is,

$$\begin{aligned}\sigma^p_{K,ij} &= \frac{1}{Q_0}\sum_n e^{-\beta E_n}\left[\beta \sum_{\nu,\nu'} \left\langle n\nu|\hat{m}_i|n\nu' \right\rangle \left\langle n\nu'|\hat{F}_{K,j}|n\nu \right\rangle \right. \\ &\quad \left. +2\sum_{m\neq n}\sum_{\nu,\mu} \frac{\sum_{\nu,\nu'} \langle n\nu|\hat{m}_i|m\mu\rangle \langle m\mu|\hat{F}_{K,j}|n\nu\rangle}{E_m - E_n}\right] \qquad (2.2.3)\end{aligned}$$

Similarly the paramagnetic susceptibility tensor $\boldsymbol{\chi}$ can be calculated on the same line as

$$\begin{aligned}\chi_{ij} &= \frac{1}{Q_0}\sum_n e^{-\beta E_n}\left[\beta\sum_{\nu,\nu'}\left\langle n\nu|\hat{m}_i|n\nu'\right\rangle\left\langle n\nu'|\hat{m}_j|n\nu\right\rangle\right. \\ &\left. +2\sum_{m\neq n}\sum_{\nu,\mu}\frac{\Sigma_{\nu,\nu'}\left\langle n\nu|\hat{m}_i|m\mu\right\rangle\left\langle m\mu|\hat{m}_j|n\nu\right\rangle}{E_m-E_n}\right] \end{aligned} \tag{2.2.4}$$

Note that in the case of paramagnetic susceptibility, we drop the superscript 'p' from the notation since the diamagnetic susceptibility is very very small compared to the paramagnetic one, one can roughly say that the total magnetic susceptibility arises due to the paramagnetism. If not mentioned elsewhere, the magnetic susceptibility always refers to the paramagnetic one.

The above sum-over-states formulations of the pNMR shifts and susceptibility in Eq. 2.2.3 and Eq. 2.2.4, respectively, only require the matrix elements of the electronic magnetic moment and hyperfine operators, and knowledge of the energy levels. The matrix elements are calculated from the wave functions of a non-perturbative Hamiltonian for a system and the energy levels are the non-perturbed energy states. In the field of computational chemistry, one uses software packages to calculate the wave function(s) and the energy level(s) using the *ab initio* methods and the methods are broadly divided into two categories: the wave function based (WFT) methods and electron density based (DFT) methods. We need a brief discussion about these methods so that one can feel the flavor of the physics behind the computations and also be aware of the associated difficulties. Quite specially, for the first principle descriptions of the actinide complexes where all the complexities bundle together [48].

2.3 Wave function based methods

According to one of the postulates of quantum mechanics, for a system in a state described by a wave function $|\Psi\rangle$, then the expectation value of an observable is given by

$$A = \left\langle\Psi\middle|\hat{A}\middle|\Psi\right\rangle \tag{2.3.1}$$

where $\hat{A}$ is the quantum operator of that observable and A is its expectation value, provided that $|\Psi\rangle$ is normalized i.e. $\langle\Psi|\Psi\rangle = 1$. In the case of a stationary state (i.e. all observables in that state are independent of time) the corresponding wave function $|\Psi\rangle$ is the solution of the time independent Schrödinger equation.

2.3.1 Time independent Schrödinger equation

The time independent Schrödinger equation is popularly written in the shorthand notation as

$$\hat{H}\,|\Psi\rangle \;=\; E_\Psi\,|\Psi\rangle \tag{2.3.2}$$

where $\hat{H}$ is the Hamiltonian operator corresponding to the total energy of the system including both the kinetic and potential energies. Eq. 2.3.2 is an eigenvalue problem where the operator $\hat{H}$ operates on an eigenvector $|\Psi\rangle$ providing the energy E_Ψ as the eigenvalue. In the case of a molecule, $\hat{H}$ considers the position vectors of the nuclei $\boldsymbol{R}_K$ and electrons $\boldsymbol{r}_i$ and gives the total energy of the molecule in a quantum sate $|\Psi\rangle$. $|\Psi\rangle$ is a stationary state solution of $\hat{H}$ and any molecular property in that quantum state can be calculated using $|\Psi\rangle$ according to Eq. 2.3.1.

2.3.2 Born-Oppenheimer approximation

Born-Oppenheimer approximation becomes an essential part of solving the molecular Schrödinger equation where the coupling between the nuclear and electronic motion is neglected. Electrons are very light particles compared to a nucleus and move nearly at the speed of light close to the nucleus. Hence, with a bold approximation, one assumes whenever the nucleus moves, the electrons follow immediately. This allows solving Eq. 2.3.2 in fixed nuclear coordinates (i.e. known $\{\boldsymbol{R}_K\}$); the kinetic energy terms of the nuclei are neglected and the nuclear-nuclear repulsion energy terms are taken as parameters in the molecular Hamiltonian. Under these assumptions, the molecular Hamiltonian only contains the electronic coordinates and solving Eq. 2.3.2 using this Hamiltonian provides the molecular electronic energy states. The N-electron molecular electronic Hamiltonian $\hat{H}_e$ (in a.u.) is given by

$$\hat{H}_e \;=\; \hat{T}_e + \hat{V}_{eK} + \hat{V}_{ee} \begin{cases} \hat{T}_e = -\sum_{i=1}^{N} \frac{1}{2}\hat{\nabla}_i^2 \\ \hat{V}_{eM} = -\sum_{i=1}^{N}\sum_{K=1}^{M} \frac{Z_K}{r_{iK}} \\ \hat{V}_{ee} = \sum_{i=1}^{N}\sum_{j>i}^{N} \frac{1}{r_{ij}} \end{cases} \tag{2.3.3}$$

where $\hat{T}_e$, $\hat{V}_{eM}$ and $\hat{V}_{ee}$ give the kinetic energy of the electrons, electron-nucleus attraction energy and electron-electron interaction energy, respectively. Z_K is the atomic number of nucleus K, $\hat{\nabla}$ the Laplacian operator. The nuclear-nuclear repulsion energy $V_{MM} = \sum_{K=1}^{M}\sum_{K'>K}^{M} \frac{Z_K Z_{K'}}{R_{KK'}}$ is added to the total electronic energy to obtain the total energy in fixed nuclear coordinates; $R_{KK'}$ is the distance between two nuclei. The solutions of the N-electron Schrödinger equation are the electronic energy levels of the system E_Φ and the multielectronic wave functions $|\Phi\rangle$,

$$\hat{H}_e \left|\Phi\right\rangle = E_\Phi \left|\Phi\right\rangle \tag{2.3.4}$$

But, the two-electron interaction term of the multielectronic Hamiltonian (Eq. 2.3.3) is the problem and makes it difficult to solve Eq. 2.3.4 exactly. If the two-electron term is not there, the multielectronic Hamiltonian is a sum of a one-electron Hamiltonian and Eq. 2.3.4 would be easily solvable. However, the electron-electron interaction energy is non-ignorable and in practical purposes, a many-electron Hamiltonian is written in terms of effective one-electron Hamiltonian and a multielectronic state $\left|\Phi\right\rangle$ is expressed in terms of Slater determinant, either by a single Slater determinant (in HF or DFT method) or a linear combination of multiple Slater determinants (in CASSCF method). A Slater determinant $\left|\Phi\right\rangle_{SD}$ is written in terms of molecular orbitals as

$$\left|\Phi\right\rangle_{SD} = \frac{1}{\sqrt{N!}} \begin{vmatrix} \phi_1(\boldsymbol{r}_1) & \phi_2(\boldsymbol{r}_1) & \cdots & \phi_N(\boldsymbol{r}_1) \\ \phi_1(\boldsymbol{r}_2) & \phi_2(\boldsymbol{r}_2) & \cdots & \phi_N(\boldsymbol{r}_2) \\ \vdots & \vdots & \ddots & \vdots \\ \phi_1(\boldsymbol{r}_N) & \phi_2(\boldsymbol{r}_N) & \cdots & \phi_N(\boldsymbol{r}_N) \end{vmatrix} \tag{2.3.5}$$

where $\frac{1}{\sqrt{N!}}$ is the normalization factor, $\phi_i(\boldsymbol{r})$ is the i$^{\text{th}}$ molecular orbital that describes the probability density of finding an electron as $\rho_i(\boldsymbol{r}) = \phi_i^*(\boldsymbol{r})\,\phi_i(\boldsymbol{r})$. The molecular orbitals form an orthonormal set i.e. $\left\langle \phi_i(\boldsymbol{r}) \middle| \phi_j(\boldsymbol{r}) \right\rangle = \delta_{ij}$. The advantages of using the Slater determinants for a multielectronic wave function are many. To mention, it follows the anti-symmetry principle and also in accordance with the probabilistic determination of finding an electron as per quantum mechanics. The total electronic energy associated to a Slater determinant is then,

$$E_{SD} = \left\langle \Phi_{SD} \middle| \hat{H}_e \middle| \Phi_{SD} \right\rangle \tag{2.3.6}$$

$$\begin{aligned} &= \sum_{i}^{occ} \left\langle \phi_i(\boldsymbol{r}) \middle| -\frac{1}{2}\hat{\nabla}^2 - \sum_{K=1}^{M} \frac{Z_K}{r_K} \middle| \phi_i(\boldsymbol{r}) \right\rangle + \\ &\sum_{i=1}^{occ}\sum_{j>i}^{occ} \left\langle \phi_i(\boldsymbol{r})\,\phi_j(\boldsymbol{r}') \middle| \frac{1}{|\boldsymbol{r}-\boldsymbol{r}'|} \middle| \phi_i(\boldsymbol{r})\,\phi_j(\boldsymbol{r}') \right\rangle - \\ &\sum_{i=1}^{occ}\sum_{j>i}^{occ} \left\langle \phi_i(\boldsymbol{r})\,\phi_j(\boldsymbol{r}') \middle| \frac{1}{|\boldsymbol{r}-\boldsymbol{r}'|} \middle| \phi_i(\boldsymbol{r}')\,\phi_j(\boldsymbol{r}) \right\rangle \end{aligned} \tag{2.3.7}$$

$$= \sum_{i=1}^{occ} \left\langle \phi_i(\boldsymbol{r}) \middle| \hat{h} \middle| \phi_i(\boldsymbol{r}) \right\rangle + \frac{1}{2}\sum_{i=1}^{occ}\sum_{j=1}^{occ} \left\langle \phi_i(\boldsymbol{r})\,\phi_j(\boldsymbol{r}') \middle\| \phi_i(\boldsymbol{r})\,\phi_j(\boldsymbol{r}') \right\rangle \tag{2.3.8}$$

$$= \sum_{i=1}^{occ} h_i + \frac{1}{2}\sum_{ij}^{occ} \left(J_{ij} - K_{ij}\right) \tag{2.3.9}$$

where the one electron term h_i comprises the kinetic and nuclear attraction energies. J_{ij} and K_{ij} are the two-electron interaction terms, the Coulomb and exchange energies, re-

spectively. Eq. 2.3.9 is solved by iterative procedure to obtain the best set of molecular orbitals which will minimize the total electronic energy, and the iterative process is commonly termed as self-consistent field (SCF) procedure. The Hartree-Fock method is the most renowned SCF procedure in the field of quantum chemistry and often considered as a starting point to solve the multielectronic Schrödinger equation.

2.3.3 Hartree-Fock method (HF-SCF)

In the Hartree-Fock theory, the energy in Eq. 2.3.6 gets minimized by variation of the orbitals, subject to the normalization constraints,

$$\langle \phi_i | \phi_j \rangle - \delta_{ij} = 0 \tag{2.3.10}$$

therefore using the method of Lagrange multipliers, a Lagrangian functional $\mathscr{L}[\{\phi_i\}]$ can be constructed as

$$\mathscr{L}[\{\phi_i\}] = E_{SD}[\{\phi_i\}] - \sum_{ij}^{occ} \varepsilon_{ij} \langle \phi_i | \phi_j \rangle - \delta_{ij} \tag{2.3.11}$$

where $E_{SD}[\{\phi_i\}]$ is the expectation value of $|\Phi_{SD}\rangle$ given by Eq. 2.3.9. ε_{ij} constitute a set of Lagrange multipliers. Minimization of E_{SD} subject to the constraints is thus obtained by minimizing the Lagrangian functional $\delta\mathscr{L} = 0$ which ultimately provides the best set of orbitals. This minimization finally results a set of N equations for the N-electron system and the equations are known as the Hartree-Fock eigenvalue equations,

$$\hat{f}(\boldsymbol{r})\,\phi_i(\boldsymbol{r}) = \varepsilon_i \phi_i(\boldsymbol{r}) \tag{2.3.12}$$

Eqs. 2.3.12 represent one particular set of orbitals, called 'canonical'. The orbital energies are Lagrange multipliers needed to satisfy the constraints. Other Lagrange multipliers, corresponding to non-canonical coupled HF equations and alternative sets of orbitals that also minimize the energy, are available. The one electron Fock operator $\hat{f}(\boldsymbol{r})$ in Eq. 2.3.12 is given by,

$$\hat{f}(\boldsymbol{r}) = \hat{h}(\boldsymbol{r}) + \sum_{j=1}^{occ} \left(J_j(\boldsymbol{r}) - K_j(\boldsymbol{r}) \right) \tag{2.3.13}$$

and the eigenvalue ε_i is the orbital energy of the i$^{\text{th}}$ occupied molecular orbital $\phi_i(\boldsymbol{r})$,

$$\varepsilon_i = \langle \phi_i(\boldsymbol{r}) | \hat{h} | \phi_i(\boldsymbol{r}) \rangle + \sum_{j}^{occ} \langle \phi_i(\boldsymbol{r})\,\phi_j(\boldsymbol{r}') \| \phi_i(\boldsymbol{r})\,\phi_j(\boldsymbol{r}') \rangle \tag{2.3.14}$$

$$= h_i + \sum_{j}^{occ} \left(J_{ij} - K_{ij} \right) \tag{2.3.15}$$

The Hartree-Fock eigenvalue problem for a multielectronic system then becomes

$$\hat{H}^{HF} |\Psi_0\rangle^{HF} = \left(\sum_{i=1}^{occ} \varepsilon_i \right) |\Psi_0\rangle^{HF} \tag{2.3.16}$$

where $\hat{H}^{HF} = \sum_{i=1}^{N} \hat{f}(\boldsymbol{r}_i)$ and $|\Psi_0\rangle^{HF}$ is the approximate solution to the ground electronic state where the N lowest orbitals are occupied. $|\Psi_0\rangle^{HF}$ is written as a single Slater determinant in terms of the N occupied molecular orbitals obtained by solving Eq. 2.3.12. The eigenvalue of Eq. 2.3.16 is the sum of the orbital energies, $\sum_i^{occ} \varepsilon_i$. However, comparing with Eq. 2.3.9, one can notice that when the ground state is approximated by a single determinant $|\Psi_0\rangle^{HF}$, the corresponding total electronic energy $E_0^{HF} \neq \sum_i^{occ} \varepsilon_i$ i.e. the total electronic ground state energy is not the sum of the orbital energies due to double counting of two-electron terms. According to Eq. 2.3.9, the ground state electronic energy in Hartree-Fock theory can be obtained as

$$E_0^{HF} = \sum_{i}^{occ} \varepsilon_i - \frac{1}{2} \sum_{ij}^{occ} (J_{ij} - K_{ij}) \tag{2.3.17}$$

For details, we recommend to read chapter 3 of the book written by Szabo and Ostlund [49]. In daily computational practices, we use atomic basis $\{|\mu\rangle, |\nu\rangle, ..\}$ to express the molecular orbitals $\phi_i(\boldsymbol{r})$ which are written as linear combinations of the atomic orbitals as $\phi_i = \sum_\nu c_{\nu i} |\nu\rangle$. So Eq. 2.3.12 can be written as

$$\hat{f} \sum_{\nu} c_{\nu i} |\nu\rangle = \varepsilon_i \sum_{\nu} c_{\nu i} |\nu\rangle \tag{2.3.18}$$

multiplying right hand side of Eq. 2.3.18 by $\langle\mu|$ and introducing the overlap matrix $S_{\mu\nu} = \langle\mu|\nu\rangle$

$$\sum_{\nu} \langle \mu | \hat{f} | \nu \rangle c_{\nu i} = \varepsilon_i \sum_{\nu} c_{\nu i} \langle \mu | \nu \rangle \tag{2.3.19}$$

$$\sum_{\nu} F_{\mu\nu} c_{\nu i} = \varepsilon_i \sum_{\nu} c_{\nu i} S_{\mu\nu} \tag{2.3.20}$$

where $F_{\mu\nu}$ are the elements of the Fock matrix $\mathbf{F}$, represented in the atomic basis $\{|\mu\rangle, |\nu\rangle ....\}$ and $c_{\nu i}$ are expansion coefficient of the i$^{\text{th}}$ molecular orbital in terms of the atomic basis $|\nu\rangle$. Eqs. 2.3.20 are called the Roothaan equations and can be written in a matrix form as

$$\mathbf{FC} = \varepsilon \mathbf{SC} \tag{2.3.21}$$

$\mathbf{C}$ is the coefficient matrix where the i$^{\text{th}}$ column corresponds to the molecular orbital in terms of the expansion coefficients $c_{\nu i}$. Up to this point, the determination of the molecular orbitals and their energies involve solving the matrix equation of Eq. 2.3.21. In most computational softwares, it is solved using iterative process to get the best set of coefficients for the molecular orbitals by minimizing the total electronic energy of the system. The energy minimization is performed based on variational approach.

The Hartree-Fock method has some limitations. The Hartree-Fock energy is always upper bound to the exact ground state solution of $\hat{H}_e$, E_0 and when the basis set approaches to the completeness, this extra missing energy is known as the correlation energy E^{corr},

$$E_{corr} = E_0 - E_0^{HF} \tag{2.3.22}$$

which can be roughly divided into two parts: the static correlation energy and the dynamic correlation energy. Usually the electronic states of the open shell metal complexes are multiconfiguration (written with multiple Slater determinants) in nature. But, the Hartree-Fock method is a single determinant method that lacks the proper descriptions for the open shell metal complexes and this leads to the so-called static correlation energy. This can be recovered using the multiconfiguration SCF method such as CASSCF.

2.3.4 Complete active space SCF method (CASSCF)

In CASSCF method [50], one expands the multielectronic wave functions as spin adapted linear combinations of configuration wave functions generated by partitioning the orbitals into three subspaces. In the first subspace, called as inactive space, all orbitals are doubly occupied. In the second subspace, termed as active space, the orbitals are called active orbitals and a full CI (Configuration Interaction) expansion is performed within these active orbitals. For example, for a d^2 metal complex, we can choose the five d orbitals as active and a multiconfiguration wave function is built as a linear combination of all the possible configurations that are generated by arranging two electrons in the five d orbitals. That is why this second subspace is usually called as the complete active space (CAS) since we consider all the possible configurations $|\Phi_I\rangle, \{I = 1,2,3,...,CI\}$. The third subspace is known as the virtual space and all the orbitals are kept unoccupied. A configuration can be expressed with a Slater determinant like the HF wave function. The multiconfiguration CAS wave functions $|\Psi\rangle_J^{CAS}$ are written as spin adapted linear combinations of the determinants $|\Phi_I\rangle$ in the form of CI as,

$$|\Psi\rangle_J^{CAS} = \sum_I^{CI} C_{IJ} |\Phi_I\rangle \tag{2.3.23}$$

where C_{IJ} are the coefficients of expansions. In practice, a CASSCF calculation is performed after an initial HF or DFT calculation which helps to choose the active orbitals from where all the determinants are constructed. The energy of the state corresponds to a CASSCF wave function $|\Psi\rangle_J^{CAS}$ is calculated as

$$E_J^{CAS} = \left\langle \Psi_J^{CAS} \left| \hat{H}_e \right| \Psi_J^{CAS} \right\rangle = \sum_{IK}^{CI} C_{IJ}^* C_{KJ} \mathscr{H}_{IK} \tag{2.3.24}$$

where $\hat{H}_e$ is the many electron Hamiltonian. Note that, $\mathscr{H}_{IK}$ is not a matrix element between two orbitals but two determinants. Now again, we are not going into the details of the CASSCF procedure but take a quick look at how $\mathscr{H}_{IK}$ looks like and finally how

we can obtain the E_J^{CAS} from there. In the second quantization notations of creation $\left(\hat{a}^{\dagger}\right)$ and annihilation $(\hat{a})$ operators, $\mathscr{H}_{IK}$ can be written in terms of the shift operator $\hat{E}_{pq}$ as follows

$$\begin{aligned}\mathscr{H}_{IK} &= \left\langle \Phi_I \left| \hat{H}_e \right| \Phi_K \right\rangle \\ &= \sum_{pq} \left(p \left| \hat{h} \right| q\right) \left\langle \Phi_I \left| \hat{E}_{pq} \right| \Phi_K \right\rangle + \\ &\quad \frac{1}{2} \sum_{pqrs} (pq|rs) \left\langle \Phi_I \left| \left(\hat{E}_{pq}\hat{E}_{rs} - \delta_{qr}\hat{E}_{ps}\right) \right| \Phi_K \right\rangle \end{aligned} \tag{2.3.25}$$

where in Eq. 2.3.25, $\hat{E}_{pq} = \left(\hat{a}^{\dagger}_{p\alpha}\hat{a}_{q\alpha} + \hat{a}^{\dagger}_{p\beta}\hat{a}_{q\beta}\right)$ and p,q,r,s are the molecular orbitals. $\left(p \left| \hat{h} \right| q\right)$ is the one-electron energy term and $(pq|rs)$ is the two-electron interaction term. The final expression of energy E_J^{CAS} now becomes,

$$\begin{aligned}E_J^{CAS} &= \sum_{pq} \left(p \left| \hat{h} \right| q\right) \sum_{IK}^{CI} C_{IJ}^{*} C_{KJ} \left\langle \Phi_I \left| \hat{E}_{pq} \right| \Phi_K \right\rangle \\ &\quad + \frac{1}{2} \sum_{pqrs} (pq|rs) \sum_{IK}^{CI} C_{IJ}^{*} C_{KJ} \left\langle \Phi_I \left| \left(\hat{E}_{pq}\hat{E}_{rs} - \delta_{qr}\hat{E}_{ps}\right) \right| \Phi_K \right\rangle \end{aligned} \tag{2.3.26}$$

The final energies of a CAS based SCF calculation are minimized w.r.t. orbital rotations while also maintaining their orthogonality. As a byproduct, some other valuable information can be obtained from a CASSCF calculation along with the energies such as: $\gamma_{pq} = \sum_{IK}^{CI} C_{IJ}^{*} C_{KJ} \left\langle \Phi_I \left| \hat{E}_{pq} \right| \Phi_K \right\rangle$ in Eq. 2.3.26 is called the one-particle density matrix, diagonalization of the matrix gives the Natural Orbitals (NOs) and their occupation numbers. The active space NOs can be plotted for the visualization. In the following chapters, we will see the active NOs of some actinide complexes.

The restricted active space self-consistent field (RASSCF) procedure is also a multiconfiguration SCF treatment, but in this case, the active orbitals are divided into different sets of orbitals (RAS1, RAS2, RAS3) and restricted excitations of the active electrons are performed in between

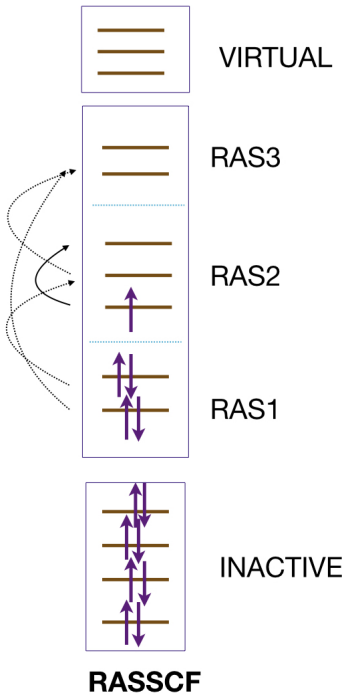

Figure 2.3.1: Partitioning of the orbitals into different subspaces in RASSCF scheme. The active orbitals in the active space are divided into three sets of orbitals: RAS1, RAS2 and RAS3 and all configurations generated by $2h-2p$ excitations are considered in the CI.

them [51]. In Fig. 2.3.1, a graphical scheme is provided which shows the different sets of orbitals in the active space. A RASSCF treatment is preferentially prescribed for an actinyl ($[AnO_2]^{2+}$) complex where the actinide in $+5$ or $+6$ oxidation state forms two strong triple bonds with the oxo (O^{2-}) groups. Hence, a large active space is considered which covers the bonding and anti-bonding orbitals of the actinyl moiety to properly address the electron correlation.

Here, we mention about the notations of CASSCF and RASSCF calculations which are used later: CAS/CASSCF(n,m)- a CASSCF calculation is performed with n electrons in m active orbitals, RAS/RASSCF$(a,x;b,y;c,z:u,v)$- a RASSCF calculation is performed with a electrons in x RAS1 orbitals, b electrons in y RAS2 orbitals and with z RAS3 orbitals, and maximum allowed number of holes and particles in RAS1 and RAS3 orbitals are u and v, respectively. Theoretically, when the basis sets used for the calculations approach to the completeness, a full CI calculation i.e. all the possible arrangements of all the electrons in all the orbitals gives the exact energy (of course, in the SF limit) of the system. But due to the computational limit, a full CI calculation is performed within the truncated active space in the CASSCF method. Due to the truncation of the active space, a CASSCF calculation fails to address the dynamic correlation energy. Unlike CASSCF, Complete Active Space Configuration Interaction (CASCI) methods are less costlier (in terms of computational time). Since in CASSCF, both the CI and orbital coefficients are optimized variationally whereas in CASCI, the CI coefficients are optimized in a predetermined set of orbitals and hence, the number of active orbitals can be increased to recover the correlation energy. Perturbation theory based treatment can also be employed to recover the electron correlation energy considering CAS based wave functions as the reference states [52, 53]. One of the method is the Complete Active Space Perturbation Theory at Second Order (CASPT2) [54].

2.3.5 Treatment of electron dynamic correlation (CASPT2)

The idea behind the perturbative treatment of electron dynamic correlation lies on slicing an Hamiltonian $\hat{H}$ as

$$\hat{H} = \hat{H}^{(0)} + \lambda \hat{H}^{(1)} \tag{2.3.27}$$

where $\hat{H}^{(0)}$ is the non-perturbative or the Zeroth order Hamiltonian and $\hat{H}^{(1)}$ is the first order perturbative Hamiltonian and λ is a small parameter. The solutions of the Schrödinger equation using Hamiltonian of Eq. 2.3.27 can also be expanded as a Taylor series in λ,

$$|\Psi_n\rangle = \left|\Psi_n^{(0)}\right\rangle + \lambda \left|\Psi_n^{(1)}\right\rangle + \lambda^2 \left|\Psi_n^{(2)}\right\rangle + .. \tag{2.3.28}$$

$$E_n = E_n^{(0)} + \lambda E_n^{(1)} + \lambda^2 E_n^{(2)} + .. \tag{2.3.29}$$

$\left|\Psi_n^{(0)}\right\rangle$ and $E_n^{(0)}$ are the solutions of $\hat{H}^{(0)}$, i.e. $\hat{H}^{(0)}\left|\Psi_n^{(0)}\right\rangle = E_n^{(0)}\left|\Psi_n^{(0)}\right\rangle$. Taking the above forms of $|\Psi_n\rangle$ and E_n, the Schrödinger equation w.r.t. $\hat{H}$ becomes

$$\hat{H}\,|\Psi_n\rangle = E_n\,|\Psi_n\rangle \tag{2.3.30}$$

$$\begin{aligned}\left(\hat{H}^{(0)} + \lambda\hat{H}^{(1)}\right)\left(\left|\Psi_n^{(0)}\right\rangle + \lambda\left|\Psi_n^{(1)}\right\rangle + \lambda^2\left|\Psi_n^{(2)}\right\rangle + ..\right) \\ = \left(E_n^{(0)} + \lambda E_n^{(1)} + \lambda^2 E_n^{(2)} + ..\right)\left(\left|\Psi_n^{(0)}\right\rangle + \lambda\left|\Psi_n^{(1)}\right\rangle + \lambda^2\left|\Psi_n^{(2)}\right\rangle + ..\right)\end{aligned} \tag{2.3.31}$$

Considering the terms up to second order in energy, the first order $E_n^{(1)}$ and second order $E_n^{(2)}$ energy corrections to $E_n^{(0)}$ can be obtained as

$$E_n^{(1)} = \left\langle \Psi_n^{(0)} \middle| \hat{H}^{(1)} \middle| \Psi_n^{(0)} \right\rangle \tag{2.3.32}$$

$$E^{(2)} = \sum_{m\neq n} \frac{\left\langle \Psi_n^{(0)} \middle| \hat{H}^{(1)} \middle| \Psi_m^{(0)} \right\rangle \left\langle \Psi_m^{(0)} \middle| \hat{H}^{(1)} \middle| \Psi_n^{(0)} \right\rangle}{E_n^{(0)} - E_m^{(0)}} \tag{2.3.33}$$

and in first order one obtains,

$$|\Psi_n\rangle^{(1)} = \sum_{m\neq n} \frac{\left\langle \Psi_m^{(0)} \middle| \hat{H}^{(1)} \middle| \Psi_n^{(0)} \right\rangle}{E_n^{(0)} - E_m^{(0)}} \left|\Psi_m^{(0)}\right\rangle \tag{2.3.34}$$

On a soft ground, CASPT2 method can be viewed as the second order correction to the CASSCF energies E_J^{CAS} using the CASSCF wave functions $|\Psi\rangle_J^{CAS}$ as the unperturbed states or reference states. CASPT2 calculation becomes highly computationally expensive as the number of orbitals which in practice are correlated, gets larger. Also CASPT2 method comes with certain problems associated with it such as the "intruder state problem" where a state from the interacting space gives large contribution to the total energy due to small energy difference w.r.t. the reference CASSCF state. So a small denominator (according to Eq. 2.3.33) is giving rise to a large contribution to the final CASPT2 energy over the reference CASSCF energy. This problem is usually solved by shifting the energy levels using level-shift technique.

2.4 Density functional theory based methods

Density functional methods are highly popular in the field of computational chemistry. We will use DFT methods to calculate the spin densities needed for the description of the contact shifts as developed in section 1.8. Here, a brief theoretical overview is pro-

vided just to be familiar with the DFT methods. The foundation of the DFT lies on the Hohenberg-Kohn theorem which states that the ground state electronic energy E_0 can be completely determined by the ground state electron density ρ_0; in other words in DFT, the energy is a functional of the electron density $E[\rho]$ and when $\rho = \rho_0$, $E_0 = E[\rho_0]$. The energy functional in DFT is written as

$$E[\rho] = F[\rho] + E_{eM}[\rho] \tag{2.4.1}$$

where the functional $F[\rho]$ consists of the kinetic energy term $T[\rho]$ and the interelectronic interaction term $E_{ee}[\rho]$, those only change with the number of electrons. The term $E_{eM}[\rho]$ is the electron-nuclear attraction energy term and system specific.

2.4.1 Kohn-Sham theory

In the Kohn-Sham theory, the functional form of $F[\rho]$ is given as

$$F[\rho] = T_s[\rho] + J[\rho] + E_{xc}[\rho] \tag{2.4.2}$$

where the electron density ρ of N-non-interacting-electron system is given by $\rho(\boldsymbol{r}) = \sum_i^{occ} |\phi_i(\boldsymbol{r})|^2$, $\phi_i(\boldsymbol{r})$ the Kohn-Sham orbitals. $T_s[\rho]$ is the Kohn-Sham kinetic energy functional, $J[\rho]$ the classical Coulomb repulsion energy functional and $E_{xc}[\rho]$ the so-called exchange-correlation energy functional. Like the Hartree-Fock equation (Eq. 2.3.12), minimization of $E[\rho]$ subject to the orthonormality constraints of the Kohn-Sham orbitals leads to the effective one-electron Fock-type equations known as the Kohn-Sham equations [55, 56],

$$\left[-\frac{\nabla^2}{2} + v_{eff}(\boldsymbol{r})\right]\phi_i(\boldsymbol{r}) = \varepsilon_i \phi_i(\boldsymbol{r}) \tag{2.4.3}$$

Eqs. 2.4.3 correspond to the canonical Kohn-Sham orbitals. The non-canonical form may also be conceivable. $v_{eff}(\boldsymbol{r})$ is the effective potential in which the electrons move and the form is given by

$$v_{eff}(\boldsymbol{r}) = v_{eM}(\boldsymbol{r}) + \int \frac{\rho(\boldsymbol{r}')}{|\boldsymbol{r} - \boldsymbol{r}'|} d^3\boldsymbol{r}' + \frac{\delta E_{xc}[\rho]}{\delta \rho(\boldsymbol{r})} \tag{2.4.4}$$

Like the Roothaan equations, the KS equations can be solve numerically in terms of atomic basis leading to matrix form

$$\mathbf{h}^{KS}\mathbf{C} = \boldsymbol{\varepsilon}\mathbf{S}\mathbf{C} \tag{2.4.5}$$

where $\mathbf{h}^{KS}$ is analogues to Fock matrix represented in the atomic basis. Eq. 2.4.5 is solved self consistently to get the best set of Kohn-Sham orbitals and their energies that corresponds to the ground electronic state energy at the Kohn-Sham level of theory.

2.4.2 Exchange-correlation functionals

The exchange-correlation energy functional $E_{xc}[\rho]$ in the expression of the effective potential $v_{eff}(\boldsymbol{r})$ (Eq. 2.4.4) is divided into the exchange $E_x[\rho]$ and correlation $E_c[\rho]$ parts and individually they can be separated into the contributions from the α and β spin densities ρ^α and ρ^β, respectively. This allows expressing their functional forms as functions of total electron density $\rho = \rho^\alpha + \rho^\beta$ and spin polarization $\rho^s = \rho^\alpha - \rho^\beta$. In the unrestricted scheme, the spin polarization plays the dominant role to introduce spin on the atoms further from the paramagnetic center and that is why unrestricted DFT is ideal to describe the spin polarization mechanism with an affordable computational cost. But the exact functional forms of the exchange and the correlation energies are unknown and usually, they are approximated [57, 58]. The approximated expressions contain different variables and based on that, they are classified according to LDA (Local Density Approximation)- when the variable is ρ and such functionals are SVWN, X_α etc; GGA (Generalized Gradient Approximation)- the variables are ρ, $\nabla\rho$ and functionals are BLYP, BP86, PBE etc; meta-GGA- the variables are ρ, $\nabla\rho$, $\nabla^2\rho$ and functionals are B95, TPSS etc; hybrid- the variables are ρ, $\nabla\rho$, *HF-exchange* and functionals are B3LYP, PBE0 etc; meta-hybrid- the variables are ρ, $\nabla\rho$, $\nabla^2\rho$, *HF-exchange* and functionals are M06, M062X, TPSSH etc.

2.5 Relativistic effects

Relativistic effects are very essential in quantum chemistry, especially for actinides, and they can be classified into two categories: Scalar Relativistic (SR) effects and spin-orbit coupling. SR effects comprise all the terms those do not depend on the spin of an electron such as the relativistic kinetic energy, mass velocity and Darwin terms. Relativistic mass of an electron (or any matter) is governed by the well known equation,

$$m_{rel} = m_0 \left(1 - \frac{v^2}{c^2}\right)^{-1/2} \tag{2.5.1}$$

where m_0 is the rest mass of the electron, v its velocity and c the speed of light. For an hydrogen like atom, estimation of v comes from the non-relativistic ground state energy E_{nrel}. According to virial theorem, for a spherically symmetric potential which behaves with $1/r$, $2T_{nrel} = -V_{nrel}$, so $T_{nrel} = -E_{nrel}$. Using $T_{nrel} = 1/2 m_0 v^2$, one can find that for a hydrogen-like atom, the velocity of the electron in $1s$ state is equals to Z (in a.u.), the atomic number. The speed of light c in a.u. is 137.036. So from Eq. 2.5.1, it is evident that the relativistic mass of an $1s$ electron increases from the rest mass for the heavier nuclei like Ln or An. The effects of this "relativistic mass increase" are: First, from an energetic point of view, as the mass (appears to) increases, the relativistic kinetic energy

increases than the non-relativistic kinetic energy $1/2m_0v^2$. Second, the $1s$ orbital and subsequently also the other s orbitals shrink more due to this mass increment and provide more screening to the nuclear charge. As a result, the effective nuclear charge on the d or f electrons decreases and the orbitals become more diffuse.

Spin-orbit (SO) interaction is a result of magnetic induction that occurs due relative movement of an electron in the potential field generated by other charge particle(s). Due to the relative movement of an electron w.r.t the nucleus, in its rest frame the electron feels a magnetic field in addition to the electric field. Mathematically, this SO interaction energy is given by

$$E_{SO} = \xi(r)\boldsymbol{l}\cdot\boldsymbol{s} \tag{2.5.2}$$

where $\xi(r)$ is the SOC parameter. From the expression of Eq. 2.5.2, it appears that SO interaction is a coupling of the electron's spin with its orbital motion. In fact, in a multielectronic atom, an electron undergoes SO interaction with other electrons due to the relative motion of the electron in the field of a second electron. Two-electron SO interaction terms in the Hamiltonian can be divided into two categories: i) spin-same-orbit coupling, and ii) spin-other-orbit coupling. The above form of SO interaction in Eq. 2.5.2 is a one-electron term and is of type spin-own-orbit coupling in the Born-Oppenheimer approximation. Spin is an intrinsic property of an electron and it is introduced to the Schrödinger-Pauli Hamiltonian in Eq. 1.2.1 to describe the behavior of an electron in a magnetic field, so-called the Zeeman splitting. But in Eq. 1.2.1, we still miss the above term of spin-orbit interaction which needs to be included *ad hoc*. The complete relativistic description of an electron is provided by the Dirac equation.

2.5.1 The four-component Dirac equation

The time independent form of the Dirac equation for an electron with a potential energy V (excluding the electron rest mass energy mc^2) is

$$\left[c(\boldsymbol{\alpha}\cdot\boldsymbol{p}) + \boldsymbol{\beta}'mc^2 + V\mathbf{I}_4\right]\psi = \varepsilon\psi \tag{2.5.3}$$

where $\boldsymbol{\alpha}_i = \begin{bmatrix} \mathbf{0} & \boldsymbol{\sigma}_i \\ \boldsymbol{\sigma}_i & \mathbf{0} \end{bmatrix}$ $i = x,y,z$ and $\boldsymbol{\beta}' = \begin{bmatrix} \mathbf{0} & \mathbf{0} \\ \mathbf{0} & -2\mathbf{I}_2 \end{bmatrix}$ are (4×4) matrices written in terms of the (2×2) block matrices; the Pauli $\boldsymbol{\sigma}_i$ and the identity $\mathbf{I}_2$ matrices and $\varepsilon = E - mc^2$. The Dirac equation is a (4×4) matrix eigenvalue equation and the relativistic wave function of the electron ψ has four components. The above equation (Eq. 2.5.3) is also written in terms of (2×2) block matrix form by partitioning the four-component wave function ψ into two two-component parts usually denoted by ψ^L and ψ^S (L= Large, S= Small),

$$\begin{bmatrix} V\mathbf{I}_2 & c\,(\boldsymbol{\sigma}\cdot\boldsymbol{p}) \\ c\,(\boldsymbol{\sigma}\cdot\boldsymbol{p}) & \left(V-2mc^2\right)\mathbf{I}_2 \end{bmatrix} \begin{bmatrix} \psi^L \\ \psi^S \end{bmatrix} = \varepsilon \begin{bmatrix} \psi^L \\ \psi^S \end{bmatrix} \tag{2.5.4}$$

$\boldsymbol{p}$ is the momentum. From Eq. 2.5.4, one can write two equations as

$$V\mathbf{I}_2\psi^L + c\,(\boldsymbol{\sigma}\cdot\boldsymbol{p})\,\psi^S = \varepsilon\psi^L \tag{2.5.5}$$

$$c\,(\boldsymbol{\sigma}\cdot\boldsymbol{p})\,\psi^L + \left(V-2mc^2\right)\mathbf{I}_2\psi^S = \varepsilon\psi^S \tag{2.5.6}$$

ψ^S can be written in terms of ψ^L using Eq. 2.5.6, $\psi^S = \frac{c(\boldsymbol{\sigma}\cdot\boldsymbol{p})}{2mc^2-(V-\varepsilon)}\psi^L$ and putting it into Eq. 2.5.5 results in

$$\left[(\boldsymbol{\sigma}\cdot\boldsymbol{p})\,K\,(\boldsymbol{\sigma}\cdot\boldsymbol{p}) + V\mathbf{I}_2\right]\psi^L = \varepsilon\psi^L \tag{2.5.7}$$

where $K = \frac{c^2}{2mc^2-(V-\varepsilon)}$. Note that in a magnetic field, $\boldsymbol{p}$ is replaced by the kinematic momentum $\boldsymbol{\pi}$ and in the non-relativistic limit $c \to \infty$; $K \to \frac{1}{2m}$, one reaches to the Schrödinger-Pauli equation where the Hamiltonian is given by Eq. 1.2.1. In the non-relativistic limit, the equation for the large component ψ^L reduces to the Schrödinger equation for an electron and the small component ψ^S vanishes. Relativistic four-component calculations for the moderate size of molecules with heavy atoms are still very expensive and that is why much of the effort has been put forward to get rid of this small component from an electronic solution.

2.5.2 Two-component approaches

2.5.2.1 ZORA approach

Zeroth Order Regular Approximation (ZORA) is based on an approximate decoupling of the large and small components. In the ZORA Hamiltonian, the denominator in the factor K is expanded (with $\frac{\varepsilon}{2mc^2-V}$ since $\varepsilon \ll 2mc^2 - V$) as follows

$$\left(2mc^2-(V-\varepsilon)\right)^{-1} = \left(2mc^2-V\right)^{-1}\left(1+\frac{\varepsilon}{2mc^2-V}\right) = \left(2mc^2-V\right)^{-1} \tag{2.5.8}$$

the expansion is limited to the zeroth order and putting the form of Eq. 2.5.8 in Eq. 2.5.7 results (with further derivation) in the final form of the one-electron ZORA Hamiltonian written as

$$H^{ZORA} = \frac{c^2p^2}{2mc^2-V} + \frac{2c^2}{\left(2mc^2-V\right)^2} + \frac{Z\boldsymbol{l}\cdot\boldsymbol{s}}{r^3} + V \tag{2.5.9}$$

Note that, the ZORA approach successfully takes into account the relativistic correction of kinetic energy of an electron and SOC term. In the next chapters, we will see the keywords 'SR-ZORA' and 'SO-ZORA' which stands for the ZORA Hamiltonian without and with the SOC term, respectively.

2.5.2.2 DKH approach

In the Douglas-Kroll-Hess (DKH) approach, direct block diagonalization of the one-electron Dirac Hamiltonian $\mathbf{H}^{Dirac}$ according to Eq. 2.5.4 is carried out by a suitable unitary transformation,

$$\mathbf{U}\mathbf{H}^{Dirac}\mathbf{U}^{\dagger} = \begin{bmatrix} \mathbf{H}_{+}^{DKH} & \mathbf{0} \\ \mathbf{0} & \mathbf{H}_{-}^{DKH} \end{bmatrix} \tag{2.5.10}$$

where $\mathbf{U}$ is the unitary matrix. Successful unitary transformation decouples the small component and the final two component equation can be written as

$$\mathbf{H}_{+}^{DKH}\Psi^{L} = \varepsilon\Psi^{L} \tag{2.5.11}$$

Like the ZORA approach, DKH Hamiltonian can be separated according to the SR and SO terms .

2.5.3 SO-RASSI method

In case of a multielectronic system, the SOC Hamiltonian includes both the one-electron (spin-own-orbit type) and two-electron SO (spin-same-orbit and spin-other-orbit type) terms. Since the evaluation of the two-electron SO integrals are computationally very expensive, an effective Fock-type one-electron SO Hamiltonian in the mean field of other atomic electrons was proposed by Hess *et al.* [59] and further implemented by Schimmelpfennig [60] known as the Atomic Mean Field Integral (AMFI) scheme.

In the MOLCAS suite of software, SOC is calculated as an interaction between different electronic states in the RASSI (Restricted Active Space State Interaction) module and the SO integrals are calculated using AMFI scheme. Since spin is the integral part of the SOC Hamiltonian, essentially excited electronic states of different spin multiplicities are also mixed with the ground SF manifold in SO-RASSI calculation. The electronic states are usually obtained from the CASSCF or RASSCF calculations. In the actinide complexes, CASPT2 correction is important for a better description of the energy levels using the CASSCF or RASSCF wave functions as reference states (termed as state-specific calculation (SS)). Sometimes in the multi-state (MS) calculation in which the effective coupling between the reference states are considered, the compositions of the CASSCF or RASSCF reference states can be changed. Unless specifically mentioned, the SOC matrices are computed in the RASSI module of MOLCAS using the MSCASPT2 wave functions and the corresponding energy levels. The eigenfunctions of the SOC matrices are used to calculate the magnetic moment matrices and the magnetic properties.

2.6 Calculation of Magnetic properties

2.6.1 Magnetic moment matrices

Magnetic moment $\boldsymbol{m}$ is a vector quantity i.e. can be defined by the three perpendicular components $i = x, y, z$. Each of the components of electronic magnetic moment of a paramagnetic center is calculated using the quantum description of the magnetic moment in terms of operators,

$$\hat{m}_i = -\mu_B \left(\hat{L}_i + g_e \hat{S}_i\right) \tag{2.6.1}$$

Within n no of SO states, the representation matrix of $\hat{m}_i$ is given by

$$\mathbf{M}_i = \begin{bmatrix} M_{i,11} & \cdots & M_{i,1n} \\ \vdots & \ddots & \vdots \\ M_{i,n1} & \cdots & M_{i,nn} \end{bmatrix}_{n \times n} \tag{2.6.2}$$

The magnetic g-factors: According to Kramers theorem of quantum mechanics, the energy eigenstates of an odd number of electrons' system are always at least doubly degenerate, meaning that one will always find at least two states $\left\{\Phi, \bar{\Phi}\right\}$ with the same energy and they are related by time reversal symmetry i.e. $\bar{\Phi} = \hat{\tau}\Phi$ where $\hat{\tau}$ is the time reversal operator. Accordingly, the SO eigenstates of an odd number of unpaired electron system from the SO-RASSI calculation are always coming as a pair with the same energy i.e. the KDs. One can use the two states of a KD to calculate the magnetic moment matrices. In the spin Hamiltonian formalism, a KD is described by pseudospin $\tilde{S} = 1/2$ and the model space is the vector space of a pure spin 1/2 system $\{|1/2, +1/2\rangle, |1/2, -1/2\rangle\}$. As the magnetic moment operators are time odd, the 2×2 magnetic moment matrices calculated within the KD are essentially traceless Hermitian in nature and can be decomposed in terms of the Pauli matrices $\boldsymbol{\sigma}_i$ as

$$-2\mathbf{M}_x = \mu_B \sum_{i=x,y,z} g_{ix} \boldsymbol{\sigma}_i \tag{2.6.3}$$

$$-2\mathbf{M}_y = \mu_B \sum_{i=x,y,z} g_{iy} \boldsymbol{\sigma}_i \tag{2.6.4}$$

$$-2\mathbf{M}_z = \mu_B \sum_{i=x,y,z} g_{iz} \boldsymbol{\sigma}_i \tag{2.6.5}$$

where g_{ix} are the coefficients of the expansion w.r.t. $\boldsymbol{\sigma}_i$ in the x direction and so on. One can construct a 3×3 matrix, usually known as the g-matrix $\mathbf{g}$ with the coefficients as

$$\mathbf{g} = \begin{pmatrix} g_{xx} & g_{xy} & g_{xz} \\ g_{yx} & g_{yy} & g_{yz} \\ g_{zx} & g_{zy} & g_{zz} \end{pmatrix} \tag{2.6.6}$$

The eigenvalues of matrix **g** are rotation dependent and can be complex numbers. For the eigenvalues to be rotational invariant and to get rid of the complex numbers, first a symmetrization is performed where the symmetric matrix **G** is given by

$$\mathbf{G} = \mathbf{g}\mathbf{g}^T \tag{2.6.7}$$

and the three principal g-factors of a KD, $g_{k=1,2,3}$ are calculated in the PAF of **G** as

$$g_k = \pm\sqrt{\tilde{G}_{kk}} \tag{2.6.8}$$

where $\tilde{G}_{kk}$ are the eigenvalues of **G**. For the sake of brevity, the positive values are usually reported in the literature.

2.6.2 Magnetization and magnetic susceptibility

In section 1.3, using statistical mechanical formulations, we have already developed the expressions of the magnetization and magnetic susceptibility for a ground J manifold undergoing Zeeman splitting in an external magnetic field B_0. Curie's Law of magnetic susceptibility describes a $1/T$ behavior and all the contributions from the excited states are taken as a temperature independent contributions (TIP) to the susceptibility. Curie's Law had been extensively used to study the magnetic properties of many Ln/An based complexes in terms of the Curie constant and the TIP. As already mentioned before, one should use Van Vleck equation (Eq. 2.2.4) to completely describe the magnetic susceptibility from a quantum mechanical point of view, as it ideally evaluates the property from the knowledge of the electronic energy states [61]. In a moment, we are going to see few expressions of magnetic susceptibility for different manifolds built on the backbone of Van Vleck equation. These expressions will be used in the following chapters to study the paramagnetic properties of the actinide complexes. Each component of the molar magnetic susceptibility tensor $\chi_{m,ii}$ can be calculated according to Eq. 2.2.4 as

$$\chi_{m,ii} = N_A\mu_0\mu_B^2\frac{1}{Q_0}\sum_n e^{-\beta E_n}\left[\beta \mathrm{Tr}\left(\mathbf{M}_{i,nn}\cdot\mathbf{M}_{i,nn}^{\dagger}\right) + 2\sum_{m\neq n}\frac{\mathrm{Tr}\left(\mathbf{M}_{i,nm}\cdot\mathbf{M}_{i,mn}^{\dagger}\right)}{E_m - E_n}\right] \tag{2.6.9}$$

$$= N_A\mu_0\mu_B^2\frac{1}{Q_0}\sum_n e^{-\beta E_n}\left[\beta \left\|\mathbf{M}_{i,nn}\right\|^2 + 2\sum_{m\neq n}\frac{\left\|\mathbf{M}_{i,nm}\right\|^2}{E_m - E_n}\right] \tag{2.6.10}$$

where $\|\|$ is the norm of a matrix and $\mathbf{M}_{i,nm}$ is the block matrix calculated with the mag-

netic moment operator $\hat{m}_i$ between the n and m manifolds, in μ_B unit. The isotropic molar magnetic susceptibility is calculated as one-third of the trace of $\boldsymbol{\chi}_m$ as $\chi_m = \left(\frac{\chi_{m,xx}+\chi_{m,yy}+\chi_{m,zz}}{3}\right)$,

$$\chi_m = N_A \mu_0 \mu_B^2 \frac{1}{Q_0} \sum_n e^{-\beta E_n} \left[\beta M_{nn}^2 + 2 \sum_{m \neq n} \frac{M_{nm}^2}{E_m - E_n} \right] \tag{2.6.11}$$

where $M_{nm}^2 = \frac{1}{3}\left(\|\mathbf{M}_{x,nm}\|^2 + \left\|\mathbf{M}_{y,nm}\right\|^2 + \|\mathbf{M}_{z,nm}\|^2 \right)$

- Model for the ground J manifold of a Ln/An free ion

  $M_{JJ}^2 = \frac{1}{3} g_J^2 J(J+1)(2J+1)$ and $Q_0 = (2J+1)$. The molar magnetic susceptibility is reduced to Curie's law as developed in section 1.4,

$$\chi_m = \frac{N_A \mu_0 \mu_B^2 g_J^2}{3 k_B T} J(J+1) \tag{2.6.12}$$

- Model for an isolated KD

  For a well isolated KD, in the PAF of its $\mathbf{g}$ tensor, $\|\mathbf{M}_{i,nn}\|^2 = \frac{1}{2} g_{i,n}^2$ where $g_{i,nn}$ are the three principal g-factors of a KD in the directions $i = x, y, z$ and $Q_0 = 2$. So Eq. 2.6.10 becomes

$$\chi_{m,ii} = \frac{N_A \mu_0 \mu_B^2}{4 k_B T} g_{i,n}^2 \tag{2.6.13}$$

  Modeling the KD with a $\tilde{S} = 1/2$, the isotropic molar magnetic susceptibility can be written as

$$\chi_m = N_A \mu_0 \mu_B^2 g_n^2 \frac{\tilde{S}\left(\tilde{S}+1\right)}{3 k_B T} \tag{2.6.14}$$

  where $g_n^2 = \frac{1}{3}\left(g_{x,n}^2 + g_{y,n}^2 + g_{z,n}^2\right)$

- Model for two isolated KDs

  We will see later that for $5f^1$ $[An^{VI}O_2]^{2+}$ complexes, there are two energetically lowest KDs which are populated at room temperature and mostly determine the magnetic properties. To model these two doublets, we assume that the PAFs of $\mathbf{g}_1$ and $\mathbf{g}_2$ of the two KDs are identical and one denotes the energy gap between the two KDs as Δ. Limiting the sum to these two states, Eq. 2.6.10 leads to

$$\chi_{m,ii} = N_A \mu_0 \mu_B^2 \left[\beta \frac{\left(e^{\beta\Delta/2} g_{i,1}^2 + e^{-\beta\Delta/2} g_{i,2}^2\right)}{4\left(e^{\beta\Delta/2} + e^{-\beta\Delta/2}\right)} + \frac{\left(e^{\beta\Delta/2} - e^{-\beta\Delta/2}\right) M_{i,12}^2}{\Delta\left(e^{\beta\Delta/2} + e^{-\beta\Delta/2}\right)} \right] \tag{2.6.15}$$

The isotropic molar magnetic susceptibility is

$$\chi_m = N_A \mu_0 \mu_B^2 \left[\beta \frac{\left(e^{\beta\Delta/2} g_1^2 + e^{-\beta\Delta/2} g_2^2\right)}{4\left(e^{\beta\Delta/2} + e^{-\beta\Delta/2}\right)} + \frac{\left(e^{\beta\Delta/2} - e^{-\beta\Delta/2}\right) M_{12}^2}{\Delta\left(e^{\beta\Delta/2} + e^{-\beta\Delta/2}\right)} \right] \tag{2.6.16}$$

- Model for an isolated NKD

  $5f^2$ $[An^{VI}O_2]^{2+}$ complexes are modeled as a non-Kramers doublet (NKD). A NKD is defined by two non-degenerate states $|1\rangle$ and $|2\rangle$ with an energy gap Δ and a Zeeman interaction in only one direction $M_{z,12}^2 = \frac{1}{2} g_z^2$, $M_{x,12}^2 = M_{y,12}^2 = 0$ and in that case Eq. 2.6.11 becomes

$$\chi_m = \frac{N_A \mu_0 \mu_B^2}{6} \left[\frac{e^{\beta\Delta/2} - e^{-\beta\Delta/2}}{\Delta\left(e^{\beta\Delta/2} + e^{-\beta\Delta/2}\right)} g_z^2 \right] \tag{2.6.17}$$

2.6.3 pNMR shifts

First principles calculation of pNMR shifts are focused on the evaluation of the resonance parameter $\sigma_{K,ij}^p$ (shielding tensor) from the wave functions according to Eq. 2.2.3. Thanks to the very effective efforts put forward by Soncini and Van den Heuvel [29] and later by Martin and Autschbach [30] to express Eq. 2.2.3 in terms of the spin Hamiltonian parameters which ultimately settled down as a work to compute the parameters from *ab initio*. Here, we give the expression given by Autschbach *et al.* for the pNMR shielding tensor $\boldsymbol{\sigma}_K^p$ written in the $\left(2\tilde{S}+1\right)$ model space of a pseudospin equals to $\tilde{S}$,

$$\boldsymbol{\sigma}_K^p = -\frac{\mu_B}{g_K \mu_N k_B T} \mathbf{g} \mathbf{Z} \mathbf{A}_K \tag{2.6.18}$$

where $\mathbf{g}$ and $\mathbf{A}_K$ are the spin Hamiltonian parameters as introduced in section 1.8, g-tensor and hyperfine tensor, respectively. $\mathbf{Z}$ takes into account the zero-field splitting (ZFS) and for an axial system in the PAF of the ZFS tensor $\mathbf{D}$, the non-zero diagonal elements of $\mathbf{Z}$ can be written with the axial zero-field splitting parameter D [30]. Pennanen and Vaara earlier used a different approach to formulate the shielding tensor and their expression of $\boldsymbol{\sigma}_K^p$ in terms of the spin Hamiltonian parameters follows [28]

$$\sigma_{K,ij}^p = -\frac{\mu_B}{g_K \mu_N k_B T} \sum_{kl} g_{ik} A_{K,lj} \left\langle \hat{S}_k \hat{S}_l \right\rangle_0 \tag{2.6.19}$$

where the quantity $\langle S_k S_l \rangle_0$ includes the ZFS in the pNMR shielding tensor and is evaluated as an statistical average in the model space of $\left|\tilde{S}, M_{\tilde{S}}\right\rangle$ representing the actual Hilbert space $|n\nu\rangle$,

$$\langle S_k S_l \rangle_0 = \frac{\sum_n e^{-\beta E_n}}{Q_0} \sum_{\tilde{S}, M_{\tilde{S}}} \left\langle \tilde{S}, M_{\tilde{S}} \middle| \hat{S}_k \hat{S}_l \middle| \tilde{S}, M_{\tilde{S}} \right\rangle \tag{2.6.20}$$

$$= \frac{\sum_n e^{-\beta E_n}}{Q_0} \sum_{\tilde{S}, M_{\tilde{S}}, M'_{\tilde{S}}} \left\langle \tilde{S}, M_{\tilde{S}} \middle| \hat{S}_k \middle| \tilde{S}, M'_{\tilde{S}} \right\rangle \left\langle \tilde{S}, M'_{\tilde{S}} \middle| \hat{S}_l \middle| \tilde{S}, M_{\tilde{S}} \right\rangle \tag{2.6.21}$$

In the absence of ZFS, such as a KD modeled by $\tilde{S} = 1/2$ or systems with $\tilde{S} > 1/2$ with $D = 0$, both Eqs. 2.6.18 and 2.6.19 give the similar expression as first obtained by Moon and Patchkovskii [62],

$$\boldsymbol{\sigma}_K^p = -\frac{\mu_B}{g_K \mu_N k_B T} \frac{\tilde{S}\left(\tilde{S}+1\right)}{3} \mathbf{g}\mathbf{A}_K \tag{2.6.22}$$

Note that in Eq. 2.6.22, evaluation of the pNMR shifts for a KD ends up as the negative one-third of the trace of the matrix product of the $\mathbf{g}$ and $\mathbf{A}_K$ tensors. We will use Eq. 2.6.22 to compute the pNMR shifts in the $5f^1$ $[An^{VI}O_2]^{2+}$ complexes where $\mathbf{g}$ and $\mathbf{A}_K$ are calculated using DFT methods. However when $D \neq 0$, Eq. 2.6.19 deviates from Eq. 2.6.18 and Sonicini *et al.* have argued that the correct expression is governed by Eq. 2.2.3 [63].

Up to this moment, we have seen the expressions of the shielding tensor based on the evaluation of the spin Hamiltonian parameters in a model space which actually represents the evaluation of the matrix elements of the parameters from the real *ab initio* Hilbert space. But to be very honest, these model equations are mostly realized for transition metal systems or some Ln/An based molecules where the ground state dictates their physics. But some questions remain such as are these models applicable for the Ln/An complexes where all the interacting states cannot be truly modeled by a pseudospin and the meaning of the ZFS parameter D is quite vague? The Soncini and Van den Heuvel expression (Eq. 2.2.3) are more general and can be applied for any system as one uses the Van Vleck equation for the evaluation of magnetic susceptibility. We are going to model Eq. 2.2.3 for the systems considered in previous section.

The operator $\hat{\boldsymbol{F}}_{K,j}$ in Eq. 2.2.3 is proportional to hyperfine coupling operator responsible for the extra shift of the observed nucleus and as we have already seen in section 1.6, the operator $\hat{\boldsymbol{F}}_{K,j}$ can be written into its dipolar and Fermi contact terms as

$$\hat{\boldsymbol{F}}_K = -\frac{\mu_0}{4\pi} \hat{\boldsymbol{m}} \cdot \mathbf{T}_K + \frac{\hat{\boldsymbol{A}}_K^c}{g_K \mu_N} \tag{2.6.23}$$

where $\hat{\boldsymbol{A}}_K^c$ is the contact hyperfine operator. The contact operator depends on the spin density operator $\hat{\boldsymbol{\rho}}^s$ that only encounters the spin density (normalized to the number of unpaired electron) at the nucleus according to Eq. 1.8.11.

2.6.3.1 Pseudocontact shifts

In the point dipole approximation, the operator $\hat{\boldsymbol{F}}_{K,j}$ is reduced to the magnetic dipole term and is responsible for the pseudocontact or dipolar shifts. In this case, the components of the shielding tensor in Eq. 2.2.3 can be expressed in terms of the block matrices of the magnetic moment operators

$$\begin{aligned}\sigma^{pc}_{K,ij} &= -\frac{\mu_0\mu_B^2}{4\pi}\frac{1}{Q_0}\sum_n e^{-\beta E_n}\sum_l T_{K,lj}\left[\beta \mathrm{Tr}\left(\mathbf{M}_{i,nn}\cdot\mathbf{M}^{\dagger}_{l,nn}\right)\right. \\ &\left. + 2\sum_{m\neq n}\frac{\mathrm{Tr}\left(\mathbf{M}_{i,nm}\cdot\mathbf{M}^{\dagger}_{l,mn}\right)}{E_m - E_n}\right] \end{aligned} \tag{2.6.24}$$

Eq. 2.6.24 of the pseudocontact shielding tensor can be completely expressed in terms of the magnetic susceptibility tensor $\boldsymbol{\chi}_m$ (in Eq. 2.6.10) and the geometric tensor of nucleus K, $\mathbf{T}_K$ (in Eq. 1.6.4) as

$$\boldsymbol{\sigma}^{pc}_K = -\frac{1}{4\pi N_A}\boldsymbol{\chi}_m\cdot\mathbf{T}_K = -\frac{1}{4\pi N_A r^5}\boldsymbol{\chi}_m\cdot\left(3\mathbf{r}_K\otimes\mathbf{r}_K - \mathbf{U}r_K^2\right) \tag{2.6.25}$$

The principal components of the shielding tensor are expressed in the PAF of the $\boldsymbol{\chi}_m$ tensor and the shielding tensor $\boldsymbol{\sigma}^{pc}_K$ in the new frame is given by

$$\mathbf{R}\cdot\boldsymbol{\sigma}^{pc}_K\cdot\mathbf{R}^T = -\frac{1}{4\pi N_A}\mathbf{R}^T\cdot\boldsymbol{\chi}_m\cdot\mathbf{R}\cdot\mathbf{R}^T\cdot\mathbf{T}_K\cdot\mathbf{R} \tag{2.6.26}$$

$$\boldsymbol{\sigma}^{pc,R}_K = -\frac{1}{4\pi N_A}\boldsymbol{\chi}_{m,D}\cdot\mathbf{T}^R_K \tag{2.6.27}$$

$\mathbf{R}$ is an orthogonal matrix which rotates the spatial coordinate in such a way that the magnetic susceptibility tensor becomes diagonal (denoted by subscript D) and $\boldsymbol{\sigma}^{pc,R}_K$ is the shielding tensor in the PAF of the susceptibility tensor. $\mathbf{T}^R_K$ is the geometric tensor in the rotated frame. Finally,

$$\delta^{pc}_K = -\frac{1}{3}\mathrm{Tr}\left(\boldsymbol{\sigma}^{pc}_K\right) = \frac{1}{12\pi N_A}\mathrm{Tr}\left(\boldsymbol{\chi}_{m,D}\cdot\mathbf{T}^R_K\right) \tag{2.6.28}$$

δ^{pc}_K is usually expressed in ppm.

In a molecule without symmetry, the PAF of the $\boldsymbol{\sigma}^{pc}_K$ tensor is in general difficult to anticipate since it depends on the number of states included in the sum and also on temperature. The case of a high symmetrical system where x, y and z belong to different irreps, the off-diagonal terms are zero. In the case of KD n, and in the PAF of the $\mathbf{g}$ tensor $\hat{M}_{i,n} = g_{i,n}\hat{S}_i$ (in μ_B unit, explicitly written outside in Eq. 2.6.24) where $\hat{S}_i$ are the spin operators operating on the pseudospin vectors of $\tilde{S} = 1/2$: the off-diagonal term in Eq. 2.6.24 disappears since $\mathrm{Tr}\left(\mathbf{M}_{i,nn}\cdot\mathbf{M}^{\dagger}_{l,nn}\right) \propto \hat{\tilde{S}}_i\hat{\tilde{S}}_j = 0, i\neq j$ and the diagonal components are related to the g-factors, $M^2_{i,nn} = \|\mathbf{M}_{i,nn}\|^2 = \frac{1}{2}g^2_{i,n}$

$$\sigma_{K,ii}^{pc} = -\frac{\mu_0\mu_B^2}{4\pi}\frac{T_{K,ii}}{Q_0}\sum_n e^{-\beta E_n}\left[\beta\left\|\mathbf{M}_{i,nn}\right\|^2 + 2\sum_{m\neq n}\frac{\left\|\mathbf{M}_{i,nm}\right\|^2}{E_m - E_n}\right] \quad (2.6.29)$$

$$= -\frac{\mu_0\mu_B^2}{4\pi}\frac{T_{K,ii}}{Q_0}\sum_n e^{-\beta E_n}\left[\frac{\beta}{2}g_{i,nn}^2 + 2\sum_{m\neq n}\frac{\left\|\mathbf{M}_{i,nm}\right\|^2}{E_m - E_n}\right] \quad (2.6.30)$$

Remember that $\mathbf{T}_K$ is traceless i.e. $T_{K,zz} = -\left(T_{K,xx} + T_{K,yy}\right)$ and in polar coordinate notation $T_{K,zz} = \frac{3\cos^2\theta_K - 1}{r_K^3} = G_K$ and $T_{K,xx} - T_{K,yy} = \frac{3\sin^2\theta_K\cos 2\phi_K}{r_K^3} = G_{K,\perp}$, Eq 2.6.29 leads to

$$\delta_K^{pc} = \frac{\mu_0\mu_B^2}{12\pi}\frac{1}{Q_0}\left\{G_K\sum_n e^{-\beta E_n}\left[\beta\Delta M_{nn} + 2\sum_{m\neq n}\frac{\Delta M_{nm}^2}{E_m - E_n}\right]\right.$$
$$\left. + G_{K,\perp}\sum_n e^{-\beta E_n}\left[\beta\delta M_{nn} + 2\sum_{m\neq n}\frac{\delta M_{nm}^2}{E_m - E_n}\right]\right\} \quad (2.6.31)$$

where $\Delta M_{nm} = \left\|\mathbf{M}_{z,nm}\right\|^2 - \frac{1}{2}\left(\left\|\mathbf{M}_{x,nm}\right\|^2 + \left\|\mathbf{M}_{y,nm}\right\|^2\right)$ and $\delta M_{nm}^2 = \frac{1}{2}\left(\left\|\mathbf{M}_{x,nm}\right\|^2 - \left\|\mathbf{M}_{y,nm}\right\|^2\right)$. In the case of axial symmetry, $\left\|\mathbf{M}_{x,nm}\right\|^2 = \left\|\mathbf{M}_{y,nm}\right\|^2$, $\delta M_{nm}^2 = 0$, Eq. 2.6.31 reduces to the axial component only,

$$\delta_K^{pc} = \frac{\mu_0\mu_B^2}{12\pi}\frac{1}{Q_0}G_K\sum_n e^{-\beta E_n}\left[\beta\Delta M_{nn} + 2\sum_{m\neq n}\frac{\Delta M_{nm}^2}{E_m - E_n}\right] \quad (2.6.32)$$

Eq. 2.6.32 indicates that the anisotropy of the magnetic moment of a paramagnetic complex induces an extra chemical (pseudocontact) shift compared to the diamagnetic reference complex as first pointed out by McConnell and Robertson [15]. If the summation in Eq. 2.6.32 runs over all the states, one can calculate the pseudocontact shifts from the axial molar magnetic susceptibility $\Delta\chi_{ax}$ as first obtained by Kurland and McGarvey [16] and later discussed in details by Bertini *et al.* [27],

$$\delta_K^{pc} = \frac{\Delta\chi_{ax}G_K}{12\pi N_A} \quad (2.6.33)$$

where $\Delta\chi_{ax} = \chi_{m,zz} - \frac{1}{2}\left(\chi_{m,xx} + \chi_{m,yy}\right) = N_A\mu_0\mu_B^2\frac{1}{Q_0}\sum_n e^{-\beta E_n}\left[\beta\Delta M_{nn} + 2\sum_{m\neq n}\frac{\Delta M_{nm}^2}{E_m - E_n}\right]$. If a system is axial, we will use Eq. 2.6.33 to evaluate the pseudocontact shifts otherwise Eq. 2.6.28 is used.

- Model for the ground J manifold of a Ln complex

  In the lanthanide complexes, the crystal field splitting of the $2J+1$ levels are in order of room temperature energy $\left(200\,\mathrm{cm}^{-1}\right)$ and all the levels are substantially populated. So in Eq. 2.6.29, the sum runs over the whole J manifold. Due to the homogeneous population in all the levels, to the first approximation, one assumes

that the magnetic moment is isotropic $\|\mathbf{M}_{i,JJ}\|^2 \propto g_J^2 J(J+1)$ i.e. recovering the spherical symmetry of the free ion. The chemical shift sums over the three components of the pNMR shielding tensor and vanishes due the geometrical factors, $\sigma_{xx}^p + \sigma_{yy}^p + \sigma_{zz}^p = \sum_i T_{K,ii}\chi_{ii} = 0$. So the T^{-1} term (Curie term) vanishes. Although the Curie term does not contribute to the observed pNMR shifts, as already discussed in section 1.5, based on the crystal field model, Bleaney had pointed out that the axial zero-field splitting of the J manifold makes the magnetic susceptibility anisotropic ,

$$\chi_{m,zz} - \chi_m = \Delta\chi_{ax}^B = -\frac{N_A\mu_0\mu_B^2 g_J^2 B_0^2 \langle J||\alpha||J\rangle}{30k_B^2T^2} J(J+1)(2J-1)(2J+3) \left[1 + \frac{ak_BT}{\Delta} + \frac{bk_B^2T^2}{\Delta^2} + \frac{ck_B^2T^2}{\Delta\Delta'}\right] \tag{2.6.34}$$

where a, b and c are the Ln^{III} ion dependent magnetic constants tabulated in Bleaney's original formulation in Ref. [17], Δ the energy gap between J and $J+1$ manifolds, Δ' the energy gap between J and $J+2$ manifolds. And as deduced by Bleaney, the pseudocontact shifts $\frac{\Delta\nu_K}{\nu_0}$ (in ppm) in the axial lanthanide complex is given by

$$\frac{\Delta\nu_K}{\nu_0} = \frac{(\chi_{m,zz} - \chi_m)}{8\pi N_A}\left(\frac{3\cos^2\theta_K - 1}{r_K^3}\right) \tag{2.6.35}$$

$$= -\frac{1}{8\pi\cancel{N_A}}\frac{\cancel{N_A}\mu_0\mu_B^2}{15k_B^2T^2} C_{Ln}^B A_2^0\langle r^2\rangle G_K$$

$$= -\frac{\mu_B^2\mu_0}{120\pi k_B^2T^2} C_{Ln}^B A_2^0\langle r^2\rangle G_K \tag{2.6.36}$$

$$= -\frac{\mu_B^2}{30k_B^2T^2} C_{Ln}^B A_2^0\langle r^2\rangle G_K \tag{2.6.37}$$

where $C_{Ln}^B = C_{Ln}^B = g_J^2\langle J||\alpha||J\rangle J(J+1)(2J-1)(2J+3)$ is the Bleaney's constant [17], $A_2^0\langle r^2\rangle$ is the second order axial CFP (in Stevens notation, $A_2^0\langle r^2\rangle = \frac{1}{2}B_0^2$).

Despite being based on a simple model, Bleaney's formula was widely explored (accepted by many at the same time also criticized) especially for the LIS in the isostructural lanthanide complexes [64]. Because, a further extension of the Bleaney's model predicts $1/T$ and $1/T^2$ dependency for the contact and dipolar shifts, respectively, for the Lanthanide complexes and helped to separate the contributions based on the T dependency [19, 20, 26]. In chapter 5, we are going to explore the CFPs in the isostructural $[Ln^{III}(DPA)_3]^{3-}$ complexes and will try to validate Bleaney's model based on the CFP B_0^2 obtained from *ab initio* with those from the pNMR shifts. Further applications of Bleaney's model for the AIS have mostly failed due to the major breakdown of the Bleaney's assumptions for the actinides because of

the larger splitting of an An J manifold by the ligand field compared to room temperature energy.

- Model for an isolated KD

  For a well isolated ground KD and in the PAF of the **g** tensor, $\left\|\mathbf{M}_{i,11}\right\|^2 = \frac{1}{2}g_{i,1}^2$, and in case of an axial system, Eq. 2.6.32 is reduced to

$$\delta_K^{pc} = \frac{\mu_0\mu_B^2}{12\pi}G_K\frac{\left(g_{\parallel,1}^2 - g_{\perp,1}^2\right)}{4k_BT} \tag{2.6.38}$$

  where $g_\parallel = g_z$ and $g_\perp = g_x = g_y$. Eq. 2.6.38 is equivalent to Eq. 2.6.33 with $\tilde{S} = 1/2$ where

$$\chi_{m,ii} = N_A\mu_0\mu_B^2 g_{i,1}^2\frac{\tilde{S}\left(\tilde{S}+1\right)}{3k_BT} \tag{2.6.39}$$

- Model for two isolated KDs

  For two energetically lowest KDs, Eq. 2.6.29 becomes

$$\sigma_{K,ii}^{pc} = -\frac{\mu_0\mu_B^2}{4\pi}T_{K,ii} \left[\beta\frac{\left(e^{\beta\Delta/2}g_{i,1}^2 + e^{-\beta\Delta/2}g_{i,2}^2\right)}{4\left(e^{\beta\Delta/2}+e^{-\beta\Delta/2}\right)} + \frac{\left(e^{\beta\Delta/2} - e^{-\beta\Delta/2}\right)M_{i,12}^2}{\Delta\left(e^{\beta\Delta/2}+e^{-\beta\Delta/2}\right)}\right] \tag{2.6.40}$$

  and in the axial symmetry $g_{x,n} = g_{y,n} = g_{\perp,n}(n = 1,2)$ and $M_{x,12}^2 = M_{y,12}^2 = M_{\perp,12}^2$. The axial components are defined according to $\Delta g_n^2 = g_{\parallel,n}^2 - g_{\perp,n}^2$ and $\Delta M_{12}^2 = M_{\parallel,12}^2 - M_{\perp,12}^2$ and Eq. 2.6.40 takes the form

$$\delta_K^{pc} = \frac{\mu_0\mu_B^2}{12\pi}G_K \left[\beta\frac{\left(e^{\beta\Delta/2}\Delta g_1^2 + e^{-\beta\Delta/2}\Delta g_2^2\right)}{4\left(e^{\beta\Delta/2}+e^{-\beta\Delta/2}\right)} + \frac{\left(e^{\beta\Delta/2} - e^{-\beta\Delta/2}\right)\Delta M_{12}^2}{\Delta\left(e^{\beta\Delta/2}+e^{-\beta\Delta/2}\right)}\right] \tag{2.6.41}$$

- Model for an isolated NKD

  In case of a well isolated NKD, Eq. 2.6.29 becomes

$$\sigma^{pc}_{K,ii} = -\frac{\mu_0\mu_B^2}{4\pi}T_{K,ii}\left[2\frac{\left(e^{\beta\Delta/2}-e^{-\beta\Delta/2}\right)M^2_{i,12}}{\Delta\left(e^{\beta\Delta/2}+e^{-\beta\Delta/2}\right)}\right] \tag{2.6.42}$$

$$= -\delta_{iz}\frac{\mu_0\mu_B^2}{4\pi}T_{K,ii}\left[\frac{\left(e^{\beta\Delta/2}-e^{-\beta\Delta/2}\right)}{2\Delta\left(e^{\beta\Delta/2}+e^{-\beta\Delta/2}\right)}g_z^2\right] \tag{2.6.43}$$

where δ_{iz} denotes the Kronecker symbol. The isotropic pNMR shift in Eq. 2.6.32 becomes

$$\delta^{pc}_{K} = \frac{\mu_0\mu_B^2}{12\pi}G_K\frac{\left(e^{\beta\Delta/2}-e^{-\beta\Delta/2}\right)}{2\Delta\left(e^{\beta\Delta/2}+e^{-\beta\Delta/2}\right)}g_z^2 \tag{2.6.44}$$

2.6.3.2 Contact shift

The contact operator of the hyperfine interaction $\hat{\boldsymbol{F}}^c_K = \frac{\hat{\boldsymbol{A}}^c_K}{g_K\mu_N}$ is responsible for the contact hyperfine shift and Eq. 2.2.3 for the diagonal component can be written as

$$\sigma^{c}_{K,ii} = \frac{1}{g_K\mu_N Q_0}\sum_n e^{-\beta E_n}\left[\beta\sum_{\nu,\nu'}\langle n\nu|\hat{m}_i|n\nu'\rangle\langle n\nu'|\hat{A}^c_{K,i}|n\nu\rangle + 2\sum_{m\neq n}\sum_{\nu,\mu}\frac{\sum_{\nu,\nu'}\langle n\nu|\hat{m}_i|m\mu\rangle\left\langle m\mu|\hat{A}^c_{K,i}|n\nu\right\rangle}{E_m-E_n}\right] \tag{2.6.45}$$

As we can see from Eq. 1.8.11, the contact shifts originate from the presence of spin density at the nucleus and are related to the spin delocalization of paramagnetic center towards the nucleus K through the chemical bonds. To the first approximation, one only considers the spin-only magnetic moment in Eq. 2.6.45 i.e.

$$\sigma^{c}_{K,ii} = \frac{1}{g_K\mu_N Q_0}\sum_n e^{-\beta E_n}\left[\beta\sum_{\nu,\nu'}\left\langle n\nu|\hat{m}^S_i|n\nu'\right\rangle\langle n\nu'|\hat{A}^c_{K,i}|n\nu\rangle + 2\sum_{m\neq n}\sum_{\nu,\mu}\frac{\sum_{\nu,\nu'}\langle n\nu|\hat{m}^S_i|m\mu\rangle\left\langle m\mu|\hat{A}^c_{K,i}|n\nu\right\rangle}{E_m-E_n}\right] \tag{2.6.46}$$

If one further assumes that the hyperfine interaction in between the states are the same and related to the proportionality constant $A^c_{K,i}$ i.e. $\langle n\nu|\hat{A}_{K,i}|m\mu\rangle = A_{K,i}\langle n\nu|\hat{S}_{K,i}|m\mu\rangle$, then Eq. 2.6.46 can be written in terms of the spin-only magnetic susceptibility $\boldsymbol{\chi}^S$ as

$$\sigma^c_{K,ii} = -\frac{1}{\mu_B\mu_N g_e g_K Q_0}\sum_n e^{-\beta E_n}\left[\beta\sum_{\nu,\nu'}\left\langle n\nu|\hat{m}^S_i|n\nu'\right\rangle\left\langle n\nu'|A^c_{K,i}\hat{m}^S_i|n\nu\right\rangle\right.$$
$$\left.+2\sum_{m\neq n}\sum_{\nu,\mu}\frac{\Sigma_{\nu,\nu'}\left\langle n\nu|\hat{m}^S_i|m\mu\right\rangle\left\langle m\mu|A^c_{K,i}\hat{m}^S_i|n\nu\right\rangle}{E_m-E_n}\right] \quad (2.6.47)$$
$$= -\frac{1}{\mu_0\mu_B\mu_N g_e g_K}A^c_{K,i}\chi^S_{ii} \quad (2.6.48)$$

The constant $A^c_{K,i}$ is related to the spin density at the nucleus. In the non-relativistic regime, spin is a good quantum number and one considers a quantization axis (let's say z axis) to define the spin density and further for $i = x,y,z$, one assumes $A^c_{K,z} = A^c_{K,x} = A^c_{K,y} = A^c_K$. Then, the isotropic contact chemical shift is given by

$$\delta^c_K = \frac{1}{N_A\mu_0\mu_B g_e\gamma_K}\frac{A^c_K}{\hbar}\chi^S_m \quad (2.6.49)$$
$$= \frac{1}{N_A\mu_0\mu_B g_e\gamma_K}\frac{A^c_K}{\hbar}\frac{\langle M^S\rangle}{B_0} \quad (2.6.50)$$

where $\gamma_K = \frac{g_K\mu_N}{\hbar}$ is the gyromagnetic factor of nucleus K, $\langle M^s\rangle$ the thermal average of electron spin magnetization.

- Model for an isolated KD

In the Hilbert space of a KD, the temperature dependent Curie term in Eq. 2.6.46 becomes

$$\sigma^p_{K,ii} = \frac{\beta}{2g_K\mu_N}\sum_\nu\sum_{\nu'}\left\langle n\nu\left|\hat{m}_i\right|n\nu'\right\rangle\left\langle n\nu'\left|\hat{A}^c_{K,i}\right|n\nu\right\rangle \quad (2.6.51)$$
$$= -\frac{\mu_B}{4g_K\mu_N k_B T}g_{i,1}A^c_K \quad (2.6.52)$$

The isotropic shift $\delta^c_K = -\frac{1}{3}\left(\sigma^c_{K,xx}+\sigma^c_{K,yy}+\sigma^c_{K,zz}\right) \propto \frac{1}{3}\left(g_{x,1}+g_{y,1}+g_{z,1}\right) \propto g_1$

$$\delta^c_K = \frac{\mu_B}{4\gamma_K k_B T}\frac{A^c_K}{\hbar}g_1 \quad (2.6.53)$$

The contact shift originates from the isotropic g-factor whereas the anisotropy of it is giving rise to the pseudocontact shift as described by Eq. 2.6.38 [65]. In the spin Hamiltonian formalism, a KD is modeled by a pseudospin $\tilde{S} = 1/2$ and Eq. 2.6.53 can be written as

$$\delta^c_K = \frac{\mu_B}{\gamma_K}\frac{A^c_K}{\hbar}g_1\frac{\tilde{S}\left(\tilde{S}+1\right)}{3k_B T} \quad (2.6.54)$$

Chapter 3

pNMR shifts in $[An^{VI}O_2]^{2+}$ complexes

3.1 Introduction

In this chapter, we will study the nature of pNMR shifts in the axially symmetric $[An^{VI}O_2]^{2+}$ complexes. In nature, the heaviest naturally occurring element, U and its man-made heavier neighbors readily form the divalent dioxo actinyl cations $[An^{VI}O_2]^{2+}$ which show large degree of complex formations with various ligands making them important moieties in the nuclear fuel cycle research. Bonding in the central $[An^{VI}O_2]^{2+}$ moiety is rather complex and occurs through the participation of the An valence $5f$, $6d$, $7s$ subshells and also from the semi-core $6p$ subshells which are quite important to maintain the linear geometry [66]. The An−O bonds are robust with two triply bonded oxygen atoms by σ and π interactions with the metal center. Rich bonding of the actinyl moiety, the strong relativistic effects of the actinide and also the immediate surroundings overly govern the physicochemical properties of the actinyl complexes and add the complication to properly determine their electronic structure, spectral and magnetic properties [67, 68]. The paramagnetic NMR shifts have been successfully used to study their electronic and magnetic properties [8, 69, 11]. Also *ab initio* calculations are becoming effective to properly describe their electronic structures, bonding and calculating their spectral and magnetic properties [70, 71, 72, 73, 74]. The choice of the first principles method needs to be subtle such that it provides a balanced description of all the underlying phenomenon. This creates the hard work which needs to be done to come up with a good method of calculations, but not necessarily the unique method.

So first, we will understand the electronic structures of the paramagnetic $5f^1$ and $5f^2$ actinyl cations and their magnetic properties. We will also present the different methods of *ab initio* calculations which were undertaken to compute their electronic structures, magnetic properties. Then we will present the pNMR shifts in the two sets of actinyl complexes, $[An^{VI}O_2(DPA)_2]^{2-}$ and $[An^{VI}O_2(TEDGA)_2]^{2+}$ where $An^{VI} = Np^{VI}$ and Pu^{VI} and analyze them with the help of *ab initio* calculations. In due course, we will highlight

the differences of their electronic structures from the Ln^{III} or An^{III}/An^{IV} complexes (see chapter 4) and how the electronic structures govern the nature of pNMR shifts and their temperature dependencies. We will build up the discussions for the pNMR shifts in these complexes following the general theoretical framework for the derivation of pNMR chemical shifts as proposed by Soncini and Van den Heuvel [29] (discussed in chapter 2). We will also present how the temperature dependent isotropic magnetic susceptibilities and pNMR shifts can be used as a probe to estimate the isotropic and anisotropic magnetic properties, respectively, in these actinyl complexes.

3.2 Free $[An^{VI}O_2]^{2+}$ cations

The actinyl complexes are highly axial, a major part of the isotropic pNMR shifts originates from their anisotropic magnetic behavior. To understand the origin of magnetic anisotropy in these complexes from first principles, one needs to first focus on the central $[An^{VI}O_2]^{2+}$ moiety and its bonding structure. Although, the An $5f$ orbitals interact more with the ligand's orbitals than the Ln $4f$, the $5f$ orbitals in the actinyls are even more perturbed due to the presence of the two oxo (O^{2-}) groups. This makes the actinyls far from the free ion and the *ab initio* results on actinyl complexes are analyzed from the perspective of the ligand field effects on the central $[An^{VI}O_2]^{2+}$ core and not on the free An^{VI} ion. The central $[An^{VI}O_2]^{2+}$ core has two triply bonded oxo O^{2-} groups with the hexavalent actinide ion. The molecular orbital diagram of the actinyl cation was first proposed by Einstein and Pryce [75] using the symmetry adapted linear combinations (SALCs) of the atomic orbitals under the $D_{\infty h}$ point group and is shown in Fig. 3.2.1. The σ bonds (σ_u, σ_g) arise due to the head-on overlap of the $5f_{\sigma_u}$ and $6d_{\sigma_g}$ atomic orbitals with the hybridized sp_z orbitals of the two oxo groups along the bonding axis. The remaining π bonds are formed due to the side-wise overlap of the $5f_{\pi_u}$ and $6d_{\pi_g}$orbitals with the $2p_x$, $2p_y$ atomic orbitals of the oxygens. The $5f_{\phi_u}$ and $5f_{\delta_u}$ atomic orbitals remain non-bonding and host the magnetic electrons in the paramagnetic cations. Due to the loss of spherical symmetry from the free actinide ion, J, L are not good quantum numbers but their projection along the z axis (taken as the quantization axis) i.e. the M_J and M_L are still good quantum numbers and are used to characterize the $5f$ orbitals. Before proceeding with the *ab initio* results, it is possible to describe the electronic structures of the $5f^1$ or $5f^2$ $[An^{VI}O_2]^{2+}$ cations "by hand" with the help of LFT and analytically express their energy levels, eigenstates and magnetic g-factors. The semi-empirical parameters used in the modelization can be taken from the *ab initio* results and used to evaluate their ligand field model values. Usually this kind of good attitude of semi-empirical modeling was more commonly practiced by the chemists/physicists before the advancement of *ab initio* computations and that is why, without being disrespectful, most of the best models in

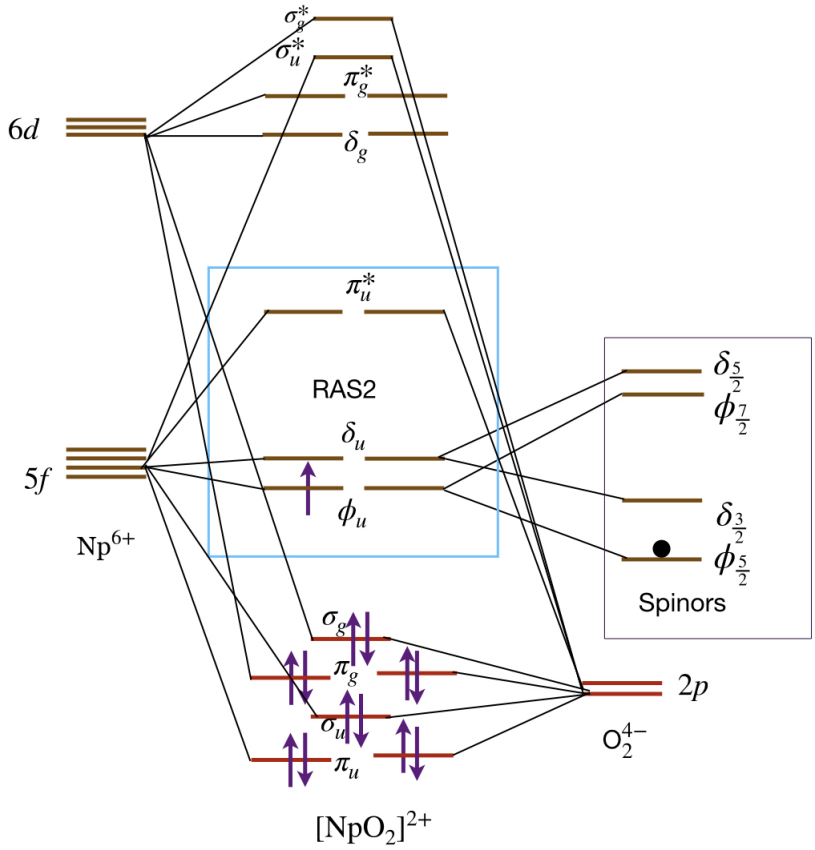

Figure 3.2.1: Molecular orbital diagram of the free neptunyl cation. The active space orbitals of the cation and the associated spinors are shown inside the boxes.

the literature are from the later half of the last century. In this case also, the ligand field modelization of $5f^1$ and $5f^2$ actinyl cations can be found in the book of Abragam and Bleaney ([36], in chapter 6). Ligand field modelization was later discussed elaborately in Ref. [73, 74] in the support of the *ab initio* results. So in the following section we will discuss the ligand field models those describe the energy levels and their probable compositions in the $5f^1$ $[NpO_2]^{2+}$ and $5f^2$ $[PuO_2]^{2+}$ cations and derive the analytical expressions of the magnetic g-factors. We will also present the *ab initio* results to find out the effectiveness of these models and further considerations.

3.2.1 Ligand field modelization

3.2.1.1 $5f^1$ $[Np^{VI}O_2]^{2+}$ cation

As already mentioned, in axial symmetry and in SF model, the $|M_L, M_S\rangle$ serve as the basis to develop the model eigenstates. In the case of SO, the eigenstates can be developed with $|M_J\rangle$. The model Hamiltonian $\hat{H}$ is a one-electron operator combining ligand field and SO effects i.e. $\hat{H} = \hat{H}^{SO} + \hat{H}^{LF}$ (LF stands with ligand field Hamiltonian only). The form of the SO operator is given in Eq. 2.5.2 with the semi-empirical constant $\xi(r)$, the

SOC parameter. In the simplest case, one can guess the probable combinations of the basis and calculate the matrix elements of $\hat{H}$ in that truncated model space. According to Hund's rules, the highest values of M_L and M_s represent the ground SF term whereas for the ground SO term, M_L and M_S are opposite in sign. So for a $5f^1$ ion, at SF level, the single unpaired electron resides in the $5f_{\phi_u}$ ($M_L = \pm 3$) orbitals and the representation of the basis $|M_L, M_S\rangle$ would be $|\pm 3, \mp 1/2\rangle$ which with SOC generates the ground Kramers eigenspinors $\phi_{5/2}$. The energetically closer $5f_{\delta_u}$ orbitals ($M_L = \pm 2$) also generates $\delta_{5/2}$ spinors with the combination of M_L and M_S as $|\pm 2, \pm 1/2\rangle$ which also interact with the ground spinors. Ligand field splitting in between $5f_{\phi_u}$ and $5f_{\delta_u}$ orbitals is taken as the semi-empirical parameter Δ (taken as a parameter). So in the truncated model space considering only the lowest $5f_{\phi_u}$ and $5f_{\delta_u}$ orbitals, the matrix elements of $\hat{H}/\xi$ is then calculated as below

$\hat{H}/\xi$	$\lvert\pm 3, \mp 1/2\rangle$	$\lvert\pm 3, \pm 1/2\rangle$	$\lvert\pm 2, \pm 1/2\rangle$	$\lvert\pm 2, \mp 1/2\rangle$
$\langle\pm 3, \mp 1/2\rvert$	**-3/2**	**0**	$\sqrt{\mathbf{3/2}}$	**0**
$\langle\pm 3, \pm 1/2\rvert$	**0**	**3/2**	**0**	**0**
$\langle\pm 2, \pm 1/2\rvert$	$\sqrt{\mathbf{3/2}}$	**0**	$\mathbf{1+\Delta'}$	**0**
$\langle\pm 2, \mp 1/2\rvert$	**0**	**0**	**0**	$\mathbf{-1+\Delta'}$

where $\Delta' = \Delta/\xi$. Note that, each of the matrix element actually corresponds to a 2×2 representation matrix (so in bold) of $\hat{H}/\xi$ which is diagonal in the corresponding doubly degenerate basis states. The four doubly degenerate eigenvalues and the corresponding eigenvectors of the above matrix are the energy levels and the eigenspinors of the single unpaired electron, and are given below with $X = \sqrt{49 + 20\Delta' + 4\Delta'^2}$,

$$E_{1/\bar{1}} = \frac{1}{4}\left(-1 + 2\Delta' - X\right) \longrightarrow \phi_1/\bar{\phi}_1 = \frac{1}{\sqrt{N}}\left(-\frac{5 + 2\Delta' + X}{2\sqrt{6}}|\pm 3, \mp 1/2\rangle + |\pm 2, \pm 1/2\rangle\right) \tag{3.2.1}$$

$$E_{2/\bar{2}} = -1 + \Delta' \longrightarrow \phi_2/\bar{\phi}_2 = |\pm 2, \mp 1/2\rangle \tag{3.2.2}$$

$$E_{3/\bar{3}} = 3/2 \longrightarrow \phi_3/\bar{\phi}_3 = |\pm 3, \pm 1/2\rangle \tag{3.2.3}$$

$$E_{4/\bar{4}} = \frac{1}{4}\left(-1 + 2\Delta' + X\right) \longrightarrow \phi_4/\bar{\phi}_4 = \frac{1}{\sqrt{N}}\left(-\frac{5 + 2\Delta' - X}{2\sqrt{6}}|\pm 3, +1/2\rangle + |\pm 2, \mp 1/2\rangle\right) \tag{3.2.4}$$

where $\frac{1}{\sqrt{N}}$ are the normalization constants. The energy level $E_{1/\bar{1}}$ has two degenerate states $\left\{\phi_1, \bar{\phi}_1\right\}$, $E_{2/\bar{2}}$ has $\left\{\phi_2, \bar{\phi}_2\right\}$ and so on. These degenerate states are the KDs of the unpaired electron.

According to Eq. 3.2.1, the two states of the KD1 $\left\{\phi_1, \bar{\phi}_1\right\}$ are explicitly written by taking the coefficients as the semi-empirical constants p, q as below

$$\phi_1 = p\,|-3,+1/2\rangle + q\,|-2,-1/2\rangle \tag{3.2.5}$$
$$\bar{\phi}_1 = p\,|+3,-1/2\rangle + q\,|+2,+1/2\rangle \tag{3.2.6}$$

where $|p|^2 + |q|^2 = 1$ i.e. the wave function must be normalized. The constants p, q are taken from the *ab initio* calculations. In the spin Hamiltonian formalism as discussed in section 1.8, a KD is modeled with a pseudospin $\tilde{S} = 1/2$ and the magnetic properties in the PAF of **g** tensor can be modeled by the three principal g-factors g_x, g_y and g_z calculated as

$$g_x = 2\mathrm{Re}\left\langle \psi \left| \hat{l}_x + 2\hat{s}_x \right| \bar{\psi} \right\rangle \tag{3.2.7}$$
$$g_y = -2\mathrm{Im}\left\langle \psi \left| \hat{l}_y + 2\hat{s}_y \right| \bar{\psi} \right\rangle \tag{3.2.8}$$
$$g_z = 2\left\langle \psi \left| \hat{l}_z + 2\hat{s}_z \right| \psi \right\rangle \tag{3.2.9}$$

In case of axial symmetry, $g_x = g_y = g_\perp$ and $g_z = g_\parallel$. So the magnetic g-factors of KD1 $\left(g_{\parallel,1}, g_{\perp,1}\right)$ is calculated within the Hilbert space of the KD1 as

$$\begin{aligned} \left|g_{\parallel,1}\right| &= \left|2\left\langle \phi_1 \left| \hat{l}_z + 2\hat{s}_z \right| \phi_1 \right\rangle\right| \\ &= \left|2\left\langle \phi_1 \left| \hat{l}_z \right| \phi_1 \right\rangle + 4\left\langle \phi_1 \left| \hat{s}_z \right| \phi_1 \right\rangle\right| \\ &= \left|-2\left(3p^2 - 2q^2\right) + 4\left(p^2/2 - 2q^2/2\right)\right| \\ &= 4\left|p^2\right| + 6\left|q^2\right| \end{aligned} \tag{3.2.10}$$

$$\begin{aligned} \left|g_{\perp,1}\right| &= \left|2\left\langle \phi_1 \left| \hat{l}_x + 2\hat{s}_x \right| \bar{\phi}_1 \right\rangle\right| \\ &= 0 \end{aligned} \tag{3.2.11}$$

The individual sign of the three g-factors is not known only the sign of their product is. Any linear combination of ϕ_1 and $\bar{\phi}_1$ also serves as basis for KD1 with the constrain that they need to be related with the time reversal symmetry. As an example, a new basis of KD1 $\{\psi_1, \bar{\psi}_1\}$ can be generated from $\left\{\phi_1, \bar{\phi}_1\right\}$ as,

$$\psi_1 = \frac{1}{\sqrt{2}}\left(\phi_1 + \bar{\phi}_1\right) \tag{3.2.12}$$
$$\bar{\psi}_1 = \hat{\tau}\psi_1 = \frac{1}{\sqrt{2}}\left(\bar{\phi}_1 - \phi_1\right) \tag{3.2.13}$$

where $\hat{\tau}$ is the time reversal operator.

Similarly for KD2,

$$\phi_2 = r|+2,-1/2\rangle \tag{3.2.14}$$
$$\bar{\phi}_2 = r|-2,+1/2\rangle \tag{3.2.15}$$

$$\begin{aligned}\left|g_{\parallel,2}\right| &= \left|2\left\langle\phi_2\left|\hat{l}_z + 2\hat{s}_z\right|\phi_2\right\rangle\right| \\ &= 2\left|r^2\right|\end{aligned} \tag{3.2.16}$$

$$\begin{aligned}\left|g_{\perp,2}\right| &= \left|2\left\langle\phi_2\left|\hat{l}_x + 2\hat{s}_x\right|\bar{\phi}_2\right\rangle\right| \\ &= 0\end{aligned} \tag{3.2.17}$$

3.2.1.2 $5f^2$ $[Pu^{VI}O_2]^{2+}$ cation

In the case of $5f^2$ $[PuO_2]^{2+}$ cation, one unpaired electron is in the $5f_{\phi_u}$ orbitals and the other unpaired electron resides in the energetically closer $5f_{\delta_u}$ orbitals. This is because both the $5f_{\phi_u}$ orbitals are in the plane, the electron-electron repulsion energy becomes larger than the ligand field splitting Δ. So to minimize the repulsion from the electron in the in-plane $5f_{\phi_u}$ orbitals, the second unpaired electron shifts to the out-of-plane excited $5f_{\delta_u}$ orbitals. According to Hund's rules, M_L and M_S should be maximized i.e. $M_L = \pm 3 \pm 2$, $M_S = \pm 1$ and M_S should be opposite i.e. the ground SF basis are $|\pm 5, \mp 1\rangle$. Remember that the model Hamiltonian $\hat{H} = \hat{H}^{SO} + \hat{H}^{LF}$ is now a two-electron Hamiltonian, but can be written as a sum of a one-electron operator. The SO operator $\hat{H}^{SO} = \sum_{i=1}^{2} \xi(i)\, \hat{l}_i \cdot \hat{s}_i = \xi \hat{\boldsymbol{L}} \cdot \hat{\boldsymbol{S}}$ with ξ as the SOC parameter taken from *ab initio* calculations. The SO term of the $\hat{H}$ mixes the excited singlet states $|\pm 4, 0\rangle$, with energy gap λ (taken as parameter), with the ground SF basis. The matrix elements of $\hat{H}/\xi$ in the model space can be calculated as below

$\hat{H}/\xi$	$\lvert\pm 5, \mp 1\rangle$	$\lvert\pm 4, 0\rangle$
$\lvert\pm 5, \mp 1\rangle$	**-5**	$\sqrt{\mathbf{11}}$
$\lvert\pm 4, 0\rangle$	$\sqrt{\mathbf{11}}$	$\boldsymbol{\lambda'}$

where $\lambda' = \lambda/\xi$. Again, each of the matrix element corresponds to a 2×2 diagonal matrix of $\hat{H}/\xi$ in the corresponding doubly degenerate basis states. The energy levels and the wave functions are calculated as following with $X = \sqrt{69 + 10\lambda' + \lambda'^{,2}}$,

$$E_{1/2} = \frac{1}{2}\left(-5+\lambda'-X\right) \longrightarrow \Omega_1/\Omega_2 = \frac{1}{\sqrt{N}}\left(-\frac{5+\lambda+X}{2\sqrt{11}}\left|\pm5,\mp1\right\rangle + \left|\pm4,0\right\rangle\right) \tag{3.2.18}$$

$$E_{3/4} = \frac{1}{2}\left(-5+\lambda'+X\right) \longrightarrow \Omega_3/\Omega_4 = \frac{1}{\sqrt{N}}\left(-\frac{5+\lambda-X}{2\sqrt{11}}\left|\pm5,\mp1\right\rangle + \left|\pm4,0\right\rangle\right) \tag{3.2.19}$$

where $\frac{1}{\sqrt{N}}$ are the normalization constants. The two states $\{\Omega_1, \Omega_2\}$ are not related by time reversal symmetry as one expects in the case for even number of unpaired electrons' system, but they are degenerate.

$$\Omega_1 = s\left|-5,+1\right\rangle + t\left|-4,0\right\rangle \tag{3.2.20}$$

$$\Omega_2 = s\left|+5,-1\right\rangle + t\left|4,0\right\rangle \tag{3.2.21}$$

s and t are coefficients, can be taken from *ab initio* calculations. These two states are called a non-Kramers doublet (NKD) and can be modeled as a pseudospin $\tilde{S} = 1/2$ system, just like a KD. There is only one non-zero g-factor associated with a NKD and calculated as follows

$$\begin{aligned}\left|g_{\parallel,NKD}\right| &= \left|2\left\langle\Omega_1\left|\hat{l}_z + 2\hat{s}_z\right|\Omega_1\right\rangle\right| \\ &= \left|2\left(-5s^2 - 4t^2\right) + 4s^2\right| \\ &= 6\left|s^2\right| + 8\left|t^2\right|\end{aligned} \tag{3.2.22}$$

3.2.2 *Ab initio* electronic structures

SO-CAS based methods have already been established as 'the methods' to compute the energy levels and the magnetic properties of the open shell Ln or An complexes [48]. In the case of free actinyl cations and also for the complexes, SO-CAS based methods have been successfully applied by Gendron *et al.* to describe their energy states and magnetic properties [73, 74]. However the data presented here are not taken from the literature since our goal is not to re-describe them, but as they are the "hot-spots" in the complexes where all the 'funs' are going on, they serve as the best testing ground so that we can apply all the methods of calculations which we are going to use later for the complexes and keep tracking of all the changes. So, according to Fig. 3.2.1, in the CAS based methods, six metallic valence orbitals are chosen as the active orbitals i.e. $5f_{\phi_u}$, $5f_{\delta_u}$ and $5f_{\pi_u^*}$ (* denotes the anti-bonding character). Charge transfer from (LMCT) or to (MLCT) the O^{2-} groups can affect the SF energy levels or in quantum chemistry language, configuration interactions of the metal based active space determinants with the charge transfer states helps to describe better the dynamic correlation. To recover the correlation energy, we

extended the active space to the bonding and anti-bonding orbitals of actinyl moiety in the RAS based methods. The variational SCF calculations are not sufficient to recover the dynamic correlation energy as there are two triple bonds and a lot of electron density is compacted along the bonds. It is worthy to mention here that RAS based calculations on the actinyl complexes were performed by Gendron *et al.* for the *ab initio* evaluation of the ^{13}C pNMR shifts in the actinyl-carbonate complexes in Ref. [9] and also by Koprowiak for the electronic structure calculations of the paramagnetic uranyl complexes during his thesis [76]. So for a better understanding, it is important to take a détour and see the results from the different methods of *ab initio* calculations on the free actinyl moieties. Computational details are provided in Appendix A.

The *ab initio* computed energy levels of the $5f^1$ $[Np^{VI}O_2]^{2+}$ cation are reported in Table 3.1, both from the SF and SO calculations. The SF wave functions of the $5f^1$ cations are symbolized with the irreps of $D_{\infty h}$ group, Φ, Δ and Π according to the symmetry of the magnetic orbitals. The composition of the first two SO KDs (KD1 & KD2) in terms of the SF wave functions are reported using their characteristic symbols in Table 3.2. In the SF ground state of the free $[Np^{VI}O_2]^{2+}$ cation, the singly unpaired electron occupies the degenerate $5f_{\phi_u}$ orbitals making the degenerate SF ground states $^2\Phi$ which with SOC generates a $^2\Phi_{5/2}$ ground KD. Second order SOC interaction with the energetically closer $^2\Delta_{5/2}$ KD generated from excited SF $^2\Delta$ states, is definitely noticed by the one-tenth presence of $^2\Delta$ states in the KD1, as also predicted in the ligand field modelization according to Eq. 3.2.6. The % of (Φ,Δ) characters of KD1 and KD2 are almost the same in all the methods; they are $(89,11)$ and $(2,98)$, respectively. The energy gap Δ (taken as a parameter in the ligand field model) between the SF ground degenerate states $^2\Phi$ and the excited states $^2\Delta$ gets reduced considering the PT2 based energy corrections on top of the corresponding variational CAS/RAS based SCF values. In both the CASPT2 and RASPT2 calculations, a reduction of Δ is by around 150-170 cm^{-1} from the corresponding SCF values. Notably, as observed from Table 3.1, extending the active space has the large impact of increasing Δ by 18% already at the variational level of calculations, after that it is reduced by the same amount in the PT2 methods. So an overall large value of Δ in the RAS based calculations than the CAS and also a better treatment of the electron dynamic correlation in the PT2 methods decreases the energy gap in between the Φ and Δ states.

For the $5f^2$ $[Pu^{VI}O_2]^{2+}$ cation, the *ab initio* energy levels are also tabulated in Table 3.1. At the SF levels, first two ground triplet states are degenerate and both belong to the SF term symbol ^3H. These two states are developed as linear combinations of the configuration states, $5f^{\uparrow}_{\phi_u} 5f^{\uparrow}_{\delta_u} \prod_b^{core} b^{\uparrow\downarrow}$ where the two unpaired electrons are mostly in the energetically lower $5f_{\phi_u}$ and $5f_{\delta_u}$ orbitals. The second unpaired electron mainly remains in the out-of-plane $5f_{\delta_u}$ orbitals to minimize the electron repulsion from the other one in

Table 3.1: Energy levels (in cm^{-1}) from SF and SO calculations. The SF wave functions correspond to the energy levels are given inside the parenthesis. In case of SO, the energy levels for the $5f^1$ $[Np^{VI}O_2]^{2+}$ cation are always doubly degenerate i.e. the KDs and the corresponding SO term symbols are inside the parenthesis. For the PT2 energy levels, the notations are the same as the SCF ones.

CASSCF		CASPT2		RASSCF		RASPT2	
SF	SO	SF	SO	SF	SO	SF	SO
			$[Np^{VI}O_2]^{2+}$				
$0(^2\Phi)$	$0(^2\Phi_{5/2})$	0	0	$0(^2\Phi)$	$0(^2\Phi_{5/2})$	0	0
$0(^2\Phi)$	$3067(^2\Delta_{3/2})$	0	2963	$0(^2\Phi)$	$3316(^2\Delta_{3/2})$	0	3122
$1325(^2\Delta)$	$8151(^2\Phi_{7/2})$	1175	8167	$1560(^2\Delta)$	$8060(^2\Phi_{7/2})$	1388	8079
$1325(^2\Delta)$	$9290(^2\Delta_{5/2})$	1175	9175	$1560(^2\Delta)$	$9471(^2\Delta_{5/2})$	1388	9337
$23895(^2\Pi)$	$26949(^2\Pi_{1/2})$	25025	28500	$25050(^2\Pi)$	$28275(^2\Pi_{1/2})$	22075	25763
$23895(^2\Pi)$	$30480(^2\Pi_{3/2})$	25025	32121	$25050(^2\Pi)$	$31373(^2\Pi_{3/2})$	22075	29020
			$[Pu^{VI}O_2]^{2+}$				
triplet		triplet		triplet		triplet	
$0(^3H)$	$0(^3H_4)$	0	0	$0(^3H)$	$0(^3H_4)$	0	0
$0(^3H)$	$0(^3H_4)$	0	0	$0(^3H)$	$0(^3H_4)$	0	0
3635	4489	3053	3138	3745	4512	2842	3165
6651	6977	4592	4857	6655	6984	4982	5263
6651	6978	4653	4899	6655	6984	5016	5292
20080	7542	15395	7585	19778	7415	15339	7467
23250	7542	26649	7585	24833	7415	23521	7467
singlet	13183	singlet	11173	singlet	13047	singlet	11455
10169	13271	6671	11709	10578	13271	7839	11778
$12137(^1\Gamma)$	13271	7312	11716	$12413(^1\Gamma)$	13271	8891	11785
$12137(^1\Gamma)$	13780	7344	11773	$12413(^1\Gamma)$	13479	8927	12420

Table 3.2: Compositions (in %) of the first two KDs of $[Np^{VI}O_2]^{2+}$ cation in terms of the SF wave functions $^2\Phi$, $^2\Delta$ and $^2\Pi$. In case of SO-ZORA/PBE0, composition of the singly occupied Kramers spinors $\phi_{5/2}$ in terms of $5f_{\phi_u}$ and $5f_{\delta_u}$ orbitals.

Method	KD	$^2\Phi$	$^2\Delta$	$^2\Pi$
SO-CASSCF	$^2\Phi_{5/2}$	89	11	-
	$^2\Delta_{3/2}$	2	98	-
SO-CASPT2	$^2\Phi_{5/2}$	89	11	-
	$^2\Delta_{3/2}$	2	98	-
SO-RASSCF	$^2\Phi_{5/2}$	89	11	-
	$^2\Delta_{3/2}$	2	98	-
SO-RASPT2	$^2\Phi_{5/2}$	89	11	-
	$^2\Delta_{3/2}$	2	98	-
SO-ZORA/PBE0	$\phi_{5/2}$	84	16	-

the in-plane $5f_{\phi_u}$ orbitals. In the SO, as modeled in subsection 3.2.1.2, the first two SO states $\{\Omega_1, \Omega_2\}$, both designated by the SO term symbol $^3H_4$ are degenerate and are well isolated from the excited states. These two degenerate states are the *ab initio* basis of the ground NKD which can be used to calculate the magnetic g-factor of the $[Pu^{VI}O_2]^{2+}$ cation. The compositions of the SF(SO)-RASSCF wave functions are given in Table 3.3. For the SF wave functions $^{2S+1}\Lambda$, compositions are given in terms of the most dominant configurations and for the NKD basis of $^3H_4$ in terms of the SF wave functions. The NKD basis are majorly weighted ($> 95\%$) by the first two ^3H states, but due to SOC, there is a little mixing (around 4%) of the low lying singlet states $^1\Gamma$ as already discussed in the ligand field modelization. The singlet states $^1\Gamma$ are around 12000 cm^{-1} at the variational SCF calculations, but the energy gaps are highly reduced with the PT2 calculations.

Table 3.3: Percentage contributions of the SF states $^{2S+1}\Lambda$ to the ground NKD basis $\{\Omega_1, \Omega_2\}$ of $^3H_4$. For the SF wave functions $^{2S+1}\Lambda$, compositions are given in terms of the most dominant configurations.

SF states	Configurations	$^3H_4(\Omega_1)$	$^3H_4(\Omega_2)$
^3H	$86\%\ 5f^{\uparrow}_{\phi\pm}5f^{\uparrow}_{\delta\pm}$	47.6	47.6
^3H	$86\%\ 5f^{\uparrow}_{\phi\pm}5f^{\uparrow}_{\delta\pm}$	47.6	47.6
$^1\Gamma$	$39\% f^{\uparrow\downarrow}_{\delta+}$; $38\%\ f^{\uparrow\downarrow}_{\delta-}$ $5\%\ f^{\uparrow}_{\phi-}f^{\downarrow}_{\pi-}$; $5\%\ f^{\uparrow}_{\phi+}f^{\downarrow}_{\pi+}$	0.0	3.7
$^1\Gamma$	$76\%\ f^{\uparrow}_{\delta+}f^{\downarrow}_{\delta-}$; $5\%\ f^{\uparrow}_{\phi+}f^{\downarrow}_{\pi-}$ $5\%\ f^{\uparrow}_{\phi-}f^{\downarrow}_{\pi+}$	3.7	0.0

3.2.3 Magnetic g-factors

The magnetic g-factors of the $[Np^{VI}O_2]^{2+}$ cation are given in Table 3.4 both from the *ab initio* calculations and the ligand field model. The parameters in the model equations are taken from the *ab initio* calculations. There is no coupling in the xy plane as one expects, so $g_\perp = 0$. $g_{\parallel,n}, (n = 1,2)$ according to the ligand field model are calculated using Eq. 3.2.10 and Eq. 3.2.16 for the KDs $^2\Phi_{5/2}$ and $^2\Delta_{3/2}$, respectively. $g_{\parallel,1}$ from the *ab initio* calculations and the ligand field model are exactly the same indicating ground Kramers spinors $\phi_{5/2}$ for the unpaired electron. $g_{\parallel,2}$ from the model slightly differs from the *ab initio* values since we excluded the energetically higher $5f_{\pi^*_u}$ orbitals from the model space and hence missing the interactions with the π spinors. $g_{\parallel,2}$ is close to value that is obtained from the $\delta_{3/2}$ Kramers spinors. So the first $f-f$ transition state in the neptunyl cation corresponds to a excitation of the unpaired electron from the $\phi_{5/2}$ spinors to the $\delta_{3/2}$ spinors. The composition of the KDs and hence the associated g-factors are not at

all affected by the different levels of theoretical calculations, although there are small differences in the energy spectrum but result in negligible effects on the magnetic properties in the case of free $[Np^{VI}O_2]^{2+}$ cation. Benchmark calculations with the relativistic DFT methods also result similar $g_{\parallel,1}$ for the ground KD.

Table 3.4: The magnetic g-factors of the $[Np^{VI}O_2]^{2+}$ cation in the $\parallel$ (along the actinyl bonding axis) and $\perp$ directions from *ab initio* calculations and ligand field model (LFM).

Method	KD	$g_\perp$ (LFM)	$g_\parallel$ (LFM)	$g_\perp$ (*ab initio*)	$g_\parallel$ (*ab initio*)
SO-CASSCF	$^2\Phi_{5/2}$	0.00	4.22	0.00	4.22
	$^2\Delta_{3/2}$	0.00	1.96	0.00	2.03
SO-CASPT2	$^2\Phi_{5/2}$	0.00	4.22	0.00	4.22
	$^2\Delta_{3/2}$	0.00	1.96	0.00	2.03
SO-RASSCF	$^2\Phi_{5/2}$	0.00	4.22	0.00	4.22
	$^2\Delta_{3/2}$	0.00	1.96	0.00	2.03
SO-RASPT2	$^2\Phi_{5/2}$	0.00	4.22	0.00	4.22
	$^2\Delta_{3/2}$	0.00	1.96	0.00	2.04
SO-ZORA/PBE0[a]	$\phi_{5/2}$			0.00	4.32
mDKS/PBE0[b]				0.00	4.21

[a]: in ADF, [b]: in ReSpect

The only non-zero g-factor $g_\parallel$ of the NKD from different methods is reported in Table 3.5. The value of $g_{\parallel,NKD}$ according to ligand field model is calculated using Eq. 3.2.22 where parameters s^2 and t^2 are taken from the RASSCF calculations as the combined weight of the first two SF states ^3H and the weight of interacting singlet states $^1\Gamma$, respectively (see Table 3.3). g-factors are roughly the same in all the *ab initio* methods indicating insignificant changes in the compositions of NKD wave functions from one method to another.

Table 3.5: The only non-zero g-factor of the NKD of $Pu^{VI}O_2{}^{2+}$ cation from *ab initio* calculations and ligand field model.

Method	$g_\parallel$ (LFM)	$g_\parallel$ (*ab initio*)
SO-CASSCF		6.10
SO-CASPT2		6.11
SO-RASSCF	6.008	6.09
SO-RASPT2		6.11

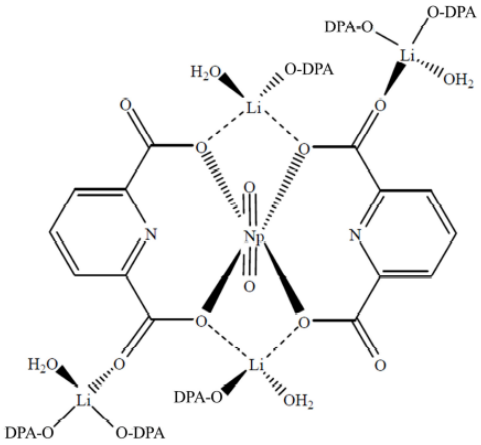

Figure 3.3.1: $Li_2An^{VI}O_2(DPA)_2 \cdot H_2O$ compound.

3.3 $[AnO_2]^{2+}$ cations chelated with the DPA ligand

3.3.1 Crystal structures

2,6-dipicolinic acid (H_2DPA) based $[An^{VI}O_2]^{2+}$ complexes were first synthesized by A. B. Yusov *et al.* [77] and their solid state structures $Li_2An^{VI}O_2(DPA)_2 \cdot H_2O$ were reported as represented in Fig. 3.3.1. The $[An^{VI}O_2(DPA)_2]^{2-}$ complex is linked to four Li^+ cations: two of them are bridging the two DPA ligands and are bonded to two oxygen atoms of the coordination sphere. The two other ones are bonded to the outermost oxygen atoms. In our work, the $Li_2An^{VI}O_2(DPA)_2 \cdot 2H_2O$ compounds where $An^{VI} = U^{VI}$, Np^{VI} and Pu^{VI} were isolated from aqueous solution and their XRD structures were determined at CEA Marcoule by M. Autillo *et al.* [11]. Furthermore, another variant of the DPA, 4-ethyl-2,6-dipicolinic acid $H_2Et-DPA$ based $[An^{VI}O_2]^{2+}$ complexes were also synthesized for the study of the ^1H pNMR shifts. Due to practical reasons, the crystals of the $H_2Et-DPA$ based compounds were not possible to isolate and so the structures were built from the XRD structures by placing the ethyl chain perpendicular to the pyridine ring. The bond distances of the first coordination sphere and the geometric parameters G_K of Eq. 2.6.33 are calculated from the XRD structures in the axial symmetry and are tabulated in Table 3.6. The ^1H nuclei of the DPA and Et-DPA ligands are numbered as presented in Fig. 3.3.2 and are averaged on chemically equivalent positions. To estimate the sensitivity of the ethyl chain position due to the rotation along $C4-C5$ bond, the geometric parameters G_K were calculated with every 10° angle. A deviation of only 1% was found for the most distant protons of the CH3 groups ($H6$). So for the interpretations of the pNMR shifts in the $[An^{VI}O_2(Et-DPA)_2]^{2-}$ complexes, the ethyl chain perpendicular to the pyridine ring is taken to avoid any bias in the interpretation due to its position.

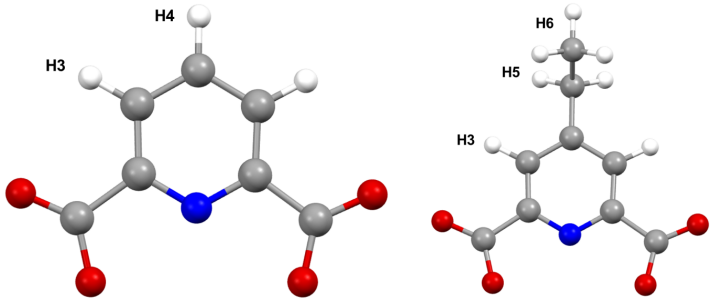

Figure 3.3.2: DPA and Et-DPA ligands with the numbering of the hydrogen atoms. Color code: blue- N, red- O, gray- C, white- H.

Table 3.6: Bond distances (Å), angles (°) and protons geometric parameters G_K (in $10^{27}m^{-3}$) in the X-rays structures of $Li_2An^{VI}O_2(DPA/Et{-}DPA)_2\cdot 2H_2O$ compounds. Protons are labeled according to Fig. 3.3.2 and are averaged on chemically equivalent positions.

	An=O	An−O	An−N	∠O=An−N	G_{H3}	G_{H4}	G_{H5}	G_{H6}
$[U^{VI}O_2(Et{-}DPA)_2]^2$	1.81	2.46	2.72	92	-5.29	-3.41	-2.39	-1.60
$Li_2U^{VI}O_2(DPA/Et{-}DPA)_2\cdot 2H_2O$	1.777(2)	2.453(2)	2.654(2)	90.1(1)	-5.77	-3.61	-2.41	-1.68
$Li_2Np^{VI}O_2(DPA/Et{-}DPA)_2\cdot 2H_2O$	1.759(1)	2.45(1)	2.648(1)	90.8(1)	-5.79	-3.61	-2.44	-1.69
$Li_2Pu^{VI}O_2(DPA/Et{-}DPA)_2\cdot 2H_2O$	1.747(3)	2.47 (2)	2.642(3)	93.0(1)	-5.82	-3.63	-2.45	-1.70

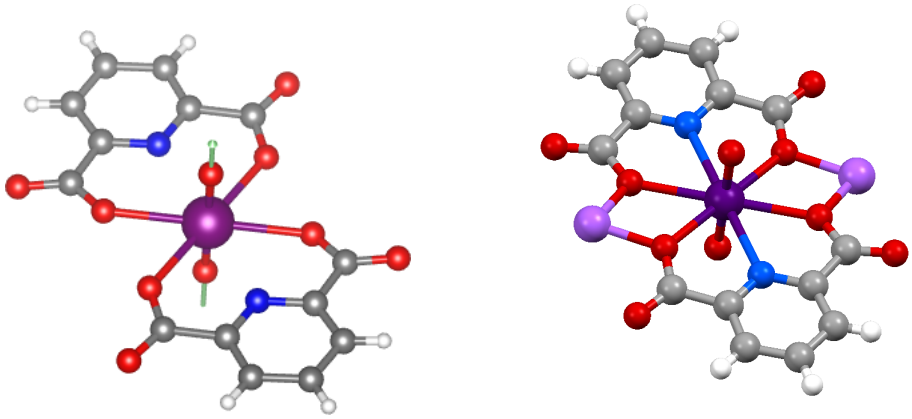

Figure 3.3.3: $[Np^{VI}O_2(DPA)_2]^{2-}$ (left) and $[Np^{VI}O_2(DPA)_2]Li_2$ (right). In the left figure, z axis is shown with the green arrow passing through the actinyl bonds. Color code: purple- Np, violet- Li, blue- N, red- O, saddle-brown- C, white- H.

3.3.2 *Ab initio* electronic structures

For the interpretation of the pNMR shifts, *ab initio* calculations were performed on the XRD structures of the paramagnetic $[An^{VI}O_2(DPA)_2]^{2-}$ complexes. We showed as well that the ethyl groups do not affect the electronic structure of the actinide and in the following, only the results for the $[An^{VI}O_2(DPA)_2]^{2-}$ are discussed. Magnetic susceptibility measured in the solid state does not fit with that in the liquid state (discussed later) in the case of $5f^1$ complexes indicating non-negligible effects due to the presence of the Li^+ counterions in the first coordination sphere as shown in Fig. 3.3.1. Two of the Li^+ cations are directly linked to the coordinating oxygen atoms of the DPA ligands which affects the electronic structure and magnetic properties . To figure out their role, *ab initio* calculations were also performed on the model complex $[Np^{VI}O_2(DPA)_2]Li_2$ (built from the XRD structure) as shown in Fig. 3.3.3. It has been observed (by a prior *ab initio* calculation) that the Li^+ cations linked to the non-coordinating oxygen atoms of the DPA ligands do not impact the electronic structure of the actinide center and are not considered in the model complex.

The electronic structures of these complexes have been computed with the SO-CAS based methods. Computational details are provided in Appendix A. As already noticed (in subsection 3.2.2) the effect of the extended CAS (RAS) based calculations on the energy levels of $[AnO_2]^{2+}$, we extended the active orbitals to the bonding and anti-bonding orbital of the actinyl cation as shown in Fig. 3.2.1. The six active orbitals of the $[Np^{VI}O_2(DPA)_2]^{2-}$ complex from the CAS(1,6) are shown in Fig. 3.3.4. It should be noted that in the coordinated actinyl complexes, due to the lowering of symmetry, one can not assign the orbitals by the M_L values as one can in the case of the free actinyl ion. This is because M_L is no longer a good quantum number, but still, for their characteristic assignments and to get

the flavor, the irreps of the central actinyl moiety are used. The orbitals are anti-bonding with the ligands' orbitals, the strongest the interaction is, the most destabilized the orbital is. The $5f_\sigma$ orbital is the most destabilized and does not need to be considered as active. The $5f_\pi$ orbitals interact with the oxo π and are strongly destabilized at more than 17000 cm^{-1}, with a small splitting due to a small interaction with the DPA ligands. Due to the lack of proper symmetry, $5f_\phi$ and $5f_\delta$ do not interact with the oxo groups' orbitals and remain non-bonding in the free actinyl, hosting the magnetic electrons. Spin density is mostly localized on the metal. In the case of free actinyl cation, $5f_\phi$ and $5f_\delta$ orbitals are doubly degenerate, but due to the presence of the ligands in the equatorial plane their degeneracies are lifted. Due to the trigonal symmetry of the equatorial ligands, the two $5f_\phi$ orbitals split by 3000 cm^{-1}; the destabilized one overlaps with the σ donating orbitals of the 6 coordinating nitrogen and oxygen atoms of the DPA, while the other one denotes a π overlap. The two $5f_\delta$ orbitals do not have any σ bonding with the orbitals of the equatorial ligands due to their equatorial nodal plane; one of them denotes a small π overlap and is destabilized by 400 cm^{-1}. As shown in Ref. [73] and also in the ligand field model in subsection 3.2.1.1, the splitting between the $5f_\phi$ and $5f_\delta$ orbitals determine the nature of the ground KD and the magnetic properties. In the free actinyl ion, the $5f_\phi$ orbitals span $e_{5/2}$ and $e_{7/2}$ spinors and the $5f_\delta$ orbitals span $e_{3/2}$ and $e_{5/2}$ spinors. In the DPA complex, the spinors $e_{5/2}$ which arises from the mixing of $5f_\delta$ and $5f_\phi$ orbitals is the ground one. Consequently, the $5f_\delta - 5f_\phi$ energy gap determines the composition of the state and plays a key role. The active space for RASSCF calculations is augmented by the σ and π orbitals of the oxo groups. This allows a better description of the electron dynamic correlation in the $[AnO_2]^{2+}$ cation and also introduces charge fluctuations as well as the spin polarization. This is evidenced by the Mulliken spin densities of +1.05 on Np and -0.03 on each O in the Np^{VI} complex and +2.1 on Pu and -0.06 on each O in the Pu^{VI} complex.

In Table 3.9, compositions of the two KDs of the $[Np^{VI}O_2(DPA)_2]^{2-}$ and $[Np^{VI}O_2(DPA)_2]Li_2$ complexes are given, obtained with the different methods of calculation. Two levels of frozen orbitals have been compared, freezing or not the $5p$ and $5d$ orbitals of the Np atom, the former scheme being the default option in MOLCAS. The effect of the $5p$ and $5d$ is in this case essential and emphasizes the effect of the correlation (denoted by * when they are correlated). And the composition can be explained from the SF energy levels in Table 3.7. Since SOC is introduced as a state interaction, the closer the states are in energy, the more they interact. The dynamic correlation correction on the SF-C(R)ASSCF energies reduces the energy gap between the Δ and Φ states as noticed in the case of free neptunyl cation also and results in a larger mixing at the SO level. In SO-CASSCF, % of (Δ,Φ) characters of KD1 and KD2 are $(95,2)$ and $(30,70)$, respectively, in the $[Np^{VI}O_2(DPA)_2]^{2-}$ complex and $(94,4)$ and $(29,71)$, respectively, in the $[Np^{VI}O_2(DPA)_2]Li_2$ complex. The composition of the SO eigenvectors of KD1 shows an

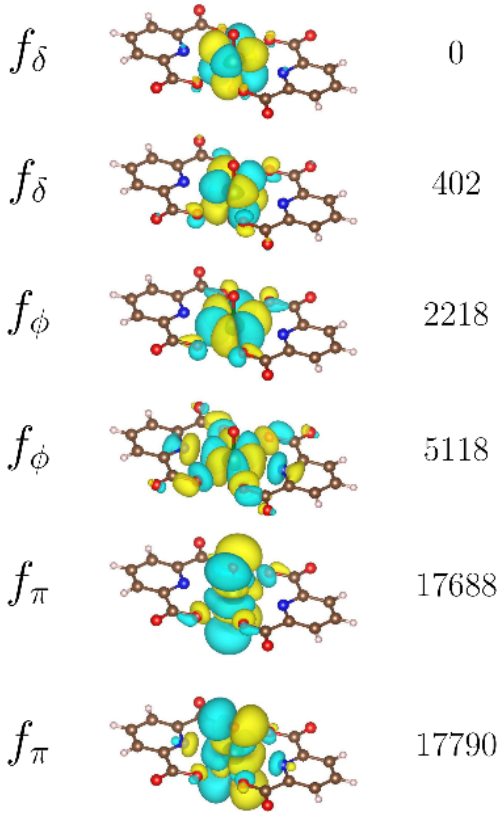

Figure 3.3.4: $5f$ active orbitals of $[Np^{VI}O_2(DPA)_2]^{2-}$. Numbers on the right side are the energies in cm^{-1}. The isovalue is 0.08 $e^-/bohr^3$.

Table 3.7: Energy levels (in cm^{-1}) of the Np^{VI} complexes from SF and SO calculations.

CASSCF		CASPT2		CASPT2*		RASSCF		RASPT2		RASPT2*	
SF	SO	SF	SO	SF	SO	SF	SO	SF	SO	SF	SO
$[Np^{VI}O_2(DPA)_2]^{2-}$											
0	0	0	0	0	0	0	0	0	0	0	0
403	820	463	625	505	455	368	455	386	418	407	333
2218	7196	1724	7007	1420	6973	1782	7052	1357	7001	1013	6696
5118	10520	5548	10638	5183	10334	4631	10004	4943	10182	4615	9944
17689	19352	20775	22310	19572	21140	18353	20062	17444	19245	17269	19158
17790	22486	20789	25367	19578	24225	18382	22967	17535	22164	17371	22082
$[Np^{VI}O_2(DPA)_2]Li_2$											
0	0	0	0	0	0	0	0	0	0	0	0
292	522	371	396	353	282	269	250	373	298	363	440
1755	7045	1338	6921	954	6898	1341	6952	952	6950	564	7068
4683	10114	5079	10260	4779	10039	4221	9658	4577	9892	4215	9765
18163	19868	19824	21467	19795	21534	18826	20630	17960	19833	17772	19872
18315	23012	19951	24570	19945	24639	18926	23534	18071	22754	17887	22798

*: $5p$ and $5d$ orbitals are correlated

increased mixing of Φ states due to successive decrease of the energy gap $\Delta\,(E1\&E2)$ and $\Phi\,(E3\&E4)$ states going from CASSCF to RASPT2 level (from 2218 cm^{-1} to 1013 cm^{-1} (see Table 3.7). In SO-RASPT2*, % of (Δ,Φ) characters of KD1 and KD2 are $(62,37)$ and $(58,40)$, respectively, in the $[Np^{VI}O_2(DPA)_2]^{2-}$ complex and $(33,67)$ and $(85,12)$, respectively, in the $[Np^{VI}O_2(DPA)_2]Li_2$ complex. For the $[Np^{VI}O_2(DPA)_2]^{2-}$ complex, restricted 2-component DFT using the PBE0 functional was performed. The composition of the single occupied spinor in terms of $5f_\delta$ and $5f_\phi$ is similar to the SO-CASSCF function (see Table 3.9). The Mulliken charges of the $[Np^{VI}O_2(DPA)_2]^{2-}$ complex with and without the two Li^+ cations are given in Table 3.8: it appears that the effect is a polarization of electron density of the DPA ligand in the presence of the positive charge which attracts the electron density towards the oxygen atoms (0.07 electron). Then, an important charge transfer from the DPA to the Li^+ cation reduces its charge to 0.48. This finally decreases the Mulliken charge by 0.12 electron on the oxygen atoms directly bonded to the Np ion, and this affects the electronic properties by lowering the ligand field effect, prominently the stabilization of the two $\Phi\,(E3\&E4)$ states by 500 cm^{-1}. KD1 has therefore a larger weight on this component. With SF-RASPT2*, $E3$ is divided by two (1013 vs. 564 cm^{-1}) by the presence of the Li^+ cations and Φ states becomes dominant in KD1, and this impacts dramatically the axiality of the **g** tensor (see next subsection). It shows that in this case, the counterions, since lying in the close vicinity of the coordination sphere, are by far not anecdotal.

Table 3.8: Mulliken charges of the oxygen atoms of the DPA ligand coordinated to Np^{VI} and of the lithium cation from SF-CASSCF calculations. In $[Np^{VI}O_2(DPA)_2]^{2-}$+2Li^+(ECP), the Li^+ cations are replaced by an ECP without any charge (from L. Seijo, unpublished, Molcas basis set).

	q_O	q_{Li}
$[Np^{VI}O_2(DPA)_2]^{2-}$	-0.68	-
$[Np^{VI}O_2(DPA)_2]^{2-}$+2Li^+(ECP)	-0.88	-
$[Np^{VI}O_2(DPA)_2]Li_2$	-0.80	0.32

In the case of $[Pu^{VI}O_2(DPA)_2]^{2-}$, the SF triplet ground state corresponds to the configurations $5f_\phi^\uparrow 5f_\delta^\uparrow \prod_b^{core} b^{\uparrow\downarrow}$, same as the free plutonyl cation. The two lowest SO states show almost similar composition and are almost degenerate without correlation. When the $5p$ and $5d$ orbitals are correlated, a gap of 84 cm^{-1} is obtained (see Table 3.10). These two states are the basis of the NKD and modeled with a pseudospin $\tilde{S}=1/2$. The ground NKD is energetically well separated from the first excited states by about 3000 cm^{-1} such that interaction with those states plays a negligible role in its magnetic properties.

Table 3.9: Compositions (in %) of the first two KDs in terms of the SF wave functions denoted by their spatial symmetry Δ, Φ and Π.

Method	KD	Δ	Φ	Π	Δ	Φ	Π
		$[Np^{VI}O_2(DPA)_2]^{2-}$			$[Np^{VI}O_2(DPA)_2]Li_2$		
SO-CASSCF	KD1	95	2	3	94	4	3
	KD2	30	70	0.2	29	71	0.2
SO-CASPT2	KD1	93	5	2	88	10	2
	KD2	31	68	0.3	34	66	0.4
SO-CASPT2*	KD1	86	12	2	65	34	1
	KD2	36	64	0.5	55	44	1
SO-RASSCF	KD1	92	6	2	75	24	2
	KD2	31	68	0.3	47	52	1
SO-RASPT2	KD1	85	13	2	56	42	0.2
	KD2	37	62	0.5	64	35	2
SO-RASPT2*	KD1	62	37	1.4	33	67	0.3
	KD2	58	40	1.7	85	12	2
SO-ZORA/PBE0		94	1.3	4.3			

*: $5p$ and $5d$ orbitals are correlated

Table 3.10: Energy levels (in cm^{-1}) of the $[Pu^{VI}O_2(DPA)_2]^{2-}$ complex from SF and SO calculations.

CASSCF		CASPT2		CASPT2*		RASSCF		RASPT2		RASPT2*	
SF	SO	SF	SO	SF	SO	SF	SO	SF	SO	SF	SO
triplet		triplet		triplet		triplet		triplet		triplet	
0	0	0	0	0	0	0	0	0	0	0	0
51	1	230	62	200	98	52	0	112	8	81	85
1506	3221	1749	2866	1886	2846	1875	3463	1673	3433	1711	3342
6413	5377	6246	4045	5260	3525	6524	5511	6211	5458	5464	5036
6491	5453	6613	4100	5628	3552	6594	5605	6308	5461	5513	5050
18277	8100	17884	8345	15077	8238	19439	8014	19274	7977	18934	7979
18370	8112	21300	8363	20560	8259	19470	8016	19343	8015	19148	8004
singlet	12310	singlet	10701	singlet	10156	singlet	12265	singlet	11988	singlet	11546
8828	12603	6912	10734	6881	10168	9457	12781	7472	12495	7228	12060
8898	12643	7151	11496	6945	11102	9954	12812	8556	12585	8608	12092
9000	13195	7704	11624	7040	11185	9961	13143	8635	13026	8643	12788
11894	14883	8124	13821	7740	13112	12241	14911	9574	14740	8761	14369
11961	14900	8368	13991	8025	13207	12307	14920	9713	14759	8860	14382

*: $5p$ and $5d$ orbitals are correlated

3.3.3 Magnetic g-factors

Magnetic g-factors of the two KDs of the Np^{VI} complexes obtained with different methods of calculation are given in Table 3.11. For $[Np^{VI}O_2(DPA)_2]^{2-}$, ground state anisotropies calculated with SO-CASSCF and SO-RASSCF methods are notably axial $(g_{\parallel,1} > g_{\perp,1})$ whereas including successive dynamic correlation with SO-CASPT2* to SO-RASPT2* methods, the anisotropy almost becomes spherical $(g_{\parallel,1} \approx g_{\perp,1})$ to planar $(g_{\parallel,1} < g_{\perp,1})$. In the variational SCF calculations, KD1 has more Δ character than Φ, that is quite opposite in the case of KD2, and hence $(g_{\parallel}, g_{\perp})$ of KD1 and KD2 are $(1.8, 0.3)$ and $(4.0, 0.4)$, respectively, in SO-CASSCF and $(1.5, 0.6)$ and $(3.7, 0.7)$, respectively, in SO-RASSCF methods. While with dynamic correlation in the PT2 calculations, they are $(1.0, 0.8)$ and $(3.0, 0.9)$, respectively, in SO-CASPT2* and $(0.9, 1.4)$ and $(1.0, 1.5)$, respectively, in SO-RASPT2*. In the ground state of $[Np^{VI}O_2(DPA)_2]Li_2$ complex, the contribution from the SF Φ states are larger than Δ and hence, the magnetic anisotropy of the KD1 becomes highly axial, $(g_{\parallel}, g_{\perp})$ of KD1 and KD2 are $(3.3, 0.9)$ and $(1.6, 1.0)$, respectively, in SO-RASPT2*.

Table 3.11: Magnetic g-factors of the Np^{VI} complexes in the $\parallel$ (along the actinyl bonding axis) and $\perp$ directions from the different methods of *ab initio* calculations. In the case of SO-ZORA/PBE0 in ADF, g-factors are calculated with the Kramers spinors with singly occupied electron.

Method	KD	$g_\perp$	$g_\parallel$	$g_\perp$	$g_\parallel$
		$[Np^{VI}O_2(DPA)_2]^{2-}$		$[Np^{VI}O_2(DPA)_2]Li_2$	
SO-CASSCF	KD1	0.3	1.8	0.3	1.9
	KD2	0.4	4.0	0.4	3.6
SO-CASPT2	KD1	0.5	1.6	0.5	1.8
	KD2	0.6	3.6	0.7	3.3
SO-CASPT2*	KD1	0.8	1.0	0.7	2.4
	KD2	0.9	3.0	0.7	2.4
SO-RASSCF	KD1	0.6	1.5	0.5	2.4
	KD2	0.7	3.7	0.8	3.0
SO-RASPT2	KD1	1.0	0.9	1.1	2.1
	KD2	1.1	2.9	1.6	0.3
SO-RASPT2*	KD1	1.4	0.9	1.0	3.3
	KD2	1.5	1.0	1.0	1.6
SO-ZORA/PBE0		0.4	1.9		

The ground NKD $(E1\&E2)$ of the $[Pu^{VI}O_2(DPA)_2]^{2-}$ complex is modeled with a pseudospin $\tilde{S} = 1/2$, and the only non-zero g-factor of the NKD is tabulated in Table 3.12 with the energy splitting between the states. The g-factor deduced from the ground NKD is insensitive to the method of calculation since the composition does not vary (see Table

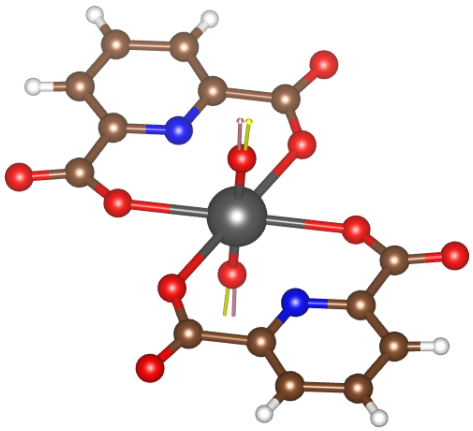

Figure 3.3.5: Principle axis of the **g** tensor of KD1 (light coral) and KD2 (light yellow) that corresponds to the g-factor $g_{\|,n}$ of $[Np^{VI}O_2(DPA)_2]^{2-}$ complex. Color code: dark gray-Np, blue- N, red- O, saddle-brown- C, white- H.

3.10) and are very close to the values of the free ion as shown Table 3.5. The **g** tensor is axial along the "yl" bond, and the equatorial values are zero, as it has to be in a NKD.

Table 3.12: The g-factor of the ground NKD ($E1\&E2$) of the $[Pu^{VI}O_2(DPA)_2]^{2-}$ complex and the splitting Δ (in cm^{-1}) of the NKD states by the ligand field.

Method	$g_{\|}$	Δ
SO-CASSCF	5.89	1
SO-CASPT2	5.70	61
SO-CASPT2*	5.73	98
SO-RASSCF	5.89	0.2
SO-RASPT2	5.85	8
SO-RASPT2*	5.84	84

3.3.4 Isotropic magnetic susceptibilities from SQUID and Evans method

For the solid $Li_2Np^{VI}O_2(DPA)_2 \cdot 2H_2O$ compound, temperature dependence of the molar magnetic susceptibility χ_m^{SQUID} between 2 and 300 K is depicted in Fig. 3.3.6. The value of 0.50 cm^3Kmol^{-1} at 300 K is below the value of an isolated ion within the *LS* coupling scheme (0.80 cm^3Kmol^{-1} for Np^{VI} with a $^2F_{5/2}$, $g_{5/2} = 6/7$ ground state). When the temperature decreases, $\chi_m^{SQUID}T$ continuously diminishes reaching 0.19 cm^3Kmol^{-1} at 3 K. The molar magnetic susceptibility in solution, χ_m^{Evans} $\left(m^3.mol^{-1}\right)$ was determined from the chemical shift difference $\Delta\delta$ between the ^1H NMR signals of working (t-$BuOH_{in}$) and reference (t-$BuOH_{out}$) solutions using the Evans method [78],

$$\chi_m^{Evans} = \frac{3\Delta\delta}{10^3\,[M]} \tag{3.3.1}$$

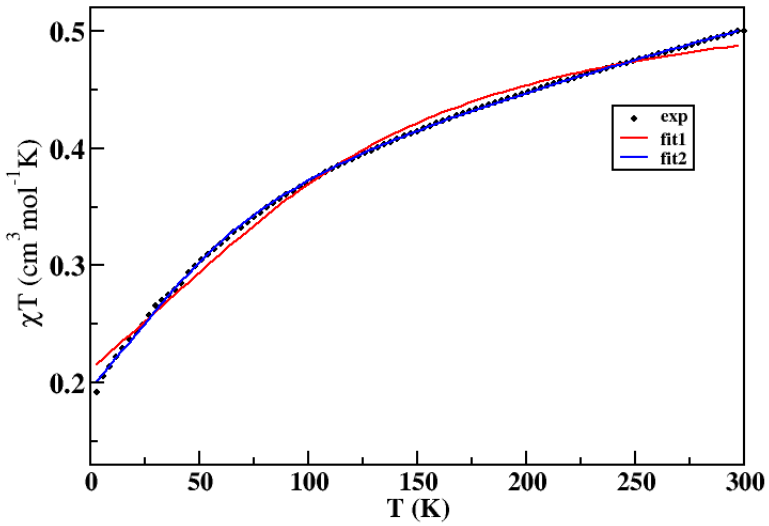

Figure 3.3.6: Molar magnetic susceptibility as a function of temperature with a field of 1 T for the $Li_2An^{VI}O_2(DPA)_2 \cdot 2H_2O$ compound. The red and blue lines show the fits using Eq. 3.3.4 without and with TIP, respectively.

where $\Delta\delta$ is dimensionless, $[M]$ is the molar concentration $\left(\text{mol.L}^{-1}\right)$ of the paramagnetic complex and χ_m^{Evans} in $\text{m}^3\text{mol}^{-1}$. The SQUID value $\chi_m^{SQUID} = (2.1 \pm 0.2) \times 10^{-8}$ $\text{m}^3\text{mol}^{-1}$at 298 K, can be compared to the value obtained from Evans method $\chi_m^{Evans} = (1.8 \pm 0.2) \times 10^{-8}$ $\text{m}^3\text{mol}^{-1}$ at 298 K. Those values are comparable, but the latter is slightly lower than the former. The techniques are different, but on the other hand, there are structural differences. The Li^+ cations are linked to one or two adjacent $Li_2[Np^{VI}O_2(DPA)_2]$ entities forming an infinite chain. As already mentioned, the cations in the 2nd position do not impact the electronic properties of the paramagnetic center, to the contrary to the Li^+ bonded to the coordinated oxygen atoms. Parker et al. have evidenced the sensitivity of the magnetic susceptibility anisotropy to the solvent in lanthanide complexes [79, 80]. The solvent molecules induce geometrical variations and transform $\Delta\chi_{ax}$ from prolate to oblate, while in the present case, counterions impact the magnetic properties through an electronic interaction with the paramagnetic center.

3.3.5 Analysis of ^{1}H pNMR shifts

^{1}H NMR spectra of $[An^{VI}O_2(DPA)_2]^{2-}$ and $[An^{VI}O_2(Et{-}DPA)_2]^{2-}$ complexes were recorded in $[D_7]$DMF at 298 K at 9.4 T. The ^{1}H spectra of $[An^{VI}O_2(Et{-}DPA)_2]^{2-}$ complexes are shown in Fig. 3.3.7 as example. The paramagnetic induced shifts δ_K^p were deduced by using the uranium complexes, $[U^{VI}O_2(DPA)_2]^{2-}$ and $[U^{VI}O_2(Et{-}DPA)_2]^{2-}$ as diamagnetic references. The chemical shifts and pNMR chemical shifts obtained at

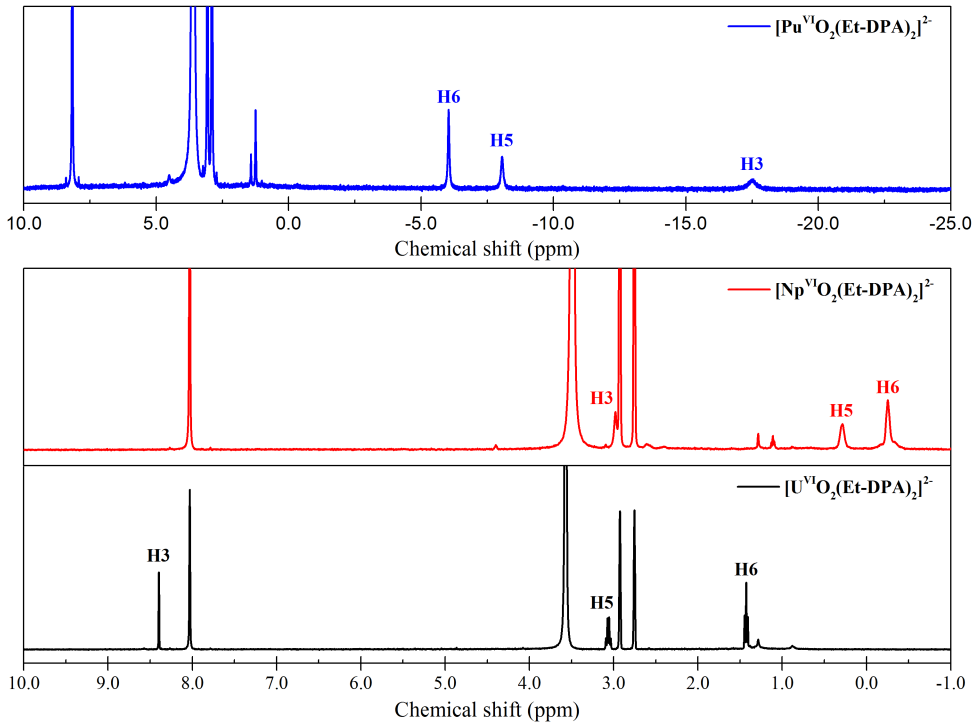

Figure 3.3.7: ^{1}H NMR spectra in $[An^{VI}O_2(Et{-}DPA)_2]^{2-}$ complexes at 298 K in $[D_7]$DMF at 9.4 T.

room temperature) are reported in Table 3.13.

Table 3.13: ^{1}H paramagnetic chemical shifts (ppm) in $[D_7]$DMF at 9.4 T and 298 K in $[An^{VI}O_2(DPA)_2]^{2-}$ and $[An^{VI}O_2(Et{-}DPA)_2]^{2-}$ complexes

	δ^p_{H3}	δ^p_{H4}	δ^p_{H5}	δ^p_{H6}
	$[An^{VI}O_2(DPA)_2]^{2-}$			
Np^{VI}	-5.94	-2.91		
Pu^{VI}	-26.31	-14.26		
	$[An^{VI}O_2(Et{-}DPA)_2]^{2-}$			
Np^{VI}	-5.51		-2.78	-1.69
Pu^{VI}	-26.02		-11.27	-7.61

- *Nature of the pNMR shifts.*

In the case of no Fermi contact contribution, the ratio $R_{K,K'}$ between the AIS of two nuclei K and K' as expressed by Eq. 2.6.33 simplifies to the ratio of their geometrical parameters G_K and $G_{K'}$

$$R_{K,K'} = \frac{\delta^p_K}{\delta^p_{K'}} = \frac{\delta^{pc}_K}{\delta^{pc}_{K'}} = \frac{G_K}{G_{K'}} \tag{3.3.2}$$

Table 3.14: $R_{K,K'}$ of Eq. 3.3.2 determined from geometrical parameters deduced from X-rays structures and from ^{1}H pNMR chemical shifts in $[D_7]$DMF at 9.4 T and 298 K in $[An^{VI}O_2(DPA)_2]^{2-}$ and $[An^{VI}O_2(Et-DPA)_2]^{2-}$ complexes.

	$\frac{G_{H3}}{G_{H4}}$	$\frac{\delta^p_{H3}}{\delta^p_{H4}}$	$\frac{G_{H3}}{G_{H5}}$	$\frac{\delta^p_{H3}}{\delta^p_{H5}}$	$\frac{G_{H5}}{G_{H6}}$	$\frac{\delta^p_{H5}}{\delta^p_{H6}}$
Np^{VI}	1.6	2.0	3.4	3.2	1.4	1.7
Pu^{VI}	1.6	1.9	3.4	3.4	1.4	1.5

In Table 3.14, the $R_{K,K'}$ determined from the X-rays structures are compared to those deduced from the ^{1}H AIS at 298 K in the Np^{VI} and Pu^{VI} complexes. The good agreement between the geometrical and AIS ratios indicates that ^{1}H AIS in those complexes are dominated by pseudocontact interactions. The spin densities determined from unrestricted DFT calculations (see Table 3.15) confirm this. The spin density tends to decrease with the distance from the paramagnetic center, except for $C4$ (para position), the largest lies on the "yl" oxygen atoms, due to the strong bonding scheme. It is negative on the coordinating atoms, and then the sign alternates, due to spin polarization, and vanishes on the protons and aliphatic carbons atoms, in accordance with the observed negligible Fermi contact AIS for the protons. In the non-coordinating carbon atoms, the spin density resides mostly in the π system of the aromatic ring and consequently does not spread to the protons.

Table 3.15: Mulliken spin populations deduced from unrestricted PBE0 calculations with a partial occupation of the $5f$ orbitals.

	$[An^{VI}O_2(Et-DPA)_2]^{2-}$				$[An^{VI}O_2(Et-DPA)_2]^{2-}$			
	Total	s	sp^2	π	Total	s	sp^2	π
Np/Pu	1.1978	0.0027			2.5001	0.0053		
O (yl)	-0.0623	-0.0006			-0.1414	-0.0009		
O (M-O)	-0.0156	-0.0005	-0.0132	-0.0035	-0.0426	-0.0009	-0.0318	-0.0117
O (C=O)	-0.0025	-0.0002	-0.0022	-0.0004	-0.0108	-0.0003	-0.0067	-0.0045
N	-0.0070	-0.0019	-0.0063	-0.0013	-0.0123	-0.0031	-0.0114	-0.0017
C (C=O)	0.0016	0.0000	-0.0002	0.0012	0.0047	0.0002	0.002	0.0038
C ortho	0.0013	0.0001	0.0003	0.0011	0.0004	0.0000	-0.0002	0.0006
C meta	-0.0004	-0.0001	-0.0003	-0.0002	0.0000	0.0000	-0.0002	0.0002
C para	0.0014	0.0001	0.0001	0.0013	0.0004	0.0000	-0.0002	0.0006
C (CH2)	-0.0001	0.0000			0.0000	0.0000		
C (CH3)	0.0000	0.0000			0.0000	0.0000		
H (meta)	0.0001	0.0000	0.0001	0.0000	0.0001	0.0000	0.0001	0.0000
H (CH2)	0.0000	0.0000			0.0000	0.0000		
H (CH3)	0.0000	0.0000			0.0000	0.0000		

- *Anisotropic magnetic susceptibilities from the pNMR shifts.*

In the axially symmetric complexes, in the case of a pure dipolar interaction, Eq. 2.6.33 holds and the axial anisotropy $\Delta\chi_{ax}$ can be obtained from ^{1}H AIS analysis. Thereby, $\Delta\chi_{ax}^{exp}$ is determined from the slope of the $\delta_K^{pc} = f(G_K)$ curves which results $\Delta\chi_{ax}^{exp} = (2.2 \pm 0.1) \times 10^{-8}$ and $(10.1 \pm 0.2) \times 10^{-8}$ m^{3}mol^{-1} at 298 K for the Np^{VI} and Pu^{VI} complexes, respectively.

The studied complexes are not strictly axial, but the presence of the two DPA ligands in the equatorial plane creates a structure sensibly equivalent to a C6 axis. The *ab initio* calculations confirm that the $\boldsymbol{\chi}$ tensor is axial along the "yl" bond and the equatorial values almost degenerate, $\chi_{xx} = \chi_{yy}$. Consequently, we assume in the following that the magnetic susceptibility tensor $\boldsymbol{\chi}$ reduces to the axial and equatorial values, $\chi_\parallel$ and $\chi_\perp$. The isotropic average and the anisotropy are then $\chi_m = \frac{1}{3}(\chi_\parallel + 2\chi_\perp)$ and $\Delta\chi_{ax} = (\chi_\parallel - \chi_\perp)$, respectively. Accordingly, the knowledge of χ_m and $\Delta\chi_{ax}$ allows to estimate $\chi_\parallel$ and $\chi_\perp$. For the $[An^{VI}O_2(DPA)_2]^{2-}$ complexes in solution, the two components of the magnetic susceptibility tensor $\chi_\parallel$ and $\chi_\perp$, are deduced from the isotropic average and anisotropic values, χ_m^{Evans} and $\Delta\chi^{exp}$, respectively, and are given in Table 3.16.

- *pNMR shifts from ab initio calculations.*

For the CAS based methods, the ^{1}H AIS were deduced from Bertini's equation (Eq. 2.6.33), using the values of $\Delta\chi_{ax}$ from the *ab initio* calculations. Soncini (Eq. 2.2.3) and Van Vleck equations (Eq. 2.2.4) split into the contributions of degenerate and non-degenerate states. In the case of a non-Kramers ion without any symmetry, the states are all non-degenerate, leading to only the 2nd term. But when the energy gaps are very small, one retrieves the Curie term. For thermal energies much larger than the energy gaps, their impact is not noticeable. The Curie values i.e. those obtained from the thermally populated energy levels, can be labeled to the values obtained from the KD1 of the Np^{VI} and from the NKD of the Pu^{VI} complexes. In this case, each component of the molar magnetic susceptibility is calculated from the magnetic g-factors as

$$\chi_{kk} = N_A \mu_0 \mu_B^2 \frac{g_{kk}^2}{4kT} \tag{3.3.3}$$

As the Pu^{VI} complex has only one non-zero magnetic g-factor, when the ligand field splitting of the two NKD states is very small compared to thermal energy (200 cm^{-1} at 298K), both isotopic and anisotropic Curie magnetic susceptibilities arise due to the non-zero g-factor. For the Np^{VI} complex, the magnetic interaction with KD2 can drastically increase the magnetic susceptibilities from the respective Curie values. The splitting of the SF energy levels highly influences the composition of the SO wave functions and their splitting. Those in turn affect the magnetic properties. AIS are calculated from 2-components DFT calculations according to Eq. 2.6.22. The isotropic

term of the HFC tensor are given in Table 3.17. The *ab initio* molar magnetic susceptibility components are given in Table 3.16 and compared to experimental values. For the $[Np^{VI}O_2(DPA)_2]^{2-}$ and $[Np^{VI}O_2(DPA)_2]Li_2$ complexes, χ is much larger than its Curie contribution, showing the importance of the Van Vleck contribution. Excited states other than KD2 do not provide any leading contribution. KD2 is slightly populated at 298 K and the large contribution of KD2 is due to its strong magnetic interaction with KD1. Due to the reduced energy gap in SO-RASPT2*, this interaction becomes larger. $\Delta\chi_{ax}^{Curie}$ decreases when more correlation is included, to become negative in the case of $[Np^{VI}O_2(DPA)_2]^{2-}$, while $\Delta\chi_{ax}$ increases. The importance of the Van Vleck contribution was already pointed out in the $[NpO_2(CO_3)]^{4-}$ complex by Gendron *et al.* [9, 10]. The SO-RASPT2* results with the $5p$ and $5d$ orbitals correlated provide values of both χ_m and $\Delta\chi_{ax}$ close to the experimental ones. χ_m is found to be smaller in $[Np^{VI}O_2(DPA)_2]^{2-}$ than in $[Np^{VI}O_2(DPA)_2]Li_2$, 1.70 vs 2.18×10^{-8} m^3mol^{-1}. This follows the trend of the experimental values $(1.8\pm0.2)\times10^{-8}$ m^3mol^{-1} for $[Np^{VI}O_2(DPA)_2]^{2-}$ complex in solution from Evans method vs $(2.1\pm0.24)\times10^{-8}$ m^3mol^{-1} for $Li_2Np^{VI}O_2(DPA)_2\cdot2H_2O$ measured with the SQUID. χ_m was evaluated with SO-ZORA using Eq. 3.3.3. The results are similar to the Curie term of the SO-CASSCF level, since only KD1 is included in the calculation.

For the $[Pu^{VI}O_2(DPA)_2]^{2-}$ complex, the results depend very little on the method. The values of χ_m and $\Delta\chi_{ax}$ 4.49 and 13.17×10^{-8} m^3mol^{-1}, respectively, with SO-RASPT2* are found to be slightly larger than the experimental values (4.06 ± 0.1) and $(10.1\pm0.2)\times10^{-8}$ m^3mol^{-1}, respectively. For all the studied complexes, $\Delta\chi_{ax}$ is positive and larger than χ_m, denoting a prolate shape of the magnetic moment of the paramagnetic center.

Results for the AIS are summarized in Table 3.18. Those results follow the conclusions for the magnetic susceptibility. The Van Vleck contribution plays a key role for the Np^{VI} complexes, for $H3$, $H5$ and $H6$, the SO-RASPT2* results are in very good agreement with the experimental values. For $H4$, they overestimate the experimental value. The HFC tensor calculated with SO-ZORA is a pure dipolar one since the calculations are performed within a restricted scheme, avoiding the spin polarization to be correctly described. As for the magnetic susceptibility, the results for the AIS are the same as the Curie contribution with SO-CASSCF.

3.3.6 Temperature dependence of the pNMR shifts and the isotropic magnetic susceptibility

^{1}H paramagnetic chemical shifts in the $[An^{VI}O_2(DPA)_2]^{2-}$ complexes are mostly dipolar, contact shifts are negligible, so according to Eq. 2.6.33, temperature dependency of the ^{1}H pNMR shifts depends on how the magnetic anisotropy changes with temperature. In the

Table 3.16: Principal components of the magnetic susceptibility tensor $\boldsymbol{\chi}$ (in 10^{-8} m^3mol^{-1}) at 298 K from experiment and *ab initio* calculations. The Curie contributions are evaluated from the ground doublet. χ_m and $\Delta\chi_{ax}$ are the isotropic average and axial anisotropic susceptibilities, respectively.

	$\chi_\perp^{Curie}$	$\chi_\parallel^{Curie}$	$\Delta\chi_{ax}^{Curie}$	χ_m^{Curie}	$\chi_\perp$	$\chi_\parallel$	$\Delta\chi_{ax}$	χ_m
$[Np^{VI}O_2(DPA)_2]^{2-}$								
Exp.	/	/	/		1.1 ± 0.2	3.3 ± 0.2	2.2 ± 0.1 [a]	1.8 ± 0.2 [b]
SO-CASSCF	0.04	1.33	1.29	0.47	0.47	1.67	1.20	0.87
SO-CASPT2	0.11	0.96	0.86	0.39	0.55	1.77	1.22	0.96
SO-CASPT2*	0.27	0.41	0.14	0.32	0.67	2.14	1.47	1.16
SO-RASSCF	0.16	0.91	0.75	0.41	0.72	2.18	1.46	1.21
SO-RASPT2	0.39	0.35	-0.04	0.38	0.81	2.36	1.55	1.33
SO-RASPT2*	0.84	0.32	-0.47	0.63	0.91	3.29	2.38	1.70
SO-ZORA/PBE0	0.06	1.44	1.39	0.51				
$[Np^{VI}O_2(DPA)_2]Li_2$								
Exp.								2.1 ± 0.2 [c]
SO-CASSCF	0.08	1.39	1.29	0.54	0.62	2.13	1.51	1.13
SO-CASPT2	0.21	1.07	0.83	0.52	0.69	2.53	1.84	1.31
SO-CASPT2*	0.44	1.68	1.14	0.91	0.77	3.65	2.88	1.74
SO-RASSCF	0.38	1.56	1.05	0.86	0.87	3.61	2.74	1.79
SO-RASPT2	0.66	1.23	0.51	0.90	0.89	3.77	2.88	1.86
SO-RASPT2*	0.30	4.18	3.80	1.66	0.80	4.89	4.09	2.18
$[Pu^{VI}O_2(DPA)_2]^{2-}$								
Exp.					0.7 ± 0.1	10.8 ± 0.2	10.1 ± 0.2 [a]	4.1 ± 0.1 [b]
SO-CASSCF	0.00	13.70	13.70	4.60	0.00	13.70	13.70	4.72
SO-CASPT2	0.00	12.76	12.76	4.29	0.17	12.80	12.63	4.42
SO-CASPT2*	0.00	12.73	12.73	4.28	0.14	12.80	12.66	4.40
SO-RASSCF	0.00	13.70	13.70	4.61	0.14	13.80	13.66	4.73
SO-RASPT2	0.00	13.52	13.52	4.54	0.17	13.50	13.33	4.66
SO-RASPT2*	0.00	13.32	13.32	4.48	0.13	13.30	13.17	4.59

* : $5p$ and $5d$ orbitals are correlated, [a]: deduced from the $\delta_K^p = f(G_K)$ plots, [b]: deduced from chemical shifts according to Evans method, [c]: from SQUID

Table 3.17: Isotropic HFC constants (in MHz) of the ^1H nuclei in the $[Np^{VI}O_2(DPA)_2]^{2-}$ complex calculated with SO-ZORA/PBE0 and deduced from g tensor. $A_{K,iso} = \frac{1}{3}\mathrm{Tr}(\mathbf{A}_K)$.

	$H3$	$H4$	$H5$	$H6$
$A_{K,iso}$	-0.23	-0.20	-0.11	-0.09
$A_{K,iso}^{dip,*}$	-0.21	-0.20	-0.10	-0.07

$$^*: A_K^{dip} = \mathrm{Tr}\left[\frac{\mu_0 g_K \mu_B \mu_N}{8\pi}\mathbf{g}\cdot\mathbf{T}_K\right]$$

Table 3.18: ^{1}H pNMR chemical shifts (in ppm) at 298 K deduced from Eq. 2.6.33. $\delta_K^{p,Curie}$ is the Curie contribution arising from the ground doublet.

Method	$\delta_{H3}^{p,Curie}$	δ_{H3}^{p}	$\delta_{H4}^{p,Curie}$	δ_{H4}^{p}	$\delta_{H5}^{p,Curie}$	δ_{H5}^{p}	$\delta_{H6}^{p,Curie}$	δ_{H6}^{p}
$[Np^{VI}O_2(DPA)_2]^{2-}/[Np^{VI}O_2(Et-DPA)_2]^{2-}$								
Exp.	/	-5.9 / -5.5	/	-2.9	/	-2.8	/	-1.7
SO-CASSCF	-3.3	-3.0	-2.1	-1.9	-1.4	-1.3	-1.0	-0.9
SO-CASPT2	-2.2	-3.1	-1.4	-1.9	-0.9	-1.3	-0.6	-0.9
SO-CASPT2*	-0.3	-3.8	-0.2	-2.4	-0.1	-1.6	-0.1	-1.1
SO-RASSCF	-1.9	-3.7	-1.2	-2.3	-0.8	-1.6	-0.5	-1.1
SO-RASPT2	0.1	-4.0	0.1	-2.5	0.0	-1.7	0.0	-1.2
SO- RASPT2*	1.2	-6.1	0.8	-3.8	0.5	-2.5	0.4	-1.8
SO-ZORA/PBE0	-3.5	/	-2.7	/	-1.7	/	-1.0	/
$[Pu^{VI}O_2(DPA)_2]^{2-}/[Pu^{VI}O_2(Et-DPA)_2]^{2-}$								
Exp.	/	-26.3 / -26.0	/	-14.3	/	-11.3	/	-7.6
SO-CASSCF	-35.2	-35.2	-21.9	-21.9	-14.8	-14.8	-10.3	-10.3
SO-CASPT2	-33.3	-32.4	-20.7	-20.3	-13.9	-13.6	-9.6	-9.4
SO-CASPT2*	-33.3	-32.5	-20.7	-21.6	-14.0	-13.7	-9.7	-9.6
SO-RASSCF	-35.2	-35.0	-21.9	-21.8	-14.8	-14.7	-10.3	-10.2
SO-RASPT2	-34.7	-34.2	-21.6	-21.3	-14.6	-14.4	-10.2	-10.0
SO- RASPT2*	-34.6	-33.7	-21.6	-21.0	-14.6	-14.2	-10.2	-9.9

* : 5p and 5d orbitals are correlated

axially symmetric Ln^{III} complexes, according to Bleaney's formula (see Eq. 2.6.34) $\Delta\chi \propto 1/T^2$, whereas according to Golding *et al.* [19] the spin-only magnetic susceptibility (Eq. 2.6.49) $\chi^s \propto 1/T$. This translates a T^{-2} and T^{-1} dependency of the pseudocontact and contact shifts, respectively, in the Ln^{III} complexes. Bleaney's model is based on the CFT and assumes that the splitting of a J manifold is in the order of room temperature energy, so that all the states get populated resulting in a vanishing Curie term $\left(T^{-1}\right)$ term for the anisotropic part of the magnetic susceptibility. Bleaney's method has been widely used to separate the pseudocontact and the contact shifts in the Ln^{III} complexes [20, 18]. Recently, a thorough studies of the pNMR shifts in the $[Ln(DPA)_3]^{3-}$ series shows that Bleaney's formula comes in handy to explain the pNMR shifts in these complexes with a less error limit in the room temperature domain. But when it comes for $[An(DPA)_3]^{3-}$ complexes, especially for the early actinides, the experimental results significantly deviates from the formulation [26]. Indeed, in the ligands' environment, the actinides are further from the free ion limit than the lanthanides as the $5f$ orbitals are more open to the ligand field and the splitting of a given J manifold in the An complex is 3-4 (around ~ 1200 cm^{-1}) times larger than in the Ln complexes (~ 300 cm^{-1}). So all the states of a J manifold in the An complex are not statistically populated, translating the presence of Curie behavior in the temperature dependence of the anisotropic magnetic susceptibility and furthermore T^{-n}

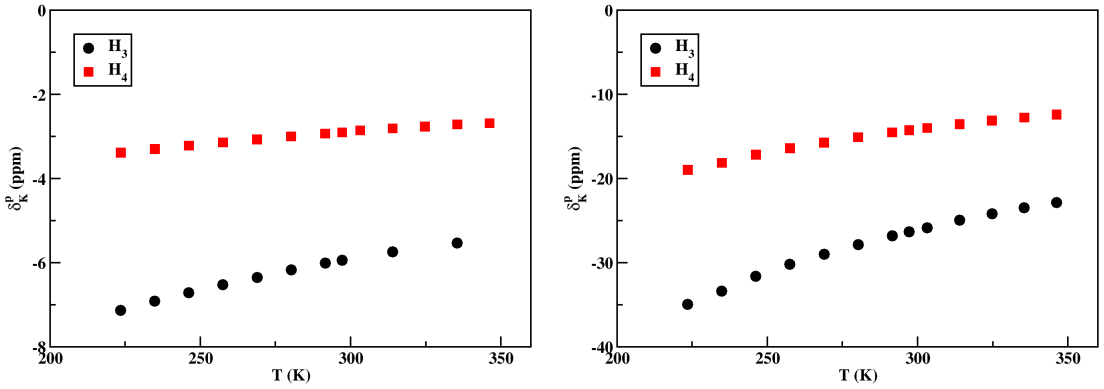

(a) (b)

Figure 3.3.8: ^{1}H pNMR chemical shifts in $[D_7]$DMF at 9.4 T as a function of temperature in the $[Np^{VI}O_2(DPA)_2]^{2-}$ complex (a) and in the $[Pu^{VI}O_2(DPA)_2]^{2-}$ (b).

with $n > 2$ might be needed to fully fit the experimental pNMR shifts as it was the case for $[An(DPA)_3]^{3-}$ complexes [26]. The actinyls are even far from the free ion and as already pointed out that the pNMR shifts in $[An^{VI}O_2(DPA)_2]^{2-}$ complexes are mostly dipolar, the temperature dependence of the pNMR shifts might show significant deviations from the Ln^{III} complexes, or even from the An^{III}/An^{IV} complexes. The temperature dependence of the AIS in the $[An^{VI}O_2(DPA)_2]^{2-}$ complexes were investigated for $H3$ and $H4$ protons as depicted in Fig. 3.3.8. The regression analysis of the $\delta_K^p = f(1/T)$ with T^{-1} and T^{-2} terms (see Table 3.19) evidences very large T^{-1} terms, even largely prevailing for the Pu^{VI} complex, whereas no contact contribution is expected. This confirms that Bleaney's method for the separation between contact and dipolar contributions is not valid for the considered complexes. In order to analyze why, the temperature dependence was analyzed according to Eq. 2.6.32. For the Np^{VI} complexes, this is completed by the magnetic susceptibility T dependence. The sum-over-states in Eq. 2.6.32 is reduced to the states playing the primordial role, two KDs for the Np^{VI} complexes and a NKD for the Pu^{VI} one.

- Fitting of the $\chi_m^{SQUID}(T)$ and $\delta_K^p(T)$ in the Np^{VI} complexes with a two KDs model

The two lowest KDs are responsible for the paramagnetic behavior of the $5f^1$ actinyl complexes. In Fig. 3.3.9, a graphical scheme is provided to quickly visualize the various magnetic interactions associated with them as developed in their ligand field modelization in subsection 3.2.1.1. The isotropic and anisotropic magnetic susceptibilities from the two KDs are modeled with the parameters shown in Fig. 3.3.9 as

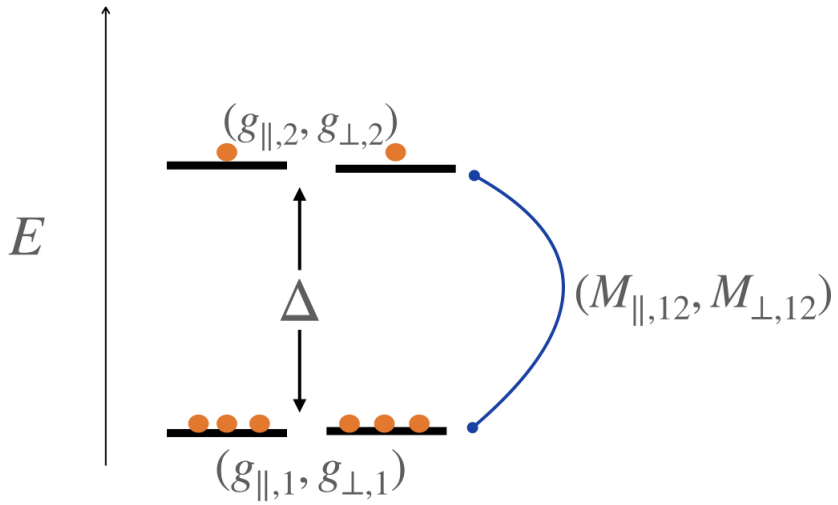

Figure 3.3.9: Scheme showing the various interactions in between two lowest KDs. The ligand field splitting is Δ, the magnetic interactions of each KD are modeled by their corresponding **g**-tensors $(g_{\perp,n}, g_{\parallel,n})$, $n = 1,2$. The magnetic interactions in between the KDs are characterized by the axial $M_{\parallel,12}$ and planar $M_{\perp,12}$ components. The orange balls are the representation of the thermal population in the states.

$$\chi_m = N_A \mu_0 \mu_B^2 \left[\beta \frac{\left(e^{\beta\Delta/2} g_1^2 + e^{-\beta\Delta/2} g_2^2\right)}{4\left(e^{\beta\Delta/2} + e^{-\beta\Delta/2}\right)} + \frac{\left(e^{\beta\Delta/2} - e^{-\beta\Delta/2}\right) M_{12}^2}{\Delta\left(e^{\beta\Delta/2} + e^{-\beta\Delta/2}\right)} \right] \quad (3.3.4)$$

$$\Delta\chi_{ax} = N_A \mu_0 \mu_B^2 \left[\beta \frac{\Delta g_1^2 e^{\beta\Delta/2} + \Delta g_2^2 e^{-\beta\Delta/2}}{4\left(e^{\Delta/2kT} + e^{-\Delta/2kT}\right)} + \frac{\left(e^{\beta\Delta/2} - e^{-\beta\Delta/2}\right) \Delta M_{12}^2}{\Delta\left(e^{\beta\Delta/2} + e^{-\beta\Delta/2}\right)} \right] \quad (3.3.5)$$

the pNMR shifts can be deduced from the $\Delta\chi_{ax}$ using the geometric information of the atoms according to Eq. 2.6.33. Details about the development of the model equations are provided in subsections 2.6.2 and 2.6.3. Here they are again shown to have a quick look.

The $\chi_m^{SQUID} T = f(T)$ curve for the solid $Li_2An^{VI}O_2(DPA)_2 \cdot 2H_2O$ as shown in Fig. 3.3.6 was fitted using Eq. 3.3.4 in the temperature range $3 - 300$ K according to four parameters: Δ the energy gap between the two KDs, g_1^2 and g_2^2 the isotropic magnetic moments of KD1 and KD2, respectively, and M_{12}^2 the isotropic coupling moment between KD1 and KD2.

The optimized parameters are given in Table 3.20. A TIP term was added to Eq. 3.3.4 which improved the quality of the fitting procedure by taking into account the effect of the other excited states. This fitting procedure was benchmarked on the SO-RASPT2* curve of the $[Np^{VI}O_2(DPA)_2]Li_2$ complex. In this way, one can compare the fitted parameters to those directly calculated as *ab initio* energy levels and matrix elements. It appears that the energy gap Δ is underestimated by 15% and 23% without and with the TIP, respectively. All fitted parameters match the *ab initio* ones within 20 %, Δ and g_2^2 being the less accurate. This confirms that the two-KDs model gathers correctly the physical effects in the

investigated temperature range. The discrepancies could arise from both the hypothesis of an axial symmetry, and mostly to the neglect of the interaction with the states out of the model space. The fitted parameters should be considered as effective ones. Surprisingly, the fit without TIP provides parameters closer to the *ab initio* ones. We will therefore consider that the fits without the TIP contribution provides an energy gap closer to the "real" one. The fitting of the experimental SQUID $\chi_m^{SQUID}T = f(T)$ curve without any TIP contribution leads to a value of $\Delta = 206$ cm^{-1} which is smaller than the *ab initio* ones. According to this fit, KD2 is more magnetic than KD1 $g_2^2 > g_1^2$ (5.4 vs 10.1) which is in good accordance with the SO-RASSCF values.

Table 3.19: Regression coefficients from $\delta_K^p = f(1/T)$ plots for $[Np^{VI}O_2(DPA)_2]^{2-}$ and $[Pu^{VI}O_2(DPA)_2]^{2-}$ complexes. The standard errors and the coefficient of determination R^2 are determined using Mathematica default options.

equation	proton	A (ppm.K)	B (ppm.K^2)	C (ppm.K^3)	E (ppm.K^5)	$1-R^2$
			$[Np^{VI}O_2(DPA)_2]^{2-}$			
$\delta_K^p = AT^{-1} + BT^{-2}$	$H3$	-2327±22	(1.65±0.05).10^5	-	-	2.10^{-5}
	$H4$	-1213±10	(1.03±0.03).10^5	-	-	3.10^{-5}
$\delta_K^p = AT^{-1} + CT^{-3} + ET^{-5}$	$H3$	-2221±29	-	(5.09±0.4).10^7	(-9.88±1.3).10^{11}	5.10^{-6}
	$H4$	-1138±14	-	(3.09±0.2).10^7	(-6.00±0.7).10^{11}	1.10^{-5}
			$[Pu^{VI}O_2(DPA)_2]^{2-}$			
$\delta_K^p = AT^{-1} + BT^{-2}$	$H3$	-7962±65	(3.7 ±1.7)·10^4	-	-	1.10^{-5}
	$H4$	-4306±38	(1.7±1)·10^4	-	-	2.10^{-5}
$\delta_K^p = AT^{-1} + CT^{-3}$	$H3$	-7887±35	-	(4.65±2.4).10^6	-	1.10^{-5}
	$H4$	-4272±20	-	(2.0±1.4).10^6	-	2.10^{-5}

The fit of the AIS curves by Eq. 2.6.41 was not successful as data are only available on a short temperature window (130 K) and it needs four independent parameters: the anisotropic magnetic parameters Δg_1^1, Δg_2^2, ΔM_{12}^2 and the energy gap Δ. This leads to an over-parametrization, taking into account all the details of experimental uncertainties. The results are unstable according to the considered protons and to the number of considered points. We tried a polynomial fit, since it allows a smoothing of the curve. Since the second KD is at the order of room temperature energy, it gets populated at the room temperature domain, so the T^{-1} term corresponds to the Curie contribution arising from the total magnetic moment of the two occupied KDs as shown in the scheme. Since Δ corresponds to the thermal energy at room temperature, many T^{-n} terms of the polynomial expansion are needed as developed in Eq. 3.3.6. Δg_1^1 and Δg_2^1 are found to be similar in the SO-RASPT2* calculation, we therefore supposed that $\Delta g_1^1 - \Delta g_2^1$ was negligible, and consequently, neglected the T^{-n} terms of even orders. The $\delta_K^p = f(1/T)$ curve was fitted by a $AT^{-1} + CT^{-3} + ET^{-5}$ function. This allows to determine the values of Δ, ΔM_{12}^2 and $\Delta g_1^2 + \Delta g_2^2$. They are given in Table 3.20. As a benchmark, the $\Delta\chi_{ax}$ curve calcu-

lated with SO-RASPT2* for the $[Np^{VI}O_2(DPA)_2]^{2-}$ complex was fitted in the 250–350 K range, both using Eq. 3.3.5 and its polynomial expansion. These parameters can be compared to those directly from the *ab initio* calculations. The fitting with the full function overestimates the value of Δ by 10% while using the polynomial expansion, it underestimates it by 20%. The magnetic parameters are well estimated by the former and slightly too large with the latter, the signs being correct in the two cases. The sign of $\Delta g_1^2 + \Delta g_2^2$ gives information about the anisotropy of the magnetization: the more positive, the more axial, the more negative, the more planar. We conclude from this benchmark that the fitting by a $AT^{-1} + CT^{-3} + ET^{-5}$ function provides parameters in reasonable agreement with the *ab initio* ones.

Table 3.20: Model parameters evaluated from *ab initio* calculations for the $[Np^{VI}O_2(DPA)_2]Li_2$ and the $[Np^{VI}O_2(DPA)_2]^{2-}$ or deduced by fitting the χ_m, $\Delta\chi_{ax}$ and δ_K^p curves. Δ in cm^{-1}.

		Δ	g_1^2	Δg_1^2	g_2^2	Δg_2^2	$\Delta g_1^2 - \Delta g_2^2$	$\Delta g_1^2 + \Delta g_2^2$	M_{12}^2	ΔM_{12}^2
					$[Np^{VI}O_2(DPA)_2]Li_2$					
SO-CASSCF	*ab initio*	522	4.0	3.6	15.5	14.9	-11.2	18.5	2.0	0.1
SO-CASPT2	*ab initio*	396	3.9	3.1	12.1	10.6	-7.5	13.8	2.6	1.2
SO-CASPT2*	*ab initio*	282	6.8	5.1	6.6	5.2	0.0	10.3	3.2	2.7
SO-RASSCF	*ab initio*	250	6.2	5.4	10.3	8.6	-3.1	14.0	3. 0	2.1
SO-RASPT2	*ab initio*	298	6.7	3.0	5.2	-2.4	5.4	0.6	4. 0	3.8
SO-RASPT2*	*ab initio*	440	12.5	9.8	4.2	1.5	8.3	11.4	2.9	1.1
	fit χ_m ‡	372	10.0		7.7				2.2	
	fit χ_m with TIP‡	338	10.0		10.0				2.2	
					$[Np^{VI}O_2(DPA)_2]^{2-}$					
SO-CASSCF	*ab initio*	820	3.5	3.2	16.3	15.8	-12.6	19.1	0.6	0.0
SO-CASPT2	*ab initio*	624	3.0	2.2	13.5	12. 4	-10.3	14.6	0.8	
SO-CASPT2*	*ab initio*	454	2.4	0.4	10.6	8.0	-7.7	8.4	1.1	2.1
SO-RASSCF	*ab initio*	455	3.1	1.9	14.4	12.9	-11.0	14.8	0.9	0.8
SO-RASPT2	*ab initio*	418	2.8	-0.1	10.8	7.6	-7.7	7.5	1.2	
SO-RASPT2*	*ab initio*	333	4.9	-1.1	5.2	-1.2	0.1	-2.3	1.5	4.5
	fit $\Delta\chi_{ax}$ #	360		-1.0		-3.0	2.0	-4.0		4.6
	fit $\Delta\chi_{ax}$ polynom %	260						-4.7		6.1
					Fit of the experimental curves					
SQUID	fit $\chi_m T$	206	5.4		10.1				3.1	
	fit $\chi_m T$ with TIP	113	5.0		7.0				1.8	
pNMR shift H3	fit polynom %	306						-6.7		5.7
pNMR shift H4	fit polynom %	306						-8.7		5.4

*: 5p and 5d orbitals are correlated, ‡: Eq. 3.3.4, T range: 3-300 K, #: Eq. 2.6.41, T range: 220-350 K, %: Eq. 3.3.6, T range: 220-350 K

The $\delta_K^p = f(1/T)$ curves were fitted according to this procedure for protons $H3$ and $H4$ in the $[Np^{VI}O_2(DPA)_2]^{2-}$ complex (see Table 3.19). One gets similar parameters for the two protons with a gap Δ of 305 cm^{-1}. $\Delta g_1^2 + \Delta g_2^2$ is found to be negative and the

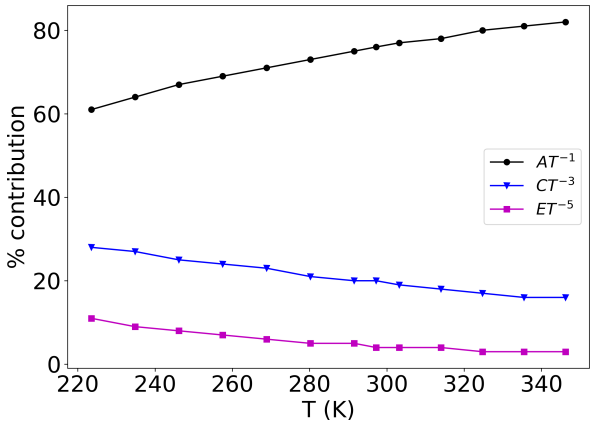

Figure 3.3.10: Percentage of the absolute contribution of the individual term of Eq. $\delta_K^p = AT^{-1} + BT^{-2} + ET^{-5}$ in the temperature range of 250-350 K. For example, in the legend $CT^{-3} = \left| C/T^3 \left(|A/T| + \left|C/T^3\right| + \left|E/T^5\right| \right)^{-1} \right| \times 100$.

coupling ΔM_{12}^2 important. The SO-RASPT2* with correlated $5d$ and $5p$ orbitals is the only calculation in Table 3.20 that provides a negative value of $\Delta g_1^2 + \Delta g_2^2$. This explains the good agreement between experiment and theory with SO-RASPT2*, temperature limit of Eq. 2.6.41. The Taylor expansion in terms of $x = \beta\Delta = \Delta'/T\,(\Delta' = \Delta/k_B)$ gives:

$$\begin{aligned} \delta_K^p \;=\; & \frac{\mu_0\mu_B^2}{12\pi k_B T} G_K \left[\frac{\Delta g_1^2 + \Delta g_2^2 + 4\Delta M_{12}^2}{8T} + \frac{\left(\Delta g_1^2 - \Delta g_2^2\right)\Delta'}{16T^2} - \frac{\Delta M_{12}^2 \Delta'^2}{24T^3} \right. \\ & \left. - \frac{\left(\Delta g_1^2 - \Delta g_2^2\right)\Delta'^3}{190T^4} + \frac{\Delta M_{12}^2 \Delta'^4}{240T^5} + \ldots \right] \end{aligned} \tag{3.3.6}$$

for the pNMR shift calculation. δ_K^p is decomposed in T^{-n} contributions where different contributions alternate in sign. Percentage of the absolute contributions are deduced. For example, absolute contributions from T^{-3} term is deduced as $\left|\%T^{-3}\right| = \left| C/T^3 \left(|A/T| + \left|C/T^3\right| + \left|E/T^5\right| \right)^{-1} \right| \times 100$ and are plotted w.r.t. $T\,(K)$ in Fig. 3.3.10 in the studied temperature range. The T^{-1} one is the dominant one, the weight of the other ones strongly diminishes at 350 K, but plays a key role at 220 K. For example due to alteration of the sign of the individual terms, actually the T^{-3} term contributes for 80% of the total delta value for $H4$.

- Fitting of the $\delta_K^p\,(T)$ in the Pu^{VI} complex with a ground NKD model

The temperature dependence of the pNMR chemical shifts for protons $H3$ and $H4$ in the $[Pu^{VI}O_2(DPA)_2]^{2-}$ complex is represented in Fig. 3.3.8. It can be fitted using Eq. 2.6.44, with two parameters, Δ the energy splitting and $g_\parallel^2$ the magnetic moment of the NKD. The fitting of the SO-RASPT2* curve according to this equation in the room temperature window leads to values of Δ and $g_\parallel^2$ in very good agreement with the *ab initio* ones (see Table 3.21). As previously for the Np^{VI} complex, the experimental incertitude renders

the fitting of the curves by Eq. 2.6.44 unfeasible and we considered the high temperature Taylor expansion of this equation terms of $x = \beta\Delta = \Delta'/T$, $(\Delta' = \Delta/k_B)$

$$\delta_K^p = \frac{\mu_0\mu_B^2}{12\pi k_B} G_K g_\parallel^2 \left(\frac{1}{4T} - \frac{\Delta'^2}{48T^3} + \frac{\Delta'^4}{480T^5} + ... \right) \tag{3.3.7}$$

The T^{-1} term is the Curie contribution for a doublet and higher order terms are due to the splitting of the doublet Δ. The fit of the $\Delta\chi_{ax} = f(1/T)$ SO-RASPT2* curve by a $AT^{-1} + CT^{-3}$ function leads to an underestimated value of Δ. The fitting of the experimental curves by Eq. 3.3.7 up to T^{-3} leads to comparable value of Δ. This is in favor of a splitting of the ground doublet in agreement with the SO-RASPT2* results. However, the T^{-1} term is by far dominant and the T^{-3} contributes for only 1% (see Fig. 3.3.11) while it is this latter term that provides the information about the energy gap; the determination of Δ from the $\delta_K^p = f(1/T)$ curve should be taken with care.

Table 3.21: Model parameters for the $[Pu^{VI}O_2(DPA)_2]^{2-}$ complex evaluated from *ab initio* calculations or deduced by fitting the $\Delta\chi_{ax}$ and δ_K^p curves. Δ in cm^{-1}.

		Δ	$g_\parallel$
$[Pu^{VI}O_2(DPA)_2]^{2-}$			
SO-CASSCF	*ab initio*	1	5.89
SO-CASPT2	*ab initio*	61	5.70
SO-CASPT2*	*ab initio*	98	5.73
SO-RASSCF	*ab initio*	0.2	5.89
SO-RASPT2	*ab initio*	8	5.85
SO-RASPT2*	*ab initio*	84	5.84
	fit $\Delta\chi_{ax}$ #	86	5.84
	fit polynom %	66	5.79
Fit of the experimental curves			
pNMR shift H3	fit polynom %	58	5.3
pNMR shift H4	fit polynom %	52	4.9

*: 5p and 5d orbitals are correlated, #: Eq. 2.6.44, T range: 220-350 K, %: Eq. 3.3.7, T range: 220-350 K

3.4 $[AnO_2]^{2+}$ cations chelated with the TEDGA ligand

3.4.1 Crystal structures

In solid state, the $[An^{VI}O_2(TEDGA)_2](Otf)_2$ compounds with An^{VI} = U^{VI} (A), Np^{VI} (B) and Pu^{VI} (C) crystallize in the triclinic space group $\left(P\bar{1}\right)$. The composition of the cationic complexes consists in a strictly linear $[An^{VI}O_2]^{2+}$ moiety with two tridentate TEDGA

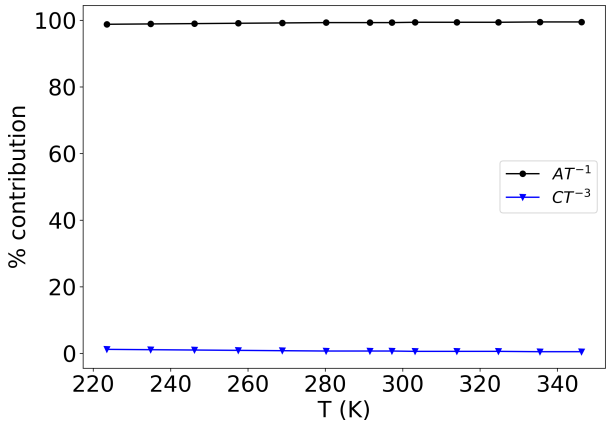

Figure 3.3.11: Percentage of the absolute contribution of the individual term of Eq. $\delta_K^p = AT^{-1} + CT^{-3}$ in the temperature range of 250-350 K for Pu^{VI} complex.

ligands in the equatorial plane. The charge compensation is provided by two OTf^- anions included in the structure. The $[U^{VI}O_2(TEDGA)_2](NO_3)_2$ (D) compound also crystallizes in the triclinic space group $\left(P\bar{1}\right)$ while the charge compensation is provided by two $NO_3{}^-$ anions[1].

From uranium to plutonium, the An=O bond distances decrease from 1.771(3) Å to 1.747(2) Å in agreement with the ionic radii contraction along the actinide series, while the equatorial plane An−O/O′ (O-carbonyl oxygen, O′- etheral oxygen) bond distances are less actinide dependent (see Table 3.22). For the two $[U^{VI}O_2(TEDGA)_2]^{2+}$ complexes, the U=O and U−O bond distances are similar but a lengthening of 0.023 Å is observed for the U−O′ bond.

The TEDGA ligands in the equatorial plane are perpendicular to the $[An^{VI}O_2]^{2+}$ moiety and keep their planar conformation. The ethyl chains of the two ligands in front of each other point in the opposite direction and minimize the ligand tilt as revealed by ∠O=An−O and ∠O=An−O′ angles close to 90°. By replacing OTf^- counterions by $NO_3{}^-$, we can note a lengthening of the U−O′ bond distance in uranyl first coordination sphere characterizing the flexibility of the TEDGA ligand.

Table 3.22: Selected bond distances $\left(\text{Å}\right)$ and bond angles (°) of the $[An^{VI}O_2(TEDGA)_2](Otf)_2$ and $[U^{VI}O_2(TEDGA)_2](NO_3)_2$ structures.

Compound	An=O	An−O	An−O′	∠O=An−O	∠O=An−O′
A	1.771(3)	2.44(1)	2.625(3)	91.2(1)	89.2(1)
B	1.753(1)	2.44(1)	2.619(1)	91.6(1)	89.1(1)
C	1.747(2)	2.43(1)	2.614(2)	91.9(1)	89.0(1)
D	1.769(2)	2.43(1)	2.648(2)	93.4(1)	89.3(1)

[1]Experimental studies are performed at CEA Marcoule by Claude Berton *et al.*

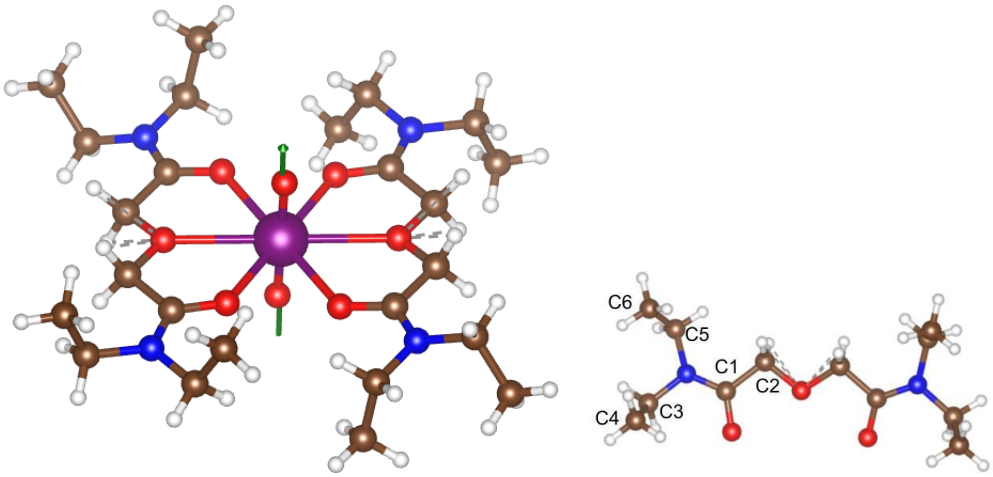

Figure 3.4.1: $[Np^{VI}O_2(TEDGA)_2]^{2+}$ complex (left) and TEDGA ligand (right) with the numbering of carbon atoms (The numbering of the chemically equivalent hydrogen atoms follows the carbon atom bonded directly). z axis is shown with the green arrow passing through the actinyl bonds. Color code: purple- Np, blue- N, red- O, saddle-brown- C, white- H.

3.4.2 *Ab initio* electronic structures

Like for the DPA complexes, SO-CAS/RAS based calculations are performed on the crystal structures of the paramagnetic $[An^{VI}O_2(TEDGA)_2]^{2+}$ complexes where $An^{VI} = Np^{VI}$ and Pu^{VI}. Computational details are provided in Appendix A. A balanced description of electron dynamic correlation is the key step to properly unravel their electronic structures, especially the lowest energy levels which play the pivotal role in determining the magnetic properties and are responsible for the observed pNMR shifts. The semi-core $5p$ and $5d$ orbitals in the central $[Np^{VI}O_2]^{2+}$ moiety are needed to be correlated during the treatment of dynamic correlation as already a significant stabilization of the Φ states are observed in the case of the DPA complex (see Table 3.7 and Fig. 3.4.2). So from now on we drop the '*' (as we used for the DPA complexes) from the label of the computational methods such that in the PT2 calculations the $5p$ and $5d$ orbitals are correlated. Also we have seen the effect of ligand field in finely tuning the nature of the SF ground state in the neptunyl DPA complex.

The *ab initio* computed energy levels of the $[Np^{VI}O_2(TEDGA)_2]^{2+}$ chelates are reported in Table 3.23 from both the SF and SO calculations. For a quick grasp of the details and comparison with the $[Np^{VI}O_2(DPA)_2]^{2-}$ complex, we plotted the SF energy levels of the two neptunyl complexes in the same figure (see Fig. 3.4.2), along with the free cation. The presence of the two charge-neutral TEDGA ligands in the equatorial plane energetically favors the $5f_\delta$ orbitals over the $5f_\phi$ in the SF ground state. Due to the strong SOC in the actinyl complexes, the nature of the ground SO KD can be completely different from the SF ground state. The compositions of the two energetically lowest KDs are given

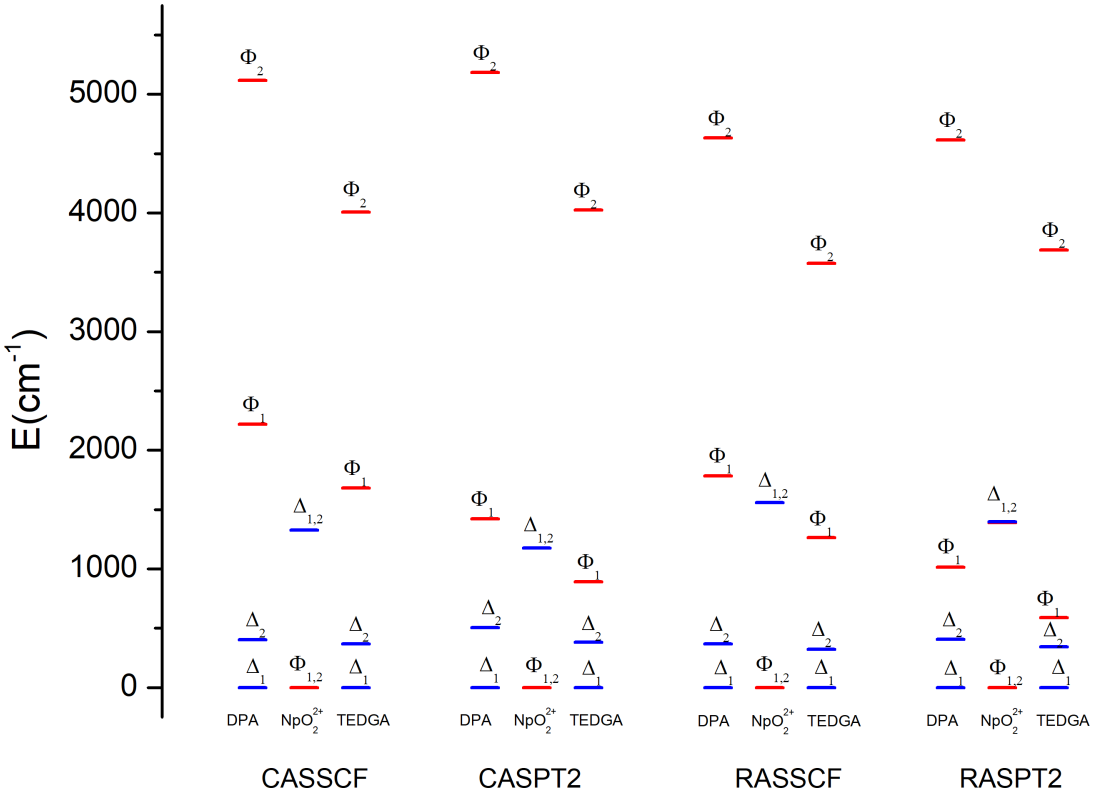

Figure 3.4.2: Splitting of the lowest SF energy levels from different methods of calculations in the $[Np^{VI}O_2]^{2+}$ cation and in the $[Np^{VI}O_2(DPA)_2]^{2-}$ (denoted by DPA) , $[Np^{VI}O_2(TEDGA)_2]^{2+}$ (denoted by TEDGA) chelates. Φ, Δ represent the SF states when the unpaired electron is in the $5f_\phi$ and $5f_\delta$ orbitals, respectively. $5p$ and $5d$ orbitals are correlated in the PT2 calculations.

in Table 3.24. In SO-CASSCF, % of (Φ, Δ) characters of KD1 and KD2 are $(15, 83)$ and $(60, 39)$, respectively, while they are completely altered when the energy corrections due to the dynamic electron correlation are considered both from the variational RAS based (RASSCF) and the perturbation theory based (CASPT2, RASPT2) calculations. In the variational SO-RASSCF (Φ, Δ) characters of KD1 and KD2 are $(60, 40)$ and $(18, 80)$, respectively, while with the perturbation theory based methods, the compositions of the two KDs are quite the same as the RASSCF ones. The alteration of the two KDs from CASSCF to the higher methods is a result of the reduced energy gap between the Δ and Φ states with the dynamic correlation. From Fig. 3.4.2, it can be noticed that the splitting of the two Δ states in the TEDGA complex remains quite the same with all the methods while the splitting of the Φ states is $30-35\%$ larger with the PT2 calculation than the corresponding SCF values. The energy gap in between the Δ and the Φ_1 states also decreases by half. This shows a parallel spectrum as already observed for the DPA complex with the overall ligand field splitting of the states are lesser than the DPA. It is not surprising to see in Fig. 3.4.2 that the splitting of equatorial $5f_\phi$ orbitals is larger than the axial $5f_\delta$, but interestingly one of the $5f_\phi$ orbital is getting more stabilization when described at the PT2 level. Bacause the interactions of the two equatorial $5f_\phi$ orbitals with the ligands are different in a trigonal ligand field environment. Like in the DPA complex, one of the $5f_\phi$ orbitals undergoes anti-bonding interaction with the ligand-orbitals.

Table 3.23: Energy levels (in cm^{-1}) from the SF and SO calculations for the $[Np^{VI}O_2(TEDGA)_2]^{2+}$ complex.

CASSCF		CASPT2		RASSCF		RASPT2	
SF	SO	SF	SO	SF	SO	SF	SO
0	0	0	0	0	0	0	0
368	349	382	418	320	297	344	601
1681	7021	891	7015	1264	7038	589	7168
4006	9589	4024	9579	3575	9267	3687	9465
18826	20468	22267	24648	19448	21371	19828	22420
18900	23613	23830	28074	19602	24273	20921	25484

For the $5f^2$ $[Pu^{VI}O_2(TEDGA)_2]^{2+}$ chelate, the energy levels are tabulated in Table 3.25. The compositions of the SF(SO)-RASSCF wave functions are given in Table 3.26 and the active NOs of the $[Pu^{VI}O_2(TEDGA)_2]^{2+}$ complex are shown in Fig. 3.4.3. For the SF wave functions $^{2S+1}\Psi$, compositions are given in terms of the most dominant configurations and for the SO $\{|1\rangle, |2\rangle\}$ in terms of the SF wave functions. The electronic configurations of the two lowest SF states $\{^3\Psi_1, ^3\Psi_2\}$ are majorly $5f_\phi^\uparrow 5f_\delta^\uparrow \prod_b^{core} b^{\uparrow\downarrow}$ i.e. the two unpaired electrons remain in the different sets of orbitals to minimize the electron repulsion from the other one. In the free plutonyl, both the ground triplet states

Table 3.24: Compositions of the first two KDs are provided in terms of the SF wave functions for the $[Np^{VI}O_2(TEDGA)_2]^{2+}$ complex. The g-factors are provided both in the $\parallel$ and $\perp$ directions. The energy gaps between the KDs, Δ (in cm^{-1}) obtained from different methods are also provided ('-ve' sign before the SO-CASSCF value indicates an alteration of the KDs).

Method	KD	Φ	Δ	Π	$g_\perp$	$g_\parallel$	Δ
SO-CASSCF	KD1	15	83	2	1.09	0.55	-359
	KD2	60	39	1	1.02	2.92	
SO-CASPT2	KD1	64	36	-	0.95	3.18	418
	KD2	14	84	2	0.92	1.40	
SO-RASSCF	KD1	60	40	-	1.14	2.95	297
	KD2	18	80	2	1.33	0.60	
SO-RASPT2	KD1	70	30	-	0.81	3.57	601
	KD2	9	89	2	0.90	1.61	
SO-ZORA/PBE0[a]					1.22	0.81	
mDKS/PBE0[b]					1.17	1.86	

[a]: in ADF, [b]: in ReSpect

are degenerate, but in the trigonal ligand environment, it splits due to different π interactions of the two $5f_\delta$ orbitals with the ligand orbitals. The splitting is larger in the PT2 calculations. The SF-RASSCF state $^3\Psi_1$ has the % contributions of $(57,30)$ from $\left(5f_{\delta+}^{\uparrow(0.66)}5f_{\phi-}^{\uparrow(0.66)}, 5f_{\delta-}^{\uparrow(0.34)}5f_{\phi+}^{\uparrow(0.34)}\right)$ configurations and the first excited triplet state $^3\Psi_2$ has $(56,31)$ from $\left(5f_{\delta-}^{\uparrow(0.64)}5f_{\phi-}^{\uparrow(0.64)}, 5f_{\delta+}^{\uparrow(0.36)}5f_{\phi+}^{\uparrow(0.36)}\right)$ configurations. In the superscript and inside $()$, natural occupation of the orbitals are given. As already mentioned, due to anti-bonding σ type interaction of the $5f_{\phi+}$ orbital with the ligands, the probability of finding an electron in the more stable $5f_{\phi-}$ increases for the lowest SF states as noticed from the large occupation numbers. With the SOC, the two NKD states $\{|1\rangle, |2\rangle\}$ are almost degenerate and show similar compositions in terms of the SF states. Some of the low lying singlet states around 10000 cm^{-1} (see Table 3.25) are contributing to the NKD and they are more stable when described by PT2 based methods. *Ab initio* calculation shows that these singlet states have occupations in the energetically higher $5f_{\pi^*}$ anti-bonding orbitals. Contributions to the ground NKD states from the SF triplet states are quite the same while the contributions differ from the singlet states.

3.4.3 Magnetic g-factors

For the $5f^1$ $[Np^{VI}O_2(TEDGA)_2]^{2+}$ complex, the magnetic g-factors $\left(g_\parallel, g_\perp\right)$ of the two lowest KDs are tabulated in Table 3.24 along with their compositions. With SO-CASSCF as the KD1 has more Δ character than Φ, $\left(g_\parallel, g_\perp\right)$ of KD1 and KD2 are $(0.55, 1.09)$ and

Table 3.25: Energy levels (in cm^{-1}) from the SF and SO calculations for the $[Pu^{VI}O_2(TEDGA)_2]^{2+}$ complex.

CASSCF		CASPT2		RASSCF		RASPT2	
SF	SO	SF	SO	SF	SO	SF	SO
triplet		triplet		triplet		triplet	
0	0	0	0	0	0	0	0
18	1	342	7	19	1	30	8
1963	3551	2413	2935	2296	3756	2403	3627
6307	5681	5489	3775	6423	5794	5275	5359
6544	5811	5571	4173	6629	5924	5410	5475
18959	7998	16506	8130	20030	7906	17739	7780
19120	8031	24913	8153	20346	7931	18142	7808
singlet	12499	singlet	10432	singlet	12423	singlet	11451
9225	12749	6286	10441	9741	12908	7911	12392
9564	12818	7235	11439	10635	12965	9116	12447
9573	13431	7293	11524	10644	13333	9237	12958
11882	14862	7698	13383	12225	14692	9936	14139
12057	14923	7826	13423	12386	14804	9941	14155

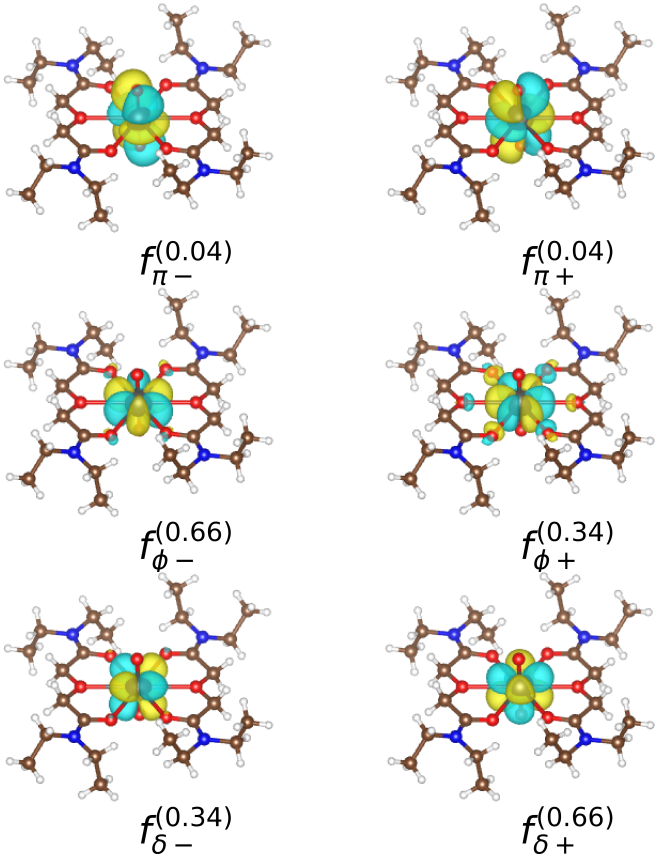

Figure 3.4.3: RAS(12,6;2,6;6:2,2), computed active NOs and their occupation numbers for the ground SF state $^3\Psi_1$ of the $[Pu^{VI}O_2(TEDGA)_2]^{2+}$ complex. The isovalue is 0.14 $e^-/bohr^3$.

Table 3.26: Percentage contributions of the SF states to the ground NKD $\{|1\rangle, |2\rangle\}$ of the $[Pu^{VI}O_2(TEDGA)_2]^{2+}$ complex from SO-RASSCF calculation. SF states in terms of the dominant configurations.

SF states	Configurations	$\|1\rangle$	$\|2\rangle$
$^3\Psi_1$	30% $5f^{\uparrow}_{\delta-}5f^{\uparrow}_{\phi+}$; 57% $5f^{\uparrow}_{\delta+}5f^{\uparrow}_{\phi-}$	46.3%	46.2%
$^3\Psi_2$	56% $5f^{\uparrow}_{\delta-}5f^{\uparrow}_{\phi-}$; 31% $5f^{\uparrow}_{\delta+}5f^{\uparrow}_{\phi+}$	46.2%	46.3%
$^1\Psi_1$	35%$f^{\uparrow\downarrow}_{\delta-}$; 40% $f^{\uparrow\downarrow}_{\delta+}$ 5% $f^{\uparrow}_{\phi-}f^{\downarrow}_{\pi-}$; 4% $f^{\uparrow}_{\phi+}f^{\downarrow}_{\pi+}$	4.9%	0.3%
$^1\Psi_2$	75% $f^{\uparrow}_{\delta-}f^{\downarrow}_{\delta+}$; 6% $f^{\uparrow}_{\phi-}f^{\downarrow}_{\pi+}$ 4% $f^{\uparrow}_{\phi+}f^{\downarrow}_{\pi-}$	0.3%	5.0%

$(2.92, 1.02)$, respectively. With better addressing the electron dynamic correlation in the RAS or PT2 based methods, KD1 is dominant from the SF Φ states which have higher orbital angular momentum than the Δ states those are now dominant in the KD2. As a result, the $g_{\parallel}$ value of KD1, $g_{\parallel,1}$ highly increases and likely $\phi_{5/2}$ Kramers spinors for the unpaired electron while $g_{\parallel,2}$ is close to 2 from plausible $\delta_{3/2}$ Kramers spinors. In the SO-RASSCF $(g_{\parallel}, g_{\perp})$ of KD1 and KD2 are $(2.95, 1.14)$ and $(0.60, 1.33)$, respectively. With the increment of the Φ behavior in KD1 in the PT2 calculations, $g_{\parallel,1}$ increases and is approaching to the free ion value (4.22 from Table 3.4). For the sake of comparison, with the DPA/Et−DPA ligands (see Tables 3.9, 3.11), the best description with the SO-RASPT2* calculation yielded $(40, 60)$ of (Φ, Δ) characters with $(g_{\parallel}, g_{\perp})$ close to $(1.4, 1.0)$ for both KDs. So, the nature of the two lowest KDs is significantly different in the TEDGA complex than in the DPA complex. Consequently, there is a subtle difference in the origins of magnetic anisotropies in the two neptunyl complexes and it can be confirmed from the pNMR shifts study.

In the $5f^2$ $[Pu^{VI}O_2(TEDGA)_2]^{2+}$ chelate, the only non-zero g-factor of the NKD $g_{\parallel}$, obtained from different methods are given in Table 3.27. The values of $g_{\parallel}$ obtained from different methods in the free plutonyl cation and also in the $[Pu^{VI}O_2(DPA)_2]^{2-}$ complex are also listed for an overall comparison. In both the plutonyl chelates, the values are close to the free ion value 6.1, revealing that the central plutonyl moieties are less perturbed by the ligand fields unlike their $5f^1$ counterparts. The variational SO-CAS(RAS)SCF values are the same 5.93 slightly higher than the DPA, 5.89. The PT2 methods tend to decrease the value than the variational methods. For TEDGA complex, the SO-CASPT2 and SO-RASPT2 NKD g-factors are 5.79 and 5.88, respectively, which again slightly higher than the DPA complex with the values 5.73 and 5.84, respectively. The equatorial ligand field tends to slightly decrease the magnitude of $g_{\parallel}$ in the complexes from the free plutonyl.

Table 3.27: The only non-zero g-factor, $g_{\|}$ of the ground NKD in the $[Pu^{VI}O_2]^{2+}$ chelates.

	SO-CASSCF	SO-CASPT2	SO-RASSCF	SO-RASPT2
$[Pu^{VI}O_2]^{2+}$	6.10	6.11	6.09	6.11
$[Pu^{VI}O_2(DPA)_2]^{2-}$	5.89	5.73	5.89	5.84
$[Pu^{VI}O_2(TEDGA)_2]^{2+}$	5.93	5.79	5.92	5.88

3.4.4 Analysis of ^{1}H and ^{13}C pNMR shifts

^{1}H and ^{13}C NMR chemical shifts of the ligand atoms in the $[An^{VI}O_2(TEDGA)_2]^{2+}$ complexes were recorded. To obtain the pNMR shifts, the $[U^{VI}O_2(TEDGA)_2]^{2+}$ complex is used as a diamagnetic reference. On one hand, the NMR shifts technique is already established as a reliable method to obtain the isotropic magnetic susceptibility χ_m in solution by Evans method [78]. On the other hand, in most of the paramagnetic metal complexes, a significant part of the isotopic pNMR shifts originates from the magnetic anisotropy of the system. So the NMR technique can be used to probe both the isotropic and the anisotropic magnetic properties [11]. We have already deduced the magnetic susceptibility tensor in the $[An^{VI}O_2(DPA)_2]^{2-}$ complexes using the data obtained from the NMR technique only. But this kind of evaluation cannot be performed for every paramagnetic system as there might be some associated experimental limitations. Specially, the χ_m obtained using Evans method depends on the concentration of paramagnetic system in the solution. Because of the stable +3 oxidation state of the Ln cations and the fact that they are non-radioactive, the task is quite easy for the Ln complexes. But, the actinides are far more prone to reduction, especially at high oxidation states, and they are also radioactive, making it difficult to accurately determine their concentrations in the solution.

The experimental pNMR shifts at 263 K are reported in Table 3.29 with the geometric factors G_K of the hydrogen and carbon atoms in the crystal structures. In the case of Pu^{VI} complex, ^{13}C NMR signals are very broad and weak, making it difficult to properly evaluate the pNMR shifts with less magnitude uncertainty and therefore they are discarded. The ratio of the pNMR shifts between any two nuclei is in close agreement to their geometric ratio implying a dominant dipolar mechanism for the observed pNMR shifts. When the contact terms are negligible, the isotropic pNMR shifts originate from the anisotropy of the electronic magnetic moments. In this case, according to Eq. 2.6.33, the slope of the $\delta_K^p = f(G_K)$ plot is the anisotropic magnetic susceptibility $\Delta\chi_{ax}$. The isotropic molar magnetic susceptibility χ_m is deduced for the Np^{VI} complex from the ^{1}H NMR shifts of t-BuOH following the Evans methods. The isotropic and anisotropic molar magnetic susceptibilities of the $[An^{VI}O_2(TEDGA)_2]^{2+}$ complexes are reported in Table 3.28 with the *ab initio* values. $\Delta\chi_{ax}$ obtained from the pNMR shifts is highly positive indicating a

prolate magnetization of the paramagnetic center.

For the Np^{VI}, the susceptibility components calculated from the ground KD (denoted by KD1) and from the two lowest KDs (denoted by KD1&2) are given in Table 3.28. For the Pu^{VI}, the values obtained from the ground NKD (denoted by NKD) states are also provided. The so-called Curie values i.e. those are obtained from the thermally populated energy levels, can be labeled to the values obtained from the KD1 of the Np^{VI} and from the NKD of the Pu^{VI} complexes. In this case, each component of the molar magnetic susceptibility is calculated from the magnetic g-factors according to Eq. 3.3.3. Note that, the *ab initio* calculation suggests that KD2 is at the order of room temperature energy which means it is slightly populated and will contribute to the $1/T$ behavior of the pNMR shifts as deduce in Eq. 3.3.6. In the Pu^{VI} complex, the ground NKD has only one non-zero magnetic g-factor and the ligand field splitting of the two NKD states is very small compared to thermal energy, so both the isotopic and anisotropic Curie magnetic susceptibilities are only linked to the non-zero g-factor. From Table 3.28, it can be noticed that the magnetic susceptibilities calculated from all the states are roughly the same as those obtained from the two KDs and from the ground NKD for the Np^{VI} and Pu^{VI} complexes, respectively. The actinyls chelated with the DPA ligands showed similar behavior. So it can be said that the two lowest KDs and the ground NKD dictate all the physics of the $5f^1$ and $5f^2$ actinyl complexes, respectively. The spin-only magnetic susceptibilities (see Table 3.28, denoted by superscript 'S') are negative while the orbital contributions are largely positive as per Hund's rules. As the orbital contributions of the magnetic electrons are largely accountable for their paramagnetic behavior, it is necessary to correctly address their electronic structure from the *ab initio* calculations to reproduce the experimental data.

From Table 3.28, it is noticed that both the SO-CASPT2 and the SO-RASSCF $\Delta\chi_{ax}$ are in close agreement to the values obtained from the pNMR shifts for the $[Np^{VI}O_2(TEDGA)_2]^{2+}$ complex. The perturbative SO-RASPT2 calculation quite overestimates the experimental value. For the isotropic part, the discrepancy in between the values of χ_m obtained from the NMR shifts using Evans method and the *ab initio* calculations are much larger. In the case of $[Pu^{VI}O_2(TEDGA)_2]^{2+}$ complex, all the *ab initio* $\Delta\chi_{ax}$ values are very close in magnitude and overestimate by 50% from the experimental value. The effects of the electron dynamic correlation on the magnetic properties of the $5f^2$ complexes are not as far as important as the $5f^1$ counterpart.

The restricted SO-DFT calculation in ADF on the $5f^1$ $[Np^{VI}O_2(TEDGA)_2]^{2+}$ complex shows an oblate like ground-state-magnetization ($g_{\perp,1}/\chi_{\perp,1} > g_{\parallel,1}/\chi_{\perp,1}$), same as the SO-CASSCF result for the KD1 and completely fails to recover the nature of the ground KD. When dynamic correlation is introduced to the CAS based results, it completely changes the nature of the KD1 and so its magnetization i.e. going from an oblate to a

Table 3.28: Magnetic susceptibilities χ_m and axial anisotropies $\Delta\chi_{ax}$ (in 10^{-8} m^3mol^{-1}) of the $[An^{VI}O_2(TEDGA)_2]^{2+}$ complexes at 263 K.

	States	$\chi_\perp$	$\chi_\parallel$	χ_m	$\Delta\chi_{ax}$	$\chi^S_\perp$	$\chi^S_\parallel$	χ^S_m	$\Delta\chi^S_{ax}$
				$[Np^{VI}O_2(TEDGA)_2]^{2+}$					
Exp				4.02[a]	4.1±0.1[b]				
SO-CASSCF	KD1	0.54	0.13	0.27	-0.41	-0.09	-0.31	-0.16	-0.23
	KD1&2	0.67	2.97	1.44	2.30	-0.26	-0.76	-0.42	-0.50
	All	0.81	2.99	1.54	2.18	-0.22	-0.75	-0.40	-0.53
SO-CASPT2	KD1	0.41	4.53	1.78	4.12	-0.09	-0.54	-0.24	-0.45
	KD1&2	0.70	5.52	2.30	4.82	-0.22	-0.86	-0.43	-0.64
	All	0.75	5.59	2.36	4.84	-0.20	-0.84	-0.41	-0.65
SO-RASSCF	KD1	0.59	3.91	1.70	3.32	-0.10	-0.43	-0.21	-0.33
	KD1&2	0.87	5.51	2.41	4.63	-0.28	-0.87	-0.47	-0.60
	All	0.94	5.54	2.48	4.60	-0.26	-0.85	-0.45	-0.60
SO-RASPT2	KD1	0.31	5.72	2.01	5.41	-0.07	-0.76	-0.30	-0.69
	KD1&2	0.70	6.14	2.52	5.44	-0.19	-0.91	-0.43	-0.72
	All	0.74	6.22	2.57	5.48	-0.12	-0.89	-0.37	-0.78
				$[Pu^{VI}O_2(TEDGA)_2]^{2+}$					
Exp					10.4[b]				
SO-CASSCF	NKD	-	15.71	5.24	15.71				
	All	0.11	15.73	5.32	15.62				
SO-CASPT2	NKD	-	15.02	5.01	15.02	-	-4.77	-1.59	-4.77
	All	0.17	15.00	5.12	14.83	-	-4.76	-1.59	-4.76
SO-RASSCF	NKD	-	15.72	5.24	15.72				
	All	0.17	15.70	5.35	15.53	-	-4.92	-1.64	-4.92
SO-RASPT2	NKD	-	15.51	5.17	15.51	-	-4.93	-1.64	-4.93
	All	0.18	15.45	5.27	15.30	-	-4.92	-1.64	-4.92

[a]: deduced from chemical shifts according to Evans method, [b]: deduced from the $\delta^p_K = f(G_K)$ plots

Table 3.29: Experimental and calculated pNMR shifts (in ppm) in the $[Np^{VI}O_2(TEDGA)_2]^{2+}$ complexes at 263 K and 9.4 T. Geometric parameters G_K (in $10^{27}m^{-3}$) are also provided for the atoms.

Method	*C*1	*C*2	*C*3	*C*4	*C*5	*C*6	*H*2	*H*3	*H*4	*H*5	*H*6
$[Np^{VI}O_2(TEDGA)_2]^{2+}$											
G_K	-25.67	-20.86	-7.64	-5.12	-4.76	-3.08	–11.39	-6.95	-4.17	-4.10	-2.53
Exp δ^p	-46.8	-37.5	-15.5	-8.4	-7.0	-4.9	-20.3	-12.8	-6.5	-8.2	-4.7
SO-CASSCF	-24.6	-20.0	-7.3	-4.9	-4.6	-3.0	-10.9	-6.7	-4.0	-3.9	-2.4
SO-CASPT2	-54.7	-44.5	-16.3	-11.0	-10.2	-6.6	-24.2	-14.8	-8.9	-8.7	-5.4
SO-RASSCF	-52.0	-42.3	-15.5	-10.4	-9.7	-6.2	-23.1	-14.1	-8.4	-8.3	-5.1
SO-RASPT2	-62.0	-50.3	-18.4	-12.3	-11.5	-7.4	-27.5	-16.8	-10.1	-9.9	-6.1
$[Pu^{VI}O_2(TEDGA)_2]^{2+}$											
G_K	-25.70	-20.89	-7.64	-5.22	-4.71	-3.07	-11.41	-6.95	-4.13	-4.07	-2.51
Exp δ^p	-	-	-	-	-	-	-53.1	-39.5	-19.7	-23.0	-13.1
SO-CASSCF	-176.8	-143.7	-52.6	-35.9	-32.4	-21.1	-78.4	-47.8	-28.4	-27.9	-17.3
SO-CASPT2	-169.9	-138.1	-50.5	-34.5	-31.1	-20.3	-74.5	-45.6	-27.1	-26.7	-16.5
SO-RASSCF	-175.8	-142.8	-52.3	-35.7	-32.2	-21.0	-78.3	-47.7	-28.3	-27.9	-17.3
SO-RASPT2	-173.2	-140.7	-51.5	-35.2	-31.7	-20.7	-76.9	-46.9	-27.9	-27.4	-16.6

prolate environment $\chi_{\perp,1} < \chi_{\parallel,1}$. So it is not only that the interaction with the excited states changes the nature of magnetization, but the nature of the ground KD itself and its magnetization completely alters when they are better described including dynamic correlation indicating the importance of its description in the first principles calculaton. The four-component mDKS calculation in ReSpect package was also benchmarked on this system but the magnetic *g*-values (see Table 3.24) are underestimated largely from the SO-RASSCF or the SO-CAS(RAS)PT2 results indicating a significantly deviated solution for the ground state.

3.4.5 Temperature dependence of the pNMR shifts

In the $[An^{VI}O_2(DPA)_2]^{2-}$ complexes, the ^{1}H pNMR shifts are mostly due to the dipolar mechanism and from their temperature dependencies, we had been able to extract the magnetic informations about the lowest energy states those play the most influential role in determining their paramagnetic behavior. To obtain similar information about the $[An^{VI}O_2(TEDGA)_2]^{2+}$ complexes, temperature dependent ^{1}H and ^{13}C pNMR shifts are recorded in a temperature window of $220-350$ K. As already mentioned, the experimental error in properly assigning the ^{13}C pNMR shifts in the Pu^{VI} complex are rather large due to the broad and weak signals, this will increase the uncertainties in the estimated parameters and therefore we did not consider the temperature dependent ^{13}C NMR spectra of the Pu^{VI} complex. Temperature dependent ^{1}H and ^{13}C pNMR shifts

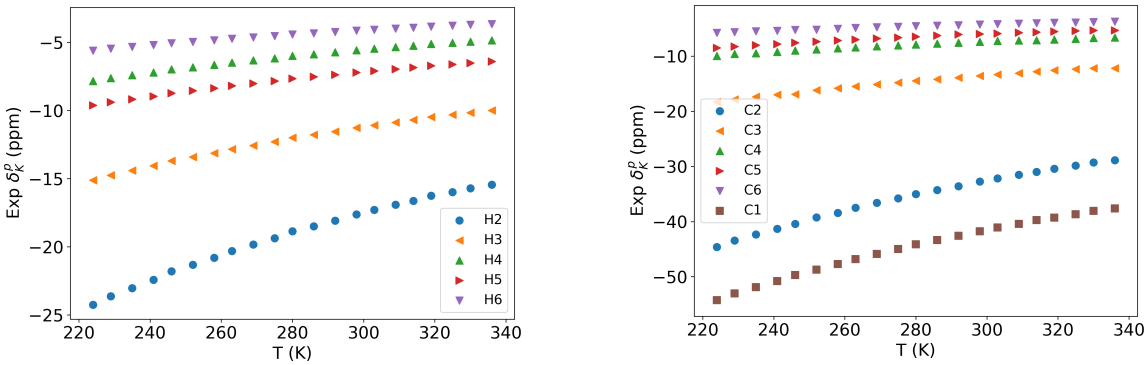

(a) (b)

Figure 3.4.4: Temperature dependent ^{1}H (a) and ^{13}C (b) pNMR shifts in the $[Np^{VI}O_2(TEDGA)_2]^{2+}$ complex.

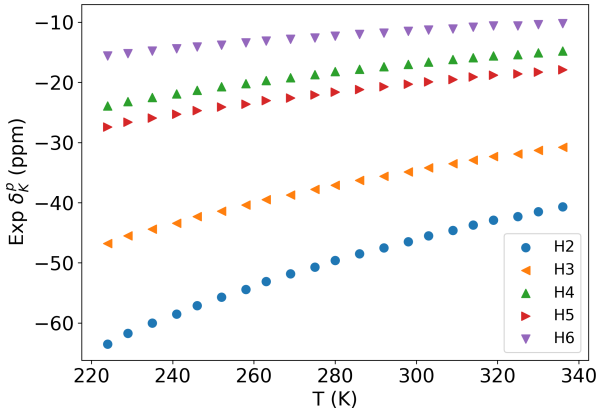

Figure 3.4.5: Temperature dependent ^{1}H pNMR shifts in the $[Pu^{VI}O_2(TEDGA)_2]^{2+}$ complex.

in the $[Np^{VI}O_2(TEDGA)_2]^{2+}$ are shown in Fig. 3.4.4 and the ^{1}H pNMR shifts in the $[Pu^{VI}O_2(TEDGA)_2]^{2+}$ complex are shown in Fig. 3.4.5

In the case of Np^{VI} complex, temperature dependent χ_m^{Evans} are deduced from the ^{1}H NMR shifts of the t-BuOH in CD_3CN solution according to Evans formula (Eq. 3.3.1) and the anisotropic magnetic susceptibilities $\Delta\chi_{ax}$ are from the pNMR shifts according to Eq. 2.6.33. Two techniques are used to evaluate the concentration of the neptunyl complex in the solution; alpha-counting analysis and UV-visible spectroscopy. Both methods provide roughly the same values. $\Delta\chi_{ax}(T)$ obtained from the plots of $\delta_K^p = f(G_K)$ for the temperature dependent ^{1}H pNMR shifts are slightly lower than those deduced from the ^{13}C pNMR shifts, 4.04 vs 4.20×10^{-8} m^3mol^{-1} at 263 K (see Fig. 3.4.6). This small discrepancy arises due to the large range of G_K for the C atoms, whereas it is small in the case of H atoms (see Table 3.29). $\Delta\chi_{ax}(T)$ obtained from the plots of the ^{1}H and ^{13}C pNMR shifts jointly with their geometric factors are in between those arising from the plots of ^{1}H and ^{13}C pNMR shifts, separately; at 263 K, it is 4.16×10^{-8} m^3mol^{-1}. $\Delta\chi_{ax}(T)$ obtained from the different plots (see Fig. 3.4.6) are slightly different, but these differences affect the parameters of the two KDs model equation (Eq. 3.3.5). In the case of the Pu^{VI} com-

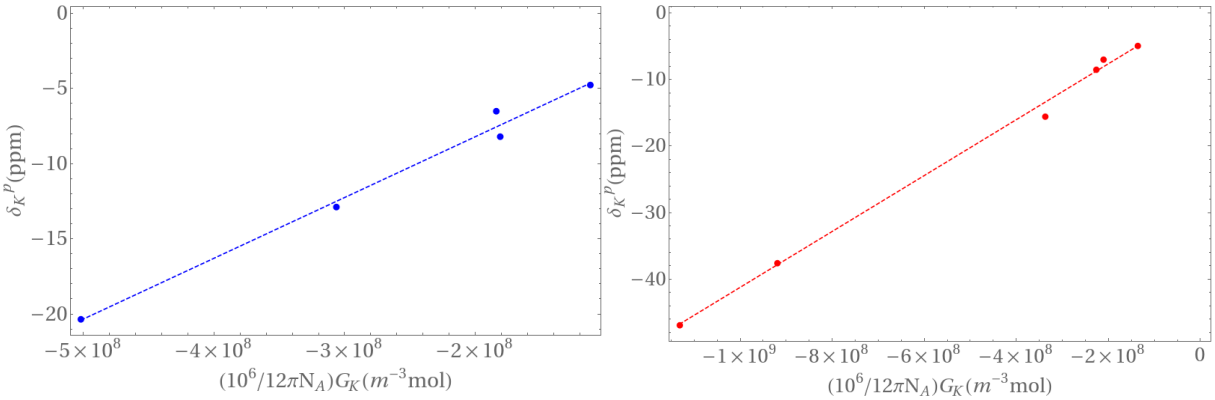

(a) ^{1}H pNMR shifts.

(b) ^{13}C pNMR shifts.

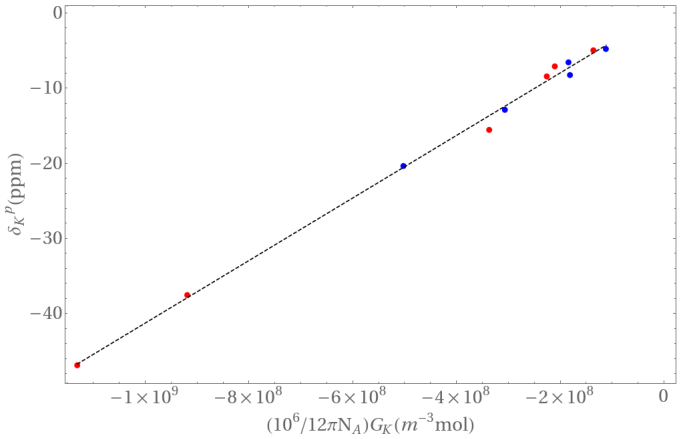

(c) ^{1}H and ^{13}C pNMR shifts.

Figure 3.4.6: Plots of δ_K^p (in ppm) at 263 K vs $\frac{10^6}{12\pi N_A}G_K$ (in m^{-3}mol). The slope provides $\Delta\chi_{ax}$ (in $\text{m}^3\text{mol}^{-1}$) at 263 K.

plex, $\Delta\chi_{ax}(T)$ are deduced from the temperature dependent ^{1}H pNMR shifts. Due to the large uncertainty in the measured concentration, the isotropic $\chi_m^{Evans}(T)$ are not reported for the Pu^{VI} complex. $\Delta\chi_{ax}(T)$ obtained from the experimental pNMR shifts and the *ab initio* SO-CASPT2 calculations are plotted in Fig. 3.4.7 for the actinyl chelates. In the insets of Fig. 3.4.7, isotropic $\chi_m(T)$ obtained from the Evans method and SO-CASPT2 calculations are plotted. The anisotropic $\Delta\chi_{ax}$ obtained from the pNMR shifts is larger for the Pu^{VI} complex than the Np^{VI} complex and in both complexes $\Delta\chi_{ax}(T)$ through the studied temperature window are positive indicates a prolate like magnetization around the actinyl centers.

- Fitting of the $\chi_m^{Evans}(T)$ and $\Delta\chi_{ax}(T)$ from the pNMR shifts in the Np^{VI} complex with a two KDs model

In the Np^{VI} complex, the two low lying KDs are largely responsible for the anisotropic behavior, the axial anisotropy of the **g** tensors of the two KDs are along the actinyl bonds. With the increase of T, KD2 is getting populated resulting in a decrease of thermal population of the more magnetic KD1 and as a result, a decrease of both the isotropic and

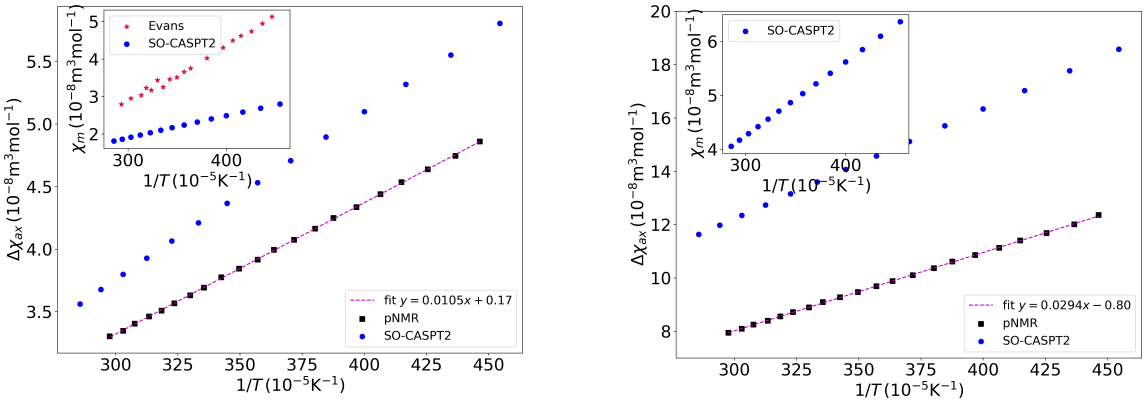

(a) $[Np^{VI}O_2(TEDGA)_2]^{2+}$ (b) $[Pu^{VI}O_2(TEDGA)_2]^{2+}$

Figure 3.4.7: Temperature dependent isotropic and anisotropic molar magnetic susceptibilities of the $[An^{VI}O_2(TEDGA)_2]^{2+}$ complexes. Experimental isotropic $\chi_m(T)$ (in 10^{-8} m^3mol^{-1}) are those deduced using Evans method and the anisotropic $\Delta\chi_{ax}(T)$ (in 10^{-8} m^3mol^{-1}) are from the ^1H and ^{13}C pNMR shifts.

the anisotropic magnetic susceptibilities can be observed in Fig. 3.4.7. *Ab initio* calculations overestimate the anisotropic behavior whereas largely underestimate the isotropic part deduced from the Evans method. To obtain the information about the two KDs, we fit the temperature dependent χ_m and $\Delta\chi_{ax}$ according to Eq. 3.3.4 and Eq. 3.3.5, respectively. From the $\chi_m(T)$, one estimates the isotropic magnetic interactions of the two KDs in terms of g_1^2, g_2^2 and M_{12}^2; and from the $\Delta\chi_{ax}(T)$ the anisotropic behavior in terms of Δg_1^2, Δg_2^2 and ΔM_{12}^2. We performed a least mean-square-deviation (MSD) fitting of the $\Delta\chi_{ax}(T)$ obtained from the pNMR shifts with Eq. 3.3.5 and the quality of fitting can be discussed in term of the MSD value (Σ) defined as

$$\Sigma = \frac{1}{n}\sum_n \left[\Delta\chi_{ax}^{2KD}(T) - \Delta\chi_{ax}^{pNMR}(T)\right]^2 \tag{3.4.1}$$

where $\Delta\chi_{ax}^{2KD}(T)$ are the anisotropic magnetic susceptibilities obtained from the two KDs according to Eq. 3.3.5. n is the number of studied points. In a similar way, the isotropic $\chi_m(T)$ obtained from Evans method is fitted with Eq. 3.3.4. Like for the DPA complexes, to be sure about the reliability of the magnitude of the parameters obtained from the fittings, benchmark studies are performed on the $\chi_m(T)$ and $\Delta\chi_{ax}(T)$ obtained from the *ab initio* SO-CASSCF and SO-CASPT2 calculations with the model equations. The difference between the *ab initio* SO-CASSCF and SO-CASPT2 results is the alteration of the KD1 and KD2 as can be noticed from their compositions (see Table 3.24) and also from the magnetic properties (see Table 3.30).

It appears that the magnetic susceptibility obtained for the $[Np^{VI}O_2(TEDGA)_2]^{2+}$ complex from Evans method is way beyond the free cation limit. At 298 K, *ab initio* magnetic susceptibility for the free $[Np^{VI}O_2]^{2+}$ cation is 2.47×10^{-8} m^3mol^{-1}; for the $[Np^{VI}O_2(DPA)_2]^{2-}$ complex, both the values obtained from Evans vs SO-RASPT2 methods are slightly reduced from the free cation, 1.82 vs 1.70×10^{-8} m^3mol^{-1}(see Table 3.16); but they dis-

agree for $[Np^{VI}O_2(TEDGA)_2]^{2+}$ complex and at 298K, Evans vs SO-CASPT2 methods results are 3.3 vs 2.10×10^{-8} m^3mol^{-1}. For the two neptunyl complexes, DPA and TEDGA, the *ab initio* χ_m are similar and reduced from the free ion value, they slightly differ in magnitude as likely the results of two different electronic structures. χ_m obtained from Evans method for the $[Np^{VI}O_2(TEDGA)_2]^{2+}$ is too large to be obtained from the two lowest KDs and indicating a huge TIP from excited states which is suspicious. Consequently, the values of the parameters obtained from the fitting of the $\chi_m^{Evans}(T)$ using the two-KDs equation (Eq. 3.3.4) are largely deviating from the *ab initio* values and become unacceptable in some cases (see Table 3.30). Another fitting where the magnetic parameters g_1^2, g_2^2 and M_{12}^2 are taken from SO-CASPT2 calculations, estimates Δ comparable to the *ab initio* results, but the quality of this fitting is very poor (large value of Σ) indicating a huge amount of TIP from the excited states. Whereas benchmark studies on SO-CASSCF and SO-CASPT2, $\chi_m(T)$ data show that the reversal of the two KDs is correctly found out using the two KDs model. As one can notice (see Table 3.30), $g_1^2 < g_2^2$ obtained from the fitting of CASSCF values and that changes for CASPT2 i.e. $g_1^2 > g_2^2$.

For the anisotropic magnetic properties of the two KDs, fitting of the anisotropic $\Delta\chi_{ax}(T)$ obtained from SO-CASSCF and SO-CASPT2 methods with Eq. 3.3.5 provides similar values to those obtained from *ab initio*. Fitting of $\Delta\chi_{ax}(T)$ obtained from the pNMR shifts with the polynomial form of the two KDs model equation (Eq. 3.3.5) was unsuccessful due to the requirement of the proper sign of the individual terms and in this case leads to imaginary values for the ligand field splitting Δ. Fitting of the $\Delta\chi_{ax}(T)$ obtained from the pNMR shifts using Eq. 3.3.5 provides Δg_1^2 close to the SO-CASPT2 value. But the anisotropic magnetic property of KD2, Δg_2^2 is highly overestimated. The values of the other parameters i.e. the anisotropic Van Vleck coupling parameter ΔM_{12}^2 and the ligand field splitting of the two KDs Δ, are not stable, but in the order of the *ab initio* values. Surprisingly, fitting of the $\Delta\chi_{ax}(T)$ obtained from ^{1}H pNMR shifts only with Eq. 3.3.5 completely fails to provide a good estimation of the anisotropic anisotropic properties for any KD, which might be due to over-parametrization. The stability of the magnitude of Δg_1^2 in all the fittings can be understood from the two-KDs model with replacing $x = \beta\Delta$ in Eq. 3.3.5 and writing in terms of the hyperbolic form as

$$\Delta\chi_{ax} = N_A\mu_0\mu_B^2\left[\beta\frac{\Delta g_1^2 e^{\beta\Delta/2}+\Delta g_2^2 e^{-\beta\Delta/2}}{4\left(e^{\beta\Delta/2}+e^{-\beta\Delta/2}\right)}+\frac{\left(e^{\beta\Delta/2}-e^{-\beta\Delta/2}\right)\Delta M_{12}^2}{\Delta\left(e^{\beta\Delta/2}+e^{-\beta\Delta/2}\right)}\right] \quad (3.4.2)$$

$$= \kappa\left[\frac{x}{\Delta}\Delta g_1^2\frac{\cosh[x/2]+\sinh[x/2]}{4\cosh[x/2]}+\frac{x}{\Delta}\Delta g_2^2\frac{\cosh[x/2]-\sinh[x/2]}{4\cosh[x/2]}+\frac{\Delta M_{12}^2}{\Delta}\tanh[x/2]\right] \quad (3.4.3)$$

In Eq. 3.4.3, $\kappa = N_A\mu_0\mu_B^2$ is a prefactor and the unit of the terms inside [ ] is in J^{-1}. The

first and second terms are the Boltzmann contributions (can be also referred as the Curie contributions as used in Ref. [9]) from KD1 and KD2, respectively, the third term is the Van Vleck contribution term. Considering the range of Δ from 300-600 cm^{-1} and T from 220-350K, the range of x covers from $1.2-4$. In Fig. 3.4.8, the plots $\Delta\chi_{ax}\left(\text{in } \kappa J^{-1}\right)$ vs x are shown where Δ, Δg_1^2, Δg_2^2 and ΔM_{12}^2 are taken from different *ab initio* calculations since they represent wide range of considerations. For the sake of comparison, the plot $\Delta\chi_{ax}\left(\text{in } \kappa J^{-1}\right)$ vs x for the $[Np^{VI}O_2(DPA)_2]^{2-}$ complex is shown with the SO-RASPT2* parameters as the method was successful to reproduce the $\Delta\chi_{ax}(T)$ obtained from pNMR shifts. At low temperature regime (higher values of x), the contribution of KD1 is dominant and controls the overall magnetic anisotropy, but at high temperature regime specially when the KD2 is increasingly populated, peeling of the $\Delta\chi_{ax}(T)$ to obtain the individual contributions is much more tedious. As this was the case for the $[Np^{VI}O_2(DPA)_2]^{2-}$ complex where ΔM_{12}^2 highly controls the magnetic anisotropy at the high temperature domain. When the Boltzmann contribution from KD2 and the Van Vleck term become negligible, very small changes in their slope may result non reliable parameters. But the impact of the parameters on the overall slope is negligible and hence these last two terms can be ignored. In this case, in the low temperature regime, KD1 mostly dictates the magnetic anisotropy and the anisotropic magnetic susceptibility is reduced to Curie contribution from KD1 and a very small contributions from the excited states is taken as parameter TIP in Eq. 3.4.4,

$$\Delta\chi_{ax} = N_A\mu_0\mu_B^2\frac{\Delta g_1^2}{4k_BT} + TIP \tag{3.4.4}$$

Δg_1^2 obtained using Eq. 3.4.4 is tabulated in Table 3.30. Interestingly, fitting of the $\Delta\chi_{ax}(T)$ obtained from the pNMR shifts confirms that the ground state magnetic anisotropy is highly axial, $\Delta g_1^2 \gg 0$ as obtained from the higher *ab initio* methods of calculations. Fitting of $\Delta\chi_{ax}(T)$ obtained from ^{1}H pNMR shifts with the one-KD model (Eq. 3.4.4) now provides a good estimation of Δg_1^2 due to reduced number of parameters; it is now 9-10, in quite good agreement with the SO-CASPT2 value indicating a SF Φ dominated ground KD and likely $\phi_{5/2}$ Kramers spinors for the unpaired electron. It shows that the ground KD is solely responsible for the magnetic anisotropy in the neptunyl TEDGA complex whereas it is the anisotropic Van Vleck contribution for the DPA complex, although the energy gap Δ between the two KDs is of the same order magnitude. This is due to magnetic parameters KD1 is highly anisotropic with TEDGA and the coupling with KD2 is rather small, while with DPA, ΔM_{12}^2 is larger and KD1 not as anisotropic. Both complexes are close to the trigonal symmetry, but the overall ligand field splittings of the Δ and Φ states are different, and it is the gap between the Δ and Φ states which finely tunes the nature of ground states and the magnetic anisotropies in the neptunyl complexes.

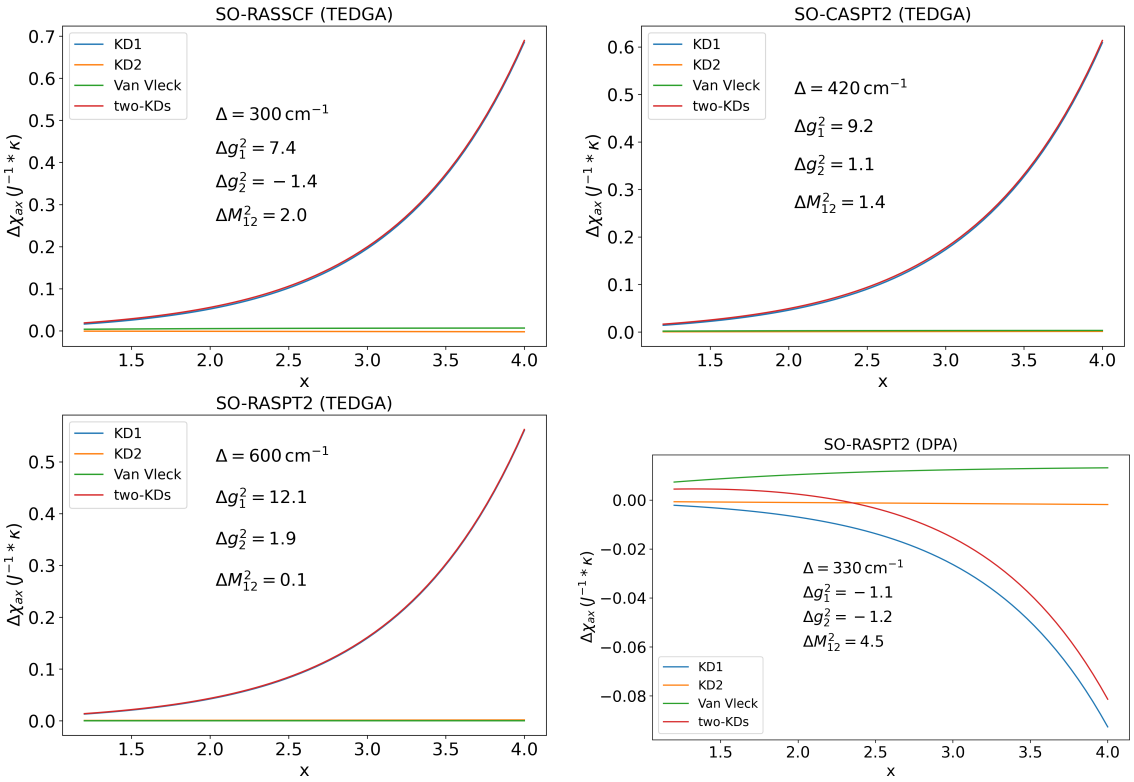

Figure 3.4.8: $\Delta\chi_{ax}\left(\text{in } \kappa\text{J}^{-1}\right)$ of Eq. 3.4.3 vs x $(x = \beta\Delta)$ are plotted with the parameters obtained from the *ab initio* calculations for the neptunyl TEDGA and DPA complexes. Inside the legends, KD1 represents Curie contribution from the ground KD (first term of Eq. 3.4.3), KD2, Curie contribution from the second KD (second term), Van Vleck, contribution from the magnetic interaction of the two KDs (third term), two-KDs, overall $\Delta\chi_{ax}\left(\text{in } \kappa\text{J}^{-1}\right)$ of the two KDs as described in Eq. 3.4.3.

Table 3.30: Model parameters evaluated from *ab initio* calculations for the $[Np^{VI}O_2(TEDGA)_2]^{2+}$ complex or deduced by fitting of the temperature dependent χ_m and $\Delta\chi_{ax}$ curves. Δ and Σ are in cm^{-1} and 10^{-16} m^6mol^{-2}, respectively.

	Δ	g_1^2	g_2^2	M_{12}^2	Δg_1^2	Δg_2^2	ΔM_{12}^2	Σ
SO-CASSCF	349	0.9	3.5	1.1	-0.9	7.5	2.2	
SO-CASPT2	418	4.0	1.2	0.9	9.2	1.1	1.4	
SO-RASSCF	297	3.8	1.3	1.0	7.4	-1.4	2.0	
SO-RASPT2	601	4.7	1.3	0.8	12.1	1.9	0.1	
CASSCF $\chi_m(T)^{\ddagger}$	263	1.6	8.1	0.3				8.35×10^{-9}
CASPT2 $\chi_m(T)^{\ddagger}$	396	4.0	2.2	1.0				6.59×10^{-8}
Evans $\chi_m(T)^{\ddagger}$	41	52.3	-18.2	-6.04				3.34×10^{-3}
Evans $\chi_m(T)^{\ddagger}$	359	4.0*	1.2*	0.9*				2.72
CASSCF $\Delta\chi_{ax}(T)^{\#}$	340				0.5	8.4	2.1	2.29×10^{-6}
CASPT2 $\Delta\chi_{ax}(T)^{\#}$	429				9.2	-0.3	1.7	2.46×10^{-9}
^{1}H & ^{13}C pNMR $\Delta\chi_{ax}(T)^{\#}$	585				8.8	9.3	0.4	2.43×10^{-5}
^{1}H & ^{13}C pNMR $\Delta\chi_{ax}(T)^{@}$					8.9			
only ^{1}H pNMR $\Delta\chi_{ax}(T)^{\#}$	99				-36.4	-66.9	28.9	5.60×10^{-5}
only^{1}H pNMR $\Delta\chi_{ax}(T)^{@}$					10.1			
only ^{13}C pNMR $\Delta\chi_{ax}(T)^{\#}$	264				9.0	11.4	-0.04	2.3×10^{-5}
only ^{13}C pNMR $\Delta\chi_{ax}(T)^{@}$					8.8			

‡: Eq. 3.3.4(2KD model), $^{\#}$: Eq. 3.3.5, T range: 220-350 K,
$^{@}$: Eq. 3.4.4(1 KD model), T range: 220-280 K ,*: SO-CASPT2 values

- Fitting of the $\Delta\chi_{ax}(T)$ in the Pu^{VI} complex with a ground NKD model

Temperature dependent anisotropic magnetic susceptibility $\Delta\chi_{ax}$ obtained from the ^1H pNMR shifts and SO-CASPT2 calculations are plotted in Fig. 3.4.7. In the case of $5f^2$ plutonyl complexes, the anisotropic magnetic susceptibility is modeled with the energetically well isolated ground NKD and the excited state contributions are very small. For a NKD, not necessarily the two states are degenerate, one only considers the Van Vleck contribution in Eq. 2.2.3 where the magnetic interaction of a NKD (M_{12}^2) is modeled with a non-zero g-factor $g_{\parallel}$ and the anisotropic molar magnetic susceptibility can be calculated in terms of $g_{\parallel}$ as

$$\Delta\chi_{ax} = N_A\mu_0\mu_B^2\frac{e^{\beta\Delta/2}-e^{-\beta\Delta/2}}{2\Delta\left(e^{\beta\Delta/2}-e^{-\beta\Delta/2}\right)}g_{\parallel}^2 \tag{3.4.5}$$

in Eq. 3.4.5, Δ is a small splitting between the two states. Fitting of the $\Delta\chi_{ax}(T)$ obtained from the pNMR shifts with Eq. 3.4.5 and its polynomial form $\left(AT^{-1}+CT^{-3}+ET^{-5}\right)$ helps to estimate both the $g_{\parallel}$ and Δ of the NKD and are tabulated in Table 3.31. Benchmark studies on the SO-CASPT2 $\Delta\chi_{ax}(T)$ successfully reproduce the *ab initio* results. $g_{\parallel}$ of the NKD obtained from the pNMR shifts are smaller than the *ab initio* results and hence points out the reason of the large disagreement between the experimental and *ab initio* calculated pNMR shifts in Table 3.29. Overestimation of the NKD g-factors from the *ab initio* calculations are also observed in the case of $[Pu^{VI}O_2(DPA)_2]^{2-}$ complex. From Table 3.28, it can be noticed that the interaction with the excited states introduces a small magnetization in the plane, which is coming from the orbital contributions of the excited states as the spin-only component $\chi_{\perp}^S$ is not observed. Hence the interaction with the excited states does not affect the magnetization along the axial direction, but leads to a planar component. Two reasons can be argued for the large disagreement of *ab initio* vs experimental pNMR shifts: on one hand, this is due to the overestimation of the orbital contribution of the NKD states and hence leads to a large $g_{\parallel}$ and on the other hand, wrong estimation of $\chi_{\perp}$ which only comes from the interaction with the excited state. Fitting of the $\Delta\chi_{ax}(T)$ from the pNMR shifts and also the *ab initio* calculations suggests that the two NKD states are almost degenerate, and when $\Delta\rightarrow 0$, $\Delta\chi_{ax}$ of Eq. 3.4.5 reduced to its Curie term i.e. $\Delta\chi_{ax} = N_A\mu_0\mu_B^2\frac{g_{\parallel}^2}{4k_BT}$. Interaction with the excited states introduce a temperature independent planar component $\chi_{\perp}$ which effectively includes the orbital contribution from the excited states and reduces the Curie $\Delta\chi_{ax}$,

$$\Delta\chi_{ax} = N_A\mu_0\mu_B^2\frac{g_{\parallel}^2}{4k_BT} - \chi_{\perp} \tag{3.4.6}$$

According to Eq. 3.4.6, the plot of $\Delta\chi_{ax} = f(1/T)$ helps to estimate $g_{\parallel}$ and $\chi_{\perp}$ (in 10^{-8} m^3mol^{-1}) and are given in Table 3.31. $g_{\parallel}$ and $\chi_{\perp}$ obtained from the pNMR shifts indicate that the orbital contributions in $[Pu^{VI}O_2]^{2+}$ complexes are overestimated from the first principles calculations of the pNMR shifts. Hence the large disagreement with the

experimental ^{1}H pNMR shifts is not also due to the ignorance of the presence of contact contributions.

Table 3.31: Model parameters evaluated from *ab initio* calculations for the $[Pu^{VI}O_2(TEDGA)_2]^{2+}$ complex or deduced by fitting the $\Delta\chi_{ax}$ curve. Δ and $\chi_\perp$ are in cm^{-1} and 10^{-8} m^3mol^{-1}, respectively.

	Δ	$g_\parallel$	$\chi_\perp$
SO-CASSCF	1	5.9	0.11
SO-CASPT2	7	5.8	0.17
SO-RASSCF	1	5.9	0.17
SO-RASPT2	8	5.9	0.17
CASPT2 $\Delta\chi_{ax}(T)^{\#}$	0	5.9	
CASPT2 $\Delta\chi_{ax}(T)^{\%}$	0.01	5.9	
CASPT2 $\Delta\chi_{ax}(T)^{@}$	-	5.9	0.12
^{1}H pNMR $\Delta\chi_{ax}(T)^{\#}$	0	4.8	
^{1}H pNMR $\Delta\chi_{ax}(T)^{\%}$	0.01	4.7	
^{1}H pNMR $\Delta\chi_{ax}(T)^{@}$	-	5.0	0.08

$^{\#}$: Eq. 3.4.5, T range: 220-350 K, $^{\%}$: Polynomial form, T range: 220-350 K, $^{@}$: Using T^{-1} Curie term, T range: 220-350 K

3.5 Conclusions

In this chapter, pNMR shifts in axially symmetric $5f^1$ neptunyl and $5f^2$ plutonyl complexes are analyzed where the AIS are measured on the ligands of $[An^{VI}O_2(DPA/Et{-}DPA)_2]^{2-}$ and $[An^{VI}O_2(TEDGA)_2]^{2+}$ complexes, $An^{VI} = Np^{VI}$ and Pu^{VI}. Magnetic susceptibility measured by NMR using the Evans method are also analyzed. In addition, solid $Li_2Np^{VI}O_2(DPA)_2\cdot 2H_2O$ compound and its SQUID magnetic susceptibility curves are also explored to find out the role of Li^+ counterions on the electronic and magnetic properties.

From the structures determined by X-rays diffraction experiments, the analysis of the pNMR chemical shifts at the different positions of the ligands showed that the Fermi contact contribution to the chemical shifts is negligible. This is confirmed by the vanishing spin populations on all hydrogen atoms as determined by unrestricted DFT calculations on $[An^{VI}O_2(Et{-}DPA)_2]^{2-}$ complexes and also quite the similar observations for the TEDGA complexes. Even the carbon or hydrogen atoms close from the paramagnetic center showed a negligible contact terms. The isotropic pNMR shifts in these complexes are arising from their high anisotropic magnetic moments. Accordingly, they were discussed in term of a pure dipolar interaction and the experimental $\Delta\chi_{ax}$ values are determined using X-rays geometrical factors. Combined with Evans method which

provides the isotropic average susceptibility χ_m, the two components of the susceptibility tensor are calculated. Wave function based calculations are performed in order to compute the electronic structure of the paramagnetic center. The Np^{VI} complexes have two low lying KDs whose composition depend subtly on the level of calculation and the correlation of the $5d$ and $5p$ orbitals plays an important role. This dramatically impacts the magnetic properties, between other the axiality of the magnetization for the neptunyl DPA complex. In the solid $Li_2Np^{VI}O_2(DPA)_2 \cdot 2H_2O$ compound, the Li^+ counterions are directly coordinated to the oxygen atoms of the coordination sphere and influence the magnetic properties of the paramagnetic center. In the presence of the Li^+ counterions, the ligand field is lower and the magnetic susceptibility larger, in agreement with the increase of the magnetic susceptibility between the SQUID and the NMR measurements in solution with Evans method. The Pu^{VI} complexes have a well isolated ground NKD, with one electron in a $5f_\delta$ and the other in a $5f_\phi$ orbital. Magnetic properties depend barely on the level of calculation and on the nature of the equatorial ligand except that a small splitting of the doublet may appear.

The AIS in the $[An^{VI}O_2(DPA/Et{-}DPA)_2]^{2-}$ and $[An^{VI}O_2(TEDGA)_2]^{2+}$ complexes are evaluated using the $\Delta\chi_{ax}$ values obtained from *ab initio* calculations. For the Np^{VI} complexes, the proper description of their electronic structures is of great importance as it not only changes the amplitude but also the sign of the calculated pNMR shifts. The two low lying KDs play a key role. In the case of $[Np^{VI}O_2(DPA/Et{-}DPA)_2]^{2-}$, magnetic interaction in between two KDs leads to a predominant Van Vleck contribution and mostly responsible for the pNMR shifts and SO-RASPT2* calculation are in good agreement with the experimental ones, whereas in the case of $[Np^{VI}O_2(TEDGA)_2]^{2+}$, it is the ground KD which is mostly responsibly for the anisotropic magnetic properties and SO-CASPT2/SO-RASSCF values are reasonably good. On the contrary, the 2-component SO-ZORA method lacks both the spin polarization and the Van Vleck contribution and completely fails to describe the nature of the ground KD. For the Pu^{VI} complexes, the calculations overestimate the $\Delta\chi_{ax}$ values due to the overestimation of the orbital contributions and consequently the pseudocontact chemical shifts.

The temperature dependences of the isotropic susceptibility and the pNMR shifts are analyzed in terms of the general Van Vleck and Soncini equations, respectively. Those equations are very similar in their forms, the former probing the isotropic magnetic parameters while the later probes the anisotropic ones. Those two equations are expressed in terms of the block matrices of the magnetic moment operator. This avoids the use of spin Hamiltonians and allows for the modeling of molecular systems where the definition of a spin Hamiltonian is not straightforward, in particular for actinide complexes. The reduction of Soncini equation to a restricted model space allows the fitting of the temperature dependence by few parameters. The regression analysis of the $\delta_K^p = f(1/T)$ curves

evidences the predominance of the T^{-1} term in both the complexes, in contradiction with Bleaney's model which assigns this term to the Fermi contact contribution. Bleaney's model applies in lanthanide complexes because all the components of the ground J manifold of the free ion are statistically populated, giving rise to an isotropic magnetization. In actinyl cations, only some of those components are populated, the room temperature magnetization is anisotropic and the dipolar contribution to T^{-1} term is proportional to the anisotropic magnetic moment of the paramagnetic center at room temperature. Further T^{-n} terms depend on the energy gap in the case of a two level system.

The experimental $\delta_K^p = f(1/T)$ and $\chi_m = f(1/T)$ are fitted according to the general Van Vleck and Soncini equations, respectively, within an axial symmetry and a reduced model space, either in its full form for the susceptibility or in its polynomial expansion for the chemical shifts. And this allows the determination of the energy gap and the magnetic moment, either isotropic from the susceptibility, or anisotropic from the chemical shifts. The fitted parameters are in good agreement with the *ab initio* results. In the Np^{VI} complexes, the energy gap between the two KDs is about 300 cm^{-1} for the DPA complex and around 300-500 cm^{-1} for the TEDGA complex. The Curie magnetization of the two KDs space is oblate in the $[Np^{VI}O_2(DPA)_2]^2$ complex, whereas the ground state magnetization in the $[Np^{VI}O_2(TEDGA)_2]^{2+}$ complex is prolate. For the Pu^{VI} complexes, the $\delta_K^p = f(1/T)$ is an almost pure T^{-1} term. The T^{-3} participates negligibly but its analysis is in favor of a splitting of the ground doublet. In the $[Pu^{VI}O_2(DPA)_2]^2$ complex, temperature dependent analysis shows a small splitting (50 cm^{-1}) of the NKD states, but in the $[Pu^{VI}O_2(TEDGA)_2]^{2+}$ complex they are almost degenerate, both the results are in agreement with the *ab initio* calculations. The non-zero g-factors of the ground NKDs are overestimated in the *ab initio* calculations, but close to the value of a free cation and independent on the nature of the ligand. So a pure dipolar interaction with the ^1H nuclei for the AIS as well as the insensitivity of the $[Pu^{VI}O_2]^{2+}$ cation to the equatorial ligands are very promising in the goal to use $[Pu^{VI}O_2]^{2+}$ cations as paramagnetic probe to get structural information. However, the predominance of the T^{-1} term in the dipolar contribution renders the unraveling of Fermi contact and dipolar contributions through a temperature analysis more difficult.

Chapter 4

pNMR shifts in An^{III} and An^{IV} complexes

4.1 Introduction

In this chapter, pNMR shifts are studied in An^{III} and An^{IV} complexes. While the ligand field splitting of the $5f$ orbitals, the electronic states and the origin of the magnetic anisotropy in the $[An^{VI}O_2]^{2+}$ complexes are quite different than in lanthanide complexes, An^{III} and An^{IV} ions show the possibility to form isostructural complexes with their lanthanide counterparts. So the ground SF and SO manifolds are the same for the isoelectronic $4f^N$ and $5f^N$ ions, the ligand field splitting of the manifolds are analogous and crystal field modelization can be used to compare the nature of magnetic anisotropy, electron-electron interaction, $J-J$ coupling and trends of covalency in between the isostructural series. SO-CAS based methods are used for both to describe their energy levels, wave functions and magnetic properties. Also, while Bleaney's theory models the LIS based on CFT, the AIS in the An^{III} and An^{IV} complexes can be explored to understand further considerations beyond the model.

AIS are studied in two sets of axially symmetric An^{IV} chelates, $[An^{IV}(DPA)_3]^{2-}$ and $[An^{IV}(DOTA)H_2O]$ where (An^{IV} = U^{IV}, Np^{IV} and Pu^{IV}). The corresponding Th^{IV} complex is used as a diamagnetic reference. Temperature dependent pNMR shifts in the $[An^{IV}(DPA)_3]^{2-}$ are measured and modeled with Bleaney's theory. The pseudocontact and contact shifts are separated based on the fitting of the temperature dependent curves. The analysis of the contact shifts are performed with DFT based spin population analysis. In $[An^{IV}(DOTA)H_2O]$ complexes, ^{17}O and ^{1}H pNMR shifts are analyzed and the two terms are separated based on *ab initio* calculations of the pseudocontact shifts. The two set of complexes are described with SO-CASPT2 method. The energy levels, CFPs and both isotropic and anisotropic magnetic susceptibilities are provided to compare the ligand environment and the nature of magnetization. Additionally, paramagnetic ion induced ^{31}P

MAS-NMR shifts are studied in solid $La_{1-x}M_xPO_4$ compounds where the paramagnetic ions M = Sm^{III}, Pu^{III}, Am^{III} are embedded in the solid $LaPO_4$ matrices. Local structure is probed with the X-ray and ^{31}P MAS-NMR spectra, and the electronic structure and magnetic properties of the paramagnetic center are analyzed by performing *ab initio* calculations on the model complex $[MLa_9(PO_4)_7]^{9+}$ with reference to experimental SQUID magnetic susceptibility and pNMR shifts.

4.2 pNMR shifts in axially symmetric $[An^{IV}(DPA)_3]^{2-}$ complexes

Actinide +IV complexes (An^{IV} = Th^{IV}, U^{IV}, Np^{IV} and Pu^{IV}) with dipicolinic acid derivatives (DPA and Et-DPA) have been studied by ^1H and ^{13}C NMR spectroscopy to understand the paramagnetic properties of this cation series. These complexes were synthesized at CEA Marcoule by M. Autillo *et al.* and their NMR spectra were recorded with every 5 K steps on temperature range 263–333 K. The isotropic molar magnetic susceptibility in solution, χ_m^{Evans} $\left(\text{in } m^3mol^{-1}\right)$ was determined from the chemical shift difference between the ^1H NMR signals of working (t-$BuOH_{in}$) and reference (t-$BuOH_{out}$) solutions using Evans method.

For the interpretation of the pNMR shifts in these complexes, *ab initio* calculations are performed to obtain their electronic structure and magnetic properties. Two structures were considered: i) the $[An^{IV}(DPA)_3]^{2-}$ complexes (An^{IV} = U^{IV}, Np^{IV} and Pu^{IV}) using the crystallographic $An^{IV}(DPA)_3(C_3H_5N_2)\cdot 3H_2O$ structures (denoted by XR and the electronic structures are discussed in section 5.7) ii) the symmetrized structure of the $[An^{IV}(DPA)_3]^{2-}$ complexes where the XR structures were symmetrized according to the D_3 point group with Chemcraft software (denoted by D_3). The ethyl groups are added according to Ref. [26], with three different angles with the aromatic ring, 0°, 45° and 90° (see Fig. 4.2.1) in order to represent the free rotation of the ethyl groups.

4.2.1 *Ab initio* electronic structures

In the solid state $An^{IV}(DPA)_3(C_3H_5N_2)\cdot 3H_2O$ compounds (An^{IV} = U^{IV}, Np^{IV} and Pu^{IV}), the energy levels, their natures and also the trends of the CFPs are broadly discussed in section 5.7. As in the solution, these complexes are axially symmetric, the pseudocontact shifts can be easily calculated using Eq. 2.6.33 and further the magnetic susceptibility tensor can be easily deduced as we have done for the $[An^{VI}O_2(DPA)_2]^{2-}$ complexes in previous chapter. But, due to the deviation from the trigonal symmetry in the crystal structures, the degeneracies of the $5f$ orbitals are lifted which causes the shifting of the axial magnetic anisotropy axis from the pseudo C_3 axis. To recover the axiality, *ab initio*

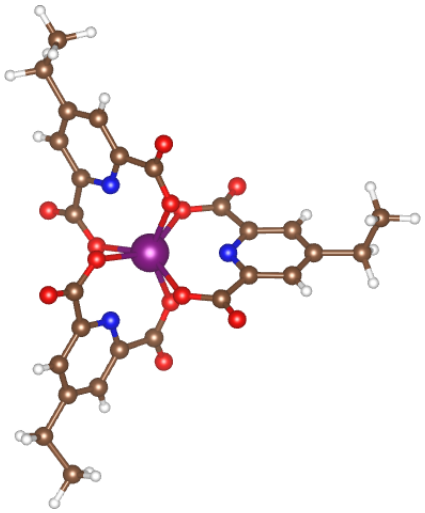

Figure 4.2.1: $[Np^{IV}(Et{-}DPA)_3]^{2-}$ complex. Color code: purple-Np, blue- N, red- O, saddle-brown- C, white- H.

calculations are performed on the D_3 structures. Computational details are provided in Appendix A. SF and SO energy levels of the symmetric $[An^{IV}(DPA)_3]^{2-}$ complexes are tabulated in Table 4.1.

The active $5f$ orbitals of the $[Np^{IV}(DPA)_3]^{2-}$ complex in D_3 symmetry are shown in Fig. 4.2.2. The lowest one, of symmetry a_2, is non bonding, then there is a group of three orbitals $(e \oplus a_2)$ denoting a π anti-bonding character with O atoms, and finally the three last ones $(a_1 \oplus e)$ with a σ anti-bonding character with the ligands. The ground LS terms for U^{IV}, Np^{IV} and Pu^{IV} ions are ^3H, ^4I and ^5I, respectively, which are split due to the presence of the ligands from 2500 cm^{-1} for U^{IV} to 4000 cm^{-1} for Pu^{IV} in the SSCASPT2 calculations. The SO states arising from the respective ground J terms are split around 1100-1500 cm^{-1}, quite larger than in the $[Ln(DPA)_3]^{3-}$ complexes (see section 5.6) where the splitting is around 300 cm^{-1}, since the $5f$ orbitals interact more with the ligands than the $4f$ ones.

In the U^{IV} complex, the ground state is non-degenerate and therefore, non-magnetic. In this case, the excited states play a key role to the susceptibility, on one hand by coupling with the excited states and on the other hand, when low lying, being populated at room temperature. In the U^{IV} complex, a triplet (163, 169 and 171 cm^{-1}) and a doublet (246 and 269 cm^{-1}) are low lying and populated at room temperature. In the Pu^{IV} complex, the ground state is a NKD (0, 4 cm^{-1}) and there is a partially populated triplet (399, 407, 450 cm^{-1}).

The lowest SO states for the Kramers Np^{IV} complex are a magnetically symmetrical KD1 with the three g-factors: 2.57, 2.69, 2.19 and a thermally populated low lying excited KD2 at 68 cm^{-1} with the g-factors: 0.04, 0.002, 3.90. Contributions from the ground LS manifold to these SO states are around 85-88 % and notably, the most important $J-J$ mixings are observed from the excited ^1G (10-11 %) for U^{IV}, ^2H (12-13 %) for Np^{IV} and (^3D

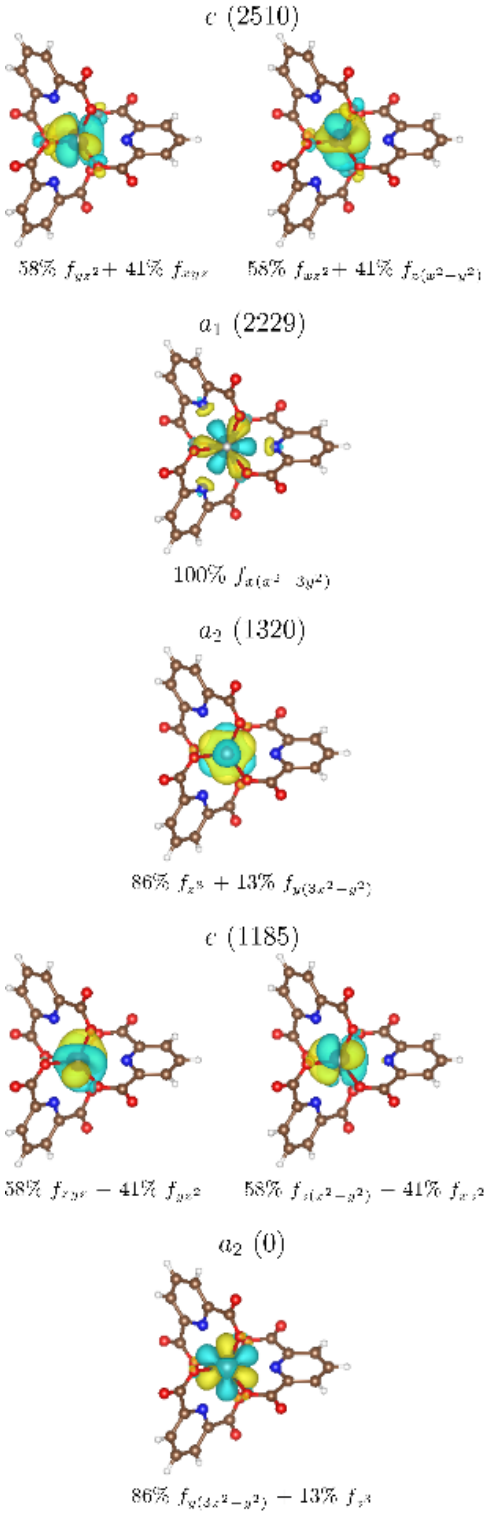

Figure 4.2.2: Canonical $5f$ active orbitals of the $[Np^{IV}(DPA)_3]^{2-}$ complex in D_3 symmetry. The canonical energies are given in parenthesis. The isosurface value is 0.14 $e^{-}bohr^{-3}$.

Table 4.1: SF and SO Energy levels (in cm^{-1}) of the symmetric $[An^{IV}(DPA)_3]^{2-}$ complexes from SF and SO-SSCASPT2 methods. Ground *J* manifolds are separated by horizontal lines.

U^{IV}		Np^{IV}		Pu^{IV}	
SF	SO	SF	SO	SF	SO
triplet		quartet		quintet	
0	0	0	0	0	0
30	163	60	0	661	4
307	169	79	68	708	399
365	171	918	68	905	407
513	246	991	488	1 427	450
620	269	1 004	488	1 452	669
1 138	827	1 448	921	1 609	1 069
1 192	832	2 018	921	2 407	1 070
2 143	1 327	2 023	1152	2 502	1 499
2 159	4 722	2 431	1152	2 533	4 589
2 560	4 730	2 783	6187	3 375	4 720
3 777	5 185	2 795	6187	3 405	4 724
3 788	5 188	3 204	6219	3 981	5 214
4 336	5 340	8 889	6219	9 972	5 219
4 436	6 311	9 004	6393	10 361	5 243
5 522	6 374	9 021	6393	10 707	5 249
5 525	6 476	9 953	6649	triplet	5 438
5 837	6 482	9 999	6649	13 900	5 455
singlet	6 773	doublet	6664	13 914	5 461
4 076	6 788	9 385	6664	13 935	5 516
4 117	6 968	9 578	6784	14 100	8 994
4 484	6 973	9 578	6784	14 110	9 216
4 690	7 335	9 598	11185	14 143	9 219
4 798	7 339	9 606	11185	14 226	9 468
4 871	7 480	9 848	11201	14 237	9 540
6 470	9 383	10 144	11201	14 434	9 540
6 548	9 400	10 146	11301	14 436	9 597
6 573	9 473	10 320	11301	14 437	9 658
11 182	9 539	10 417	11653	14 576	9 663
11 334	9 664	10 418	11653	singlet	9 673
12 877	9 846	12 805		21 313	
				21 326	
				21 360	
				21 681	

(9-10 %) for Pu^{IV} manifolds. As the splittings of the ground J manifolds of these An^{IV} complexes are larger than the room temperature energy, the thermal population in the low lying SO states will change with temperature giving rise to a complex T dependency of the magnetic properties.

The CFPs in the symmetric $[An^{IV}(DPA)_3]^{2-}$ complexes are deduced using ITO method and compared to the XRD results (see Table 4.2). According to the trigonal symmetry, six CFPs, $B_0^2, B_0^4, B_0^6, \bar{B}_3^4, \bar{B}_3^6, \bar{B}_6^6$ dominate and they are in the same range in both D_3 and XR structures of the U^{IV} and Np^{IV} complexes, but larger in the D_3 structure of Pu^{IV} complex. The total strength parameter S (Eq. 5.3.7) effectively includes all the CFPs and compares the strength of the metal-ligand interactions in the isostructural series. It is slightly reduced in the D_3 structure than the XR of the U^{IV} and Np^{IV} complexes, but increases in the D_3 Pu^{IV} complex. The overall ligand field strength is highly reduced in the Pu^{IV} complex as observed from a sharp decrease in the magnitude of S. The second order axial CFP B_0^2 (or $A_2^0 \langle r^2 \rangle$ in Stevens notation) as used in Bleaney's theory for axially symmetric Ln^{III} complexes (see Eq. 2.6.34) is dominant in the Pu^{IV} complex, but the fourth and sixth orders are larger in the U^{IV} and Np^{IV} complexes limiting the interpretations of the pNMR shifts according to Bleaney's model. The dominance of the 4th and 6th orders CFPs are an indication of the larger covalency in the former two complexes, whereas $J-J$ mixing and a decrease of covalency in the Pu^{IV} complex result in the overall decrease of the ligand field strength, and hence the decrease of the 4th and 6th orders CFPs.

Table 4.2: CFPs (in cm^{-1}) in the D_3 and XR structures of the $[An^{IV}(DPA)_3]^{2-}$ complexes. The z axis is the pseudo C_3 axis.

	U^{IV}		Np^{IV}		Pu^{IV}	
	D_3	XR	D_3	XR	D_3	XR
B_0^2	607	552	783	253	2174	654
B_0^4	-1021	-1353	-1548	-1787	-328	-359
$\bar{B}_3^4$	2980	3192	2066	2052	371	194
B_0^6	-836	-886	-1066	-1121	-161	-167
$\bar{B}_3^6$	1116	1126	1857	2004	134	94
$\bar{B}_6^6$	1307	1446	2268	2316	174	99
S	944	1026	957	983	576	311
S^2	271	271	350	158	972	490
S^4	1445	1563	1102	1148	206	206
S^6	714	763	1187	1248	97	92
S_0	493	570	690	682	979	319
S_3	1471	512	1216	889	182	68
S_6	512	568	889	908	68	39

4.2.2 Evans and *ab initio* magnetic susceptibilities

For the $[An^{IV}(DPA)_3]^{2-}$ complexes, the isotropic magnetic susceptibilities χ_m^{Evans} as deduced by Evans method in $[D_7]$DMF solution are given in Table 4.3. According to Eq. 2.6.28, the dipolar contribution to the AIS arises from the anisotropy of the magnetic susceptibility tensor. The determination of the experimental $\boldsymbol{\chi}$ tensor is possible within an axial symmetry by combining the χ_m determined by the Evans method with the $\Delta\chi_{ax}$ deduced from pNMR chemical shifts [11].

Table 4.3: Principal components of the magnetic susceptibility tensor (in 10^{-8} m^3mol^{-1}) at 298 K from SO-SSCASPT2 calculations for the $[An^{IV}(DPA)_3]^{2-}$ complexes and from SO-CASSCF for the $[Ln^{III}(DPA)_3]^{2-}$ complexes (all complexes are in D_3 structures). Spin-only magnetic susceptibilities are denoted by superscript S. Experimental molar magnetic susceptibilities χ_m^{Evans} (in 10^{-8} m^3mol^{-1}) are given for comparison.

	χ_m^{Evans}	$\chi_\perp^{Cal}$	$\chi_\parallel^{Cal}$	$\Delta\chi_{ax}^{Cal}$	χ_m^{Cal}	$\chi_\perp^{S,Cal}$	$\chi_\parallel^{S,Cal}$	$\Delta\chi_{ax}^{S,Cal}$	$\chi_m^{S,Cal}$
U^{IV}	5.1 (±0.1)	5.15	6.03	0.88	5.44	-1.19	-1.33	-0.15	-1.24
Np^{IV}	5.0 (±0.3)	4.48	5.70	1.22	4.88	-1.60	-2.03	-0.43	-1.75
Pu^{IV}	1.8 (±0.2)	2.30	2.09	-0.21	2.23	-1.36	-1.73	-0.37	-1.48
Nd^{III}		6.33	6.85	0.52	6.50	-2.13	-2.34	-0.21	-2.20
Ho^{III}		56.49	60.47	3.98	57.82	11.15	11.92	0.76	11.41
Yb^{III}		11.57	8.78	-2.79	10.64	1.46	1.11	-0.34	1.34

The magnetic susceptibility tensors $\boldsymbol{\chi}$ calculated for the D_3 $[An^{IV}(DPA)_3]^{2-}$ complexes with SO-SSCASPT2 method are given in Table 4.3 and compared to the experimental χ_m^{Evans} values. Due the axial symmetry, $\boldsymbol{\chi}$ reduces to its $\chi_\perp$ and $\chi_\parallel$ components. Results for the structure $An^{IV}(DPA)_3(C_3H_5N_2)\cdot 3H_2O$ issued from the crystallographic data are given in Table 4.4 for the sake of comparison. The χ_m^{Cal} values differ slightly between the two structures while in the XR structures, the magnetic anisotropy axes are highly deviated from the pseudo C_3 axis, as already mentioned due to breaking of degenerate $5f$ orbitals. The $\boldsymbol{\chi}$ tensors deduced from the XR structures are not axial, as one can notice from the angles θ (in Table 4.4) standing for the deviations of the main principal axes w.r.t. the z axis. The main principal axes of the magnetic susceptibility tensors of the U^{IV} complexes are shown in Fig. 4.2.3; shifting of the anisotropy axis form the pseudo C_3 axis (z axis) results chemically equivalent nuclei as magnetically non-equivalent and giving rise to different pseudocontact shifts.

The isotropic magnetic susceptibilities χ_m^{Cal} calculated with SO-SSCASPT2 at 298 K are in rather good agreement with the experimental values, χ_m^{Evans}. The small anisotropies of the $\boldsymbol{\chi}$ tensors are due to the spherical coordination sphere.

Table 4.4: Principal components (χ_1, χ_2, χ_3) of the magnetic susceptibility tensors $\boldsymbol{\chi}$ (10^{-8} m^3mol^{-1}) at 298 K from SO-SSCASPT2 calculations for the $[An^{IV}(DPA)_3]^{2-}$ complexes in the XR structures.

	χ_1^{Cal}	χ_2^{Cal}	χ_3^{cal}	χ_m^{Cal}	angle $\theta°$ $\left(\overrightarrow{\chi_3} \vee \overrightarrow{C_3}\right)$
U^{IV}	4.73	4.86	6.52	5.37	43
Np^{IV}	4.39	4.62	5.32	4.78	18
Pu^{IV}	2.40	2.00	1.92	2.11	47

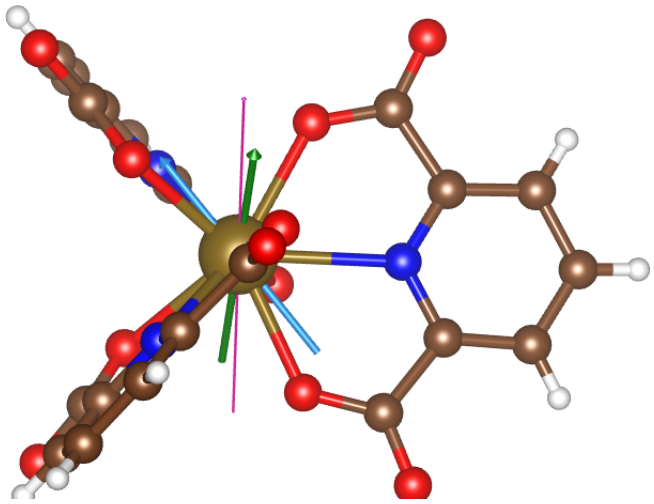

Figure 4.2.3: Main principal axes of $\boldsymbol{\chi}$ tensors of the $[U^{IV}(DPA)_3]^{2-}$ complexes. The light-blue arrow represents the anisotropic susceptibility axis for the complex in XR structure and the green arrow in D_3. The pseudo C_3 axis is shown in purple color.

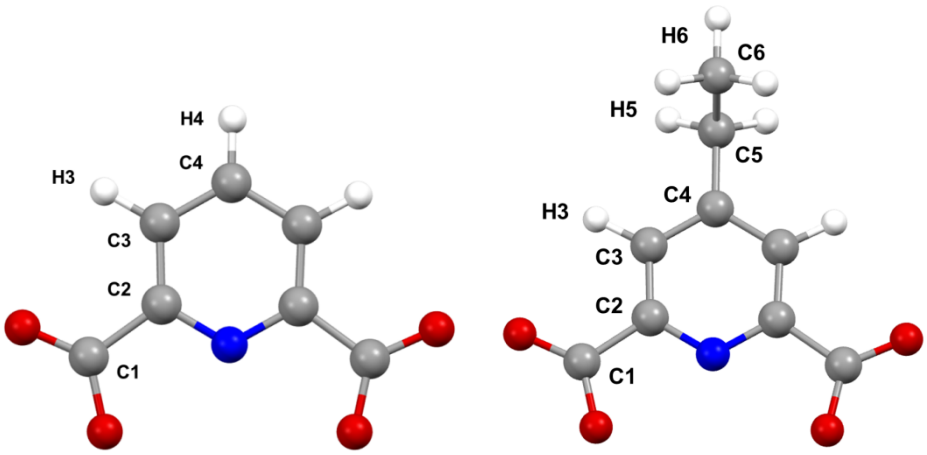

Figure 4.2.4: DPA^{2-} (left) and $Et{-}DPA^{2-}$ (right) ligands with the numbering of the ^{1}H and ^{13}C nuclei.

4.2.3 Analysis of ^{1}H and ^{13}C pNMR shifts

Both $[An^{IV}(DPA)_3]^{2-}$ and $[An^{IV}(Et{-}DPA)_3]^{2-}$ complexes were studied by NMR spectroscopy as the later provides supplementary ^{1}H and ^{13}C nuclei further from the paramagnetic center. ^{1}H NMR spectra in the An^{IV} complexes were recorded in $[D_7]$DMF at 298 K. Fig. 4.2.5 shows the ^{1}H spectra in $[An^{IV}(Et{-}DPA)_3]^{2-}$ complexes as example. The paramagnetic contributions to the chemical shifts were deduced by using $[Th^{IV}(DPA)_3]^{2-}$ and $[Th^{IV}(Et{-}DPA)_3]^{2-}$ as diamagnetic references. Chemical shifts obtained at room temperature are reported in Table 4.5. The labeling of the atoms on the DPA and Et-DPA ligands are shown in Fig. 4.2.4.

In the case of an axial symmetry, Eq. 2.6.28 simplifies to Eq. 2.6.33 with the vanishing of the rhombic component of the magnetic susceptibility tensor. In the solid compounds, the complex is not strictly axial, due the presence of the counterions. This leads to a reorientation of the $\boldsymbol{\chi}$ tensor determined from SO-CASPT2 calculation (as shown in Fig. 4.2.3), and to an important splitting of the ^{1}H and ^{13}C signals corresponding to the different non-equivalent positions in the crystal structures. One expects the complex to be symmetrical in solution. The symmetric structure leads to an axial $\boldsymbol{\chi}$ tensor and a unique ^{1}H and ^{13}C geometrical factor for each chemically equivalent atom, as reported in Table 4.6. Averaged values of G_K parameters were considered for the CH_2 ($H5$) and CH_3 (H6) groups of the ethyl chains within $[An^{IV}(Et{-}DPA)_3]^{2-}$ complexes. Furthermore, different positions of the ethyl groups were considered in order to represent the free rotation of an ethyl group. The ethyl groups do not affect the electronic structure and magnetic properties of the central actinide center.

In the case of no Fermi contact contributions, the ratio between the paramagnetic chemical shifts of two nuclei K and K' simplifies to the ratio of the geometrical factors as shown

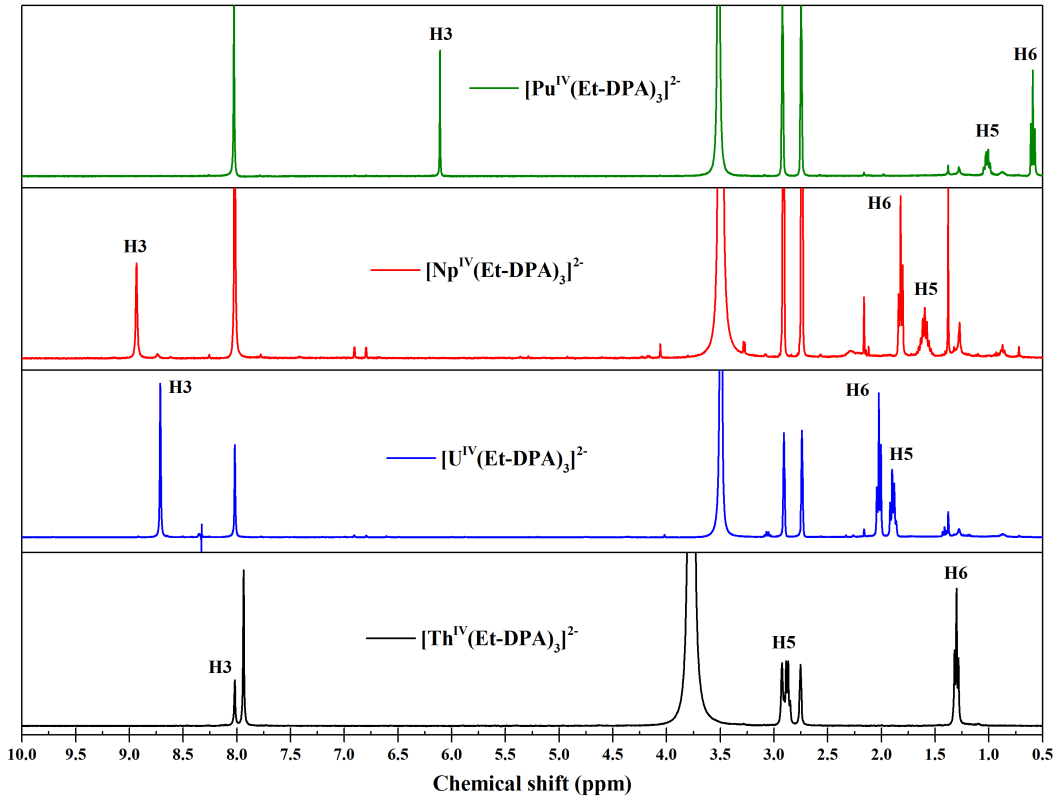

Figure 4.2.5: ^{1}H NMR spectra of $[An^{IV}(Et{-}DPA)_3]^{2-}$ complexes in $[D_7]$DMF solution at 9.4 T and 298 K.

Table 4.5: Chemical shifts δ_K (in ppm) and paramagnetic chemical shifts δ_K^p (in ppm) of ^{1}H and ^{13}C nuclei in $[An^{IV}(Et{-}DPA)_3]^{2-}$ complexes in $[D_7]$DMF solution at 9.4 T and 298 K.

		*C*1	*C*2	*C*3	*C*4	*C*5	*C*6	*H*3	*H*4	*H*5	*H*6
Th^{IV}	δ_K	171.5	151.6	125.0	159.2	28.4	28.4	8.29/7.95[a]	8.11	2.89	1.31
U^{IV}	δ_K	113.3	147.3	153.5	155.6	35.3	35.3	8.66/8.72	12.94	1.90	2.04
	δ_K^p	-58.2	-4.3	28.6	-3.6	7.0	-5.0	0.37/0.77	4.83	-0.99	0.73
Np^{IV}	δ_K	97.5	156.9	160.9	152.0	34.5	8.7	9.11/8.94	11.97	1.61	1.83
	δ_K^p	-74.1	5.3	35.9	-7.2	6.2	-5.1	0.82/0.99	3.86	-1.28	0.52
Pu^{IV}	δ_K	144.6	150.1	139.4	151.1	34.3	10.4	6.28/6.11	8.11	1.01	0.59
	δ_K^p	-27.0	-1.5	14.4	-8.1	5.9	-3.4	-2.01/-1.84	0.00	-1.88	-0.72

[a]:$[An^{IV}(DPA)_3]^{2-}/[An^{IV}(Et{-}DPA)_3]^{2-}$

Table 4.6: Geometric factors G_K (in 10^{-3} Å^{-3}) and pseudocontact contributions δ_K^{pc} (in ppm) to the ^{1}H and ^{13}C AIS in the $[An^{IV}(DPA)_3]^{2-}$ and $[An^{IV}(Et{-}DPA)_3]^{2-}$ complexes deduced with D_3 structures using SO-SSCASPT2 magnetic susceptibility tensors.

		*C*1	*C*2	*C*3	*C*4	*C*5	*C*6	*H*3	*H*4	*H*5	*H*6
U^{IV}	G_K	-1.7	-19.8	-8.2	-6.7	-3.1	-2.2	-4.6	-5.6(1)	-2.4(3)	-2.2(9)
	δ_K^{pc}	0.7	7.7	3.2	2.6	1.2	0.8	1.8	2.2	0.9	0.9
Np^{IV}	G_K	-1.4	-20.2	-8.4	-6.9	-3.2	-2.3	-4.6	-5.6(2)	-2.5(4)	-2.3(8)
	δ_K^{pc}	0.7	10.9	4.5	3.7	1.7	1.2	2.5	3.0	1.3	1.3
Pu^{IV}	G_K	-1.3	-20.4	-8.4	-6.9	-3.2	-2.2	-4.6	-5.4(1)	-2.5(3)	-2.2(7)
	δ_K^{pc}	-0.1	-1.9	-0.8	-0.6	-0.3	-0.2	-0.4	-0.5	-0.2	-0.2

in Eq. 3.3.2. $R_{K,K'}$ calculated from the geometric factors (in the XR structures) and from the AIS of the ^{1}H nuclei in the $[An^{IV}(Et{-}DPA)_3]^{2-}$ complexes are tabulated in Table 4.7. The strong deviations between $R_{K,K'}$ values calculated from XR structures and experimental ^{1}H pNMR chemical shifts can not be explained by some structural variations between solid-state (XR) and solution (D_3), but only by the presence of a non-negligible Fermi contact term. The results clearly show that such a simplification can not be done in the case of the An^{IV} complexes as previously highlighted for some Ln^{III} cations in $[Ln^{III}(Et{-}DPA)_3]^{3-}$ complexes or for $[An^{III}(Et{-}DPA)_3]^{3-}$ complexes (see Table 4.7, data are taken from Ref. [26]). This behavior has been already observed for the light Ln^{III} cations particularly with Nd^{III} and Eu^{III} cations while a very good agreement was observed for the second part of the Ln^{III} series (Ln^{III} = Tb^{III} - Yb^{III}) (see Ref. [26]). This can be attributed to the weakness of the magnetic anisotropy $\Delta\chi_{ax}$ associated to the compactness of the coordination sphere of the complexes, close to a spherical structure. This leads to small dipolar contributions to the pNMR chemical shifts, according to Eq. 2.6.33.

The ^{13}C NMR and pNMR shifts in the $[An^{IV}(Et{-}DPA)_3]^{2-}$ complexes were recorded in [D_7]DMF at 298 K and are also reported in Table 4.5. As for ^{1}H nuclei, δ_K^{pc} are estimated from Eq. 2.6.33 using the $\boldsymbol{\chi}$ tensor deduced from SO-SSCASPT2 results and the Fermi contact shifts are calculated as $\delta_K^c = \delta_K^p - \delta_K^{pc}$. A systematic derivation of axial pseudocontact shift formula (Eq. 2.6.33) from the general Soncini and van den Heuvel equation (Eq. 2.2.3 and as derived in subsection 2.6.3) shows a positive sign before the equation. So if the geometric factors G_K are negative, a positive $\Delta\chi_{ax}$ will lead to negative pseudocontact shifts and vice versa. But it has been observed that using Eq. 2.6.33 leads to systematic opposite signs of the dipolar contribution as compared to the sign of the AIS, specially on the distant H atoms and consequently leading to systematic large contact contributions.

Table 4.7: $R_{K,K'}$ (according to Eq. 3.3.2) from the geometrical factors and the AIS for the ^{1}H nuclei in the $[An^{IV}(DPA)_3]^{2-}$ and $[Ln^{III}(DPA)_3]^{3-}$ complexes at 9.4 T and 298 K. D_3 structures are considered for the geometric parameters.

	$\frac{G_{H3}}{G_{H4}}$	$\frac{\delta^p_{H3}}{\delta^p_{H4}}$	$\frac{G_{H3}}{G_{H6}}$	$\frac{\delta^p_{H3}}{\delta^p_{H6}}$	$\frac{G_{H5}}{G_{H6}}$	$\frac{\delta^p_{H5}}{\delta^p_{H6}}$
U^{IV}	0.82 ± 0.01	0.08	2.25 ± 0.9	1.05	1.20 ± 0.6	-1.36
Np^{IV}	0.82 ± 0.01	0.21	2.17 ±0.6	1.90	1.18 ± 0.6	-2.46
Pu^{IV}	0.86 ± 0.01	∞	2.29 ±0.8	2.56	1.25 ± 0.7	2.61
Nd^{III}[a]	/	/	2.28 ± 0.01	3.8	1.28 ± 0.01	-0.1
Eu^{III}[a]	/	/	=	4.1	=	0.1
Tb^{III}-Yb^{III}[a]	/	/	=	2.2 ± 0.2	=	1.4 ± 0.2
Am^{III}[a]	/	/	=	-5.2	=	-13.3

[a]: Ref. [26]

The possibility that the *ab initio* $\Delta\chi_{ax}$ are themselves wrong is not ignored and only can be justified if we have experimental evaluation of the $\Delta\chi_{ax}$. However to be confident with the SO-SSCASPT2 results and to check the sign before Eq. 2.6.33, we considered the two late Ln^{III} complexes $[Ho^{III}(Et{-}DPA)_3]^{2-}$ and $[Yb^{III}(Et{-}DPA)_3]^{2-}$. The LIS are expected to be essentially dipolar in nature [22] and opposite in sign as one can expect from the magnetization trend in the lanthanide +3 series which alters almost in every quarter following the alteration of sign of $\langle J\|\alpha\|J\rangle$ in Bleaney's Equation (Eq. 2.6.34). $\langle J\|\alpha\|J\rangle$ '-ve' for Ho^{III} and '+ve' for Yb^{III}. $\Delta\chi_{ax}$ are calculated for these complexes and the dipolar shifts are collected in Table 4.8 along with the geometric factors and the total LIS of the ligands' nuclei. From Table 4.8, we can notice that indeed, the LIS of the distant protons alternate in sign from Ho^{III} to Yb^{III} as expected from the alteration of the nature of magnetization. *Ab initio* $\Delta\chi_{ax}$ also changes sign going from prolate to oblate (see Table 4.3) from Ho^{III} to Yb^{III}. Calculated ^{1}H dipolar shifts according to Eq. 2.6.33 with the *ab initio* $\Delta\chi_{ax}$ are not close to the experimental pNMR shifts which introduce large contact contributions (see δ^c_K from Table 4.8). But the ratios of the geometric factors and the experimental pNMR shifts do not show a large disagreement [26] and also do not validate the presence of large contact contributions as also shown by Desreux and Reilley in the $[Yb^{III}(DPA)_3]^{2-}$ complex [22]. These benchmark studies show that $\Delta\chi_{ax}$ evaluated using CAS based methods for the lanthanide and actinide complexes with dipicolinic acid derivatives have systematically opposite sign compared to the experimental ones obtained from the pNMR shifts study [26]. In the case of lanthanides, as one expects the LIS to be dominated by dipolar mechanism and also confirmed by previous studies [22], a systematic opposite $\Delta\chi_{ax}$ from *ab initio* calculations leads to large contact shifts for the distant protons. In the actinide complexes, the geometric ratios in Table 4.7 indicate the presence of significant amount of contact contribution to the ^{1}H AIS, and although the

ab initio $\Delta\chi_{ax}$ are suspicious, but their magnitudes are very small. So one can conclude that the AIS are clearly dominated by contact contributions, especially the ^{13}C AIS. So we did not rely on the *ab initio* $\Delta\chi_{ax}$ to separate the contact and pseudocontact shifts in the actinide dipicolinic acid complexes, rather from the temperature dependent AIS, we are able to separate the two contributions and presented in Table 4.9 (the temperature dependent fittings are discussed in next section).

Table 4.8: LIS (in ppm) of the ligands' nuclei and their geometric factors (in 10^{-3} Å^{-3}) in the $[Ho^{III}(Et{-}DPA)_3]^{2-}$ and $[Yb^{III}(Et{-}DPA)_3]^{2-}$ complexes. Pseudocontact shifts δ_K^{pc} (in ppm) are calculated from the *ab initio* $\Delta\chi_{ax}$ using Eq. 2.6.33 and the contact shifts are, $\delta_K^c = \delta_K^p - \delta_K^{pc}$.

		*C*1	*C*2	*C*3	*C*4	*C*5	*C*6	*H*3	*H*5	*H*6
Ho^{III}	δ_K^p	-16.8	46.6	-42.0	45.8	2.8	9.7	11.18	8.22	5.36
	G_K	-0.3	-20.3	-8.4	-6.9	-3.2	-2.3	-4.6	-2.6(4)	-2.3(9)
	δ_K^{pc}	-0.5	-35.6	-14.7	-12.1	-5.6	-4.0	-7.99	-4.5(6)	-4.06
	δ_K^c	-16.3	82.2	-27.4	58.0	8.4	13.6	19.2	12.7(5)	9.4(9)
Yb^{III}	δ_K^p	-16.0	-28.7	-15.1	-5.0	7.0	-5.0	-4.27	-0.99	-0.73
	G_K	-0.1	-20.8	-8.5	-7.0	-3.1	-2.1	-4.6	-2.5(6)	-2.3(8)
	δ_K^{pc}	0.1	25.5	10.5	8.6	3.8	2.7	5.67	3.0(5)	2.8(9)
	δ_K^{c+}	-16.1	-54.2	-25.6	-13.6	3.2	-7.7	-10.39	-4.0(4)	-3.5(9)

In these An^{IV} complexes, low magnetic anisotropy due to the spherical coordination sphere leads to Fermi contact shifts as main contribution for most of the ^{13}C nuclei as presented Table 4.9. As an exception, the Fermi contact contribution obtained for *C*2 nuclei being strong in U^{IV} complex drastically decrease across the series to be negligible for Pu^{IV}. The pseudocontact contribution appears not to be the dominant one, except for *C*2 and the protons, where the contact contribution is rather small.

The Fermi HFC constant A_K^c depends on the spin density $\rho^s(\boldsymbol{r}_K)$ at nucleus K according to Eq. 1.8.11 and in the non-relativistic theory taking z as the quantization axis, spin density at K can be calculated as the difference between the alpha and beta spin densities $\rho^s(\boldsymbol{r}_K) = \rho^\alpha(\boldsymbol{r}_K) - \rho^\beta(\boldsymbol{r}_K)$. $\rho^s(\boldsymbol{r}_K)$ results from the combination of two mechanisms, the spin delocalization and spin polarization. The first mechanism leads to positive spin density throughout the molecule; it is more important for the nuclei directly bonded to the paramagnetic cation and is expected to drop quickly when the number of bonds between the paramagnetic center and the observed nuclei increases. Conversely, the second mechanism propagates the spin density away from the paramagnetic center by alternating sign. Eq. 2.6.49 allows an evaluation of the HFC constants A_K^c, using the values of the spin-only magnetic susceptibility $\chi_m^{S,Cal}$ calculated using SO-SSCASPT2 method (see

Table 4.9: Pseudocontact and contact contributions to the ^{13}C and ^{1}H AIS (in ppm) in $[An^{IV}(DPA)_3]^{2-}$ and $[An^{IV}(Et{-}DPA)_3]^{2-}$ complexes in $[D_7]$DMF solution at 9.4 T and 298 K. From the temperature dependence study of AIS according to Eq. 4.2.4, $\delta_K^{pc,Exp}$ is estimated and the contact shifts $\delta_K^{c,Exp} = \delta_K^p - \delta_K^{pc,Exp}$.

		$C1$	$C2$	$C3$	$C4$	$C5$	$C6$	$H3$	$H4$	$H5$	$H6$
U^{IV}	δ_K^p	-58.2	-4.3	28.6	-3.6	7.0	-5.0	0.4/0.8[a]	4.83	-0.99	0.73
	$\delta_K^{pc,Exp}$	0.45	5.18	2.18	1.76	0.82	0.58	1.19		0.66	0.52
	$\delta_K^{c,Exp}$	-58.59	-9.5	26.42	-5.39	6.17	-5.61	-0.42		-1.65	0.2
Np^{IV}	δ_K^p	-74.1	5.3	35.9	-7.2	6.2	-5.1	0.82/0.99	3.86	-1.28	0.52
	$\delta_K^{pc,Exp}$	0.48	7.07	2.93	2.45	1.14	0.8	1.65		0.91	0.71
	$\delta_K^{c,Exp}$	-74.7	-1.75	32.97	-9.74	5.11	-5.92	-0.64		-2.19	-0.19
Pu^{IV}	δ_K^p	-26.96	-1.50	14.10	-8.06	5.94	-3.36	-2.01/-1.84	0.0	-1.88	-0.72
	$\delta_K^{pc,Exp}$	-0.27	-4.02	-1.67	-1.4	-0.65	-0.46	-0.94		-0.52	-0.41
	$\delta_K^{c,Exp}$	-26.67	2.53	15.87	-6.71	6.59	-2.93	-0.9		-1.36	-0.31

[a]:$[An^{IV}(DPA)_3]^{2-}$/$[An^{IV}(Et{-}DPA)_3]^{2-}$

Table 4.3) and are presented in Table 4.10. For ^{13}C nuclei located on the pyridine unit in $[An^{IV}(DPA)_3]^{2-}$ complexes, the alternation of positive and negative A_K^c values indicates that spin polarization mechanism dominates. The same observation can be made for $[Ln^{III}(Et{-}DPA)_3]^{3-}$ and $[Am^{III}(Et{-}DPA)_3]^{3-}$ complexes. For the ^{13}C nuclei of the COO^- units ($C1$), the A_K^c values are the largest and positive which is the sign of a spin delocalization for these nuclei close from the paramagnetic center.

Table 4.10: Fermi HFC constants A_K^c (in MHz) deduced from the contact shifts in Table 4.9 according to Eq. 2.6.49.

	$C1$	$C2$	$C3$	$C4$	$C5$	$C6$	$H3$	$H4$	$H5$	$H6$
U^{IV}	0.72	0.15	-0.31	0.08	-0.07	0.07	0.07/0.05[a]	-0.13	0.09	0.01
Np^{IV}	0.65	0.05	-0.27	0.09	-0.04	0.05	0.06/0.05	-0.03	0.09	0.03
Pu^{IV}	0.27	0.00	-0.15	0.08	-0.06	0.03	0.06/0.06	-0.02	0.07	0.02
Nd^{III}	0.01	0.00	-0.13	0.04	-0.04	0.03	-0.01	/	0.02	0.004
Eu^{III}	-0.01	-0.02	-0.12	0.04	0.02	-0.01	-0.02	/	0.01	-0.002
Am^{III}	0.079	0.031	-0.056	0.048	-0.010	0.012	0.011	/	0.016	0.002
Yb^{III}	-0.18	-0.04	-0.05	0.04	0.12	-0.03	0.04	/	0.09	0.09

[a]:$[An^{IV}(DPA)_3]^{2-}$/$[An^{IV}(Et{-}DPA)_3]^{2-}$

- Spin density calculations.

^{13}C pNMR shifts are mostly dominated by the contact contributions and are direct consequences of the presence of spin densities at the nuclei, so we try to rationalize the spin population in the ligands. Unrestricted SR-DFT was successful to interpret HFC constants in the isotropic $4f^7$ $Gd^{III}-H_2O$ complexes [81] as well as ^1H pNMR shifts in isostructural series [82]. Following this line, we performed Mulliken spin population analysis using unrestricted SR-DFT with a fractional occupation of the seven $5f$ orbitals of the $[An^{IV}(DPA/Et-DPA)_3]^{2-}$ complexes. Spin polarization is well described by an unrestricted calculation by allowing the spatial parts of the alpha and beta orbitals to be different. For the sake of comparison, evaluation of the spin population from a CASSCF calculation only accounts the spin delocalization. The fractional occupancy in the $5f$ orbitals in DFT resembles the average of configurations (see Table 4.11) like the CASSCF wave functions and allows for an equivalent population of all the magnetic orbitals. The Mulliken atomic spin populations calculated with the CASSCF and unrestricted DFT methods are presented in Fig. 4.2.6 and broken down in the atomic σ and π orbitals for PBE0 calculations (Table 4.13).

Table 4.11: Mulliken spin populations in the $5f$ orbitals of the $[Np^{IV}(DPA)_3]^{2-}$ complex from SO-CASSCF. This population is estimated as an average over the SF components issued from the ground ^4I manifold according to their weight in the SO wave function.

	KD1	KD2
$5f_{\pm3}$	0.76	0.75
$5f_{\pm2}$	0.70	0.68
$5f_{\pm1}$	0.63	0.66
$5f_0$	0.39	0.40

In Fig. 4.2.6 and Fig. 4.2.7, the atomic and *s* orbitals' spin populations per unpaired electron of the $[An^{IV}(Et-DPA)_3]^{2-}$ complexes from different methods are presented, respectively and to see the pattern in the series, the same is also done keeping the method fixed (furthermore in Fig. 4.2.8). The CASSCF spin populations are the highest for the bonding oxygen ($O1$) and nitrogen atoms and become rapidly negligible after few bonds from the paramagnetic center as expected from a spin delocalization mechanism. Calculated spin populations using unrestricted DFT are much higher which shows that spin polarization mechanism dominates the spin distribution onto the ligands even for the closest nuclei as previously reported for $Gd^{III}-H_2O$ complexes.

The experimental ^{13}C HFC constants A_K^c from Table 4.10 are used to calculate the spin densities at the nucleus $\rho^s(\boldsymbol{r}_K)$ according to Eq. 1.8.11 and are compared with those obtained from different functionals in Table 4.12. The M062X functional correctly predicts the alternation of spin in the C framework when compared with the experiment.

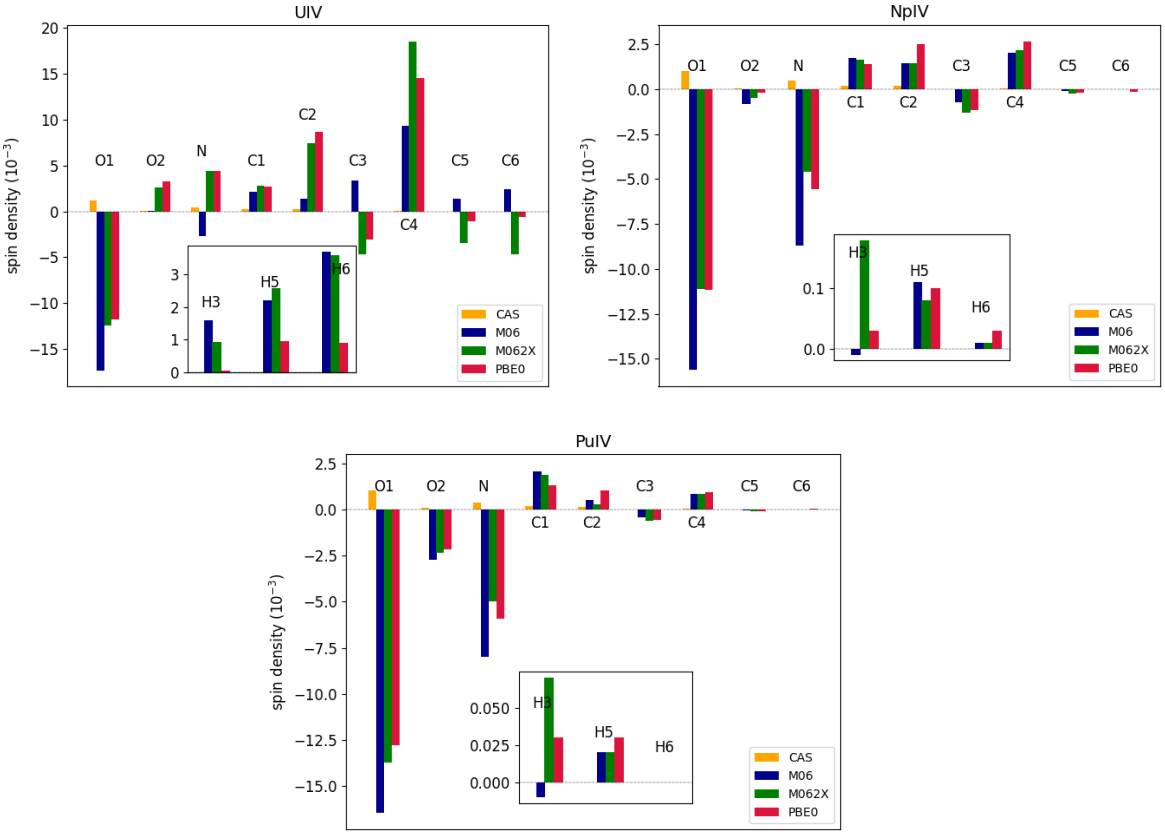

Figure 4.2.6: Mulliken atomic spin populations per unpaired electron of the $[An^{IV}(Et-DPA)_3]^{2-}$ complexes calculated with CASSCF and unrestricted DFT methods.

Table 4.12: $\rho^s(\boldsymbol{r}_K)/N$ evaluated according Eq. 1.8.11 from the A_K^c of Table 4.10 and Mulliken spin populations in the s orbitals' ρ_s^s/N of the $[An^{IV}(Et-DPA)_3]^{2-}$ complexes from different functional.

			$C1$	$C2$	$C3$	$C4$	$C5$	$C6$
U^{IV}	$\rho^s(\boldsymbol{r}_K)/N$	exp	4.3	0.88	-1.86	0.45	-0.42	0.43
	ρ_s^s/N	M06	-0.26	-0.29	-1.14	-0.25	-0.66	-3.4
		M062X	0.18	1.8	-2.57	6.33	-1.74	-3.48
		PBE0	-0.35	0.4	-0.65	1.2	-0.6	-0.35
Np^{IV}	$\rho^s(\boldsymbol{r}_K)/N$	exp	3.87	0.29	-1.62	0.56	-0.23	0.33
	ρ_s^s/N	M06	-0.04	-0.4	0.26	-0.11	-0.01	0
		M062X	0.29	0.44	-0.52	0.76	-0.08	0.01
		PBE0	-0.13	0.17	-0.1	0.2	-0.1	-0.13
Pu^{IV}	$\rho^s(\boldsymbol{r}_K)/N$	exp	2.18	-0.03	-1.23	0.61	-0.5	0.26
	ρ_s^s/N	M06	0.22	-0.18	0.1	-0.04	0	0
		M062X	0.43	0.14	-0.19	0.29	-0.03	0
		PBE0	-0.03	0.08	-0.05	0.05	-0.05	-0.03

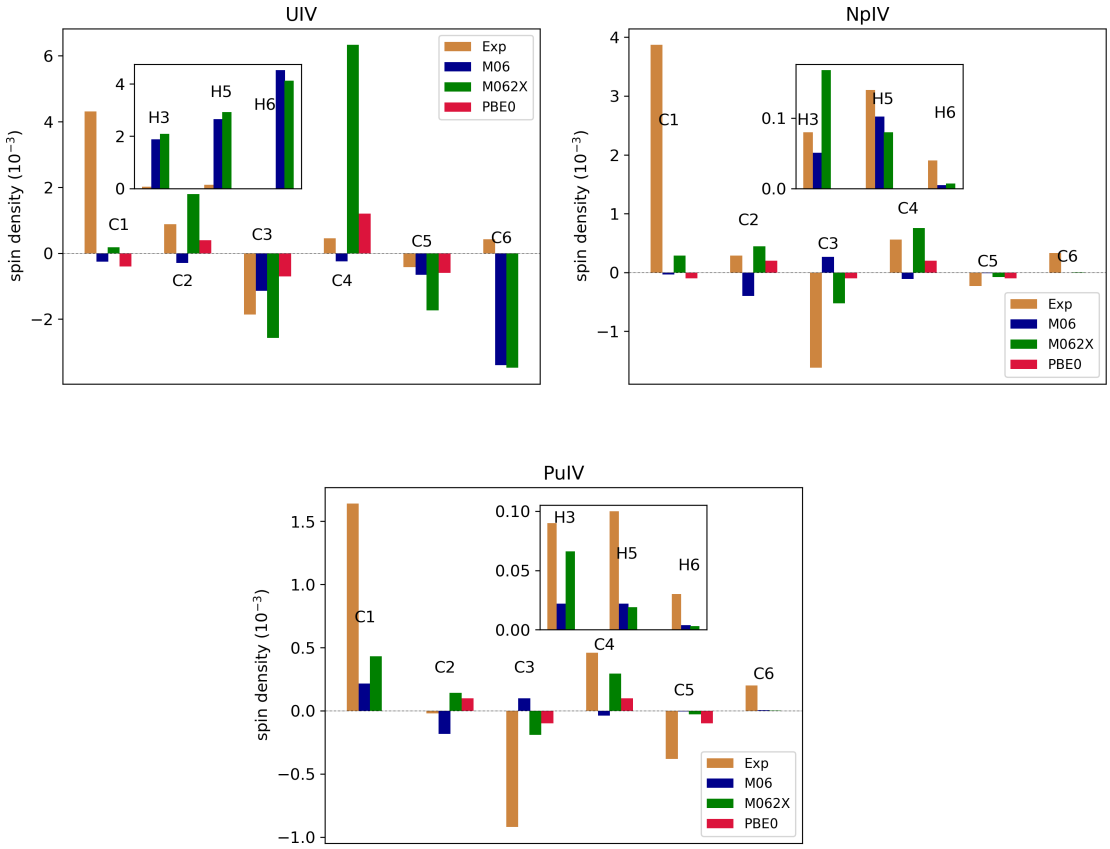

Figure 4.2.7: Mulliken atomic *s* orbitals' spin populations per unpaired electron of the $[An^{IV}(Et{-}DPA)_3]^{2-}$ complexes calculated with CASSCF and unrestricted DFT methods.

Table 4.13: Mulliken atomic spin populations partitioned within σ and π components of the ligand deduced from UPBE0 for the $[An^{IV}(DPA/Et{-}DPA)_3]^{2-}$ complexes.

		*O*1	*C*1	*O*2	*N*	*C*2	*C*3	*C*4	*C*5
U^{IV}	σ	-0.02	-0.0007	-0.0012	-0.0082	0.001	-0.0027	0.0045	-0.0032
	π	-0.0101	0.0071	0.0101	0.0265	0.0191	-0.0061	0.0351	-0.0005
Np^{IV}	σ	-0.0241	0.0004	-0.003	-0.0166	0.001	-0.0012	0.0011	-0.0007
	π	-0.0106	0.0049	0.0031	-0.0013	0.0073	-0.0031	0.0082	-0.0002
Pu^{IV}	σ	-0.037	0.0015	-0.0056	-0.0056	0.0005	-0.001	0.0004	-0.0004
	π	-0.0138	0.0053	-0.0025	-0.0039	0.0041	-0.0017	0.0039	-0.0002

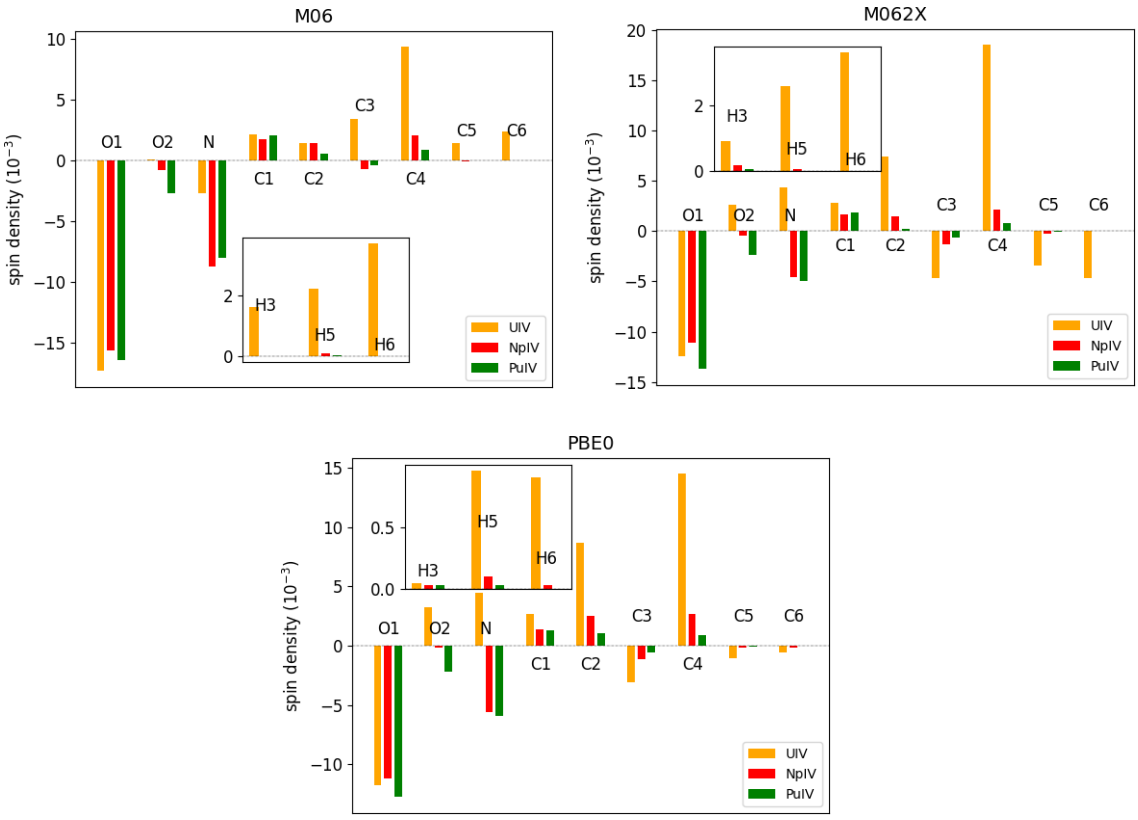

Figure 4.2.8: Mulliken atomic spin populations per unpaired electron of the $[An^{IV}(Et{-}DPA)_3]^{2-}$ complexes calculated with unrestricted DFT methods.

The PBE0 functional manages to reproduce the spin alteration in the pyridine unit, but assigns an opposite spin for the carboxylate carbon $(C1)$, whereas the M06 functional mostly gives the opposite to that obtained from M062X and also the experiment. When compared with the atomic spin populations, the spin populations in the s orbitals of the carbon atoms have the same sign as the atomic one for M062X, whereas the spin alters for $C1$ in the case of PBE0 and completely for all the C atoms in M06. About the relative magnitude, $\rho^s(\boldsymbol{r}_K)/N$-exp decreases along within the series going from U^{IV} to Pu^{IV} (see Table 4.12), as usually following the same trend of experimental hyperfine coupling constants A_K^c (see Table 4.10). The spin populations in the s-orbitals ρ_s^s/N deduced from the DFT calculations are in the order of $\rho^s(\boldsymbol{r}_K)/N$-exp, better matching with M062X with the correct evaluation of the sign. The very trend is also observed for the calculated ρ_s^s/N (see Fig. 4.2.8), they decrease along with the series following the same declines of atomic spin populations. The total atomic spin on the Np^{IV} and Pu^{IV} center from the DFT calculations are found to be greater than 3 and 4, respectively indicating a ligand to metal spin polarization. But, surprisingly, a spin deficient U^{IV} center (i.e. $\rho^s < 2$) is obtained from all the DFT calculations indicating more spin delocalization from metal to the ligand.

So it appears from the DFT calculations that the spin populations in the s orbitals of the carbon atoms roughly proportional to the total atomic spin, i.e. the largest the spin on

the atom, the largest on the nucleus, but that simple one-to-one correspondence cannot be drawn as far as the sign is considered. As described by Adamo et al. [83] for aromatic free radicals, large positive spin are obtained on the ortho ($C2$) and para ($C4$) carbons of the pyridine unit whereas the meta ($C3$) and ethyl ($C5$) have the opposite signs and reduced magnitudes. Surprisingly all the DFT calculations assign a very small amount of spin on the closest carboxylate carbon ($C1$), by far showing the most disagreement with the values obtained from the contact shifts. It is worth to mention here that atomic charges and spin of a molecule are not directly spectroscopic and depend on the methods of *ab initio* calculations. Often for the quantitative estimations, special basis sets are recommended [84, 85] which have larger exponents in the primitive s-type functions, but that kind of integration will lose the flavor of the atomic orbitals of the considered ANO basis sets. As already pointed out, the spin alteration indicates a dominant spin polarization mechanism over the spin delocalization further from the paramagnetic center.

4.2.4 Temperature dependence of the pNMR shifts

Like the An^{VI} complexes, ^1H and ^{13}C NMR spectra of $[An^{IV}(DPA)_3]^{2-}$ and $[An^{IV}(Et{-}DPA)_3]^{2-}$ complexes were recorded on the temperature range 263 – 333 K and corrected from the diamagnetic Th^{IV} reference. For Ln^{III} complexes, the separation of contact and pseudo-contact contributions can be performed by using their respective temperature variation. According to Bleaney's theory, the pseudocontact and contact shifts behave as functions of T^{-2} and T^{-1}, respectively [17, 19] which formally indicates that the contact shifts in Eq. 2.6.49 and the anisotropic magnetic susceptibility $\Delta\chi_{ax}$ of the lanthanide center in Eq. 2.6.33 can be written as

$$\delta_K^p = \frac{1}{\mu_0\mu_B g_e \gamma_K}\frac{A_K^c}{\hbar}\frac{s}{T} + \frac{1}{12\pi N_A}G_K\frac{c}{T^2} \tag{4.2.1}$$

$$= \frac{\alpha_K^c}{T} + \frac{\alpha_K^{pc}}{T^2} \tag{4.2.2}$$

where $\Delta\chi_{ax} = \frac{c}{T^2}$ and $\chi^s = \frac{s}{T}$ and c, s are metal dependent constants. Consequently, the linear regression of $\delta_K^p T = f(1/T)$ curves allows to evaluate the two contributions, the slope and the intercept leading to the pseudocontact and contact terms, respectively [20]. Though it has been pointed out that additional terms might be required to improve the quality of the fittings in the actinide complexes as they bear additional physics of the actinide chemistry such as larger ligand field splitting [26, 11]. But in any case, Bleaney's theory has been applied in this case also and the linear regression of the $\delta_K^p T = f(1/T)$ curves puts forward some anomaly such as one would expect that α_K^{pc} should be proportional to G_K as according to Eq. 4.2.2, $\alpha_K^{pc} = G_K\beta^{pc}$ where $\beta^{pc} = \frac{c}{12\pi N_A}$ is independent of the NMR active nucleus. However, from Tables 4.14 and 4.15, one can notice the ratio of two α_K^{pc} is not in agreement with the geometric ratio.

Table 4.14: Ratio of the geometrical parameters $R_{K,K'}$ and ratio of slopes of $\delta_K^p T = f(1/T)$ (according to Eq. 4.2.2) for ^{13}C AIS in $[An^{IV}(Et{-}DPA)_3]^{2-}$ complexes.

	$\frac{G_{C1}}{G_{C6}}$	$\frac{\alpha_{C1}^{pc}}{\alpha_{C6}^{pc}}$	$\frac{G_{C2}}{G_{C6}}$	$\frac{\alpha_{C2}^{pc}}{\alpha_{C6}^{pc}}$	$\frac{G_{C3}}{G_{C6}}$	$\frac{\alpha_{C3}^{pc}}{\alpha_{C6}^{pc}}$	$\frac{G_{C4}}{G_{C6}}$	$\frac{\alpha_{C4}^{pc}}{\alpha_{C6}^{pc}}$	$\frac{G_{C5}}{G_{C6}}$	$\frac{\alpha_{C5}^{pc}}{\alpha_{C6}^{pc}}$
U^{IV}	0.77	-97.76	8.95	8.28	3.71	2.04	3.04	21.29	1.41	0.88
Np^{IV}	0.6	-23.48	9	26.76	3.72	4.91	3.06	-6.55	1.42	12.14
Pu^{IV}	0.58	27.2	9.07	6.07	3.74	-68.62	3.06	-34.06	1.42	/

Table 4.15: Ratio of the geometrical parameters $R_{K,K'}$ and ratio of slopes of $\delta_K^p T = f(1/T)$ (according to Eq. 4.2.2) for ^{1}H AIS in $[An^{IV}(DPA/Et{-}DPA)_3]^{2-}$ complexes.

	$\frac{G_{H3}}{G_{H4}}$	$\frac{\alpha_{H3}^{pc}}{\alpha_{H4}^{pc}}$	$\frac{G_{H3}}{G_{H5}}$	$\frac{\alpha_{H3}^{pc}}{\alpha_{H5}^{pc}}$	$\frac{G_{H5}}{G_{H6}}$	$\frac{\alpha_{H5}^{pc}}{\alpha_{H6}^{pc}}$
U^{IV}	0.82	-6.7	2.25	2.8	1.20	3.3
Np^{IV}	0.82	2.3	2.17	2.9	1.18	1.6
Pu^{IV}	0.86	0.5	2.29	1.6	1.25	0.4

In Ref. [26], the fit of the temperature dependent AIS was largely improved by considering higher orders in the temperature expansion of δ_K^c and δ_K^{pc}. In order to determine which terms to consider, we analyzed the temperature dependence of the theoretical $\chi_m^{S,Cal}$ and $\Delta\chi_{ax}^{Cal}$ values. As shown in Tables 4.16 and 4.17, while the T^{-1} variation is dominant (more than 80%) for $\chi_m^{S,Cal}$, a T^{-3} term should be added to T^{-2} for $\Delta\chi_{ax}^{Cal}$ to have a quantitative description.

Table 4.16: Linear regression of $\chi_m^{S,Cal}T = f(1/T)$ from SO-SSCASPT2 for $[An^{IV}(DPA)_3]^{2-}$ complexes. R^2 is the coefficient of determination. $\chi_m^S = \frac{s}{T} + \frac{s'}{T^2}$. s and s' are in $K \cdot m^2 \cdot mol^{-1}$ and $K^2 \cdot m^2 \cdot mol^{-1}$, respectively.

	$s\ (10^{-6})$	$s'\ (10^{-4})$	% s	% s'	R^2
U^{IV}	-4.03	1.07	91	9	0.999
Np^{IV}	-6.13	2.76	87	13	0.999
Pu^{IV}	-5.68	3.78	82	18	0.999

However we have already seen in the previous chapter that the large ligand field splitting in the actinide complexes and the thermal inaccessibility of all the ground J states can lead to T^{-1} contribution in the $\Delta\chi_{ax}$. Hill *et al.* [20] argued that large discrepancies in between the ratios of the slopes and the ratios of the intercepts of different nuclei cannot be explained with a T^{-1} dipolar term, but rather is the evidence of the presence of contact

Table 4.17: Linear regression of $\Delta\chi_{ax}^{Cal}T^2 = f(1/T)$ from SO-SSCASPT2 for $[An^{IV}(DPA)_3]^{2-}$ complexes. R^2 is the coefficient of determination. $\Delta\chi_{ax} = \frac{c}{T^2} + \frac{c'}{T^3}$, c and c' are in $K^2 \cdot m^2 \cdot mol^{-1}$ and $K^3 \cdot m^2 \cdot mol^{-1}$, respectively.

	$c\ (10^{-6})$	$c'\ (10^{-4})$	% c	% c'	R^2
U^{IV}	0.25	-0.0017	65	35	0.996
Np^{IV}	0.4	-0.0024	65	35	0.999
Pu^{IV}	-0.33	0.0013	54	46	0.995

interaction. This is the case observed during the fitting of the temperature dependent AIS in the $[An^{IV}(DPA/Et{-}DPA)_3]^{2-}$ complexes. This suggests to add a T^{-3} term in Eq. 4.2.2

$$\delta_K^p = \frac{1}{\mu_0\mu_B g_e \gamma_K}\frac{A_K^c}{\hbar}\frac{s}{T} + \frac{1}{12\pi N_A}G_K\frac{c}{T^2}\left(1+\frac{\tau}{T}\right) \quad (4.2.3)$$

$$= \frac{\alpha_K^c}{T} + \frac{\beta^{pc}}{T^2}\left(1+\frac{\tau}{T}\right)G_K \quad (4.2.4)$$

where $\Delta\chi_{ax} = \frac{c}{T^2}\left(1+\frac{\tau}{T}\right)$. All the AIS temperature variations were fitted simultaneously according to Eq. 4.2.4 (for example, fitting of the AIS in the $[Np^{IV}(Et{-}DPA)_3]^{2-}$ complex is shown in Fig. 4.2.9), as a polynomial regression at third order of the $\delta_K^p = f(1/T)$ curves. The values of α^{pc}, α_K^c and τ are optimized to fit NMR experimental data while the geometrical factors G_K are constrained to the values reported Table 4.6. The quality of the fit given by the agreement factor AF and the metal dependent constants β^{pc} and τ are tabulated in Table 4.18

Table 4.18: Fitting parameters β^{pc} (10^{-23} $m^3.K^2$) and τ (K) of Eq. 4.2.4 for ^1H and ^{13}C paramagnetic shifts in $[An^{IV}(Et{-}DPA)_3]^{2-}$ complexes. Experimental ($\Delta\chi_{ax}^{Exp}$) and SO-CASPT2 ($\Delta\chi_{ax}^{Cal}$) axial anisotropy (in 10^{-8} $m^3.mol^{-1}$) are given at 298K.

	β^{pc}	τ	AF[a]	$\Delta\chi_{ax}^{Cal}$	$\Delta\chi_{ax}^{Exp}$	$\chi_{\perp}^{exp}$	$\chi_{\parallel}^{exp}$
U^{IV}	-3.39 (± 0.05)	-93 (± 1)	1.4 %	0.9	-0.59 (± 0.08)	5.30	4.71
Np^{IV}	-2.23 (± 0.02)	126 (± 1)	1.1 %	1.23	-0.80 (± 0.09)	5.27	4.47
Pu^{IV}	1.07 (± 0.02)	203 (± 3)	1.4 %	-0.21	0.45 (± 0.06)	1.65	2.10

[a]: $AF = \left[\sum_K \left(\delta_K^p - \delta_K^p(\text{Eq. 4.2.4})\right)^2 / \left(\delta_K^p\right)^2\right]$

Under the conditions mentioned above, we reached an excellent fit of experimental data by using Eq. 4.2.4, the T^{-3} term contributing from 24% for U^{IV} to 40 % for Pu^{IV} in the paramagnetic chemical shits at 300 K. More than to demonstrate the necessity to include this term in the temperature variation of An^{IV} paramagnetic chemical shifts, we were able

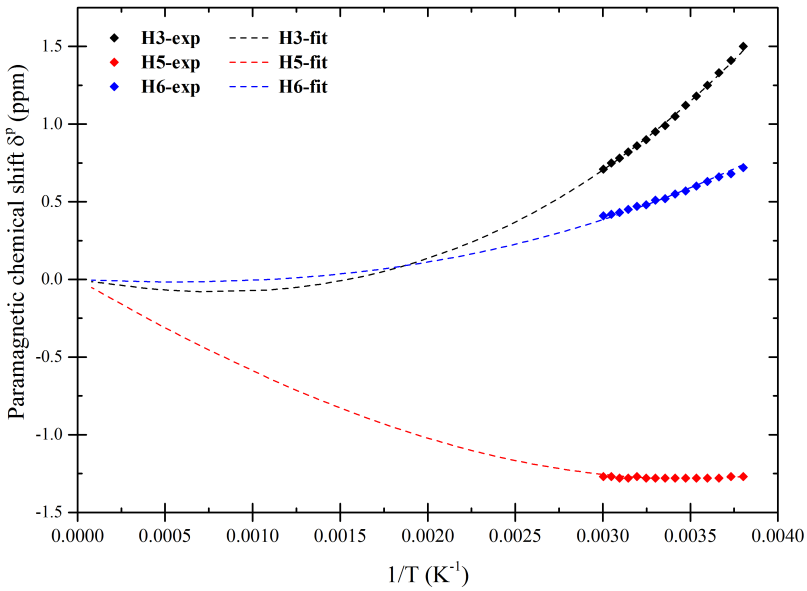

Figure 4.2.9: ^{1}H and ^{13}C paramagnetic chemical shifts (ppm) of $[Np^{IV}(Et{-}DPA)_3]^{2-}$ complexes versus the reverse of temperature (K^{-1}).

to obtain the anisotropy of the molar magnetic susceptibility $\Delta\chi_{ax}^{Exp}$ (see Table 4.18) from experimental data. As already It can be noticed that *ab initio* calculations determine the wrong nature of the magnetic isotropy. This information exposes the difficulties to properly compute the An^{IV} magnetic properties in order to predict their magnetic anisotropy. This is particularly true in the case of low anisotropy complexes where a quantitative analysis requires a very accurate description. The temperature dependence fitting of the AIS according to Eq. 4.2.4 helps to separate the pseudocontact and contact shifts, at 298 K the pseudocontact shifts $\delta_K^{pc,Exp}$ obtained from the temperature dependence study are tabulated in Table 4.9 and the Fermi contact shifts are be evaluated as $\delta_K^{c,Exp} = \delta_K^{p} - \delta_K^{pc,Exp}$ (see Table 4.9).

4.3 pNMR shifts in axially symmetric $[An^{IV}(DOTA)H_2O]$ complexes

Lanthanide(III)-DOTA complexes have long been studied [31] owing to their remarkable thermodynamic stability [86] and as MRI (Magnetic Resonance Imaging) probes [81, 34, 87]. In solution, they are easily characterized by ^{1}H NMR spectroscopy because their rigid structures lead to six non-equivalent protons more or less shifted according to the nature of the paramagnetic center. Crystal structure determinations reveal that the first coordination sphere of the metallic cation is made of four cyclene nitrogens, four carboxyl oxygen atoms and completed with one water molecule in capping position [88]. Due to

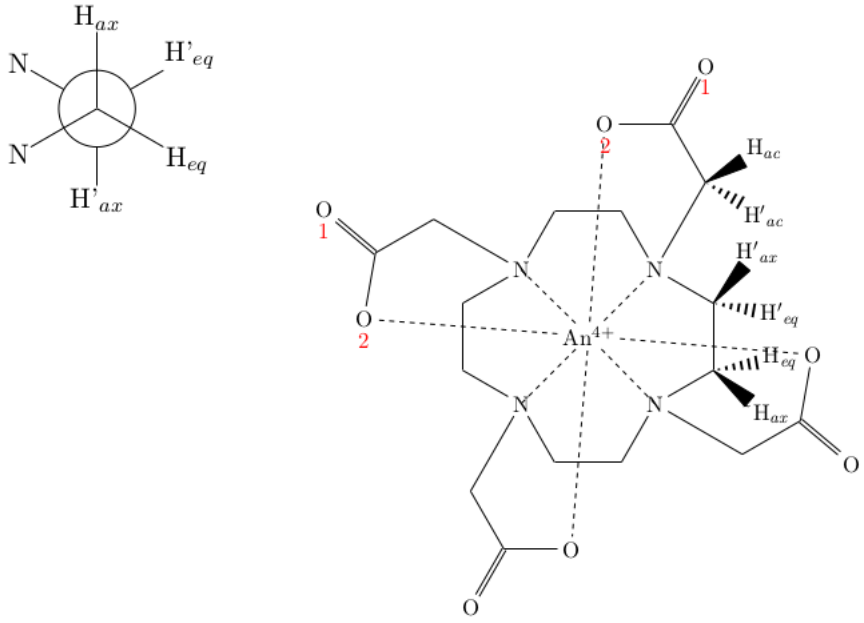

Figure 4.3.1: ^{1}H labels of [An^{IV}(DOTA)H_2O] complex.

the fast exchange in solution, the bound water signal has never been observed by NMR. Although DOTA complex structures are rigid, a slow interconversion process takes place at NMR time scale between two enantiomeric pairs of Ln(III)-DOTA complexes (Square Antiprismatic and Twisted Antiprismatic geometries written as SAP and TSAP, respectively) [89, 34]. Despite it comes as no surprise, the induced chemical shift of the bound oxygen was found mainly contact in origin [81], the ^{1}H LIS also show the dominance of the contact terms [34]. It turns out that metallic complexes of DOTA represent convenient systems to study the paramagnetic effect of less studied cations such as the An^{IV}. Indeed, conversely to the Ln^{III} series few data have been reported about the An^{IV} induced paramagnetic shift.

[An^{IV}(DOTA)H_2O] complexes where An^{IV} = Th^{IV}, U^{IV}, Np^{IV} and Pu^{IV} have been characterized in solid state by X-ray diffraction and in solution by NMR spectroscopy [1]. The dynamics of the complexes are analyzed and the contact contributions arising from the actinide paramagnetism are probed owing to ^{17}O spectra. Finally these experimental results are rationalized with theoretical calculations.

All NMR spectra of [An^{IV}(DOTA)H_2O] complexes from U^{IV} to Pu^{IV} recorded in water at room temperature present non-equivalent CH2 protons confirming a rigid structure of the DOTA ligands where the coordination sphere consists of four nitrogen and four oxygen atoms. XRD results show that a water molecule completes the first coordination sphere to a coordination number of nine in capping position of a bis square-antiprism (SAP). Probably because of the +4 charge of the An cation, no other isomer is observed as noticed with

[1] Experimental studies are performed by Claude Berthon *et al.* at CEA Marcoule, France

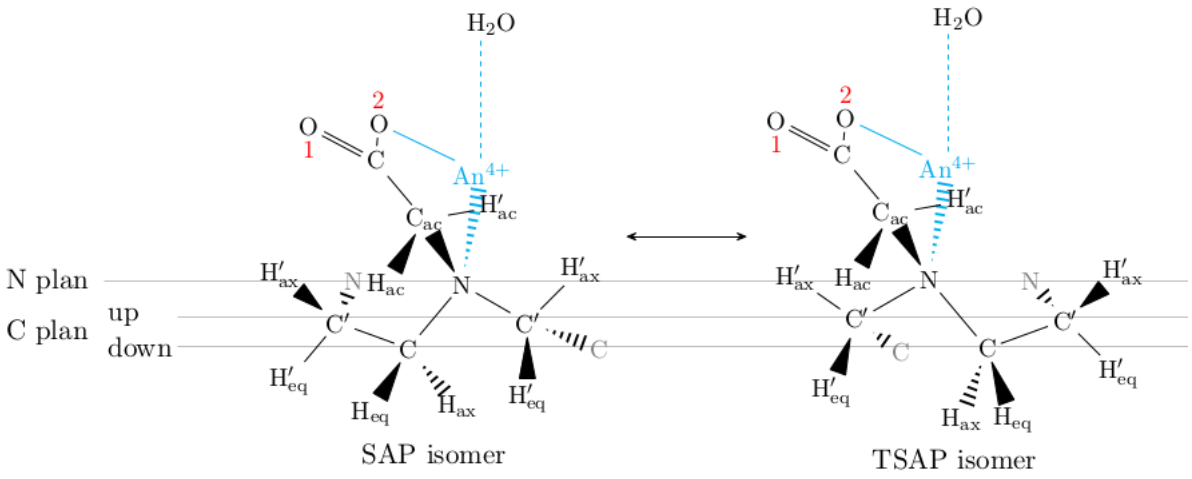

Figure 4.3.2: H and C labeling of DOTA complex isomers. Carbons are up of the cyclen ring in one DOTA isomer and move down in the other one.

Ln^{III} complexes of DOTA (isomer noted TSAP). However further experimental analysis indicates the presence of the TSAP isomer for the U^{IV} complex. To analyze the AIS in these complexes, we performed *ab initio* calculations on the symmetrized structures of the $[An^{IV}(DOTA)H_2O]$ complexes. For U^{IV} complex, two isomers are considered and for the rest, their SAP isomeric forms are considered.

4.3.1 *Ab initio* electronic structures

The energy levels and wave functions of the $[An^{IV}(DOTA)H_2O]$ complexes have been calculated with CASPT2 methods. Computational details are provided in Appendix A. SF and SO energy levels are given in Table 4.19. While in the $[An^{IV}(DPA)_3]^{2-}$ complexes, the crystal field environment is trigonal, in the $[An^{IV}(DOTA)H_2O]$ complexes, it corresponds to a tetragonal symmetry and accordingly five CFPs, B_0^2, B_0^4, B_0^6, $\bar{B}_4^4$, $\bar{B}_4^6$ are dominant (see Table 4.20). The ground SF manifold of the An^{IV} ions splits by ligand field around 3100-4800 cm^{-1}. In the SO level, the ground J manifolds of the U^{IV} $\left({}^3H_4\right)$ are split by 2500 (in SAP isomer) / 1800 (in TSAP isomer) cm^{-1}, for Np^{IV} $\left({}^4I_{9/2}\right)$ 1800 $cm^{-1}$and for Pu^{IV} $\left({}^5I_4\right)$ 2240 cm^{-1}. One notices that in the U^{IV} complexes, ligand field splitting is reduced in the TSAP isomeric structure compared to the SAP form. For the non-Kramers ions U^{IV} and Pu^{IV}, at room temperature domain (220-350 K) four and five energetically lowest states (see Table 4.19), respectively, are populated. The states largely contribute to the magnetic properties due to significant thermal populations which ensure large Van Vleck contributions (according to second terms of Eqs. 2.2.4, 2.2.3) to the magnetic properties, the contribution is reduced as the energy of the state increases.

In the [Np^{IV}(DOTA)H_2O] complex, since the SO levels are always doubly degenerate, at room temperature domain, two energetically lowest KDs (Table 4.19) are populated and can contribute to the magnetic properties both from the first and second terms of Eqs. 2.2.4, 2.2.3. Magnetic g-factors $(g_{i,n};\ i = 1,2,3,\ n = 1,2)$ of the two KDs are: 1.39, 3.98, 0.11 for KD1 and 1.22, 3.67, 1.73 for KD2.

CFPs are calculated from the energy levels and wave functions of the ground L and J manifolds using ITO method (discussed in section 5.3) and are tabulated in Table 4.20. The difference between the CFPs extracted from a given L and J manifolds is that in the case of later, one effectively includes the $J-J$ mixing which is quite important in the case of An complexes. As mentioned previously, according to the tetragonal symmetry of the ligand environment five CFPs are dominant. However, some CFPs, which are related to rhombic environment ($\bar{B}_2^2$, $\bar{B}_2^4$, $\bar{B}_2^6$) are found non-negligible, especially they are large in the [Pu^{IV}(DOTA)H_2O] complex. The total strength parameter S (Eq. 5.3.7) helps to compare the ligand field strength along a periodic series. The strength parameters corresponding to the splittings of the J manifolds decrease from U^{IV} to Np^{IV} and then highly increase from Np^{IV} to Pu^{IV} (see Fig. 4.3.3). The S parameters of the L manifolds also show the same trend, quite largely increases for Pu^{IV} than the other two. S is slightly reduced in the TSAP isomeric form as compared to the SAP from of the [U^{IV}(DOTA)H_2O] complex, as the overall energy splitting is reduced in the TSAP isomer. Strength parameters in the [An^{IV}(DOTA)H_2O] series are larger than the [$An^{VI}(DPA)_3]^{2-}$ complexes following the larger ligand splittings in the DOTA complexes. Strength parameter along the series sharply increases in the Pu^{IV} DOTA complex but decreases in the Pu^{IV} DPA indicating the strong impact of $J-J$ coupling for Pu^{IV}. Strength parameters of L and J manifolds are close for the U^{IV} complexes, whereas they deviate for Np^{IV} and Pu^{IV} complexes, again indicating the importance of $J-J$ mixing along the series.

4.3.2 Analysis of ^{17}O and ^{1}H pNMR shifts

^{1}H and ^{17}O NMR spectra of [An^{IV}(D^{17}OTA)H_2O] complexes in D_2O were recorded from 278 K to 358 K . NMR signals of the coordinated water molecule are not observed due to the fast exchange with the bulk at room temperature. The pNMR shifts are deduced using the signals of [Th^{IV}(D^{17}OTA)H_2O] as diamagnetic reference. For ^{17}O NMR spectra, chemical shifts are referenced to the ^{17}O signal of the water. ^{17}O signals of the oxygen atoms $O2$ (chelating), bound to the metallic center U, Np and Pu are easily assigned owing to their larger paramagnetic shifts compared to the $O1$ (non chelating) free oxygen atoms. The NMR shifts and the paramagnetic chemical shifts of the nuclei are reported in Table 4.23. With the paramagnetic An^{IV} cation, the ^{1}H NMR spectra exhibits six signals at room temperature as there are six chemically and magnetically non-equivalent protons (see Fig. 4.3.1).

Table 4.19: SF/SO-CASPT2 energy levels (in cm^{-1}) of the $[An^{IV}(DOTA)H_2O]$ complexes. Ground *L* and *J* manifolds are separated by horizontal lines.

U^{IV} SAP		U^{IV} TSAP		Np^{IV} SAP		Pu^{IV} SAP	
SF	SO	SF	SO	SF	SO	SF	SO
triplet		triplet		quartet		quintet	
0	0	0	0	0	0	0	0
91	275	365	82	846	0	1003	130
365	305	557	95	942	46	1149	147
1180	562	636	191	2052	46	1718	200
1442	1612	1596	1357	2228	997	1819	330
1579	1780	1848	1374	2361	997	2188	1588
2291	1861	2574	1504	2657	1114	2321	1623
2911	1920	2667	1545	2663	1114	2437	1670
3257	2492	2735	1803	2843	1299	3159	2240
3568	5065	2966	4484	3532	1299	3317	4927
3672	5143	3102	4822	3942	6074	4333	5045
5008	5335	4718	4946	4021	6074	4363	5075
5086	5701	4803	5074	4286	6387	4736	5222
5336	5798	4805	5221	8958	6387	10177	5628
5819	6455	5688	6368	8995	6602	10314	5734
6209	6755	5837	6532	10031	6602	triplet	5785
6525	6928	5941	6570	10336	6748	13423	6045
6588	6995	6155	6608	10814	6748	13459	6162
singlet	7571	singlet	7334	doublet	6990	13517	6211
4230	7584	4264	7430	9537	6990	14010	6236
4362	7626	4425	7589	9560	7084	14021	9489
4639	8440	4689	7923	9696	7084	14057	9507
4680	8655	4707	8046	10397	10310	14460	9570
6184	8678	5573	8056	10449	10310	14615	9580
6434	8713	5841	8119	10508	10947	14659	9837
6682	9458	6120	8963	10585	10947	14748	10022
7280	9471	7084	9210	10842	11268	14759	10094
7595	9590	7337	9338	10913		14932	10154
10393	9990	9928	9445	11074		15045	10193
11953	10283	11587		11130		singlet	10398
12041	10288	11767		12885		20584	10401
12841	10296	12137		13100		20773	10425
12868	10359	12591		13362		20809	10498
15112	10772	15047		13396		20843	13152

Table 4.20: CFPs (in cm^{-1}) in the $[An^{IV}(DOTA)H_2O]$ series calculated with ITO method from SF and SO-CASPT2.

	U^{IV}(SAP)		U^{IV}(TSAP)		Np^{IV}		Pu^{IV}	
	$J=4$	$L=5$	$J=4$	$L=5$	$J=9/2$	$L=6$	$J=4$	$L=6$
B_0^2	-3034	-2461	-1659	-1490	-3671	-3962	-6012	-4760
B_0^4	1582	-792	478	-585	2420	2594	2377	1202
B_0^6	292	-949	293	-859	415	893	1365	522
$\tilde{B}_2^2$	110	99	78	87	144	138	675	442
$\tilde{B}_2^4$	220	264	380	324	178	392	827	589
$\tilde{B}_4^4$	5029	4473	5295	4655	2331	2084	7929	6953
$\tilde{B}_2^6$	119	35	126	375	141	257	195	195
$\tilde{B}_4^6$	2299	5008	1471	3717	3139	4664	4676	4491
$\tilde{B}_6^6$	182	127	329	125	51	44.	116	106

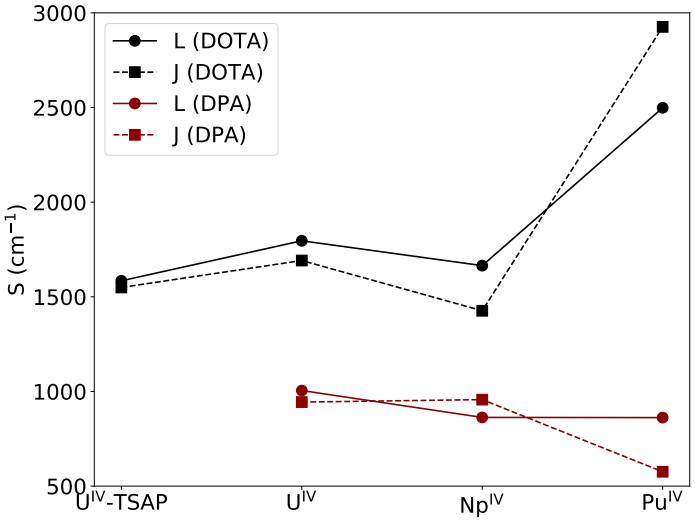

Figure 4.3.3: Strength parameters (in cm^{-1}) in the $[An^{IV}(DOTA)H_2O]$ complexes from the SF L and SO J manifolds from SO-CASPT2. The strength parameters in the D_3 $[An^{VI}(DPA)_3]^{2-}$ complexes from SO-SSCASPT2 are plotted for comparison.

To analyze the nature of the pNMR shifts, the magnetic susceptibility components are calculated with SO-CASPT2 method (see Table 4.21). The sign of the $\Delta\chi_{ax}$ is negative for U^{IV} and Np^{IV} complexes (whereas the sign is positive for the DPA complexes) indicating a large magnetization in the perpendicular direction of the $An-OH_2$ bond. It must be noted that the An ions are sightly below the plane formed by the coordinating O atoms and they are considered inside the cage formed by the DOTA ligand. It has been showed in the $[Yb(DOTAM)X^y]^{3-y}$ complexes that the anisotropy of the magnetization highly depends on the axially coordinated ligand X [90] which affects the LIS. For the Pu^{IV} complex, three principal components of the magnetic susceptibility tensor are shown in Fig. 4.3.4. Clearly, assigning the type of the axiality is not well justifiable as the two components of the perpendicular directions show large rhombicity $(\chi_{22,\perp} - \chi_{11,\perp})$. However, on an average in the perpendicular directions of the $Pu-OH_2$ bond there is less magnetization than along the bond and hence a positive $\Delta\chi_{ax}$ and a large rhombic term $\delta\chi_{rh}$ contribute to the dipolar pNMR shifts according to Eq. 2.6.31.

Table 4.21: Molar magnetic susceptibilities χ_m and axial anisotropies $\Delta\chi_{ax}$ (in 10^{-8} m^3mol^{-1}) of the $[An^{IV}(DOTA)H_2O]$ complexes from SO-CASPT2 method. For U^{IV} complex, susceptibilities for the two isomers (SAP and TSAP) are provided.

		$\chi_\perp$	$\chi_\parallel$	$\Delta\chi_{ax}$	χ_m	$\chi^S_\perp$	$\chi^S_\parallel$	$\Delta\chi^S_{ax}$	χ^S_m
U^{IV}	SAP	5.85	0.74	-5.10	4.14	-1.48	0.00	1.48	-1.0
	TSAP	6.29	1.16	-5.13	4.58	-1.55	-0.18	1.37	-1.09
Np^{IV}	SAP	5.73	1.79	-3.94	4.42	-2.23	-0.58	1.66	-1.68
Pu^{IV}	SAP	2.33[a]	2.86	0.53	2.50	-1.51[a]	-1.66	-0.15	-1.56

[a]: Averaged over the two unequal perpendicular components $(\chi_{11,\perp} < \chi_{22,\perp})$ as shown in Fig. 4.3.4.

Geometric factors of the nuclei are provided in Table 4.22. A noticeable difference in the geometric factors can be observed between the SAP and TSAP isomers. Geometric ratio $R_{K,K'}$ (Eq. 3.3.2) of two nuclei is not always in agreement with the corresponding pNMR shifts ratio $\delta^p_K/\delta^p_{K'}$ and this indicates the presence of contact terms. Since in the solution the complexes are axially symmetric, pseudocontact shifts δ^{pc}_K are calculated according to Eq. 2.6.33 and are provided in Table 4.23. Due to the presence of large rhombicity of the magnetic susceptibility tensor $\boldsymbol{\chi}$, for the Pu^{IV} complex, pseudocontact shifts are calculated according to Eq. 2.6.28 and are compared to the results from the axial formula (Eq. 2.6.33) in Table 4.23. Contact shifts δ^c_K are evaluated from the experimental pNMR shifts δ^p_K after subtracting the calculated δ^{pc}_K. Large contact shifts are observed for the chelating oxygen atoms $O2$ as expected due to having large spin population. But interestingly, the sign of the contact shifts changes for the $O2$ in the Pu^{IV} complex. $\gamma_{^{17}O}$ is negative and the isotropic spin-only magnetic susceptibilities χ^S_m are also negative for

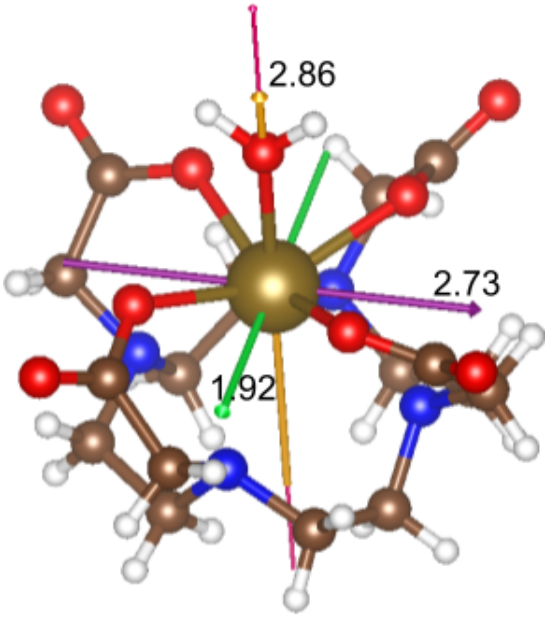

Figure 4.3.4: Principal axes of $\boldsymbol{\chi}$ tensor of the [Pu^{IV}(DOTA)H_2O] complex. The symmetry axis z is shown in purple color.

these complexes, so according to Eq. 2.6.49, large beta spin is present on the $O2$ nuclei in the U^{IV} and Np^{IV} complexes, whereas the opposite sign of the contact shift indicates large alpha spin in the case of Pu^{IV} complex. Unrestricted DFT calculations will be employed for the quantitative analysis of the spin population [81] and to get the details of the underlying mechanism of spin delocalization vs spin polarization. As χ_m^S is negative for all the complexes, the changes in the sign of contact shifts clearly indicates spin delocalization plays the dominant role to introduce large beta spin on the adjacent ^{17}O nuclei in the U^{IV} and Np^{IV} complexes. Whereas in the Pu^{IV} complex spin polarization takes over the spin delocalization probably due to the increased number of unpaired electrons, and hence large beta spin population on the Pu^{IV} center effectively induces greater spin polarization than the other two metal centers.

Table 4.22: Mean geometrical factor G_K (in 10^{-28} m^{-3}) of the proton and oxygen nuclei calculated from XRD data.

		$O1$	$O2$	H'_{ac}	H_{ac}	H_{ax}	H_{eq}	H'_{ax}	H'_{eq}
U^{IV}	SAP	-0.9931	-5.8974	-2.0144	-0.8806	2.7322	0.6283	-0.8424	0.4982
	TSAP	-1.0432	-6.3924	-1.8382	-0.8493	2.8731	0.6683	-0.8303	0.4971
Np^{IV}	SAP	-1.0432	-6.3040	-1.8933	-0.8859	2.9014	0.6559	-0.8742	0.4867
Pu^{IV}	SAP	-1.0525	-6.4493	-1.8979	-0.8729	2.8876	0.6440	-0.8838	0.4864

Table 4.23: Pseudocontact δ_K^{pc} and contact δ_K^c contributions to the AIS (in ppm) in $[An^{IV}(DOTA)H_2O]$ complexes in D_2O solution at 9.4 T and 298 K. δ_K^{pc} is calculated from Eq. 2.6.33 using the $\Delta\chi_{ax}$ values from Table 4.21 and δ_K^c is deduced as $\delta_K^p - \delta_K^{pc}$.

			$O1$	$O2$	H'_{ac}	H_{ac}	H_{ax}	H_{eq}	H'_{ax}	H'_{eq}
Th^{IV}		δ_K	323.9	323.9	3.7	3.7	3.5	2.7	2.9	2.9
U^{IV}	SAP	δ_K	365.4	1154.3	38.3	19.1	-56.6	-5.9	21.5	0.6
		δ_K^p	41.5	830.4	34.6	15.5	-60.2	-8.6	18.6	-2.3
		δ_K^{pc}	22.3	132.5	45.2	19.8	-61.4	-14.1	18.9	-11.2
		δ_K^c	19.2	697.9	-10.7	-4.3	1.2	5.5	-0.3	8.9
Np^{IV}	SAP	δ_K	357.6	724.8	27.2	20.3	-40.0	2.6	17.0	6.9
		δ_K^p	33.7	400.9	23.5	16.6	-43.6	-0.1	14.1	4.0
		δ_K^{pc}	18.1	109.4	32.9	15.4	-50.3	-11.4	15.2	-8.4
		δ_K^c	15.6	291.5	-9.3	1.3	6.8	11.3	-1.1	12.4
Pu^{IV}	SAP	δ_K	383.6	-57.2	9.2	2.8	0.9	5.4	2.9	10.2
		δ_K^p	59.7	-381.1	5.5	-0.9	-2.6	2.7	0.0	7.3
		$\delta_K^{pc:a}$	-2.5	-15.1	-4.4	-2.0	6.7	1.5	-2.1	1.1
		$\delta_K^{pc:b}$			-4.5	-2.1	-2.1	1.2	1.5	6.8
		$\delta_K^{c\,a}$	62.2	-366	9.9	1.1	-9.3	1.2	2.1	6.2
		$\delta_K^{c\,b}$			10	1.2	-0.5	1.5	-1.5	0.5

$^{:a}$: Calculated according to Eq. 2.6.33 with the geometric factors from Table 4.22 $^{:b}$: Calculated according to Eq. 2.6.28, $\delta_K^{c\,a} = \delta_K^p - \delta_K^{pc:a}$, $\delta_K^{c\,b} = \delta_K^p - \delta_K^{pc:b}$

4.4 ^{31}P pNMR shifts in $La_{1-x}M_xPO_4$ compounds; M = Sm^{III}, Pu^{III}, Am^{III}

Crystalline monazites are promising for the encapsulation of nuclear wastes due to their high chemical and self-irradiation stability. Local structure and magnetism of the M cations, where M = Sm^{III}, Pu^{III} and Am^{III} embedded in $LaPO_4$ matrices are studied by X-ray diffraction and solid-state ^{31}P MAS-NMR [2]. The synthesized $La_{1-x}M_xPO_4$ matrices contains an amount of paramagnetic metal less than 10 percent i.e. $0 \leq x \leq 0.10$. The rare-earth containing $La_{1-x}Sm^{III}{}_xPO_4$ system is the electronic counterpart of the actinide containing $La_{1-x}Pu^{III}{}_xPO_4$ with the $4f^5$ vs $5f^5$ configurations. The $5f^6$ actinide ion Am^{III} containing $La_{1-x}Am^{III}{}_xPO_4$ matrice is also mixed with a small amount (less than 3%) of pure $AmPO_4$ as confirmed by the presence of their characteristic ^{31}P NMR signal and also from the XRD; the lanthanide based analogue is the compound with Eu^{III} ion as published in Ref [91, 92]. They crystallize in the monazite $(P21/n)$ space group; each paramagnetic M site has a coordination number of nine and each P site is linked as a tetrahedron with four non-equivalent O sites. Around coordination sphere of the paramagnetic metal center, seven phosphate groups are present, four of them are directly linked to the monodentate O atoms, and the remaining three are attached to the bidentate oxygen atoms as shown in Fig. 4.4.1. The ^{31}P pNMR shifts in the paramagnetic $La_{1-x}M_xPO_4$ are deduced using NMR shifts in $LaPO_4$. In $LaPO_4$, only one NMR signal is observed whereas in the paramagnetic systems several peaks are observed implying magnetically different P atoms. But the assignments of the pNMR shifts to the associated P atoms were a non-trivial task, except one can only count number of extra induced peaks from the diamagnetic signal.

4.4.1 *Ab initio* electronic structures

SO-CAS based electronic structure calculations were performed using MOLCAS 7.8 suite of software on the model clusters $[MLa_9(PO_4)_7]^{9+}$ based on the XRD structure of $LaPO_4$ [93]. Computational details are provided in Appendix A. The substitution of the central Ln^{III} cation by either Sm^{III} or Pu^{III} without deforming the coordination sphere was justified by the close ionic radii for the La, Sm and Pu trivalent ions (1.17, 1.10 and 1.14 Å , respectively). Since the substituted cations are more contracted than the cations of the host crystal, one can expect the deformation to be negligible. This cluster consists of the central M cation and the 9 next nearest neighbors La^{III} cations completed with the neighboring PO_4 polyhedra. This cluster was further embedded in a sphere of point charges

[2] Experimental studies were performed in European Commission, Joint Research Centre (JRC), Karlsruhe, Germany by Laura Martel *et al.*

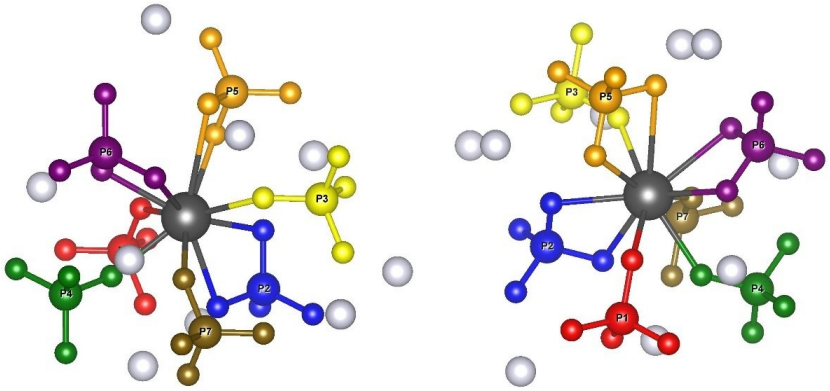

Figure 4.4.1: Numbering of the different phosphate groups. Monodentate: *P*1 (red), *P*3 (yellow), *P*4 (green), *P*7 (brown). Bidentate: *P*2 (blue), *P*5 (orange), *P*6 (purple). Two orientations are proposed.

of radius 20 Å. The charges were deduced using LoProp charge analysis [94] after a restricted Hartree-Fock (RHF) calculation on $[La_{10}(PO_4)_7]^{9+}$ with ANO-RCC-DZP basis: +2.4, +2.0, -1.1 on La, P, O, respectively.

In Table 4.24, we present the energy of the levels calculated by the SF-CASSCF method. The ground J manifold of both the Sm^{III} and Pu^{III} is ${}^6H_{5/2}$. In the $[MLa_9(PO_4)_7]^{9+}$, the ground LS terms ${}^6H$ split by 500 and 1200 cm^{-1} at the SF-CASSCF level for Sm^{III} and Pu^{III}, respectively. The ground J term of the Am^{III} free ion is a non-degenerate ${}^7F_0$ term. The LS ${}^7F$ term of the $[Am^{III}La_9(PO_4)_7]^{9+}$ complex splits by 1200 cm^{-1}. The larger splitting in the actinide complex denotes the larger interaction between the cation and the ligand in actinide complexes [95, 26].

In Table 4.25, we report the energy of the levels including SOC. The ${}^6H_{5/2}$ term in $[Sm^{III}La_9(PO_4)_7]^{9+}$ splits by 250 cm^{-1} and the introduction of spin quartets in the state interaction does not influence the results. On the contrary, for the Pu^{III} complex, the splitting of the ground term depends on the number of spin quartets included in the calculation, due to a large $J-J$ mixing. For actinide complexes, the inclusion of dynamical correlation as for example CASPT2, is necessary to approach quantitative results.

In order to quantify the effect of the number of quartets and the dynamical correlation, the $[PuCl_6]^{3-}$ complex was used as a benchmark (see Table 4.26). It shows that the splitting of the ground ${}^6H_{5/2}$ term is very sensitive to the quartets and to dynamical correlation and a large number of quartet states is necessary. While the SO-CASSCF calculation with the sextet states only gives a splitting of 223 cm^{-1}, it is reduced to 39 cm^{-1} with quartets and doublets and dynamical correlation. It should be noted that the energy gap between the ${}^6H_{5/2}$ and ${}^6H_{7/2}$ manifolds is affected by the doublets. Since this level of description is not possible for a cluster as large as $[Pu^{III}La_9(PO_4)_7]^{9+}$, the energies were fitted on the experimental curves, but the nature of the states, as characterized by the g-factors (see

Table 4.24: SF-CASSCF energies (in cm^{-1}) of the $[MLa_9(PO_4)_7]^{9+}$ complexes.

Sm^{III}		Pu^{III}		Am^{III}		
sextets	quartets	sextets	quartets	septets	quintets	triplets
0	22342	0	16252	0	18608	33462
6	22345	71	16278	328	18689	33527
275	22441	621	16390	439	18713	33558
284	22448	695	16449	578	18781	33662
327	22486	842	16483	1087	18826	33674
363	22489	975	16497	1200	20536	33711
390	22500	1050	16537	1270	20557	33751
418	22513	1150	16619		20606	33773
450	22539	1169	16690		20643	33805
498	22554	1212	16720		20737	33912
512	22566	1238	16752		20785	
6928	22594	5289	16796		20855	
6943	22649	5418	16823		20925	
6971	22670	5509	16831		20940	
7029	22700	5562	16951		21038	
7048	22709	5589	16963		21072	
7088	22732	5690	17025		21121	
7124	22742	5810	17039		21130	

Table 4.27) are taken from the SO-CASSCF calculation.

4.4.2 SQUID vs *ab initio* magnetic susceptibilities

Temperature dependent magnetic susceptibilities of the $La_{1-x}Sm^{III}{}_xPO_4$, $La_{1-x}Pu^{III}{}_xPO_4$ where $x = 0.1, 1$ for both and $AmPO_4$ compounds are recorded and are shown in Fig. 4.4.2. We did not analyze $La_{0.96}Am_x^{0.04}PO_4$ because its contribution will overlap with that of $AmPO_4$. For $La_{0.90}Pu^{III}{}_{0.10}PO_4$, while both XRD and NMR confirm a solid-solution, an unexpected ferromagnetic impurity was detected and in the case of $PuPO_4$ anti-ferromagnetic transition is observed at 4 K. The deduced experimental effective moment values are: 1.36 μ_B for $AmPO_4$ (T = 300K), 1.40 μ_B for $La_{0.90}Pu^{III}{}_{0.10}PO_4$ (T = 300K) and 0.88 μ_B for $PuPO_4$. They agree with the free ion values of 1.55 μ_B for Sm^{III} (T = 300K) and 0.85 μ_B for Pu^{III} [97]. This reflects the localized nature of the f electrons.

Ab initio calculated magnetic susceptibilities of the model cluster $[MLa_9(PO_4)_7]^{9+}$ are also shown in Fig. 4.4.2 for comparison. For the Sm^{III} and Am^{III} complexes, the magnetic susceptibility curves deduced from the *ab initio* calculations reproduce well the experimental data (Fig. 4.4.2 a, Fig. 4.4.2 c). But for the Pu^{III} complex, the *ab initio* curves do not fit the experimental ones (Fig. 4.4.2 b). Using $[PuCl_6]^{3-}$ complex (Table 4.26), we observed that the $J-J$ mixing with excited J manifolds by SOC plays a key role and

Table 4.25: SO-CASSCF energies (in cm^{-1}) of the $[MLa_9(PO_4)_7]^{9+}$ complexes. The number of SF states included in the state interaction is specified. Ground *J* manifolds are separated by horizontal lines.

Sm^{III}		Pu^{III}				Am^{III}	
21sext	21sext-100quar	21sext	21sext-75quar	21sext-100quar	21sext-150quar	7sept-25quin	7sept-25quin-10trip
0	0	0	0	0	0	0	0
0	0	0	0	0	0	988	1627
186	179	383	453	271	363	1321	1965
186	179	383	453	271	363	1357	1988
254	239	504	649	439	500	3205	4378
254	239	504	649	439	500	3327	4489
910	1068	1760	2622	2500	2667	3383	4551
910	1068	1760	2622	2500	2667	3447	4631
988	1140	1922	2812	2645	2824	3646	4825
988	1140	1922	2812	2645	2824	5981	7333
1103	1263	2207	3143	3037	3116	6001	7344
1103	1263	2207	3143	3037	3116	6014	7401
1135	1296	2302	3270	3151	3225	6075	7466
1135	1296	2302	3270	3151	3225	6105	7509
2034	2324	3955	5590	5396	5602	6135	7531
2034	2324	3955	5590	5396	5602	6141	7598
2090	2376	4077	5716	5507	5721	8171	9854
2090	2376	4077	5716	5507	5721	8381	10075
2186	2470	4261	5944	5700	5914	8435	10189
2186	2470	4261	5944	5700	5914	8599	10258

Table 4.26: Energies (in cm^{-1}) of the $[PuCl_6]^{3-}$ complex, from CAS based calculations and experiment. The degeneracy of the states (deg) is also mentioned.

		SF-CASSCF	SF-CASPT2		SO-CASSCF			SO-CASPT2			SO-CASSCF [95]	SO-NEVPT2 [95]	Exp [96]
	deg			deg	21sext-	21sext-100quar	21sext-100quar-100quar-	21sext-	21sext-100quar	21sext-100quar-100quar-			
sextets	3	0	0	2	0	0	0	0	0	0	0	0	0
	2	320	257	4	223	215	77	223	210	39	47	91	13-76
	3	435	406	2	1719	1757	2342	1696	1736	2446			
	3	968	1124	2	1895	1894	2634	1874	1860	2829			
	3	5047	3216	4	1959	1989	2635	1988	2016	2809			
	1	5228	3336	2	3892	3877	5139	3854	3829	5514			
	3	5230	3724	4	4079	3919	5360	4085	3873	5805			
	3	22012	15994	4	4132	4019	5463	4156	3992	5947			
quartets	3	16034	13288	4	6626	5968	7496	6127	5062	7878			
	1	16043	13526	2	6720	6048	7750	5470	5404	8372			
	3	16115	13304										
	1	16229	13674										
	3	16270	13712										
	3	16307	14034										
	2	16495	14113										

Table 4.27: g-factors of the three first Kramers doublets in the $[MLa_9(PO_4)_7]^{9+}$ complexes determined from SO-CASSCF calculations

	Sm^{III}			Pu^{III}										
	21sext-100quar			21sext			21sext-75quar			21sext-100quar			21sext-100quar		
	g_1	g_2	g_3	g_1	g_2	g_3	g_1	g_2	g_3	g_1	g_2	g_3	g_1	g_2	g_3
KD1	0.99	0.16	0.06	0.62	0.12	0.22	1.05	0.17	0.01	1.16	0.12	0.21	1.13	0.20	0.03
KD2	0.66	0.40	0.10	0.52	0.18	0.82	0.66	0.29	0.41	0.74	0.14	0.39	0.73	0.48	0.22
KD3	1.19	0.67	0.04	1.28	0.45	0.19	1.28	0.64	0.00	1.11	0.81	0.09	1.28	0.65	0.04

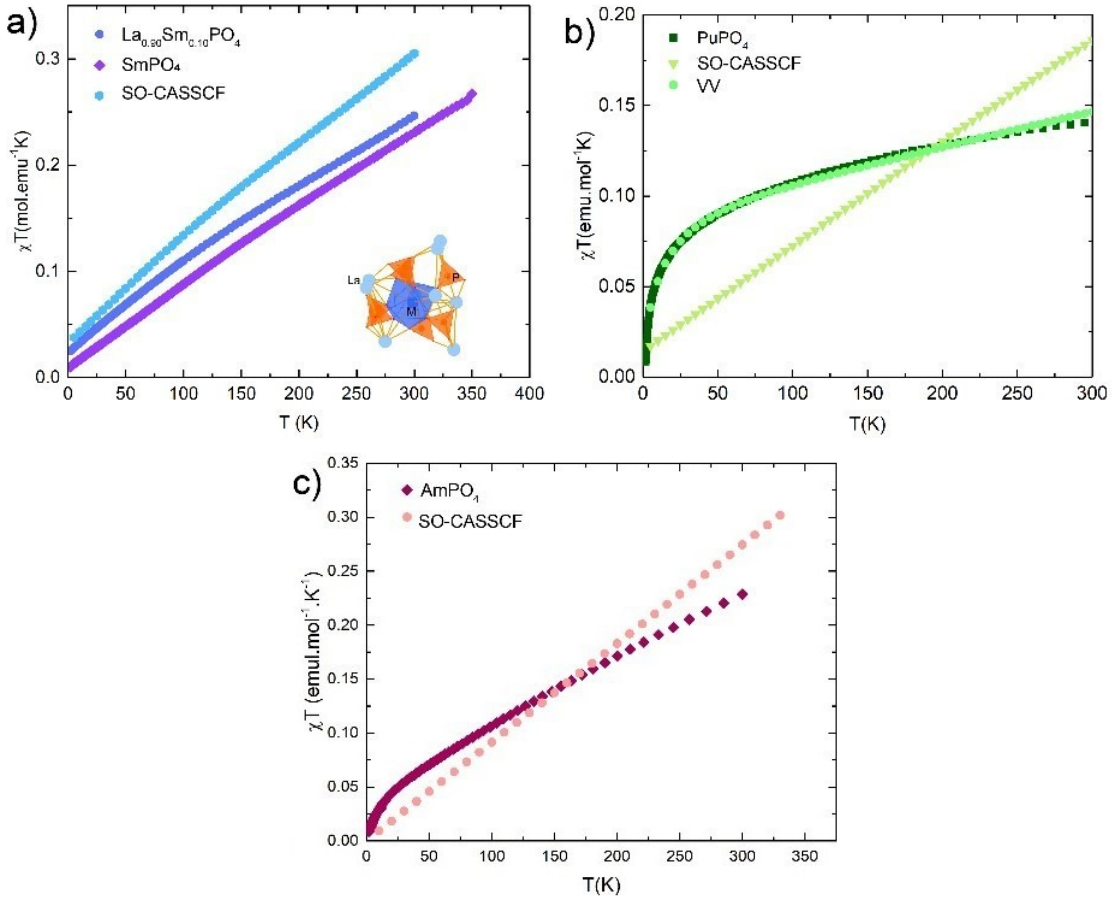

Figure 4.4.2: Experimental and computed magnetic susceptibilities (in emu.K.mol^{-1}) vs T (in K) of a). $La_{1-x}Sm^{III}{}_xPO_4$ ($x = 0.01$ and 1), b) $PuPO_4$ and c) $AmPO_4$.

drastically reduces the energy gaps within the ground J manifold. A correct description needs many excited states and dynamical correlation, which is not feasible in the present case. Therefore, the energy gaps were determined by fitting the experimental χT curve, as described below. As the magnetic properties of the three KDs of the ground $J = 5/2$ manifold are not affected by the number of quartet states (see Table 4.27), one can write a model Van Vleck (VV) equation of Eq. 2.6.11 for the three lowest KDs as

$$\begin{aligned}\chi T \;=\; & \frac{N_A\mu_0\mu_B^2}{3}\frac{1}{Q_0}\left[M_{11}^2 + M_{22}^2 e^{-\frac{\Delta_2}{k_BT}} + M_{33}^2 e^{-\frac{\Delta_3}{k_BT}} + 2k_BT* \right. \\ & \left. \left\{ M_{12}^2\frac{1-e^{-\frac{\Delta_2}{k_BT}}}{\Delta_2} + M_{13}^2\frac{1-e^{-\frac{\Delta_3}{k_BT}}}{\Delta_3} + M_{23}^2\frac{e^{-\frac{\Delta_2}{k_BT}} - e^{-\frac{\Delta_3}{k_BT}}}{\Delta_3-\Delta_2} \right\} \right] + \chi_{TIP}T \end{aligned} \tag{4.4.1}$$

where N_A is the Avogadro number, Q_0 the partition function, Δ_2 and Δ_3 the energy gaps for KD2 and KD3 with the ground state, respectively. M_{II}^2 characterizes the magnetic moment of KDI, with $M_{II}^2 = \frac{1}{2}\left(g_{1,I}^2 + g_{2,I}^2 + g_{3,I}^2\right)$, $g_{i,I}$, $i = 1,2,3$ the three g-factors of the I$^{\text{th}}$ KD and $M_{IJ}^2 = \|\mathbf{M}_{x,IJ}\|^2 + \left\|\mathbf{M}_{y,IJ}\right\|^2 + \|\mathbf{M}_{z,IJ}\|^2$ and $M_{i,IJ}^2$, $i = x,y,z$ the block magnetic moment matrix within the I and J manifolds, in terms of μ_B. The direction of the principal axis of the **g** tensor for the ground KD with the largest g-factor is represented in Fig. 4.4.3 and the g-factors are given in Table 4.27. While the energy gaps vary with the numbers of SF states included in the state interaction, the compositions of the three KDs are roughly unaffected (see Table 4.28). According to the SO-CASSCF results, expressed in the PAF of the **g**-tensor of KD1, KD1 is by 91% M_J=±5/2, KD2 by 82% M_J=±3/2 and KD3 by 78% M_J=±1/2. In other terms, with a quantization axis taken as the magnetic axis of KD1, the three KDs can be approximated by pure M_J states. This is confirmed by Table 4.28, where the magnetic factors appearing in Eq. 4.4.1 are similar. The fit of χT vs T was performed considering pure M_J: this allows the determination of three parameters, Δ_2, Δ_3 and χ_{TIP}. Only the points above 3 K were considered. We obtained two solutions with different orderings of the states. For the 1st solution, the M_J=±1/2 doublet is the ground state, and the M_J=±5/2 and M_J=±3/2 doublets lie 21 and 92 cm^{-1} above, respectively. For the 2nd solution, the M_J=±3/2 doublet is the ground state, and the M_J=±5/2 and M_J=±1/2 lie 15 and 83 cm^{-1} above, respectively. The two fits obtained are called VV1 and VV2, respectively, are remarkably similar. The fit with the magnetic moments issued from the *ab initio* calculations leads to roughly the same energies and in better agreement with those published for $PuPd_2Sn$ [97] and $PuCl_3$ [98] (as shown in Fig. 4.4.4). It shows that there is a low-lying doublet at around 20 cm^{-1}, a much lower value than the SO-CASSCF one. It confirms that, as in the $[PuCl_6]^{3-}$ complex, the $J-J$ mixing plays a key role to determine the low-lying states.

Finally, the CFPs were determined from CASSCF calculations according to the ITO procedure. They depend on the Cartesian frame in which the molecule is described. The

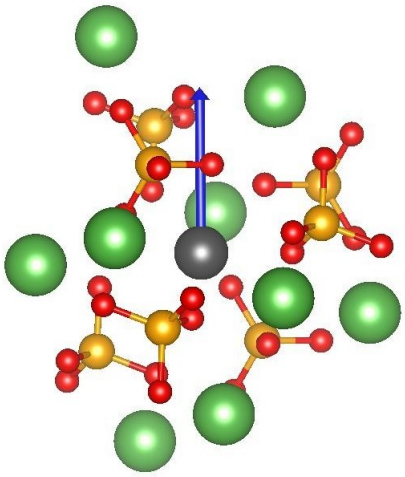

Figure 4.4.3: Direction of the main principal axis of the ground KD of the $[Pu^{III}La_9(PO_4)_7]^{9+}$ complex, from SO-CASSCF (21sext-150quar).

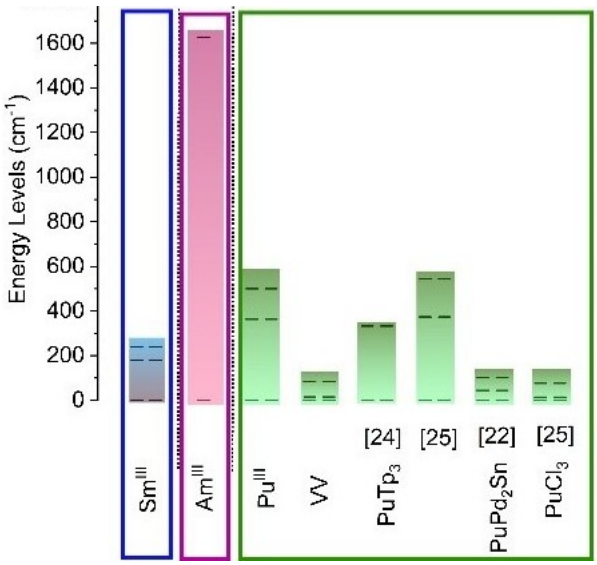

Figure 4.4.4: Energy levels determined in the present study (Table 4.25) using SO-CASSCF for Sm^{III}, Am^{III}, Pu^{III} and a Van Vleck fit (VV). The energy levels were compared with the literature: $PuTp_3$ from Magnani *et al.* [7] and Gaggioli and Gagliardi [99], $PuPd_2Sn$ [97] and $PuCl_3$ [98]

Table 4.28: Magnetic parameters (in μ_B^2) for the three lowest KDs in the $[Pu^{III}La_9(PO_4)_7]^{9+}$ complex calculated with SO-CASSCF (21sext-150quar). They are compared to pure M_J KD1=±1/2; KD2=±3/2; KD3=±5/2.

	M_{11}^2	M_{22}^2	M_{33}^2	M_{12}^2	M_{13}^2	M_{23}^2
pure M_J	0.77	0.36	1.02	0.65	0	0.40
SO-CASSCF	0.71	0.35	0.95	0.56	0.12	0.62

complexes are rather spherical and there is no obvious choice for the z axis. According to the SO-CASSCF calculation, the **g** tensor of the ground KD is axial, but with small values of g. The crystal field strength parameter S defined according to Eq. 5.3.7 allows to evaluate the strength of ligand field with only one parameter. It is furthermore rotation invariant. In the following, we will restrict the discussion of the ligand field to this parameter, and to its derivatives of k^{th} order. The CFPs originate from the position and nature of the ligands and are deduced as effective parameters that incorporate other physical effects, as electron-electron interaction and $J-J$ mixing. The CFPs are represented in Fig. 4.4.5. The comparison between the SF-CASSCF and SO-CASSCF parameters allows to gauge the effect of $J-J$ mixing. S is worth 230 cm^{-1} for the Sm^{III} complex and is more than twice larger for its actinide counterpart, due to larger covalent effects. It is slightly smaller for the Am^{III} complex, following the usual trend within a series. The strength parameters of different orders S^k follow the same trends. With SOC, CFPs can not be calculated from the ground state of the Sm^{III} complex since it has a non-degenerate ground state with $J=0$. From the $J=5/2$ manifold, they can be calculated up to the 4th order. While S is about the same from SO-CASSCF as from SF-CASSCF, the strength parameter deduced from the fitted values for Pu^{III} is lower since the splitting of the states is largely reduced. And finally, the strength parameter of the actinide complex is smaller than its lanthanide counterpart.

4.4.3 Analysis of ^{31}P pNMR shifts

- Experimental ^{31}P MAS NMR spectra

^{31}P MAS NMR of $La_{1-x}M_xPO_4$ are recorded to probe the local structure and magnetism and also to analyze the metal content in an atomic scale. To deduce the paramagnetic chemical shifts, the ^{31}P NMR peak that corresponds to the signal of the diamagnetic $P(OLa)_7$ unit (see peak 1 of Fig. 4.4.6 and Fig. 4.4.7) is used as a reference. To be noted that the ^{31}P NMR peaks which do not vary with composition (peak 2-5 of Fig. 4.4.6) correspond to the unit $P(OLa)_6(OM)_1$ and these extra induced shifts are dictated by the M cation paramagnetism. As the signal of the $P(OLa)_5(OM)_2$ units are overlapping ($La_{1-x}M_xPO_4$ with $x \neq 0.01$), we did not attribute them. They are in the range of 3 to 10 ppm for the Sm^{III} complex, -24 to -92 ppm for the Pu^{III} complex and 27 to 106 ppm for the Am^{III} complex (see Table 4.29). These paramagnetic shifts are further separated in contact and pseudocontact shifts. The former arises from the delocalization of the spin density of the paramagnetic cation towards the P nucleus through the bonds (Eq. 2.6.49) and the later from the through space dipolar interaction between the electronic magnetic moment of the magnetic center and the nuclear magnetic moment of the nucleus (Eq. 2.6.28).

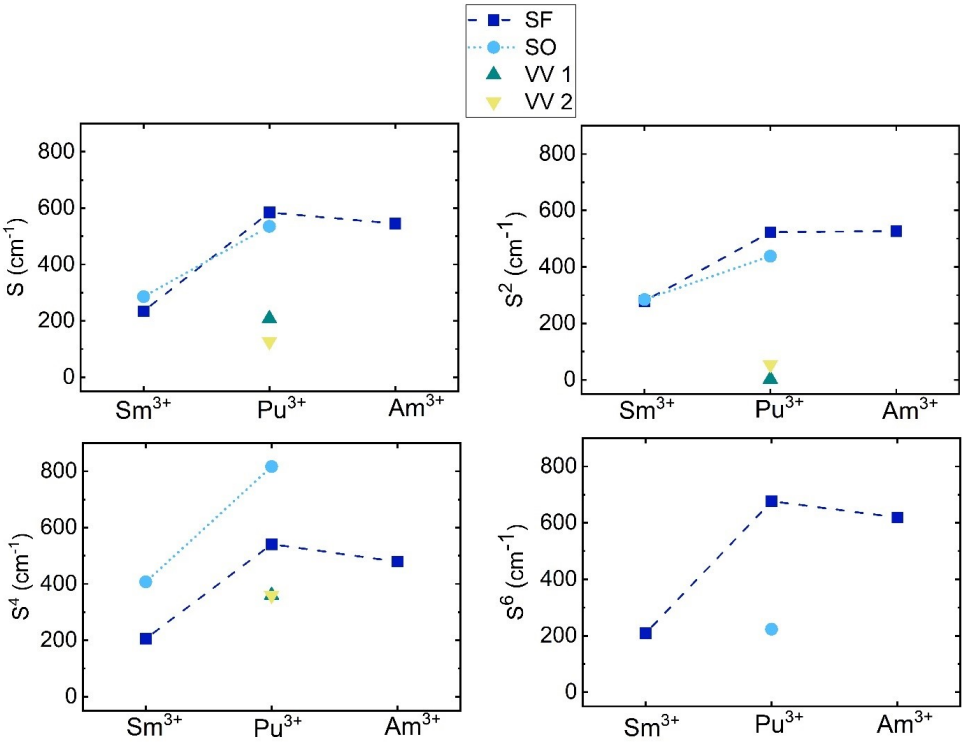

Figure 4.4.5: Strength parameters (total and of 2nd, 4th and 6th orders, in cm^{-1}) in the $[MLa_9(PO_4)_7]^{9+}$ complexes. They are deduced using the ITO procedure from the ground L manifold at SF-CASSCF level, from the ground J manifold at SO-CASSCF level, or from the fit of the experimental curve according to Eq. 4.4.1.

Table 4.29: Experimental ^{31}P NMR shifts in the $La_{1-x}M_xPO_4$ complexes. The uncertainties are of ± 0.2 ppm.

Peak $n°$	$La_{1-x}Sm^{III}{}_xPO_4$				$La_{1-x}Pu^{III}{}_xPO_4$				$La_{1-x}Am^{III}{}_xPO_4$
	0.01	0.05	0.1		0.01	0.05	0.1		0.04
1	-4.3	-4.5	-4.5	1	-4.5	-4.7	-4.6	1	-4.5
2	-0.6	-0.8	-0.8	2	-27.9	-28.5	-28.9	2	22.8
3	1.7	1.7	1.7	3	-31.8	-31.9	-32.2	3	20.1
4		5.5	5.5	4	-48.7	-48.8	-48.6	4	50.4
				5	-69.8	-69.9	-69.9	5	78.6
				6		-57.0	-57.4	6	43.4
				7		-75.9	-76.2	7	106.9
				8		-97.1	-96.6	8	280.9*
				9			-126.3		

*: ^{31}P NMR signal in $AmPO_4$

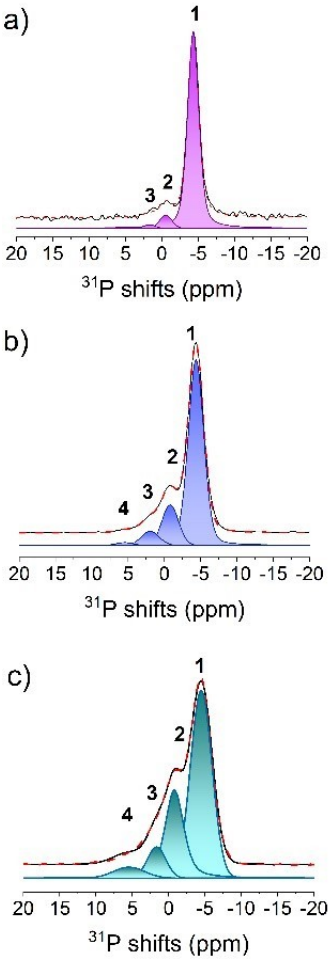

(a) ^{31}P MAS NMR spectra of a) $La_{0.99}Sm^{III}_{0.01}PO_4$, b) $La_{0.95}Sm^{III}_{0.05}PO_4$, c) $La_{0.90}Sm^{III}_{0.10}PO_4$,

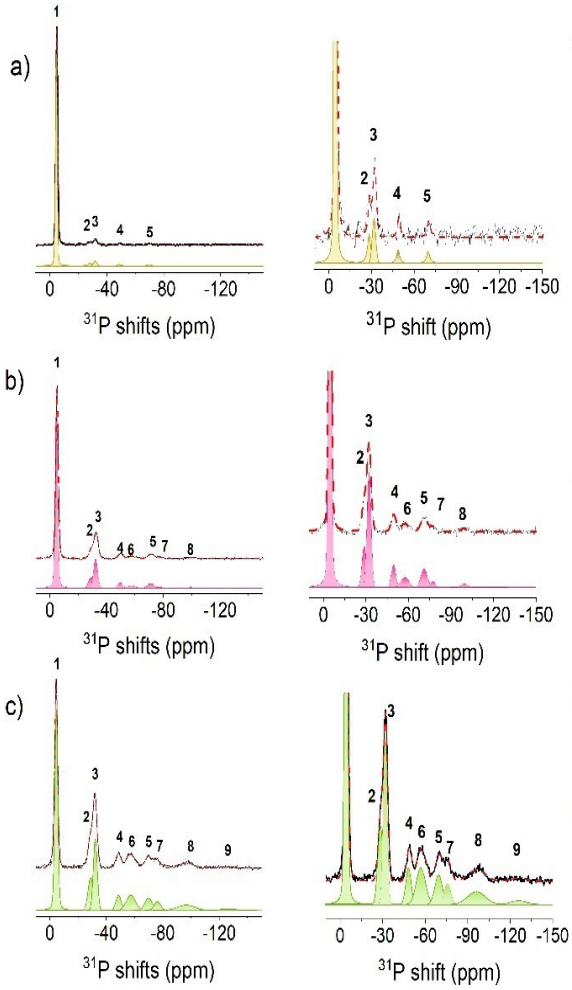

(b) ^{31}P MAS NMR spectra of a) $La_{0.99}Pu^{III}_{0.01}PO_4$, b) $La_{0.95}Pu^{III}_{0.05}PO_4$, c) $La_{0.90}Pu^{III}_{0.10}PO_4$,

Figure 4.4.6: ^{31}P MAS NMR spectra in the $La_{1-x}M_xPO_4$ compounds where M = Sm^{III}, Pu^{III} are present in variable concentrations. Peak 1 corresponds to the signal where a P atom is surrounded by the diamagnetic La^{III} cations and no paramagnetic ions in close vicinity. With the increase of metal content, ^{31}P MAS NMR spectra changes due to the change of local structure which can be explained as follows: with the increase of metal concentration three P sites can be linked with the NMR peaks, diamagnetic $P(OLa)_7$ unit (peak 1), $P(OLa)_6(OM)_1$ (peak 2-5), $P(OLa)_5(OM)_2$ unit.

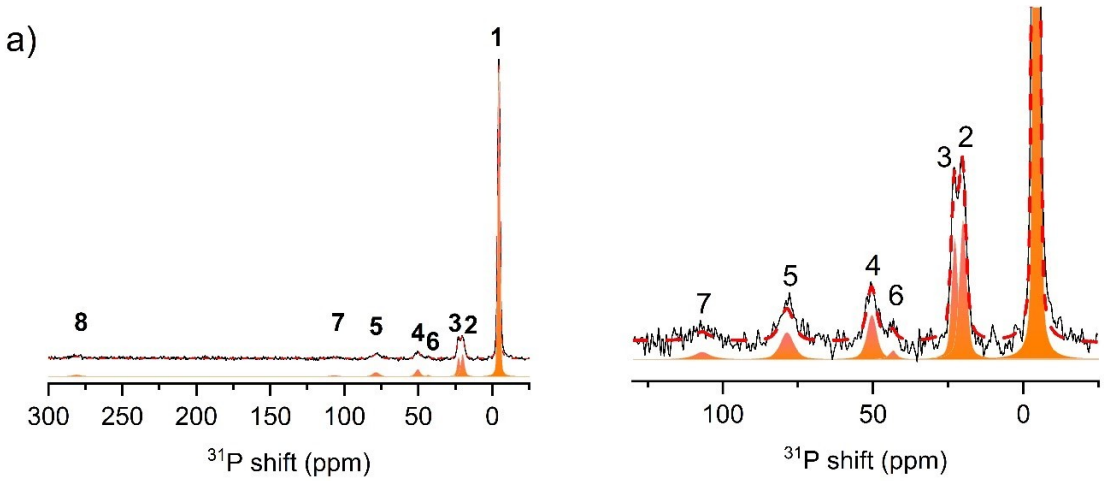

Figure 4.4.7: ^{31}P MAS NMR spectra in the $La_{0.96}Am^{III}{}_{0.04}PO_4$. Peak 8 corresponds to the NMR signal in the $AmPO_4$ which is also mixed (less than 4 %) with the compund.

- Pseudocontact shifts

In order to analyze the pseudocontact contribution according to Eq. 2.6.28, we computed the magnetic susceptibility component using the model systems $[MLa_9(PO_4)_7]^{9+}$ from SO-CASSCF methods. The magnetic susceptibility tensors deduced from SO-CASSCF results as summarized in Table 4.30. In order to evaluate the interaction with the excited J manifolds, different SO spaces were considered: all states, the ground and first J manifolds $(J;J+1)$, and only the ground J manifold (GS J), except for the Am^{III} complex where $J=0$ leads to a non-magnetic state. For the three complexes, the $J;J+1$ space provides results similar to all space, but different from the GS J space. It shows that the states higher that the $J+1$ manifold do not contribute quantitatively to the magnetic susceptibility, while the $J+1$ manifold contributes qualitatively. This later manifold is not statistically populated and contributes by 2nd order Zeeman interaction with the GS J manifold. The orbit and spin contributions, χ^L and χ^S, are evaluated by replacing the total magnetic moment by its orbit or spin counterpart contribution. In the Sm^{III} and Pu^{III} complexes, in the GS $J=5/2$ space, the spin and orbit contributions, χ^S and χ^L, are opposite in sign, in accordance with Hund's rules, and this leads to quite small values of χ_{iso}. The orbit contribution is the largest, consequently positive, and the spin contribution negative. As pointed out by Bleaney [17], the effect of the $J+1$ manifold is large for Sm^{III} complex and reverses the sign of the spin contribution. This is confirmed by the present study. The coupling with the $7/2$ manifold reduces the orbit contribution, reverses the sign of the spin contribution, and since now the two contributions are additive, χ_{iso} is larger. χ^L and χ^S from the GS J space are similar for the Sm^{III} and the Pu^{III} complexes. The splitting of the ground $5/2$ manifold is smaller in the later than in the former (90 against 240 cm^{-1}, fitted energies are considered here for the Pu^{III} complex); those small splittings allow the three KDs to be populated at room temperature, and the smaller split-

ting in the Pu^{III} complex leads to slightly larger values for the magnetic susceptibility. For this complex, the effect of the $7/2$ manifold is reduced compared to the Sm^{III} one, since it lies higher in energy (2500 vs 1000 cm^{-1}) due the larger SOC in the actinide. The orbit contribution decreases, as the spin one does, without any reversal of sign. It means, that for the Pu^{III} complex, spin and orbit are opposite in sign, leading to a smaller χ_{iso} than for the Sm^{III} complex. In the Am^{III} complex, χ^L and χ^S are similar and opposite. But since $\chi_{iso} = \chi^L + 2\chi^S$, χ^S is positive and χ^L negative. To conclude, χ^S is positive in the Sm^{III} and Am^{III} complexes, and negative in the Pu^{III} one.

Table 4.30: Components of the magnetic susceptibility tensor (in 10^{-3} cm^3mol^{-1}) from SO-CASSCF for the $[MLa_9(PO_4)_7]^{9+}$ complexes at 309 K. L and S denote the orbit and spin contributions. Different spaces for SO interaction were considered. For the Pu^{III} complex, fitted energy levels are used.

M	states	χ_1^L	χ_1^S	χ_1	χ_2^L	χ_2^S	χ_2	χ_3^L	χ_3^S	χ_3	χ_{iso}
Sm^{III}	all	0.77	0.19	1.15	0.80	0.16	1.12	1.41	-0.32	0.78	1.01
	$J;J+1$	0.77	0.19	1.14	0.81	0.15	1.11	1.43	-0.33	0.77	
	GS J	1.44	-0.55	0.33	1.45	-0.58	0.30	1.86	-0.82	0.23	
Pu^{III}	all	1.37	-0.36	0.64	1.33	-0.35	0.62	1.21	-0.37	0.47	0.58
	$J;J+1$	1.38	-0.37	0.64	1.33	-0.36	0.61	1.22	0.37	1.97	
	GS J	1.61	-0.62	0.36	1.56	-0.61	0.34	1.43	-0.59	0.24	
Am^{III}	all	-1.23	1.17	1.12	-0.72	0.79	0.87	-0.81	0.83	0.85	0.95
	$J;J+1$	-1.15	1.17	1.19	-0.77	0.79	0.81	-0.80	0.83	0.85	

Table 4.31: Pseudocontact contributions (in ppm) to the paramagnetic shifts at 309 K in the $[MLa_9(PO_4)_7]^{9+}$ complexes evaluated using Eq. 2.6.28. The P atoms are labeled according to Fig. 4.4.1.

P site	Sm^{III}	Pu^{III}	Am^{III}
$P1$	2.82	1.24	-2.61
$P2$	6.65	2.99	11.79
$P3$	3.01	1.05	-1.77
$P4$	-1.99	-0.97	-1.80
$P5$	-5.87	-2.44	-3.10
$P6$	6.04	2.73	10.87
$P7$	-5.85	-2.50	-3.91

The three principal components of the susceptibility tensor are rather similar, in accordance with the compactness of the ligands around the paramagnetic center, forming a

roughly spherical coordination sphere. That is why the dipolar contributions to the pseudocontact shifts (see Table 4.31) were evaluated according to Eq. 2.6.28, and not from the anisotropic axial component, $\Delta\chi_{ax}$ according to Eq. 2.6.33, as it is often the case. Those values are positive or negative depending on the position of the considered P atom, and less than 10 ppm, in absolute value. The values are slightly larger for the Sm^{III} and Am^{III} complexes, following the slightly larger values for χ_{iso}. The calculated pseudocontact shifts of the P atoms are in the range of the experimental ^{31}P pNMR shifts for the Sm^{III} complex, but much smaller for the Pu^{III} and Am^{III} complexes. This shows that the contact contribution is dominant in the two actinide complexes.

- Contact shifts

The contact shifts depend on χ^S and on the contact HFC parameter A_K^c, as expressed by Eq. 2.6.49. The most shifted peaks are expected to correspond to P atoms possessing the largest spin density at the nucleus. The delocalization of the spin density from the paramagnetic center to the phosphate depends on the bonding scheme. There are two types of binding schemes of the phosphate ligands with a given Pu center: four of them bind through one oxygen atom and are monodentate, while the three other ones bind through two oxygen atoms and are bidentate (as shown in Fig. 4.4.1). The Pu−O distances vary from 2.48 to 2.78 Å and the ∠Pu−O−P from 94.6 to 144°. The Mulliken spin densities in the *s* orbitals of the phosphorus atoms deduced from CASSCF calculations are different for the seven P atoms (see Table 4.32). While insignificant in the Sm^{III} complex, it lies in the 0.0004-0.0020 range for the Pu^{III} and Am^{III} complexes. Fig. 4.4.8 represents the dependence of $q_s(P)$ in the $[Pu^{III}La_9(PO_4)_7]^{9+}$ complex. One should underline that only the spin delocalization is described by our CASSCF calculations. A larger active space should be considered for the description of the spin polarization. On the 1st scheme, $q_s(P)$ is compared to the whole Mulliken spin density on the same P atom $q(P)$ (see Table 4.32). As expected, they are proportional, but with different proportionality rates for monodentate and bidentate phosphates. $q(P)$ is in general larger for the bidentate, but $q_s(P)$ is in general not. The Pu−O distance is larger for the bidentate, and consequently, the Mulliken charge $q(O)$ of the O bridging atom is smaller. There is a main trend that $q_s(P)$ increases with $q(O)$, but not linearly. Inversely, there is a main trend of decrease of $q_s(P)$ in terms of the Pu−O distance (see Fig. 4.4.8 d). Fig. 4.4.8 c shows how $q_s(P)$ depends on the ∠Pu−O−P angles. For the monodentate phosphates, the largest the angle, the largest the spin density in the *s* orbitals of the P atom. For the bidentate, $q_s(P)$ is the largest when the two angles are the same, corresponding to a symmetrical bonding by the two oxygen atoms. This supports the impact of the Fermi contact interaction on the different paramagnetic shifts, especially for the actinides, despite the unique crystallographic P site.

Table 4.32: Mulliken charges ($\times 10^3$) on the P atoms, total and in the *s* orbitals, from CASSCF calculations in the complexes $[MLa_9(PO_4)_7]^{9+}$. The P atoms are labeled according to Fig. 4.4.1

P site	Sm^{III}		Pu^{III}		Am^{III}	
	tot	*s*	tot	*s*	tot	*s*
*P*1	0.09	0.00	0.38	0.01	0.35	0.02
*P*2	0.23	0.03	0.96	0.14	0.89	0.12
*P*3	0.12	0.02	0.81	0.15	0.70	0.13
*P*4	0.12	0.02	0.54	0.13	0.52	0.13
*P*5	0.14	0.01	0.84	0.09	0.71	0.07
*P*6	0.18	0.02	0.87	0.13	0.82	0.12
*P*7	0.14	0.03	0.64	0.15	0.61	0.15

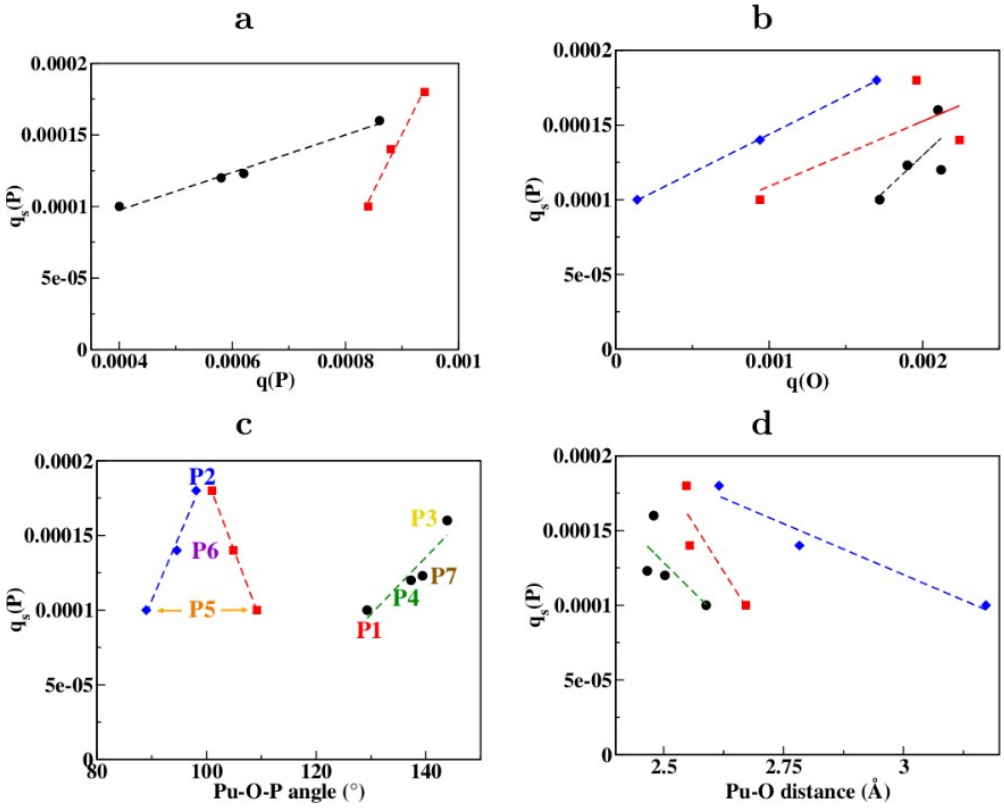

Figure 4.4.8: Mulliken spin density in the *s* orbitals of the P atoms against the Mulliken spin density on P and bridging O atoms, ∠Pu−O−P angles and Pu−O distance in the $[Pu^{III}La_9(PO_4)_7]^{9+}$ complex, from CASSCF. Black: monodentate phosphates, red and blue: bidentate phosphates, with smaller and larger angles, respectively. Dashed lines represent linear regressions.

4.5 Conclusions

The paramagnetic properties of An^{IV} cations in solution were investigated by actinide induced NMR chemical shifts in the complexes formed with dipicolinic acid derivatives (DPA and Et−DPA) and DOTA ligands. Interpretation of experimental data was carried out by performing *ab initio* evaluation of the magnetic properties. In the solutions these complexes are strictly axial, SO-CASPT2 based calculations of the anisotropic susceptibility $\Delta\chi_{ax}$ are used to separate the pseudocontact and contact terms and the spin-only molar magnetic susceptibility χ_m^S are also evaluated to interpret the contact terms. There is significant contact contribution to the paramagnetic chemical shifts even for protons further from the actinide center which happens to be quite small in the lanthanide counterpart.

In the $[An^{IV}(DPA)_3]^{2-}$ complexes, it is revealed that the deviations from a mainly pseudocontact shift on ^1H paramagnetic shift are not principally induced by a greater delocalization of the spin density on the ligand when going from Ln^{III} to An^{IV}, as it is expected from more covalent metal-ligand interaction. But, the dominance of the Fermi contact shift in the ^1H paramagnetic chemical shifts was related to weak $\Delta\chi_{ax}$ values. In the same way, it has been demonstrated that ^{13}C paramagnetic chemical shifts were dominated by the Fermi contact contribution. The subsequent calculation of the HFC constants A_K^c, were compared to spin density calculations using unrestricted SR-DFT based methods. It is shown that spin polarization mechanism dominates in the ^{13}C Fermi contact shifts of complexes.

The possibility to separate pseudocontact and contact shifts considering Bleaney's hypotheses of their temperature dependencies for Ln^{III} was investigated. From the consistency between experimental data and SO-CASPT2 calculations, we conclude that the contact contribution could be approximated as a $\delta_K^c = f(1/T)$ law. The theoretical description of the pseudocontact term revealed the limits to reduce the variation of the paramagnetic susceptibility to its $1/T^2$ component only. For An^{IV} cations, SO-CASPT2 calculations showed that the temperature variation of $\Delta\chi_{ax}$ could be reduced to I/T^2 and $1/T^3$ terms. Experimental data were successfully fitted by *ab initio* calculations, leading to a good agreement with experimental $\Delta\chi_{ax}^{exp}$ values and the individual components $\chi_{\parallel}^{exp}$, $\chi_{\perp}^{exp}$.

In the $[An^{IV}(DOTA)H_2O]$ complexes, like the DPA complexes, large contact shifts are estimated in ^1H paramagnetic chemical shifts based on the first principles description of the pseudocontact shifts. The magnetization of the actinide center mostly lies perpendicular to $An-OH_2$ bond resulting a negative $\Delta\chi_{ax}$, except for Pu^{IV} with a positive $\Delta\chi_{ax}$ with a large rhombicity of the susceptibility tensor as also noticed from the presence of the CFPs related to rhombic environment. The chelating oxygen atoms show large AIS

mostly originated from a dominant contact mechanism. However, the opposite sign of the contact shifts for the coordinating O atoms is pointing out a subtle difference in the underlying mechanism of their origin: dominant spin delocalization in the U^{IV} and Np^{IV} complexes vs dominant spin polarization in the Pu^{IV} complex.

In the $La_{1-x}M_xPO_4$ compounds, the pNMR shifts are used to probe the local structure and magnetism around the paramagnetic metal centers. While all the ^{31}P nuclei around the diamagnetic ions are chemically equivalent, they are magnetically non-equivalent close to paramagnetic ions and that results in additional MAS-NMR signals. The analysis of the magnetic susceptibility data indicates a small splitting of the ground $J = 5/2$ manifold of Pu^{III}, even smaller than the lanthanide counterpart Sm^{III}. *Ab initio* calculations quite overestimate the splitting for Pu^{III} where $J - J$ coupling plays a major role in dictating the splitting which needs to be described correctly. All the ions maintain their free ion character as the magnetic moments are close to the free ion limit. The analysis of the pNMR shifts suggests that the contact contributions are dominant in the ^{31}P AIS whereas in the LIS, they are quite small and both the contact and pseudocontact terms are on the same order. This is as expected due to large overlap of the actinide $5f$ shells with the ligands' orbitals whereas the lanthanide $4f$ shells are quite "buried" inside the atom and participate less in the bonding. The analysis of the Mulliken spin densities clearly differentiates the monodentate phosphates from the bidentate ones and underlines the reason for the large range of the AIS observed in the ^{31}P MAS-NMR spectra.

Chapter 5

Crystal field parameters in Ln^{III} and An^{IV} complexes with the DPA ligand

5.1 Introduction

In this chapter, we will introduce the crystal field theory which describes the interaction of the f^N electrons of a paramagnetic Ln/An ion with the ligand environment. In due course, we will be also familiar with how to model the interaction by means of few parameters such that they can be evaluated either by fitting the experimental data or from *ab initio* methods. The advantage of using such a parametric evaluation is that it projects all the information and complexity into the parameters, that are easy to handle and can be used to compare from one system to another. Since the introduction of the CFT in the 1930s by Hans Bethe and John H. van Vleck, it has been widely used to interpret the spectral and magnetic properties of the open shell metal complexes [100, 101, 102]. The theory is based on a empirical model that best describes the interaction of the unpaired electrons with the ligand environment by means of few parameters. The number of the parameters decreases with the symmetry. Early, the parameters were extracted by fitting the experimental data. But in last few decades, successful descriptions of the open shell metal complexes with the first principles methods help to evaluate these parameters *ab initio*. Here we will mostly deal with the *ab initio* evaluation of the crystal field parameters. A DFT based evaluation of the parameters was first proposed earlier in the 2000s by Atanosov e*t al.* [103, 104] and then it was extended to wave function based derivation [105]. In the equivalent operator formalism where the matrix elements are computed in the equivalent representation of the *ab initio* space $(\Psi_I, I = 1,..,2X+1; X = L \text{ or } J)$ by the angular momentum space of the free-ion $|L, M_L, S, M_s\rangle$ (SF) or $|L, S, J, M_J\rangle$ (SO), the CFPs are extracted as effective parameters with the appropriate spin Hamiltonian written as

$$\hat{H}_{CF}(X) = \sum_{k=2,4,6} \alpha_X^k \sum_{q=-k}^{k} B_q^k \hat{O}_q^k(X) \tag{5.1.1}$$

where $\hat{O}_q^k$ are the 'spin operators' acting on the model space of X manifold, B_q^k the CFPs, α_X^k the reduced matrix elements. We will discuss in details about Eq. 5.1.1 in section 5.3. Eq. 5.1.1 provides a theoretical framework for modeling the ion environment by means of corresponding spin Hamiltonian parameters. They can be deduced from the first principles calculations.

So now the questions arise, what is the significance of these parameters and how are they useful? In the context of pNMR shifts, the remarkable work of Bleaney in the 1970s [17] connects the CFT with the descriptions of the pNMR shifts in the Ln complexes as discussed in section 1.5. Bleaney's formula as given by Eq. 2.6.34 helps to model the pNMR shifts (more precisely the pseudocontact shifts) with only one CFP. In his theory, the magnetic anisotropy in an axially symmetric lanthanide complex was successfully modeled with the single CFP B_0^2. In recent studies, modeling of the experimental pNMR shifts in the $[Ln^{III}(DPA)_3]^{3-}$ series with Bleaney's formula showed that the only CFP is constant along the series [26]. In the domain of molecular magnetism, the CFPs are used to model the zero-field splitting tensor and reproduce the transition spectra in the EPR spectroscopy [106]. Ln based single molecular magnets have become a craze in last two decades [107, 108] and the CFPs have been used to rationalize the ligand environment which finely tunes their magnetic anisotropy and the relaxation process [109].

In this chapter, we will focus on the *ab initio* evaluation of the CFPs in the isostructural $[Ln^{III}(DPA)_3]^{3-}$ complexes where Ln=Ce−Yb and in the $[An^{IV}(DPA)_3]^{2-}$ complexes where An = Th, U, Np and Pu complexes. Their electronic structures are computed *ab initio* using CAS based methods which are highly successful to provide a good estimate of the magnetic properties for Ln/An complexes, permitting a balanced description of the relativistic and correlation effects, both playing key roles in those complexes [48]. The wave functions and the corresponding energy levels of a manifold (either a L manifold or a J manifold of the free-ion) are used to extract the CFPs using two formalisms: (i) AILFT method which evaluates the CFPs from the splitting of the seven f orbitals due to the ligands and hence captures the one-electron pictures (ii) ITO method which extracts the CFPs from the many-electron energy levels and effectively includes the many electron effects in the CFPs. We will discuss the trends of the CFPs along with the two series and also compare them in between the Ln^{III} and An^{IV}. We will also compare the parameters from AILFT and ITO to understand whether the CFPs are transferable from the orbital to the many-electron picture or not. We will also see the effect of SOC on the CFPs in the two series. Another important aspect of comparing the CFPs along a series, namely 'the trend of covalency' is also pointed out [110, 111].

5.2 Model Hamiltonian in the CFT

The model Hamiltonian in the CFT that describes the f^N electrons in the crystal environment is as follows[1]

$$\hat{\mathscr{H}}_{CF} = \hat{\mathscr{H}}_0 + \hat{V}_{res} + \hat{V}_{CF} + \hat{\mathscr{H}}_{SO} \tag{5.2.1}$$

where $\hat{\mathscr{H}}_0$ is the free-ion electronic Hamiltonian (in a.u.) in the central-field approximation and written as a sum over the one-electron Hamiltonian $\hat{h}_i$ as

$$\hat{\mathscr{H}}_0 = \sum_{i=1}^{N} \hat{h}_i = \sum_{i=1}^{N} \left(\hat{T}_i - \frac{Z^*}{r_i} + \hat{v}_{ee}(i) \right) \tag{5.2.2}$$

where the summation runs over all the N number of f electrons, $\hat{T}_i$ the kinetic energy of the i^{th} electron, next the attraction of the electrons by the screened charge of the metal nucleus Z^*, $\hat{v}_{ee}$ is the potential energy of an electron in the mean field of other electrons. The missing electron-electron repulsion energy is included in V_{res} which is called the residual Coulomb potential energy term given by

$$V_{res} = \sum_{i>j}^{N} \frac{1}{r_{ij}} - \sum_{i=1}^{N} \hat{v}_{ee}(i) \tag{5.2.3}$$

$\hat{\mathscr{H}}_{SO}$ only considers the one-electron term (spin-own-orbit type) of the SO interactions derived from the Dirac-Coulomb-Breit Hamiltonian and expressed as

$$\hat{\mathscr{H}}_{SO} = \sum_{i=1}^{N} \xi(r_i)\, \hat{l}_i \cdot \hat{s}_i = \lambda \hat{\boldsymbol{L}} \cdot \hat{\boldsymbol{S}} \tag{5.2.4}$$

where $\xi(r) = -\frac{1}{r}\frac{dU(r)}{dr}$ with a spherically symmetric potential $U(r)$ for the electrons. In the Russell-Saunders coupling scheme $\sum_{i=1}^{N} \xi(r_i) = \lambda = \pm\frac{\xi_{nl}}{2S}$ ($2S$ is the number of the unpaired f electrons) is the SOC parameter. $\hat{\boldsymbol{L}}$ is the total orbital angular momentum of the f electrons and $\hat{\boldsymbol{S}}$ is the total spin angular momentum. The matrix elements of the spin-orbit Hamiltonian in Eq. 5.2.4 can be easily calculated by expressing $\hat{\boldsymbol{L}} \cdot \hat{\boldsymbol{S}}$ in terms of Ladder operators as

$$\hat{\boldsymbol{L}} \cdot \hat{\boldsymbol{S}} = \hat{L}_z \hat{S}_z + \frac{\hat{L}_+ \hat{S}_- + \hat{L}_- \hat{S}_+}{2} \tag{5.2.5}$$

where $\hat{L}_\pm = \hat{L}_x \pm i\hat{L}_y$ and $\hat{S}_\pm = \hat{S}_x \pm i\hat{S}_y$

The many electron operator $\hat{V}_{CF}$ is also written as a sum of the one-electron Hamiltonian $\hat{v}_{CF}(i)$ as

[1] List of abbreviations is given at the beginning of the thesis.

$$\hat{V}_{CF} = \sum_{i=1}^{N} \hat{v}_{CF}(i) \tag{5.2.6}$$

$\hat{v}_{CF}$ is potential energy that an electron have due to surroundings and is expressed as

$$\hat{v}_{CF}(1) = \sum_{I}^{N_s} \frac{Z}{|\boldsymbol{R}_I - \boldsymbol{r}|} = \sum_{I}^{N_s} \frac{Z}{\sqrt{r^2 + a^2 - 2ar\cos\omega_I}} \tag{5.2.7}$$

where r and a are the lengths of the position vectors of the electron ($\boldsymbol{r}$) and the I$^{\text{th}}$ point charge ($\boldsymbol{R}_I$), respectively. ω_I is the angle between the two vectors. The summation runs over all the N_s number of point charges (for O_h symmetry, $N_s = 6$, for T_d, $N_s = 4$) with charge $-Z$ (in a.u.) (for simplicity, we are considering similar amount of charge on each point).

Now Eq. 5.2.7 can be expanded in terms of the Legendre polynomials $P_k(x)$ with $x = \cos\omega_I$ as

$$\hat{v}_{CF}(1) = Z \sum_{I=1}^{N_s} \sum_{k=0}^{\infty} \frac{r^k}{a_I^{k+1}} P_k(\cos\omega_I) \tag{5.2.8}$$

and if the length $a > r$ the series converges which means the electrons are highly localized on the metal center.

$P_k(\cos\omega_I)$ can be expanded with the additional theorem of spherical harmonics,

$$P_k(\cos\omega_I) = \frac{4\pi}{2k+1} \sum_{q=-k}^{k} Y_k^q(\theta,\phi) Y_k^{q*}(\theta_I,\phi_I) \tag{5.2.9}$$

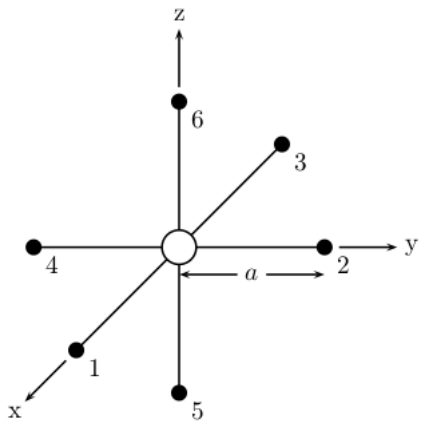

Figure 5.2.1: The point charges around a metal ion in an octahedral symmetry. ◯ the metal ion, • the point charges. The distance between the metal and the point charges are a units.

where $Y_k^{q*}(\theta_I,\phi_I) = (-1)^q Y_k^{-q}(\theta_I,\phi_I)$; θ and ϕ are the angular coordinates of the electron and θ_I and ϕ_I are the angular coordinates of the point charges. So from Eqs. 5.2.8 and5.2.9 we can write,

$$\hat{v}_{CF}(1) = \frac{4\pi}{2k+1} Z \sum_{I=1}^{N_s} \sum_{k=0}^{\infty} \sum_{q=-k}^{k} \frac{r^k}{a_I^{k+1}} Y_k^q(\theta,\phi) Y_k^{q*}(\theta_I,\phi_I) \tag{5.2.10}$$

$$= \sum_{k=0}^{\infty} \sum_{q=-k}^{k} B_k^q r^k Y_k^q(\theta,\phi) \tag{5.2.11}$$

$$= \sum_{k=0}^{\infty} \sum_{q=-k}^{k} \hat{v}_k^q \tag{5.2.12}$$

In Eq. 5.2.11, the CFPs, $B_k^q = (-1)^q \frac{4\pi}{2k+1} Z \sum_{I=1}^{N_s} \frac{1}{a^{k+1}} Y_k^{-q}(\theta_I,\phi_I) = (-1)^q B_k^{-q*}$ are depen-

dent on the positions and charges of the ligands and the symmetry of the surroundings. The matrix elements in between two configurations Ψ and Ψ' in which an electron occupation differs from one to another in the f orbitals can be calculated as

$$\begin{aligned}
\left\langle \Psi|\hat{v}_{CF}|\Psi' \right\rangle &= \sum_{k=0}^{\infty}\sum_{q=-k}^{k} \left\langle \phi_a|\hat{v}_k^q|\phi_b \right\rangle && (5.2.13)\\
&= \sum_{k=0}^{\infty}\sum_{q=-k}^{k} B_k^q \int R_a(l_1;r)R_b(l_2;r)r^k r^2 dr \\
&\quad \int Y_{l_1}^{m_1 *}(\theta,\phi)Y_k^q(\theta,\phi)Y_{l_2}^{m_2}(\theta,\phi)\sin\theta d\theta d\phi \delta(m_s,m_{s'}) && (5.2.14)\\
&= \sum_{k=0}^{\infty}\left\langle r^k \right\rangle \sum_{q=-k}^{k} B_k^q \left\langle Y_{l_1}^{m_1}|Y_k^q|Y_{l_2}^{m_2} \right\rangle && (5.2.15)
\end{aligned}$$

$\delta(m_s,m_{s'})$ is the Kronecker symbol and equal to 1 for similar spin orbitals $m_s = m'_s$, otherwise 0. According to the triangle rule of Clebsch-Gordan, these following conditions must be fulfilled in order the integrals in Eq. 5.2.15 not to vanish,

$$q = m_1 + m_2 \tag{5.2.16}$$

and

$$|l_1 - l_2| \leq k \leq |l_1 + l_2| \tag{5.2.17}$$

In the case of transition metals (d orbitals with $l = 2$) terms with $k > 4$ will not contribute and for Ln/An (f orbitals with $l = 3$) $k > 6$ will not contribute in the crystal field splitting. The first term, with $k = 0$, does not contribute to crystal field splitting of a given manifold. Also the crystal field operator is a time-even operator, so essentially, there will be no harmonics of odd k in the expression of Eq. 5.2.12. Hence in principle, there are 27 CFPs required to model the crystal field splitting of the f orbitals. But this number is reduced with the symmetry of the ligand environment. For example, in the case of O_h symmetry, only two CFPs are left and they are easily deduced by fitting the experimental data or from the first principles calculations.

5.3 Crystal field Hamiltonian in terms of tensor operators

CFT models the splitting of the f orbitals by the field created by the ligands surrounding the metal center. The theory is based on the empirical parameters, known as the CFPs, that effectively includes all the interactions of the f^N electrons of the metal ion with the

ligands. The evaluation of the matrix elements of the crystal field operator in Eq. 5.2.12 depends on the radial part of the f orbitals. If one assumes that all the f orbitals have the same radial expansion, then $\hat{v}_k^q$ operators (or their many-electron counterparts) acting in the Hilbert space of the Slater determinants may be replaced by the tensor operators $\hat{O}_q^k$ acting in either the l (one electron), L (SF), or J (SO) manifolds. Eq. 5.2.6 is then equivalent to

$$\hat{V}_{CF}(X) = \sum_{k=2,4,6} \alpha_X^k \sum_{q=-k}^{k} B_q^k \hat{O}_q^k(X) \tag{5.3.1}$$

where $\alpha_X^k = \left\langle X \left\| \alpha^k \right\| X \right\rangle$ represents the reduced matrix elements of second, fourth, and sixth orders, respectively, $X = l, L, J$ according to the considered manifold. The α_l^k elements are determined by the number of f electrons N, the α_L^k elements by N and L, and the α_J^k elements by N, L, and J. These reduced matrix elements have been tabulated for the ground state of each lanthanides ion [36]. Two different paths were followed for calculating the matrix elements of the tensor operators $\hat{O}_q^k$, let us say from the Hilbert space of a J manifold i.e. $\hat{O}_q^k(J)$. In Stevens pathway, as already mentioned in section 1.5, each $\hat{O}_q^k$ is expressed by the Cartesian components $\hat{J}_x$, $\hat{J}_y$, $\hat{J}_z$ and their linearly independent multiplicative terms or in terms of the ladder operators $\hat{J}_\pm$ and their higher order terms. In Stevens notation, the crystal field Hamiltonian is commonly written as

$$\hat{V}_{CF}(J) = \sum_{k=2,4,6} \alpha_X^k \sum_{q=-k}^{k} A_k^q \left\langle r^k \right\rangle \hat{O}_q^k(J) \tag{5.3.2}$$

where $A_k^q \left\langle r^k \right\rangle$ are the CFPs in Stevens notations. Note that, the CFPs explicitly contain the radial dependencies and separation of $A_k^q \left\langle r^k \right\rangle$ to obtain the actual parameters A_k^q is not straight forward in the case of molecules.

In the second approach, the $\hat{O}_q^k$ operators with $k \geq 2$ are derived successively from order 1 operators $\left(\hat{O}_0^1, \hat{O}_{\pm 1}^1\right)$ using the recursive formula,

$$\hat{O}_q^k = N_k (-1)^q \sum_{q_1, q_2} \begin{pmatrix} k-1 & 1 & k \\ q_1 & q_2 & -q \end{pmatrix} \hat{O}_{q_1}^{k-1} \hat{O}_{q_2}^1 \tag{5.3.3}$$

where the 2×3 array denotes the $3j$ symbol and N_k is the constant ensuring the normalization of the square sum of the $3j$ symbols and depends only on order k. The matrix elements of $\hat{O}_q^k$ are then calculated from the J manifold using Wigner-Eckart theorem as

$$\left\langle J, M_J \left| \hat{O}_q^k \right| J, M_J' \right\rangle = (-1)^{J - M_J} \left\langle J \left\| \hat{O}^k \right\| J \right\rangle \begin{pmatrix} J & k & J \\ -M_J & q & M_J' \end{pmatrix} \tag{5.3.4}$$

where $\left\langle J \left\| \hat{O}^k \right\| J \right\rangle$ are the reduced matrix elements α_J^k written explicitly in Eq. 5.3.1. The

CFPs in Eq. 5.3.1 are written in Wybourne convention [35] $\left(B_q^k\right)$ and throughout this chapter this convention is used. One needs a prefactor going from Stevens notation to Wybourne.

The CFPs depend on the orientation of the molecule in the $\{x,y,z\}$ frame. They are in general imaginary and any rotation around the z axis affects the phase factor mixing of B_q^k and B_{-q}^k . For the Ln or An DPA chelates, z is chosen as the pseudo C_3 axis as shown in Fig. 5.3.1 and the choice of the x and y axes is arbitrary. Hence, only the norm of these parameters is considered.

$$\bar{B}_q^k = \sqrt{\left|B_q^k\right|^2 + \left|B_{-q}^k\right|^2} \tag{5.3.5}$$

For the sake of comparison, rotational invariants are defined in order to reduce the large number of CFPs to fewer parameters. We considered the strength parameter of k^{th} order,

$$S^k = \left[\frac{1}{2k+1}\sum_{q=-k}^{k}\left|B_q^k\right|^2\right]^{1/2} \tag{5.3.6}$$

and the strength parameter as defined by Chang *et al.* [112]

$$S = \left[\frac{1}{3}\sum_k \frac{1}{2k+1}\sum_{q=-k}^{k}\left|B_q^k\right|^2\right]^{1/2} \tag{5.3.7}$$

These two strength parameters are rotational invariant. To quantify the symmetry about the z axis, the strength parameter of q^{th} index is considered,

$$S_q = \left[\sum_k \frac{1}{2k+1}\left|B_q^k\right|^2\right]^{1/2} \tag{5.3.8}$$

This parameter is not rotational invariant, but it is invariant to rotations about the z axis. The parameter S allows the strength of the ligand field to be evaluated with only one parameter and gives an idea of the overall splitting of the ground J manifold. In this chapter, CFPs are deduced using two methods: the ITO method in which the CFPs are deduced from the many-electron energies and wave functions of the considered J manifold following a matrix decomposition technique; the AILFT method which is essentially a least-square fitting procedure and the CFPs are extracted from the one electron picture.

5.4 Crystal field parameters by ITO method

This method has been proposed by Ungur and Chibotaru [113]. The CFPs are deduced from the $2J+1$ wave functions $|\Psi_I\rangle$ and the corresponding energies E_I of a J manifold

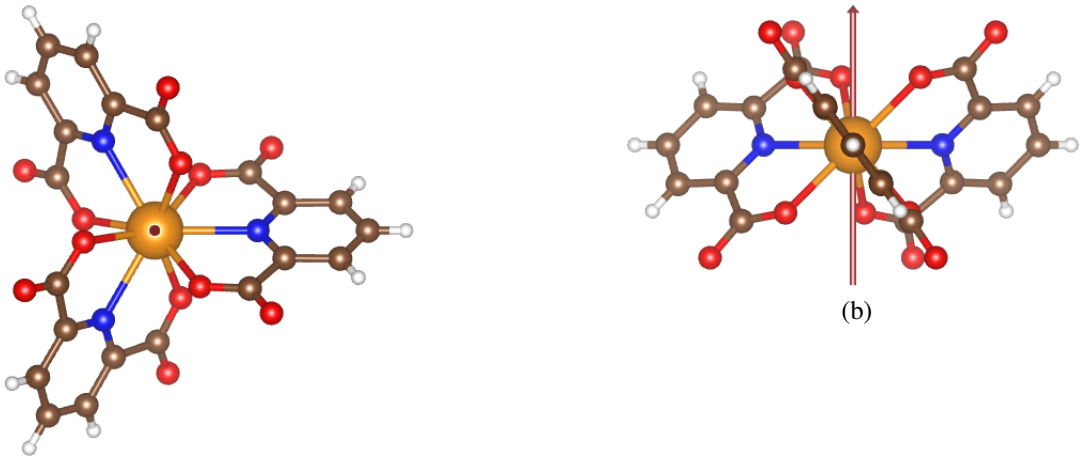

(a) (b)

Figure 5.3.1: $[Ln^{III}(DPA)_3]^{3-}$ complexes, (a) top view (b) side view. Color code: orange- Nd, blue- N, red- O, saddle-brown- C, white- H. z axis is shown in light red color.

calculated with a CAS based methods. This supposes that this manifold is well separated from the other ones and easily identifiable. In a first step, the *ab initio* $2J+1$ states must be assigned to the $|J,M_J\rangle$ $(M_J = -J,J)$ of the model space. This is the key step. Noting that the $|J,M_J\rangle$ are innately eigenvectors of the Z component of the total angular momentum operator $\hat{J}_z$, and according to Wigner-Eckart theorem, of the Z component of the magnetic moment $\hat{M}_z$. Consequently, diagonalizing the matrix representation of $\hat{M}_z$ in the set of the $\{|\Psi_I\rangle\}$ provides the eigenvectors $\left\{\left|\tilde{\Psi}_M\right\rangle\right\}$ which are the *ab initio* counterparts of the model $|J,M_J\rangle$. A phase factor must be assigned for the one to one correspondence. This can be achieved in a way such that the super-diagonals of $\hat{M}_x$ and $\hat{M}_y$ become real and imaginary, respectively. Finally, the Hamiltonian matrix $\mathbf{H}^{AI}$ (AI stands for *ab initio*), which is diagonal in the original set $|\Psi_I\rangle$, is expressed in the $\left\{\left|\tilde{\Psi}_M\right\rangle\right\}$ basis. $\mathbf{H}^{AI}$ is the matrix to be decomposed in terms of "spin matrices" $\mathbf{\Omega}_q^{(k)}$ of $\hat{O}_q^k$ generated in the Hilbert space of the J according to Eq. 5.3.4 in order to obtain the CFPs.

$$\mathbf{H}^{AI} = \sum_{k=0}^{2J}\sum_{q=-k}^{k}(-1)^q Q_q^{(k)}\mathbf{\Omega}_q^{(k)} \tag{5.4.1}$$

The expansion coefficients are obtained by orthogonal projection

$$Q_q^{(k)} = \frac{2k+1}{\left|\left\langle J\left\|O^{(k)}\right\|J\right\rangle\right|^2}(-1)^q \mathrm{Tr}\left(\mathbf{\Omega}_{-q}^{(k)\dagger}\mathbf{H}^{AI}\right) \tag{5.4.2}$$

Tr denotes the trace and † the conjugate transpose. Since the size $\mathbf{H}^{AI}$ is $2J+1$, Eq. 5.4.2 leads to $(2J+1)^2$ coefficients $Q_q^{(k)}$. Because the CFPs are obtained by a decomposition technique, there is no loss of information. $Q_0^{(0)}$ is zero, and as the Hamiltonian is a time-even operator, the terms with odd values of k vanish. Parameters with $k > 6$ appear to be negligible in the case of wave functions built from pure f orbitals. The correspondence

between the model space $|J,M_J\rangle$ and the many-electron *ab initio* wave functions is based on the similarity between the *ab initio* $\mathbf{M}_u^{AI}$ $(u=x,y,z)$ and the model $\mathbf{M}_u^J$ matrices of the magnetic moment components operators

$$\delta m_u = \sqrt{\mathrm{Tr}\left(\mathbf{M}_u^J - \mathbf{M}_u^{AI}\right)^\dagger \left(\mathbf{M}_u^J - \mathbf{M}_u^{AI}\right)} \tag{5.4.3}$$

An another index δh is introduced for quantifying the similarity between the *ab initio* representation matrix $\mathbf{H}^{AI}$ and the model matrix up to 6th order $\tilde{\mathbf{H}}$

$$\delta h = \sqrt{\mathrm{Tr}\left(\tilde{\mathbf{H}} - \mathbf{H}^{AI}\right)^\dagger \left(\tilde{\mathbf{H}} - \mathbf{H}^{AI}\right)} \tag{5.4.4}$$

5.5 Crystal field parameters by AILFT method

This method was developed by Atanasov, in a first time with Daul using DFT calculations [103, 104] then with Neese for WFT [105]. The SO-CASSCF calculations provide the energies E_I and wave functions Ψ_I^{AI} of all M states arising from the $4f^N$ configuration. They are developed as

$$|\Psi\rangle_I^{AI} = \sum_{J=1}^{CI} C_{IJ}\,|\Phi\rangle_J \tag{5.5.1}$$

with Φ_J a Slater determinant with N occupied f orbitals. The Hamiltonian matrix $\mathbf{H}^{AI}$ is built in the basis of the $|\Phi\rangle_J$ expressed in terms of the real f orbitals. Since the *ab initio* f orbitals are close to pure metallic f orbitals, the correspondence with their model counterpart is easily performed. The model Hamiltonian of Eq. 5.2.1 depends on the parameters p_i , (i) the Slater-Condon parameters for electron-electron repulsion F^2 , F^4 and F^6, (ii) the 27 CFPs associated to f orbitals, i.e. one parameter for each independent ligand field matrix elements $\langle f_m\,|\hat{v}_{CF}|\,f_{m'}\rangle$, (iii) the effective one-electron SOC parameter $\xi\,(r)$. Its matrix $\mathbf{H}^{LFT}\,(p_i)$ is expressed in the same basis of Slater determinants as the electronic structure calculations. The correspondence element-by-element of the two matrices leads to the equations to be solved. The problem is by far over-determined, but all equations are linear in the unknowns.

Those $M\,(M-1)\,/2$ equations arise from $\mathbf{H}^{LFT}\,(p_i) = \mathbf{H}^{AI}$ (AI stand for *ab initio*) and may be written in the form

$$\mathbf{AP} = \mathbf{Y} \tag{5.5.2}$$

where $\mathbf{P} = \{p_i\}$. The parameter vector $\boldsymbol{P}$ is then determined by a least-square procedure according to

$$\mathbf{P} = \left(\mathbf{A}^{\dagger}\mathbf{A}\right)^{-1}\mathbf{A}^{\dagger}\mathbf{Y} \tag{5.5.3}$$

5.6 Crystal field parameters in the $[Ln^{III}(DPA)_3]^{3-}$ chelates

- *XRD structures and ab initio energy levels.*

The $Ln^{III}(DPA)_3(C_3H_5N_2)\cdot 3H_2O$; Ln=Ce−Yb series of compounds is isostructural.[2] The complexes have been structurally characterized by X-ray diffraction, except for Pr^{III}, and crystallize in the triclinic space group $P1$ [26]. The coordination sphere contains three DPA^{2-} ligands that form a distorted tricapped trigonal prism (see Fig. 5.3.1). Each of the DPA^{2-} is tri-coordinated with the metal center using the two carboylate-O atoms and the pyridine-N atom. The distances between the metal center and coordinated O atoms range from 2.51 (Ce−O) to 2.37 Å (Yb−O) and the distance of the coordinated N atoms changes from 2.63 (Ce−N) to 2.45 Å (Yb−N). The systematic decrease in the bond lengths along the series follows the trend of lanthanide contraction. Due to the presence of counter ions, the ternary symmetry is slightly distorted, and for a given complex, the distances between the metal ion and the three ligands differ by about 0.1 Å. The oxygen atoms are closer than the nitrogen ones, and are more electronegative, as confirmed by the LoProp charges [94] of around -0.77 on O and -0.32 on N respectively. The LoProp charges on central Ln^{III} ion is close to +2.50 for all along the series. The angle between the oxygen atoms and the pseudo C_3 axis is rather constant along the series at around 46°. This denotes that the coordinated ligand environment is prolate. The z axis is perpendicular to the plane formed by the three nitrogen atoms as shown in Fig. 5.3.1.

The energy levels from SO-CASSCF calculations in MOLCAS (denoted by M) and ORCA[3] (denoted by O) are tabulated in Table 5.1. Computational details are provided in Appendix A. In both softwares, the energy levels are almost similar in magnitude although they are calculated with different basis sets and with slightly different approximations. This shows a parallelism between the two codes at the CASSCF level. The ligand field splittings of the ground J manifolds of the Ln^{III} ions are plotted in Fig. 5.6.1 and the CFPs are extracted from the energy levels and the wave functions of the corresponding J manifold. The *ab initio* SF ground *LS* and the SO ground J manifolds are easily identifiable using three Hund's rules and usually they are well separated. In the lanthanide complexes, the energy splitting of the free-ion Hamiltonian (see Eq. 5.2.1) states follow

[2] All the $Ln^{III}(DPA)_3(C_3H_5N_2)\cdot 3H_2O$ compounds were synthesized by Claude Berthon *et al.* at CEA Marcoule, France.

[3] SO-CASSCF/AILFT calculations on $[Ln(DPA)_3]^{3-}$ complexes were performed by Dr. Julie Jung at Los Alamos National Laboratory (LANL), New Mexico, USA using ORCA. The results are discussed here for the sake of comparison with SO-CASSCF/ITO results in MOLCAS.

Table 5.1: Energy (in cm^{-1}) of the $[Ln^{III}(DPA)_3]^{3-}$ series calculated with SO-CASSCF. Ground J values are also given. The energies of the ground J manifolds are separated by horizontal lines.

	Ce		Pr		Nd		Sm		Eu		Tb		Dy		Ho		Er		Tm		Yb	
J	5/2		4		9/2		5/2		0		6		15/2		8		15/2		6		7/2	
	M	O	M	O	M	O	M	O	M	O	M	O	M	O	M	O	M	O	M	O	M	O
	0	0	0	0	0	0	0	0	0	0	0	0	0	0	0	0	0	0	0		0	0
	0	0	18	20	0	0	0	0	340	334	1	0	0	0	6	6	0	0	18	18	0	0
	349	349	43	47	48	46	75	74	367	360	56	65	19	20	7	8	20	22	53	55	42	41
	349	349	68	74	48	46	75	74	416	412	61	70	19	20	53	53	20	22	104	108	42	41
	390	391	144	145	155	157	120	125	1015	976	72	82	40	39	66	64	99	99	126	127	118	117
	390	391	152	156	155	157	120	125	1034	994	93	108	40	39	92	89	99	99	171	172	118	117
	2328	2311	255	261	300	298	1035	1029	1079	1037	97	183	61	55	114	112	130	131	194	200	229	232
	2328	2311	315	320	300	298	1035	1029	1106	1063	173	187	61	55	118	116	130	131	201	205	229	232
	2639	2615	471	476	374	369	1081	1070	1131	1084	177	202	99	94	128	127	181	182	231	241	10355	
	2639	2615	2286		374	369	1081	1070	1959	1856	191	205	99	94	180	176	181	182	239	249	10355	
	2805	2787	2294		2076		1176	1161	1994	1888	191	218	158	161	184	180	241	242	259	262	10403	
	2805	2787	2301		2076		1176	1161	2003	1896	209	220	158	161	212	210	241	242	268	275	10403	
	2914	2894	2317		2091		1255	1239	2005	1901	211		211	215	270	265	268	268	287	292	10516	
	2914	2894	2352		2091		1255	1239	2025	1918	2250		211	215	272	266	268	268	6825		10516	
			2363		2137		2325		2047	1939	2284		261	265	285	280	324	324	6839			
			2417		2137		2325		2052	1944	2295		261	265	296	292	324	324	6915			
			2430		2179		2349		2947		2329		3485		297	293	6675		6925			
			2555		2179		2349		2965		2339		3485		5185		6703		6930			

M: in MOLCAS, O: in ORCA

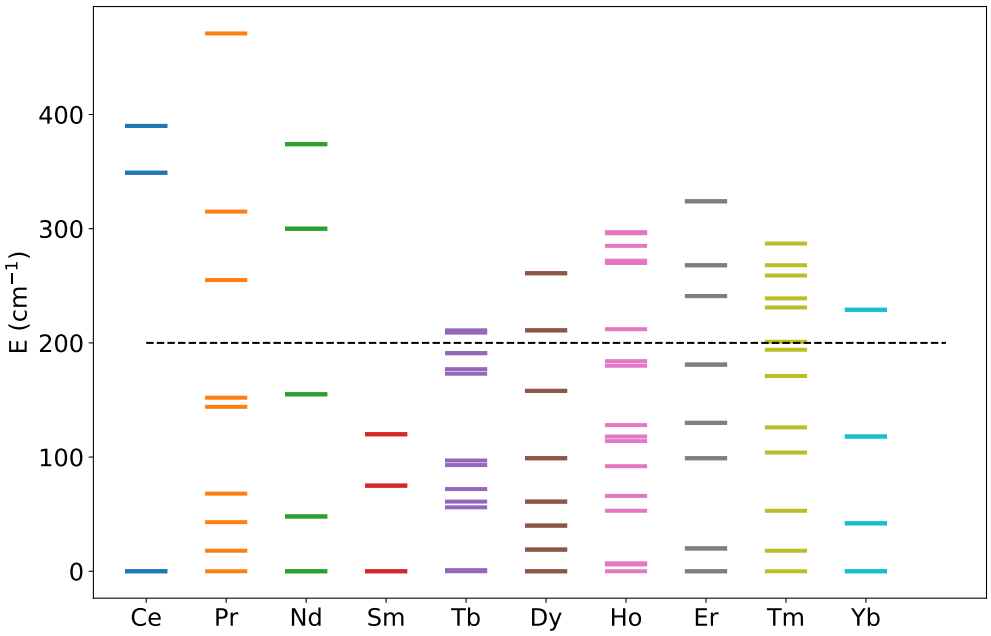

Figure 5.6.1: Ligand field splittings (in cm^{-1}) of the ground J manifolds in the $[Ln^{III}(DPA)_3]^{3-}$ series calculated with the SO-CASSCF method. Room temperature energy is shown by the horizontal line.

the order $\hat{V}_{res} \gg \hat{\mathscr{H}}_{SO} > \hat{V}_{CF}$. The ligand field splittings of the ground LS terms ranges from $500-1000$ cm^{-1} in SF-CASSCF calculations; they are larger in the first half of the series. The splitting of the ground J manifold by the ligand field is around 300 cm^{-1} quite less than the energy separation between the J and $J+1$ manifolds (see Table 5.1). The weight of the ground LS manifold to the ground J wave functions is around 98% quite larger that the An^{IV} series where it is 86-88%. This shows that the $J-J$ coupling is not as important in the Ln as it is in the An complexes. At room temperature (200 cm^{-1}), as a first approximation, all the states of a J manifold are significantly populated and the magnetic anisotropies of the states are canceling each other resulting in an isotropic Curie behavior of the magnetic properties. The anisotropy originates from the ligand field splitting of the J manifold and hence CFPs are useful to model it.

The anisotropic magnetic information of the ground state can be obtained by running experiments (such as EPR) at very low temperature. The nature of the ground state magnetic anisotropies of the Ln^{III} ions in a highly axial environment are nicely discussed in details in the article published by Rinehart and Long [114]. The energy levels of the Kramers ions (Ce^{III}, Nd^{III}, Sm^{III}, Dy^{III}, Er^{III}, Yb^{III}) with odd number of unpaired electrons are doubly degenerate i.e. the KDs. The magnetic properties of a KD are modeled with the **g** tensor. The principal g-factors of the ground KDs are listed in Table 5.2. The ground state magnetic anisotropies are axial for Ce^{III}, Nd^{III}, Dy^{III} ions, whereas they are planar for Sm^{III}, Er^{III}, Yb^{III}. The **g** tensor anisotropy axes are significantly deviated from the pseudo C_3 axis as shown by the value of α (the angle between the principal axis of $g_{\|}$

and z axis) in Table 5.2. This shows that the Hilbert space of the ground KD cannot be modeled with pure M_J states, rather they are highly mixed.

Table 5.2: g-factors of the ground KD for the $[Ln^{III}(DPA)_3]^{3-}$ series with odd number of electrons. $g_{\parallel}$ is the g-value whose principal axis is making the smallest angle α (in °)with the pseudo C_3 axis.

Ln	$g_{\perp}$	$g_{\perp}$	$g_{\parallel}$	$\alpha(°)$
Ce	0.9	0.4	2.2	7
Nd	3.0	1.9	2.6	42
Sm	0.1	0.8	0.2	35
Dy	4.3	1.0	14.6	42
Er	3.7	12.5	1.6	6
Yb	2.4	6.1	1.2	31

- *Crystal field and strength parameters.*

CFPs were calculated with both AILFT and ITO methods. For ITO, the manifolds with $J < 3$ do not provide CFPs of 6th order since the expansion of Eq. 5.4.1 is limited to $2J$. This artificially leads to smaller strength parameters S and S_q, due to the restricted sum of terms. To overcome this limitation, the CFPs of 6th order (and all orders for Eu^{III}) are deduced from the 1st excited J manifolds. The CFPs calculated by ITO and AILFT methods are tabulated in Tables 5.4 and 5.5. The one-to-one mapping of the *ab initio* states and the model states $|J,M_J\rangle$ of the free-ion are performed by minimizing the distances δm_u, defined in Eq. 5.4.3 with $u = x,y,z$ and they are tabulated in Table 5.3. The model and *ab initio* magnetization matrices differ more in the first half of the series, especially for Nd^{III} and Sm^{III}. In the second half of the series, the values of δm_u are smaller than the first half and they almost vanish for Yb^{III}. The same tendency is observed for δh (defined in Eq. 5.4.4) in Table 5.3 which quantifies the similarity of the *ab initio* and model matrices expanded up to the sixth order. This manifests that Ln^{III} ions in the second half of the series are more close to the free-ion than the first half ions which are more perturbed by the ligand field of the three DPA^{2-} ions. This is in agreement with the large ligand field splittings of the ^{2S+1}L or J terms of the free-ion (as shown in Fig. 5.6.1) obtained from CASSCF calculations in the first half of the series.

The two methods give similar CFPs. This confirms that CFPs extracted from orbital and many-electron levels are very close due to the small ZFS of the $4f$ orbitals. While B_0^2, B_0^4, B_0^6, $\bar{B}_3^4$, $\bar{B}_3^6$, and $\bar{B}_6^6$ are worth several hundred wave numbers, all the other parameters are smaller than 100 cm^{-1}. This is in agreement with the approximate threefold symmetry of the complexes. These six dominant CFPs are plotted for the series in Fig. 5.6.2.

Table 5.3: δm_u $(u = x,y,z)$ (in μ_B) and δh (in cm^{-1}) distances between *ab initio* and model matrices for the $[Ln^{III}(DPA)_3]^{3-}$ complexes.

Ln	g_J	δm_x	δm_y	δm_z	δh
Ce	6/7	0.30	0.30	0.23	0
Pr	4/5	0.30	0.28	0.17	18
Nd	8/11	0.51	0.48	0.18	36
Sm	2/7	0.55	0.60	0.28	0
Tb	3/2	0.23	0.25	0.17	3
Dy	4/3	0.24	0.22	0.19	6
Ho	5/4	0.22	0.21	0.18	3
Er	6/5	0.13	0.13	0.09	2
Tm	7/6	0.06	0.06	0.04	3
Yb	8/7	0.03	0.03	0.02	0

Table 5.4: CFPs (in cm^{-1}) in the $[Ln^{III}(DPA)_3]^{3-}$ series calculated with ITO.

Ln	B_0^2	$\tilde{B}_1^2$	$\tilde{B}_2^2$	B_0^4	$\tilde{B}_1^4$	$\tilde{B}_2^4$	$\tilde{B}_3^4$	$\tilde{B}_4^4$	B_0^6	$\tilde{B}_1^6$	$\tilde{B}_2^6$	$\tilde{B}_3^6$	$\tilde{B}_4^6$	$\tilde{B}_5^6$	$\tilde{B}_6^6$
Ce	276	66	61	-720	26	75	985	71	-687	30	94	897	10	107	838
Pr	206	67	58	-648	41	69	749	31	-523	29	88	662	43	88	774
Nd	123	90	59	-540	22	39	524	17	-423	32	75	602	48	98	733
Sm	217	58	79	-260	45	60	477	99	-362	22	76	412	31	64	636
Eu	240	71	36	-206	10	86	457	38	-491	35	60	335	42	86	490
Tb	223	77	54	-445	16	50	456	13	-471	45	33	397	27	47	628
Dy	207	83	55	-414	8	47	362	31	-340	25	49	337	31	50	546
Ho	211	82	51	-317	7	29	287	20	-327	21	43	317	28	44	500
Er	265	76	41	-319	12	43	317	44	-331	10	43	290	13	36	461
Tm	223	90	57	-258	3	31	249	24	-278	21	38	264	28	41	437
Yb	210	90	52	-251	3	27	222	17	-274	19	36	238	29	35	394

Table 5.5: CFPs (in cm^{-1}) in the $[Ln^{III}(DPA)_3]^{3-}$ series calculated with AILFT.

Ln	B_0^2	$\bar{B}_1^2$	$\bar{B}_2^2$	B_0^4	$\bar{B}_1^4$	$\bar{B}_2^4$	$\bar{B}_3^4$	$\bar{B}_4^4$	B_0^6	$\bar{B}_1^6$	$\bar{B}_2^6$	$\bar{B}_3^6$	$\bar{B}_4^6$	$\bar{B}_5^6$	$\bar{B}_6^6$
Ce	282	78	62	-740	35	52	941	48	-510	15	113	789	40	120	889
Pr	278	70	69	-672	31	55	823	37	-513	13	98	710	33	95	856
Nd	265	79	60	-589	23	48	699	34	-478	13	85	627	19	89	779
Sm	240	83	56	-471	17	43	525	31	-403	14	67	487	18	71	649
Eu	239	85	54	-427	18	38	466	29	-380	15	60	442	17	65	599
Tb	223	76	50	-351	11	41	363	21	-335	12	49	358	20	49	522
Dy	234	81	54	-325	13	38	328	22	-327	12	47	333	20	47	496
Ho	236	79	49	-294	10	31	289	19	-310	11	40	301	19	39	460
Er	238	75	44	-272	10	31	260	17	-296	12	38	276	17	36	435
Tm	236	85	54	-251	11	31	233	18	-278	12	36	253	20	36	409
Yb	230	87	50	-239	9	27	213	18	-266	12	32	232	19	30	392

Indeed, within the trigonal C_3 point group, only those six CFPs would be non-zero. B_0^2 is positive while B_0^4 and B_0^6 are negative, and the remaining three CFPs are of the same order of magnitude. The positive sign of B_0^2 is in agreement with prolate environment of the ligands field around the metal center. All the CFPs are transferable along the series with an overall decrease in magnitude. This confirms that the effects of ligands and central ion are decorrelated and independently described by the parameters B_q^k and α_J^k of Eq. 5.3.1, respectively. In the case of high axial symmetry as the assumptions taken in Ref. [114], the energy splitting of the $|M_J|$ states can be modeled with only one CFP B_0^2 as

$$E_{|M_J|} = \alpha_J^2 B_0^2 \left\langle J, M_J \left| \hat{O}_0^2 \right| J, M_J \right\rangle \quad (5.6.1)$$

$$= \alpha_J^2 B_0^2 \left(3M_J^2 - J(J+1)\right) \quad (5.6.2)$$

The sign of α_J^2 alternates in every quarter of the Ln series. If the sign of B_0^2 is positive; when $\alpha_J^2 > 0$, the lower energy states are dominated by the lower M_J values and vice versa. So according to it, the nature of the ground state magnetization alternates between planar and axial following the sign of α_J^2. In the case of Ce^{III}, Nd^{III} and Dy^{III} α_J^2 is negative where as for Sm^{III}, Er^{III} and Yb^{III}, it is positive. So one would expect that the ground state magnetization should be axial for the former while it is planar for the later trio. These trends are hardly reproduced in the *ab initio* **g** tensor of the ground KD i.e. one can still be able to assign the axiality or planarity. However since the 4th and 6th orders CFPs, as well as the ternary non-diagonal parameters are non-negligible, the ground states are by far from modeling them with the pure M_J eigenstates. Another domain in which CFPs are successfully applied is the modeling of paramagnetic NMR shifts of lanthanide complexes. According to Bleaney's formula in Eq. 2.6.34, the pseu-

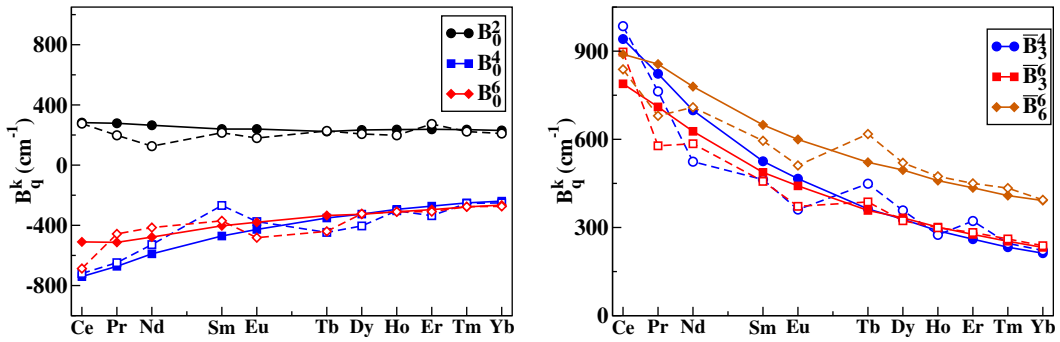

Figure 5.6.2: Dominant CFPs in the $[Ln^{III}(DPA)_3]^{3-}$ series. Full line: AILFT; dashed line: ITO

docontact shifts in the axially symmetric Ln^{III} complexes depend on the 2nd order CFP B_0^2 (in Stevens notation, $B_0^2 = 2A_2^0\langle r^2\rangle$). B_0^2 can be evaluated from pNMR shifts within the lanthanide series, assuming it is constant throughout the series. In Ref. [26], pNMR shifts in the $[Ln^{III}(DPA)_3]^{3-}$ series were measured and modeled according to Bleaney's theory, and B_0^2 was determined to be 51 with an arbitrary unit applying. This corresponds to 62 cm^{-1} after unit conversion. This value is four times smaller than the value of 250 cm^{-1} obtained from *ab initio* calculations. However, it should be noted from Fig. 5.6.2 that B_0^2 is almost constant across the series and is the only CFP showing this trend, which supports Bleaney's theory. It shows that Bleaney's B_0^2 which parametrizes the entire magnetic anisotropy according to Eq. 2.6.34 in a single parameter, is not clearly related to the "true" B_0^2.

The strength parameters are tabulated in Tables 5.6 and 5.7 and the dominated parameters are represented in Fig. 5.6.3. As discussed in Section 5.3, the strength parameter S defined by Eq. 5.3.7 gathers in only one parameter the 27 CFPs and allows an easy evaluation of the strength of the metal-ligand interaction. This facilitates the comparison between two complexes. The CFPs decrease in magnitude along the series. In the pure electrostatic picture, according to Eq. 5.2.11, the CFPs are determined by the position and charge of the ligands, as well as by the radial expansion of the $4f$ orbitals. Due to the lanthanide contraction along the series, the ionic radius decreases and concomitantly the $4f$ orbitals are becoming more inner shell. As a consequence, the coordination sphere shrinks along the series. In an isostructural series, the structural changes are smooth and, as a first approximation, because they are determined only by the ligands, the CFPs may be considered as transferable from one lanthanide ion to another inside a series, as observed by Abragam and Bleaney [36]. Figure 5.6.3 denotes a smooth variation of the CFPs; one may say, as a first approximation, that they are transferable from one ion to the next one with a small variation. But one may not say that they are constant across the whole series. As was shown in Ref. [115], the trends in the many-electron spectra are

much more tricky to analyze, because of the large variation of the α_J^k, especially of α_J^2 which changes three times of sign along the series.

Table 5.6: Strength parameters (in cm^{-1}) in the $[Ln^{III}(DPA)_3]^{3-}$ series calculated with ITO.

Ln	S	S^2	S^4	S^6	S_0	S_1	S_2	S_3	S_4	S_5	S_6
Ce	434	136	525	521	330	45	64	583	34	42	329
Pr	350	108	416	428	276	48	60	438	22	35	304
Nd	292	88	306	394	222	59	51	342	20	38	288
Sm	241	115	248	316	164	43	65	277	48	25	249
Eu	218	119	230	274	186	47	52	252	24	34	192
Tb	249	116	262	321	221	52	43	265	12	18	246
Dy	212	112	221	271	191	54	46	216	19	20	214
Ho	187	112	173	251	168	53	39	184	14	17	196
Er	188	130	186	234	184	49	37	188	21	14	181
Tm	166	120	147	216	153	58	42	157	16	16	171
Yb	153	115	135	197	147	57	38	140	14	14	155

Table 5.7: Strength parameters (in cm^{-1}) in the $[Ln^{III}(DPA)_3]^{3-}$ series calculated with AILFT.

Ln	S	S^2	S^4	S^6	S_0	S_1	S_2	S_3	S_4	S_5	S_6
Ce	417	141	509	492	311	52	64	541	27	47	349
Pr	381	139	449	462	293	47	63	478	22	37	336
Nd	337	134	385	417	265	51	55	411	18	35	306
Sm	269	124	294	340	221	53	49	313	16	28	255
Eu	247	124	263	312	207	55	45	280	15	25	235
Tb	206	115	209	267	180	48	42	221	13	19	205
Dy	195	121	190	253	176	52	43	202	13	18	194
Ho	180	121	169	233	168	50	38	180	11	15	180
Er	169	120	154	219	162	48	35	164	11	14	171
Tm	160	123	139	205	155	54	40	148	11	14	160
Yb	152	121	129	194	150	55	36	135	11	12	154

The variation of the CFPs along the series is smoother with AILFT than with ITO (see Fig. 5.6.2). In the first half, the ITO values are smaller than the AILFT values, while the opposite trend is found in the second half. Also, there are more irregularities in the ITO values, especially in the first half of the series. In the first half, the value of J is small according to 3rd Hund's rule, and the different J manifolds are closer to each other according to Landé rule. One could suspect the SOC between the J manifolds to be at the origin of those irregularities. The CFPs deduced before and after the inclusion of SOC, within the L and

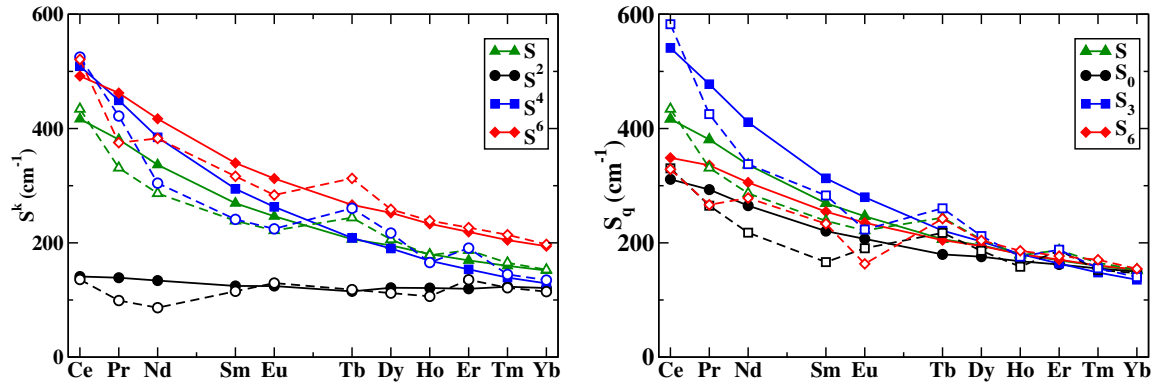

Figure 5.6.3: Strength parameters for the $[Ln^{III}(DPA)_3]^{3-}$ series. Full line: AILFT; dashed line: ITO.

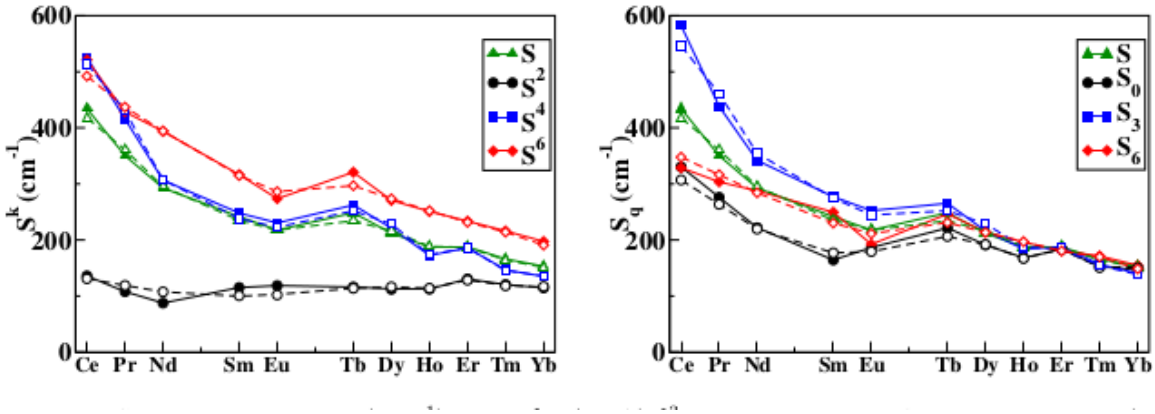

Figure 5.6.4: Strength parameters (in cm^{-1}) in the $[Ln^{III}(DPA)_3]^{3-}$ series calculated from the ground J (plain line) and the L (dashed line) manifolds.

J ground manifolds, respectively, are shown on Fig. 5.6.4. They are found to be very similar.

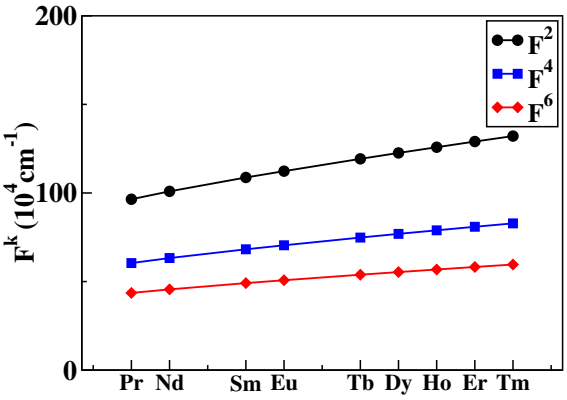

Figure 5.6.5: Slater-Condon parameters (in cm^{-1}) in the $[Ln^{III}(DPA)_3]^{3-}$ series.

It shows that the $J-J$ coupling, which is more important in the beginning of the series, does not affect the CFPs. The Slater–Condon parameters, which describe the electron–electron interaction, increase (see Fig. 5.6.5). These tendencies show that the overlap of the metallic and ligand orbitals, which is tiny, decreases in the series. Finally, the difference between AILFT and ITO CFPs should be imputed to electron-electron effects. The former method determines the CFPs at the one-electron level, while the parameters for electron-electron repulsion and SOC are determined independently with additional parameters. In the ITO method, the CFPs are determined from the decomposition of the many-electron wave functions, and describe the other interactions in an effective way. One may not conclude that one approach is more reliable than the other one: AILFT provides one-electron CFPs and, with the knowledge of Slater-Condon parameters and the SOC constant, the energy of all the states arising from the $4f^N$ configuration might be calculated. The ITO technique provides effective many electron CFPs, and is specific to each *J* manifold. For magnetic properties which arise only from the ground *J* manifold, ITO are recommended since they reproduce exactly the energies of this manifold, while for spectrocopies involving excited *J* manifolds, AILFT are more suitable.

Point charge model

In order to analyze those variations, a point charge (PC) model has been considered, where each atom of the ligands is represented by a PC deduced from its LoProp *ab initio* value. The electrostatic potential created by the PC model and the *ab initio* ligands are similar (see Table 5.8). The PC and *ab initio* strength parameters are compared in Figure 5.6.6.

The PC strength parameter is rather constant in the series. Since the dipole and quadrupole moments determined from both models are almost identical, the difference between PC and *ab initio* calculations represent covalent contributions, which include combined effects of bonding, charge donation and polarization. In the electrostatic model, the CF is axial and dominated by 2nd order terms (S^2 and S_0 dominant), while the other terms are almost negligible. This prevalence of the 2nd order for electrostatic models was already observed in $PrCl_3$ and sandwich complexes [115]. It confirms that 4th, 6th and non-axial

Table 5.8: Dipole d_u (in D) and quadrupole Q_{uv} (in $D \cdot Å$) moments in the $[Ln^{III}(DPA)_3]^{3-}$ series, full *ab initio* (AI) and with the point charge model (PC).

Ln		d_x	d_y	d_z	Q_{xx}	Q_{xy}	Q_{xz}	Q_{yz}	Q_{yz}	Q_{zz}
Ce	AI	1.55	1.22	1.01	17.11	-5.48	3.00	42.02	4.68	-59.13
	PC	1.42	1.30	-1.10	19.05	-5.08	2.77	43.38	4.70	-62.43
Pr	AI	-1.02	1.10	0.88	19.37	7.81	4.25	41.21	-4.39	-60.58
	PC	-0.85	1.17	0.98	20.83	7.73	4.21	42.04	-4.43	-62.87
Nd	AI	-1.05	1.41	0.74	19.90	7.90	4.49	41.08	-3.80	-60.98
	PC	-0.90	1.48	0.81	21.50	7.65	4.24	42.00	-3.84	-63.51
Sm	AI	-0.92	1.46	0.63	20.94	7.75	4.26	41.07	-3.70	-62.02
	PC	-0.75	1.53	0.71	22.50	7.48	4.00	42.04	-3.85	-64.54
Eu	AI	-0.99	1.55	0.63	21.17	7.15	3.88	41.30	-3.45	-62.48
	PC	-0.85	1.60	0.70	23.16	6.97	3.77	41.93	-3.72	-65.08
Tb	AI	0.96	1.28	-0.57	20.12	-3.82	2.66	42.77	4.08	-62.90
	PC	0.79	1.38	-0.67	21.76	-3.74	2.36	43.76	4.23	-65.52
Dy	AI	-0.91	1.42	0.58	21.90	6.67	4.03	41.42	-3.83	-63.31
	PC	-0.75	1.50	0.66	23.39	6.45	3.81	42.38	-3.94	-65.77
Ho	AI	-0.76	1.40	0.52	22.32	6.38	3.84	41.30	-3.57	-63.62
	PC	-0.59	1.46	0.61	23.88	6.20	3.61	42.46	-3.67	-66.34
Er	AI	0.94	1.31	-0.37	21.01	-3.08	2.85	41.99	3.90	-63.00
	PC	0.77	1.40	-0.44	22.76	-3.04	2.52	43.02	4.08	-65.78
Tm	AI	-0.87	1.45	0.54	22.50	5.97	3.90	41.35	-3.31	-63.84
	PC	-0.69	1.51	0.63	24.11	5.83	3.65	42.57	-3.52	-66.68
Yb	AI	-0.80	1.42	0.51	22.97	5.79	3.77	40.87	-3.73	-63.84
	PC	-0.62	1.51	0.59	24.67	5.78	3.35	42.15	-3.85	-66.82

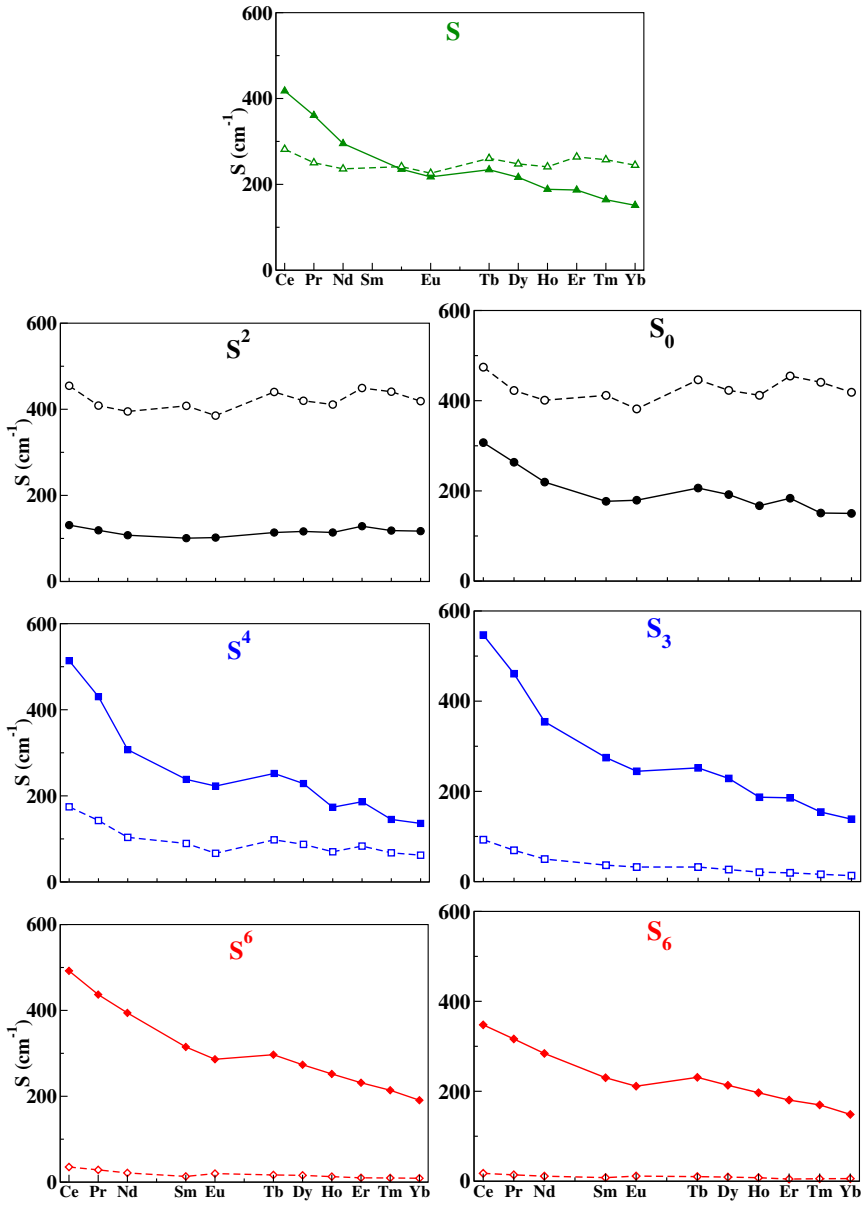

Figure 5.6.6: Strength parameters for the $[Ln^{III}(DPA)_3]^{3-}$ series determined by the ITO method. Full line: *ab initio*; dashed line: PC model.

contributions arise mostly from non-electrostatic effects, as polarization of f orbitals, orthogonality issues, electron correlation and covalent effects. As already mentioned, the PC model leads to a rather constant value of S. The difference between the *ab initio* and the PC curves is rather constant for the 2nd order, and tends to decrease for the 4th and 6th orders.

In a pure electrostatic picture, the closer the charges, the larger the interaction and the CFPs. But the trend along a series is not as simple since there are two opposite effects: i) according to the contraction of the $4f$ orbitals, the CFPs should decrease, but ii) following the shrinking of the coordination sphere, the CFPs should increase. As mentioned before, the contraction of the coordination sphere and the decrease in the spatial distribution of

the $4f$ electrons lead to opposite trends along the series, and the interweaved effects lead to a rather constant value of S. Consequently, the decrease of the strength parameters which is observed in Figure 5.6.6 with the full ligands arises from the overlap between the lanthanide and ligand orbitals, namely covalent effects. The $4f$ being inner shell, they participate little to the covalent bonding itself, which involves mostly $5s$, $5p$ and $6d$ orbitals. It was shown in Ref. [115], that both the direct overlap between the $4f$ and the orbitals of the ligands, and the indirect interaction through the more outer shell orbitals affect the CFPs. As in this previous work, covalent effects reduce the CFPs of 2nd order and increase the other CFPs, and more specifically the off-diagonal terms with $q \neq 0$.

5.7 CFPs in the $[An^{IV}(DPA)_3]^{2-}$ chelates

- *XRD structures and ab initio energy levels.*

The $An^{IV}(DPA)_3(C_3H_5N_2)\cdot 3H_2O$ compounds where An = Th, U, Np and Pu are isostructural and crystallize in the monoclinic space group $P21/c$.[4] The structures are quite analogues to that of Ln^{III} ions except with the longer metal-ligand coordinate bonds. From Th^{IV} to Pu^{IV}, the An−O and An−N distances decrease from 2.427 to 2.354 Å and 2.598 to 2.500 Å, respectively. The distances follow the trends of the contraction of ionic radius along the series. It is observed that the Ln^{III}−O and An^{IV}−O distances are similar for the same ionic radius whereas the An^{IV}−N distances are significantly longer (0.1 Å) than the Ln^{III}−N distances [23]. The LoProp charges on the coordinating O and N atoms are −0.81 and −0.35, respectively, and those on the metal center ranges from 3.17 (U^{IV}) to 3.21 (Pu^{IV}). Their magnitudes suggest that quite larger charge transfer mechanisms (LMCT, MLCT, LLCT) are interweaving in the $[An^{IV}(DPA)_3]^{2-}$ than those in the $[Ln^{III}(DPA)_3]^{3-}$ series.

First principles calculations were performed for the $[An^{IV}(DPA)_3]^{2-}$ series on the crystallographic structures with SF-CASSCF, SO-CASSCF, SO-NEVPT2[5] and SO-CASPT2 methods. In the actinide complexes, the energy splitting of the free-ion Hamiltonian states according to Eq. 5.2.1 follows the order $\hat{V}_{res} \gg \hat{V}_{CF} \approx \hat{\mathscr{H}}_{SO}$ i.e. the ligand field splitting is in the same order of the SO splitting. At the SF level, the states arising from the ground *LS* free-ion term split due to the interaction with the ligands, but the splitting is smaller than the energy difference with the next *LS* manifold, and the states of the complex may be labeled after the free-ion *LS* term. At SO level, the free-ion J terms are rather close

[4] All the $An^{IV}(DPA)_3(C_3H_5N_2)\cdot 3H_2O$ compounds were synthesized by Claude Berthon *et al.* at CEA Marcoule, France.

[5] SO-NEVPT2/AILFT calculations on $[An^{IV}(DPA)_3]^{2-}$ complexes were performed by Dr. Julie Jung at Los Alamos National Laboratory (LANL), New Mexico, USA using ORCA. The results are discussed here for the sake of comparison with the SO-(SS/MS)CASPT2/ITO results in MOLCAS.

in energy, the $J-J$ mixing is important, and the different J manifolds overlap. The *ab initio* SO energy levels are given in Table 5.9. The ground *LS* term spreads over about 2800 cm^{-1} for U^{IV}, 3500 cm^{-1} for Np^{IV}, and 4000 cm^{-1} for Pu^{IV}. It is much larger than for the $[Ln^{III}(DPA)_3]^{3-}$ complexes ($500-1000$ cm^{-1}) because in the An, the $5f$ orbitals interact more with the ligand orbitals. The CASPT2 and NEVPT2 energies are different, which is expected since the two methods are based on different formalisms. The energy splittings of the ground *LS* terms are generally larger with NEVPT2 than with CASPT2. SSCASPT2 and MSCASPT2 do not provide the same energies: with SSCASPT2, the perturbation is calculated individually for each CASSCF state while with MSCASPT2, an effective coupling between the CASSCF states is estimated, hence leading to different wave functions and different energies. The energy of the second *LS* manifold is lowered, due to a larger compactness of the electron density, and consequently a larger dynamical correlation. The largest deviation between NEVPT2 and CASPT2 is reached for the U^{IV} complex, especially for SSCASPT2 with a deviation of 700 cm^{-1}. The deviation between the different methods is about 100 cm^{-1} for the ground *LS* manifold, and can reach 1000 cm^{-1} for the 2nd *LS* manifold. At SO level, the inclusion of dynamical correlation does not impact strongly the overall splitting of the ground J term, but it impacts the energy of the different states arising from this term. In SO calculations, the overall splitting of the ground J term is 1500 cm^{-1}, to be compared to 300 cm^{-1} in the analog Ln^{III} series. This splitting depends only slightly on the method: with SO-NEVPT2, it is always larger than with SO-CASSCF, and more generally, all energies of the ground J manifold are larger. Conversely, there is no systematic trend for CASPT2: it may decrease or increase the energy of the second J manifold, depending on the method. The weight of the ground *LS* manifold to the ground J wave functions is 86-88% for the three complexes at different levels of calculations while close to 98% in the Ln^{III} series, much higher than the An^{IV}. This indicates a strong $J-J$ mixing in the An due to the larger SOC in the An compared to Ln. In all cases, the $J-J$ mixing occurs mostly from the states arising from the terms ^1G for U^{IV}, ^2H for Np^{IV} and ^3D for Pu^{IV}. The magnetic g-factors of the ground KD of Np^{IV} are: 2.82, 2.46, 1.92 with SO-CASSCF, 2.73, 2.61, 1.93 with SO-SSCASPT2, and 3.43, 1.28, 0.42 with SO-MSCASPT2: the SO-MSCASPT2 values are different since this method affects the composition of the wave functions.

- *Crystal field and strength parameters*.

The CFPs have been deduced from the *ab initio* calculations using both the AILFT and ITO methods and tabulated in Table 5.11. Six CFPs i.e. $B_0^2, B_0^4, B_0^6, \bar{B}_3^4, \bar{B}_3^6, \bar{B}_6^6$ are again dominated in accordance with the trigonal symmetry. Like the $[Ln^{III}(DPA)_3]^{3-}$ complexes, B_0^2 is positive while $\bar{B}_0^4$ and $\bar{B}_0^6$, are negative. However, since the ITO is essentially a matrix decomposition technique, in the case of $J=4$ (U^{IV}, Pu^{IV}) or $9/2$ (Np^{IV}), the

Table 5.9: Energy (in cm^{-1}) of the $[An^{IV}(DPA)_3]^{2-}$ series from SO-CASSCF (CAS), SO-SSCASPT2 (SS-PT2), SO-MSCASPT2 (MS-PT2) and SO-NEVPT2 (NEV) calculations. The energies of the ground *J* manifolds are separated by horizontal lines.

U^{IV}					Np^{IV}					Pu^{IV}				
CAS(O)	CAS(M)	SSPT2(M)	MSPT2(M)	NEV(O)	CAS(O)	CAS(M)	SSPT2(M)	MSPT2(M)	NEV(O)	CAS(O)	CAS(M)	SSPT2(M)	MSPT2(M)	NEV(O)
0	0	0	0	0	0	0	0	0		0	0	0	0	0
41	50	100	200	85	0	0	0	0		95	96	113	150	119
201	199	194	204	238	138	139	90	44	161	460	460	508	525	526
218	212	230	380	258	138	139	90	44	161	465	467	546	583	537
346	355	236	393	426	517	518	474	465	606	556	557	620	612	647
442	449	316	474	543	517	518	474	465	606	682	700	706	727	855
945	944	843	950	1091	991	999	939	894	1154	1021	1039	1112	1152	1262
1049	1049	966	1037	1205	991	999	939	894	1154	1059	1078	1162	1237	1304
1499	1505	1413	1591	1731	1247	1246	1225	1196	1456	1344	1388	1549	1522	1653
5335	5329	4789	4378	4545	1247	1246	1225	1196	1456	5103	4853	4983	4991	5457
5352	5345	4805	4471	4578	6079	6010	6173	6084	6389	5179	4935	5028	5088	5556
6115	6100	5235	5177	4816	6079	6010	6173	6084	6389	5229	4988	5091	5134	5621
6125	6112	5268	5220	4892	6117	6045	6222	6189	6426	5455	5247	5445	5415	5914
6221	6185	5381	5357	4905	6117	6045	6222	6189	6426	5464	5264	5465	5497	5929
6309	6260	6301	6307	6371	6269	6200	6403	6289	6600	5552	5337	5497	5529	6043
6518	6490	6372	6557	6414	6269	6200	6403	6289	6600	5560	5339	5523	5537	6060
	6618	6477	6611			6382	6586	6553			5382	5592	5608	
	6634	6549	6654			6382	6586	6553			5397	5686	5740	
	6854	6835	6911			6490	6703	6715			5485	5738	5809	

(O): in ORCA, (M): in MOLCAS

expansion sums up to 8th order for the decomposition of the *ab initio* $\mathbf{H}^{AI}$. In the frame of CFT with wave functions built with pure f orbitals, according to Eqs. 5.2.15 and 5.2.17 the terms of orders larger than 6 vanish due to the $3j$ symbol selection rules. The larger δh, the more important terms of 8th order are. In Table 5.10 , the values of δh are larger than in the Ln^{III} analog series, but are still reasonably small, which proves the reminiscence of the free-ion electronic structure. The largest δh are found for the Pu^{IV} derivative, when SOC is included, in accordance with the CFPs for the Pu^{IV} derivative being more different between AILFT and ITO. While δh is worth at most 40 cm^{-1} in the Ln^{III} series, it is worth up to 100 cm^{-1} in the An^{IV} series. It shows that the 8th order terms are not completely negligible in actinide complexes: the effect of the 8th order on the matrix elements and eigenvalues is of several 10 of cm^{-1}. This might have a quantitative effect but the fundamentals of CFT keeps qualitatively correct for those actinide complexes. The one-to-one mapping of the *ab initio* states and the models states $|J,M_J\rangle$ are performed by minimizing the distances δm_u, defined in Eq. 5.4.3 with $u = x,y,z$ and they are tabulated in Table 5.10. The model and *ab initio* magnetization matrices differ more in the $[An^{IV}(DPA)_3]^{2-}$ complexes than the analog Ln^{III} series. The central metal ion in the $[Pu^{IV}(DPA)_3]^{2-}$ is by far the most deviated from the free-ion character as noticed by the large values of δm_u.

Table 5.10: δm_u (in μ_B) and δh (in cm^{-1}) distances between *ab initio* and model matrices for the $[An^{IV}(DPA)_3]^{2-}$ complexes.

	δm_x	δm_y	δm_z	δh
	U^{IV}			
SF-CASSCF	0.90	0.92	0.89	761
SO-CASSCF	0.51	0.5	0.49	80
SO-SSCASPT2	0.49	0.48	0.42	124
SO-MSCASPT2	0.51	0.5	0.49	199
	Np^{IV}			
SF-CASSCF	0.53	0.53	0.56	300
SO-CASSCF	0.7	0.73	0.39	171
SO-SSCASPT2	0.73	0.75	0.4	219
SO-MSCASPT2	0.69	0.77	0.35	142
	Pu^{IV}			
SF-CASSCF	0.45	0.45	0.48	214
SO-CASSCF	1.03	0.99	0.39	217
SO-SSCASPT2	1.94	2.12	0.51	488
SO-MSCASPT2	1.13	1.15	0.39	256

The Slater–Condon and SOC parameters are plotted in Fig. 5.7.1. The Slater-Condon parameters increase in the series in accordance with the contraction of $5f$ orbitals and to the increase of the number of electrons. F^4 and F^6 are similar to the experimental ones while

Table 5.11: CFPs (in cm^{-1}) in the $[An^{IV}(DPA)_3]^{2-}$ series calculated with AILFT and ITO.

		B_0^2	$\bar{B}_1^2$	$\bar{B}_2^2$	B_0^4	$\bar{B}_1^4$	$\bar{B}_2^4$	$\bar{B}_3^4$	$\bar{B}_4^4$	B_0^6	$\bar{B}_1^6$	$\bar{B}_2^6$	$\bar{B}_3^6$	$\bar{B}_4^6$	$\bar{B}_5^6$	$\bar{B}_6^6$
								U^{IV}								
ITO	SF-CASSCF	935	218	38	-1538	397	206	3231	86	-1005	120	67	2439	58	190	3345
	SO-CASSCF	662	217	26	-2324	382	172	3006	80	-1056	64	32	1368	58	132	1780
	SO-SSCASPT2	552	168	50	-1354	349	192	3193	42	-886	41	87	1127	128	75	1447
	SO-MSCASPT2	477	88	32	-1269	56	344	3647	332	-1146	104	490	1054	273	98	1422
AILFT	SO-CASSCF	647	280	35	-2202	574	135	3034	138	-1681	40	259	2541	279	118	3210
	SO-NEVPT2	553	227	26	-1729	473	92	2495	128	-1488	34	239	2388	259	98	3095
								Np^{IV}								
ITO	SF-CASSCF	970	193	24	-1373	264	42	1940	56	-1729	176	65	2345	157	287	3099
	SO-CASSCF	329	179	40	-1927	221	58	1732	73	-1127	118	62	1959	125	256	2460
	SO-SSCASPT2	254	163	62	-1788	305	130	2053	66	-1121	175	39	2005	125	242	2316
	SO-MSCASPT2	-181	291	146	-1920	421	272	2533	127	-624	198	161	1897	134	288	2252
AILFT	SO-CASSCF	619	206	6	-1930	469	119	2507	99	-1747	44	193	2326	196	115	3102
	SO-NEVPT2	496	166	5	-1435	355	90	1934	78	-1321	32	141	1713	137	86	2337
								Pu^{IV}								
ITO	SF-CASSCF	252	140	24	-1623	469	148	2374	111	-1599	35	195	2385	168	183	2848
	SO-CASSCF	1016	182	201	-174	70	10	292	6	-137	4	16	164	6	12	189
	SO-SSCASPT2	654	425	453	359	180	37	195	236	-167	78	71	95	100	34	99
	SO-MSCASPT2	1624	122	361	-199	65	34	312	27	-129	3	20	186	10	18	196
AILFT	SO-CASSCF	622	171	27	-1910	502	168	2356	84	-1689	40	183	2218	156	155	2911
	SO-NEVPT2	482	130	20	-1434	382	128	1792	63	-1394	33	146	1804	127	128	2389

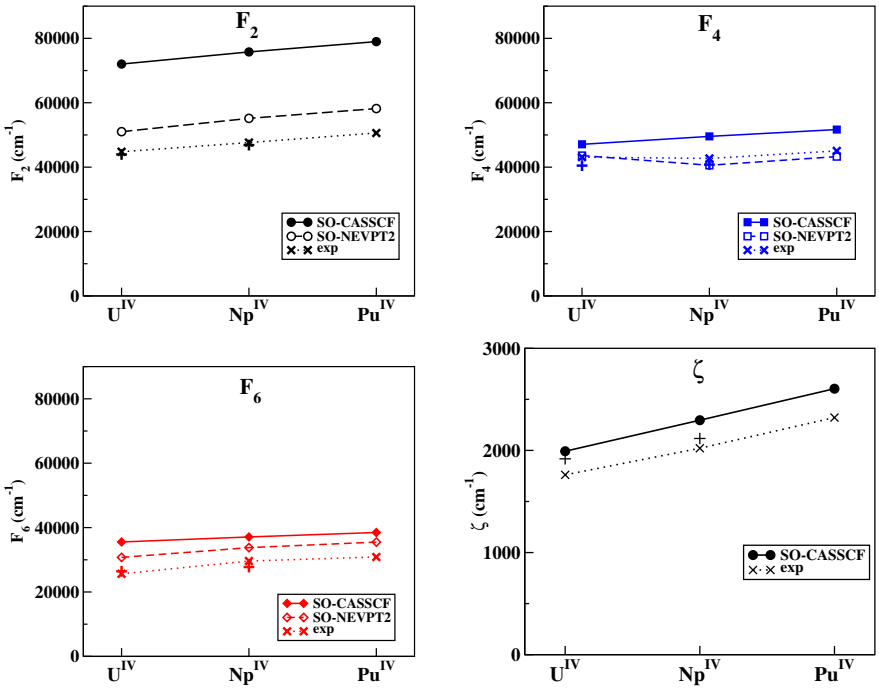

Figure 5.7.1: Slater-Condon parameters (cm^{-1}) in the $[An^{IV}(DPA)_3]^{2-}$ series.

F^2 is larger, as it was the case for the $[AnCl_6]^{3-}$ [95]. As discussed in Ref. [95], it might be due to the incomplete description of the dynamical correlation, and to the different definition of the parameters, since the fitting of experimental data include more terms, as for example three body terms. The SOC parameter ξ is slightly overestimated with respect to experiment, but the trend is the same. It increases in the series following the increase of the nuclear charge and follows the trends described in Ref. [95]. The nephelauxetic reduction factors $\alpha = \left(1 - p/p^{FI}\right) \times 100$ where p and p^{FI} represent the value in the complex and in the free-ion respectively for inter-electronic repulsion integrals and the SOC parameter have been deduced, and compared to the Ln^{III} analog series, using the free-ion values of Ref. [95] in Fig. 5.7.2. This reduction arises from covalent effects, both due the electron "cloud expansion" (delocalization) on the ligands and to a the better shielding the nucleus [116]. At the CASSCF level, the reduction is about 5%, which is slightly smaller than in the series, where it is about 6%, but much larger than in the Ln^{III} analog series where for the beginning of the series, it is only worth 2%. It is much smaller than in $3d$ transition metal complexes [117].

The strength parameters are tabulated in Table 5.12 and the largest parameters are represented in Fig. 5.7.3. The total strength parameter S is reduced in the ITO method from U^{IV} to Pu^{IV} with a sharp decrease for Pu^{IV} in the SO calculation. The 2nd order strength parameter S^2 is around 300 cm^{-1}, against 150 cm^{-1} in the Ln^{III} series, while the 4th and 6th orders S^4 and S^6 are around 1200 cm^{-1}, against 300 cm^{-1} in the Ln^{III} series. While S^2 , S^4 and S^6 are rotation invariants, the S_q strength parameters are not. The CFPs may be deduced from the ground L manifold using SF-CASSCF energies and wave func-

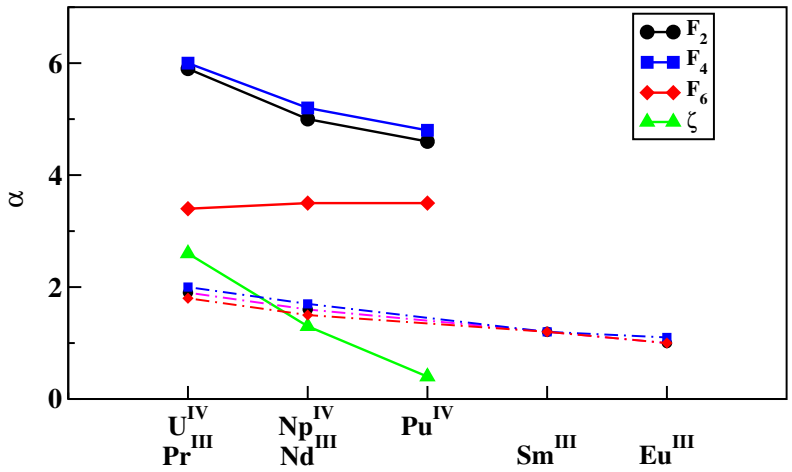

Figure 5.7.2: Nephelauxetic reduction factors α (in %) calculated with AILFT in the $[Ln^{III}(DPA)_3]^{3-}$ (dashed, Ref. [39]) and $[An^{IV}(DPA)_3]^{2-}$ (plain) series. Free-ion data are taken from Ref. [95].

tions: at this level, the ITO CFPs contain many-electron effects, which are included in the Slater–Condon parameters in the AILFT method. At the SO-CASSCF level, they are deduced from the ground J manifold and then, the ITO CFPs additionally contain the $J-J$ mixing with excited LS terms. The SF-CASSCF/ITO CFPs are very close to the CASSCF/AILFT ones; this shows that the building of the many-electron wave functions from the $5f$ orbitals is close to that of the free-ion as in lanthanide complexes. But the SO-CASSCF/ITO differ slightly from the SF-CASSCF/ITO ones due to the larger $J-J$ mixing in the actinide complexes, which also tends to reduce the total strength parameter. This effect is more pronounced for the Pu^{IV} derivative, most likely because Pu^{IV} holds more f electrons, and hence, a richer electronic structure. PT2 does not impact strongly.

In the $[Ln^{III}(DPA)_3]^{3-}$ series, comparing with the point change model, we have seen that the decrease of the strength parameter in the series arises from covalent effects in their general meaning, namely any orbital effect including bonding, charge donation and polarization. Covalent effects are even more complex to analyze with actinides, and have been the object of many studies [118, 2, 119]. The empty $6d$ metal orbitals play a key role for bonding and charge donation [120], $5f$ orbitals are more available to covalent interaction with the ligands due to their larger spatial expansion as compared to the filled $6s$, $6p$ shells. But the shielding becomes more and more efficient in the series, with the contraction of the $5f$ orbitals.

5.8 Conclusions

In this chapter, CFPs deduced from the *ab initio* energy levels and wave functions of the Ln^{III} and An^{IV} complexes with the DPA^{2-} ligands are presented. All the 27 CFPs are

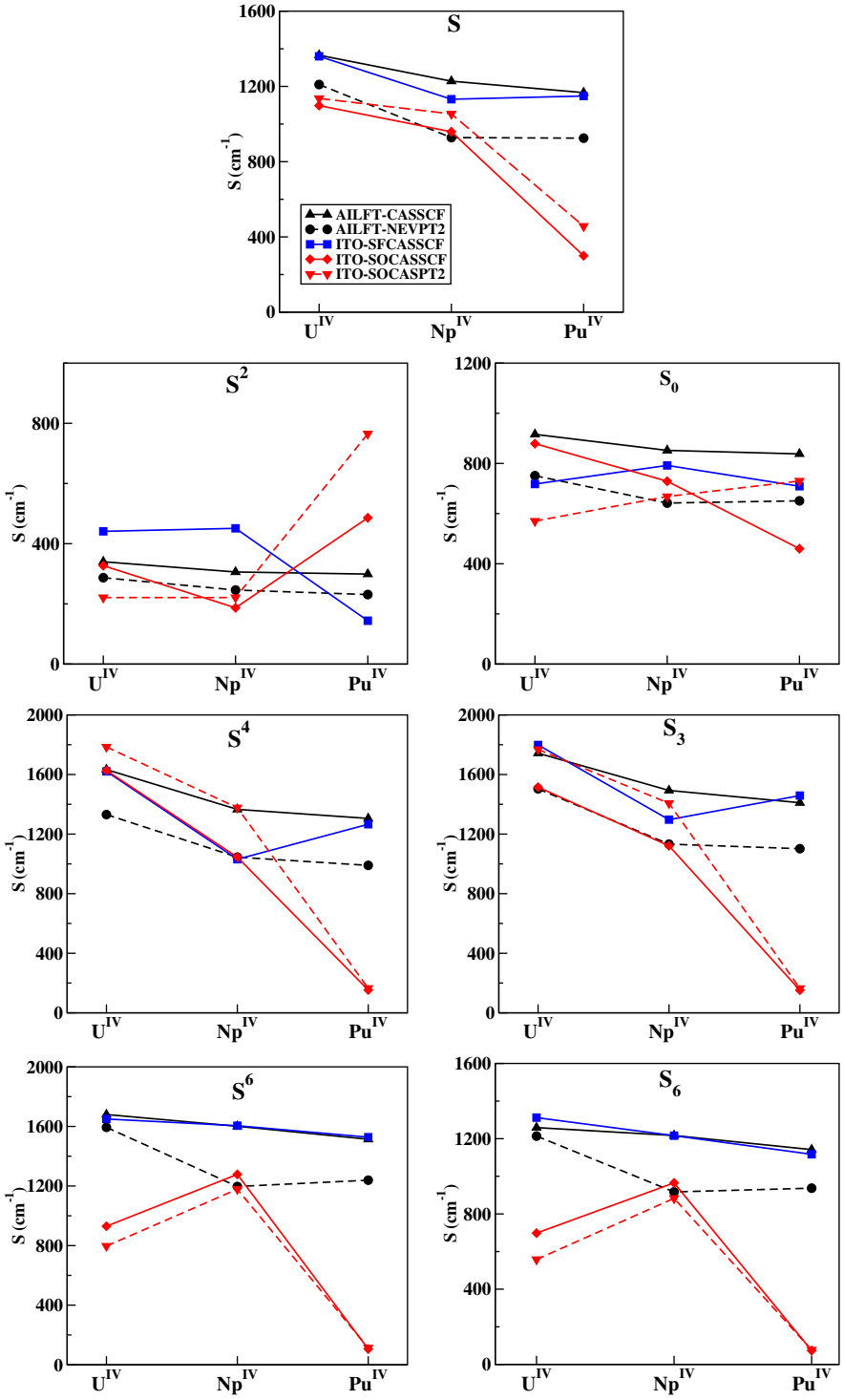

Figure 5.7.3: Strength parameters (in cm^{-1}) in the $[An^{IV}(DPA)_3]^{2-}$ series calculated with different methods.

Table 5.12: Strength parameters (in cm^{-1}) in the $[An^{IV}(DPA)_3]^{2-}$ series calculated with AILFT and ITO.

		S	S^2	S^4	S^6	S_0	S_1	S_2	S_3	S_4	S_5	S_6
						U^{IV}						
ITO	SF-CASSCF	1005	430	1202	1183	718	168	73	1272	33	53	928
	SO-CASSCF	856	312	1274	690	880	161	59	1071	31	37	494
	SO-SSCASPT2	762	259	1164	567	570	139	72	1109	38	21	401
	SO-MSCASPT2	836	217	1297	606	570	52	178	1250	134	27	394
AILFT	SO-CASSCF	1036	316	1266	1232	916	229	86	1233	90	33	890
	SO-NEVPT2	909	268	1025	1165	751	188	74	1063	84	27	858
						Np^{IV}						
ITO	SF-CASSCF	863	442	797	1184	792	133	25	1104	127	582	1223
	SO-CASSCF	741	168	867	931	729	114	31	1171	108	383	1033
	SO-SSCASPT2	749	138	914	909	682	134	53	1190	142	384	1122
	SO-MSCASPT2	794	167	1073	842	668	199	120	1314	197	254	1295
AILFT	SO-CASSCF	935	292	1067	1182	852	182	67	1056	64	32	860
	SO-NEVPT2	707	234	812	885	642	140	49	801	46	24	648
						Pu^{IV}						
ITO	SF-CASSCF	862	129	729	756	709	169	74	1261	218	539	1323
	SO-CASSCF	283	470	144	123	460	85	90	133	31	46	141
	SO-SSCASPT2	256	403	321	271	319	200	204	175	116	59	95
	SO-MSCASPT2	439	746	192	187	730	59	162	146	31	46	150
AILFT	SO-CASSCF	893	289	1027	1121	838	184	77	998	52	43	807
	SO-NEVPT2	706	223	777	918	651	140	59	779	41	36	663

extracted using two methods- AILFT and ITO. AILFT is based on the fitting of the CF matrix written at the orbital level, whereas the ITO method involves a decomposition of the Hamiltonian matrix for a J manifold. The overall energy splitting of the ground J manifold in the Ln^{III} series is around room temperature energy, strongly supports Bleaney's modelization of the pNMR shifts in the axially symmetric lanthanide complexes with the single CFP B_0^2. In Russell-Saunders coupling scheme, the weight of the *ab initio* ground ^{2S+1}L manifold to the ground J manifold is higher in the Ln^{III} (98%) than the An^{IV} (86%) manifests a strong $J-J$ coupling in the An series. In the actinide complexes, the perturbation energy corrections with SO-NEVPT2 in ORCA and with SO-CASPT2 in MOLCAS provide similar energetic spectra.

In the Ln^{III} series, the two methods lead to very similar CFPs, which confirms that the ZFS occurs mostly at the orbital level, as has been shown previously for lanthanides [115]. However, small discrepancies between AILFT and ITO reveal many-electron effects on the CFPs: This tends to decrease the CFPs in the first half of the series and to increase them in the second half. The relative magnitudes decrease along the series but the decease is rather smooth indicates isostructural ligand binding and no major conformational change along with the series. So the CFPs are transferable as one expects for isostructural series. It has been shown that within a PC model reproducing the electrostatic potential of the ligands, the CFPs are rather constant across the series; as a result of counterbalance between the shrinking of the coordination sphere and the greater compactness of the $4f$ orbitals. The decrease in the CFPs across the series is consequently attributed to covalent effects, defined as all effects beyond electrostatic interactions. They comprise bonding, charge transfer, and polarization effects. They are not restricted to the overlap of the $4f$ and ligand orbitals. Covalent bonding mostly occurs through the more outer-shell orbitals, that is, the $6s$ and $5d$ orbitals; the change in the electron density of the lanthanide center affects the splitting of the $4f$ orbitals, and thus the CFPs.

In the An^{IV} complexes, the CFPs at the SF level seem to be transferable but the addition of SOC makes it difficult to conclude. CFPs deduced from SO calculations are more irregular, which is most likely a consequence of significant $J-J$ mixing. Notably for the Pu^{IV} complex that is most affected by the $J-J$ mixing, although quantitatively similar as for the two other complexes. All the CFPs are larger than the Ln^{III} analog series and in the case of An^{IV}, 4th and 6th orders are important.

B_0^2 is positive in both the Ln^{III} and An^{IV} complexes which is related to the prolate environment of ligand environments. This shows a structural similarity in both series. But for similar ionic radii, when the $Ln^{III}-O$ and $An^{IV}-O$ bond distances are rather similar, the $An^{IV}-N$ distances are larger that the $Ln^{III}-N$ distances. This indicates minor structural changes in the coordination sphere in terms of biting angle and a readjustment of the adjacent bond lengths. When B_0^2 is dominant, one can predict with simple rules the

anisotropy of the magnetic properties, like the single molecule magnets properties or the pseudocontact term for paramagnetic chemical shifts using Bleaney's theory. But it appears that the non-zero 4th and 6th order CFPs as per the trigonal environment are more important than the 2nd order and this upraises doubts in confidently applying Bleaney's theory for the Ln^{III} series [37]. But Bleaney's B_0^2 is meaningfully close to the B_0^2 of the point change model and assumed to be considerably larger than the higher orders. Indeed, in the point charge model of the Ln^{III} series, the 2nd order CFP is dominant than the 4th and 6th order. The 4th and 6th order CFPs are related to the covalency in the molecules which decreases along the $[Ln^{III}(DPA)_3]^{3-}$ series. This reveals that the modelization of the magnetic anisotropy in the Ln^{III} chelates in terms of the single CFP B_0^2 (which is dominant in the point charge model) in Eq. 5.6.2 and in Bleaney's theory (see Eq. 2.6.34) effectively includes the effects from higher order terms and not related to the 'actual' B_0^2. In the An^{IV} complexes, the higher order terms are even much larger, clearly showing an overload on B_0^2 for the same modelization.

Appendix A

Computational details

Chapter 3

$[An^{VI}O_2]^{2+}$ cations, An = Np, Pu

- Wave function based electronic structure calculations in MOLCAS 7.8 [121]
  - Relativistic Hamiltonian: DKH2 [122]
  - Variational SCF methods: CASSCF(n,6) [50] and RASSCF$(12,6;n,6;6:2,2)$ [123], $n =$ no of $5f$ electrons
  - Perturbation Theory methods: CASPT2 [54] and RASPT2 [124]
  - Spin-orbit coupling: As a state interaction in SO-RASSI module [125]
  - Spin-orbit Integrals: Calculated using AMFI approximations [126]
  - Basis sets: ANO-RCC, quality of polarization- TZP (for all atoms) [127, 128]
  - No. of SF states: 6 doublets for Np^{VI} complexes; 15 triplets and 21 singlets for Pu^{VI} complex
  - g-factors : Calculated according to Ref. [129]
- DFT based electronic structure calculations in ADF
  - Relativistic Hamiltonian: SO-ZORA (2-component) [130]
  - Functional: PBE0 [131] (with restricted open scheme)
  - Basis sets: All-electron doubly polarizes triple-ζ^2 TZ2P (for Np) [132], jcpl augmented version of TZ2P (O) [133]
  - g-factors, hyperfine values: Calculated with the ESR module [134, 42]
- DFT based electronic structure calculations in ReSpect

- Relativistic Hamiltonian: 4-component matrix Dirac-Kohn-Sham (mDKS)
- Nuclear model: Gaussian
- Basis sets: Dyall's all-electron uncontracted basis sets of valence double-ζ (26s23p17d12f2g) (for Np), uncontracted pc-1 (for O) [135].

$[An^{VI}O_2(DPA/Et-DPA)_2]^2$ complexes, An = Np, Pu

- Wave function based electronic structure calculations in MOLCAS 7.8 [121]
  - Relativistic Hamiltonian: DKH2 [122]
  - Variational SCF methods: CASSCF(n,6) [50] and RASSCF(12, 6; n, 6; 6 : 2, 2) [123]
  - Perturbation Theory methods: CASPT2 [54] and RASPT2 [124]
  - Spin-orbit coupling: As a state interaction in SO-RASSI module [125]
  - Spin-orbit Integrals: Calculated using AMFI approximations [126]
  - Basis sets: ANO-RCC, quality of polarization- TZP (for An, N, O), DZP (for C, Li), DZ (for H) [127, 128]
  - No. of SF states: 6 doublets for Np^{VI} complexes; 15 triplets and 21 singlets in SO-CASPT2 and 8 triplets and 14 singlets in SO-RASPT2 for Pu^{VI} complex
  - g-factors : Calculated according to Ref. [129]
- DFT based electronic structure calculations in ADF
  - Relativistic Hamiltonian: SO-ZORA (2-component) [130]
  - Functional: PBE0 [131] (with restricted open scheme)
  - Basis sets: All-electron doubly polarizes triple-ζ^2 TZ2P (for Np) [132], jcpl augmented version of TZ2P (N, O, C, H) [133]
  - g-factors, hyperfine values: Calculated with the ESR module [134, 42]
- DFT based spin densities calculations in MOLCAS 7.8
  - Functional: PBE0 [131] (with Unrestricted scheme)
  - Fractional occupations of the $5f$ orbitals (1e/2e in 4 orbitals for Np^{VI}/ Pu^{VI} complex)
  - Basis sets: ANO-RCC, quality of polarization- TZP (for all atoms)

$[An^{VI}O_2(TEDGA)_2]^{2+}$ complexes, An = Np, Pu

- Wave function based electronic structure calculations in MOLCAS 7.8 [121]
  - Relativistic Hamiltonian: DKH2 [122]
  - Variational SCF methods: CASSCF(n,6) [50] and RASSCF(12,6;n,6;6 : 2,2) [123]
  - Perturbation Theory methods: CASPT2 [54] and RASPT2 [124]
  - Spin-orbit coupling: As a state interaction in SO-RASSI module [125]
  - Spin-orbit Integrals: Calculated using AMFI approximations [126]
  - Basis sets: ANO-RCC, quality of polarization- TZP (for An, N, O), DZP (for C, Li), DZ (for H) [127, 128]
  - No. of SF states: 6 doublets for Np^{VI} complexes; 15 triplets and 21 singlets in SO-CASPT2 and 8 triplets and 14 singlets in SO-RASPT2 for Pu^{VI} complex
  - g-factors : Calculated according to Ref. [129]
- DFT based electronic structure calculations in ADF
  - Relativistic Hamiltonian: SO-ZORA (2-component) [130]
  - Functional: PBE0 [131] (with restricted open scheme)
  - Basis sets: All-electron doubly polarizes triple-ζ^2 TZ2P (for Np) [132], jcpl augmented version of TZ2P (N, O, C, H) [133]
  - g-factors, hyperfine values: Calculated with the ESR module [134, 42]
- DFT based electronic structure calculations in ReSpect
  - Relativistic Hamiltonian: 4-component matrix Dirac-Kohn-Sham (mDKS)
  - Nuclear model: Gaussian
  - Basis sets: Dyall's all-electron uncontracted basis sets of valence double-ζ (26s 23p 17d 12f 2g) (for Np), uncontracted pc-1 (for N, O) [135], uncontracted pcJ-1 (for C, H) [136, 137]
  - Paramagnetic NMR shifts: Calculated according to Ref. [138]
- DFT based spin densities calculations in MOLCAS 7.8
  - Functional: PBE0 [131] (with Unrestricted scheme)
  - Fractional occupations of the 5f orbitals (1e/2e in 4 orbitals for Np^{VI}/ Pu^{VI} complex)
  - Basis sets: ANO-RCC, quality of polarization- TZP (for all atoms) [127, 128]

Chapter 4

$[An^{IV}(DPA)_3]^{3-}$ complexes, An= U, Np, Pu

- Wave function based electronic structure calculations in MOLCAS 7.8 [121]
  - Symmetrization of the crystal structures: Using Chemcraft software [139]
  - Relativistic Hamiltonian: DKH2 [122]
  - Variational SCF methods: CASSCF(n, 7) [50]
  - Perturbation Theory methods: CASPT2 [54] with level shift 0.3 a.u. either state-specific (SS) or multi-state (MS) level
  - Spin-orbit coupling: As a state interaction in SO-RASSI module [125]
  - Spin-orbit Integrals: Calculated using AMFI approximations [126]
  - Basis sets: ANO-RCC, quality of polarization- TZP (for An) [127], TZP (for O, N), DZP (C), DZ (H) [128]
  - No. of SF states: With the highest values of S and 27 singlets (for U), 43 doublets (for Np), 32 triplets and 17 singlets (for Pu)
  - g-factors : Calculated according to Ref. [129]
  - CFPs: Calculated with a local program written in Mathematica
- DFT based spin densities calculations in MOLCAS 7.8
  - Functional: M06 [140], M062X [141], PBE0 [131] (with Unrestricted scheme)
  - Fractional occupations of the $5f$ orbitals
  - Basis sets: ANO-RCC, quality of polarization- TZP (for all atoms) [127, 128]

$[An^{IV}(DOTA)H_2O]$ complexes, An= U, Np, Pu

- Wave function based electronic structure calculations in MOLCAS 7.8 [121]
  - Symmetrization of the crystal structures: Using Chemcraft software [139]
  - Relativistic Hamiltonian: DKH2 [122]
  - Variational SCF methods: CASSCF(n, 7) [50]
  - Perturbation Theory methods: CASPT2 [54] with level shift 0.3 a.u. either state-specific (SS) or multi-state (MS) level
  - Spin orbit coupling: As a state interaction in SO-RASSI module [125]
  - Spin orbit Integrals: Calculated using AMFI approximations [126]

- Basis sets: ANO-RCC, quality of polarization- TZP (for An) [127], TZP (for O, N), DZP (C), DZ (H) [128]
- No. of SF states: With the highest values of S and 28 singlets (for U), 43 doublets (for Np), 35 triplets and 17 singlets (for Pu)
- g-factors : Calculated according to Ref. [129]
- CFPs: Calculated with a local program written in Mathematica

$[M^{III}La_9(PO_4)_7]^{9+}$ complexes, M= Sm, Np, Pu

- Wave function based electronic structure calculations in MOLCAS 7.8 [121]
  - Relativistic Hamiltonian: DKH2 [122]
  - Variational SCF methods: CASSCF(n, 7) [50]
  - Spin orbit coupling: As a state interaction in SO-RASSI module [125]
  - Spin orbit Integrals: Calculated using AMFI approximations [126]
  - Basis sets: ANO-RCC, quality of polarization- QZP (for M) [127], TZP (for P, O) [128] and ECP-LanL2DZ (for La) [142]
  - g-factors : Calculated according to Ref. [129]
  - CFPs: Calculated with a local program written in Mathematica
- DFT based spin densities calculations in MOLCAS 7.8
  - Functional: PBE0 [131] (with Unrestricted scheme)
  - Fractional occupations of the $5f$ orbitals
  - Basis sets: ANO-RCC, quality of polarization- QZP (for Pu) [127], TZP (for P, O) [128] and ECP-LanL2DZ (for Ln) [142]

Chapter 5

$[Ln^{III}(DPA)_3]^{3-}$ complexes, Ln = Ce, Yb

- Wave function based electronic structure calculations in MOLCAS 7.8 [121]
  - Relativistic Hamiltonian: DKH2 [122]
  - Variational SCF methods: CASSCF(n, 7) [50]
  - Spin orbit coupling: As a state interaction in SO-RASSI module [125]
  - Spin orbit Integrals: Calculated using AMFI approximations [126]

- Basis sets: ANO-RCC, quality of polarization- QZP (for Ln), TZP (for O, N, C, H) [127, 128]
- No. of SF states: With the highest values of S and 27 singlets (for Pr, Tm), 43 doublets (for Nd, Er), 86 quartets (for Sm), 42 quintets (for Eu, Tb), 108 quartets (for Dy), 99 triplets (for Ho), 35 quartets (for Er), or 2 triplets (for Tm)
- g-factors : Calculated according to Ref. [129]
- CFPs: Calculated with a local program written in Mathematica

- Wave function based electronic structure calculations in ORCA 4.0 [143]
  - Relativistic Hamiltonian: DKH2 [144, 53]
  - Variational SCF methods: CASSCF(n, 7) [50]
  - Spin orbit coupling: In a mean-field fashion (SOMF) by using quasi-degenerate perturbation theory (QDPT) [145] and by allowing all SF-CASSCF states to mix through SOMF operator.
  - Basis sets: All electron SARC2-QZVP (for Ln) [146], def2-TZVPP (for O, N, C, H) [147, 148]
  - AUTOAUX feature [149] was used to automatically generate auxiliary basis sets for the resolution of identity approximation (RI-JK) [150]

$[An^{IV}(DPA)_3]^{2-}$ complexes, An = U, Np, Pu

- Wave function based electronic structure calculations in MOLCAS 7.8 [121]
  - Relativistic Hamiltonian: DKH2 [122]
  - Variational SCF methods: CASSCF(n, 7) [50]
  - Perturbation Theory methods: CASPT2 [54] with level shift 0.3 a.u. either state-specific (SS) or multi-state (MS) level
  - Spin orbit coupling: As a state interaction in SO-RASSI module [125],
  - Spin orbit Integrals: Calculated using AMFI approximations [126]
  - Basis sets: ANO-RCC, quality of polarization- QZP (for An) [127], TZP (for O, N), DZP (C), DZ (H) [128]
  - No. of SF states: With the highest values of S and 28 singlets (for U), 35 doublets (for Np), 60 triplets and 20 singlets (for Pu)
  - g-factors : Calculated according to Ref. [129]
  - CFPs: Calculated with a local program written in Mathematica

- Wave function based electronic structure calculations in ORCA 4.0 [143]
  - Relativistic Hamiltonian: DKH2 [144, 53]
  - Variational SCF methods: CASSCF(n, 7) [50]
  - Spin orbit coupling: In a mean-field fashion (SOMF) by using quasi-degenerate perturbation theory (QDPT) [145] and by allowing all SF-CASSCF states to mix through SOMF operator.
  - Basis sets: All electron TZVPP (for An) [151], def2-TZVPP (for O, N, C, H) [147, 148]
  - AUTOAUX feature [149] was used to automatically generate auxiliary basis sets for the resolution of identity approximation (RI-JK) [150]

General conclusions and perspectives

The system and chapter-specific conclusions are stated at the end of their respective chapters. Here, we devote some additional lines to draw some more general conclusions about the thesis and future perspectives.

In this thesis, paramagnetic chemical shifts in several actinide complexes are analyzed with the help of *ab initio* calculations and theoretical models have been developed to estimate the paramagnetic properties of the actinide center from the temperature dependent data. With close collaborations with the experimental groups, systematic studies of the AIS are carried out in different systems where the actinides are present in various oxidation states ranging from +6 (in the actinyls) to +3 and from highly axial to the spherical ligand field environment. Bleaney's theory for the LIS has been also investigated and additional temperature dependent terms are figured out for the considered actinide complexes. *Ab initio* computed electronic structures and magnetic anisotropies are rationalized with the help of crystal field theory and the periodic trends of electron-electron repulsion, $J-J$ coupling, covalency, etc. in the lanthanides and the early actinides are achieved in terms of the crystal field parameters. Our work strongly supports the paramagnetic chemical shifts technique as a potential alternative to probe the magnetic properties and metal ligand bonding. When the pseudocontact terms are dominant, pNMR shifts combined with measured isotropic susceptibility allow deducing the magnetic susceptibility tensor for an axial system. On the other hand, in a spherical ligand environment when they are mostly contact with origin, the pNMR shifts can be useful to analyze spin delocalization on the ligands, and compare the trends in a series, and therefore the degree of covalency.

However, accurate separation of the contact and pseudocontact contributions remains a challenge. Both Bleaney's temperature dependent and Reilley's structure independent methods depend on the metal dependent parameters which are unknown for the actinides and might need a theoretician for help. And ironically also, the *ab initio* calculations of electronic structures and magnetic properties are not straightforward as the strong interweaving of many-electron effects, SOC, $J-J$ coupling, intricate bonding interactions with the ligands should be properly addressed. The orbital contribution of the unpaired electrons and low lying excited states play a major role in determining the magnetic prop-

erties in lanthanide and actinide complexes. Electron dynamic correlation and $J-J$ mixing strongly impact (especially in the actinides) the splitting and nature of the lowest energetic states, those, in turn, affect the magnetic response properties such as the magnetic susceptibility and pNMR shifts. Also, when the symmetry of the ligand field environment reduces, the determination of the anisotropic magnetic properties becomes more elusive.

The two contributions in the pNMR shifts are very distinct in their origin. The pseudocontact shifts originate from the magnetic anisotropy of the paramagnetic center, and hence demand the multireference *ab initio* methods to properly address the electronic structures of an open shell system. On the other hand, the contact shifts are the result of metal-ligand spin delocalization and single determinant unrestricted DFT based approaches are reasonably good in addressing the metal-ligand spin polarization and delocalization, but fail to properly describe the paramagnetic center. Modeling of pNMR shifts in terms of spin Hamiltonian parameters was already developed a long time ago, but the evaluation of the parameters from *ab initio* is not as easy as pie and follows different approaches, either DFT based approach or a hybrid of DFT and multireference approach. In our work, DFT based evaluation of the spin densities comes as a relief to interpret the contact shifts.

But, multireference wave functions based calculation of the pNMR shifts according to the general Soncini and Van den Heuven formula is still a nontrivial task. There have been reports in the literature of large active space based pNMR calculations based on Soncini's expression. These computations, however, are far from routine, and they are currently suffered by a poor description of spin polarization (which is very sensitive to the dynamic correlation). Range-separation approaches that combine the advantages of DFT and WFT or DMRG methodologies for the handling of large active spaces are also conceivable for a proper description of pNMR shifts or treatment of spin polarization via perturbation theory. Despite the fact that the quantum mechanical description of the pNMR shifts is known, significant research efforts must be dedicated to the development of computational methods to compute them from first principles, as Paul Dirac once said,

> "The fundamental laws necessary for the mathematical treatment of a large part of physics and the whole of chemistry are thus completely known, and the difficulty lies only in the fact that application of these laws leads to equations that are too complex to be solved."

List of publications

1. Jung, J.; Islam, M. A.; Pecoraro, V. L.; Mallah, T.; Berthon, C.; Bolvin, H. Derivation of Lanthanide Series Crystal Field Parameters From First Principles. *Chem.Eur. J.* **2019**, *25*, 15112–15122.

2. Autillo, M.; Islam, M. A.; Jung, J.; Pilmé, J.; Galland, N.; Guerin, L.; Moisy, P.; Berthon, C.; Tamain, C.; Bolvin, H. Crystallographic structure and crystal field parameters in the [An IV (DPA) 3] 2- series, An= Th, U, Np, Pu. *PCCP.* **2020**, *22*, 14293–14308.

3. Autillo, M.; Islam, M. A.; Héron, J.; Guérin, L.; Acher, E.; Tamain, C.; Illy, M.-C.; Moisy, P.; Colineau, E.; Griveau, J.-C., *et al*. Temperature Dependence of 1H Paramagnetic Chemical Shifts in Actinide Complexes, Beyond Bleaney's Theory: The AnVIO22+–Dipicolinic Acid Complexes (An= Np, Pu) as an Example. *Chem.Eur. J.* **2021**, *27*, 7138–7153.

4. Martel, L.; Islam, M. A.; Popa, K.; Vigier, J.-F.; Colineau, E.; Bolvin, H.; Griveau, J.-C. Local structure and magnetism of La1-xMxPO4 (M=Sm, 239Pu, 241Am) explained by experimental and computational analyses. *J. Phys. Chem. C* **2021** (accepted).

5. Islam, M.; Autillo, M.; A.; Guérin, L.; Tamain, C.; Acher, E.; Moisy, P.; Bolvin, H.; Berthon, C. Study of AnIV complexes with dipicolinic acid derivatives (An=U, Np, Pu) by paramagnetic NMR spectroscopy. (ongoing manuscript).

6. Islam, M. A; Autillo, M.; Tamain, C.; Poulin-Ponnelle, C.; Berthon, C.; Bolvin, H. Probing the origin of magnetic anistropy in actinyl-TEDGA (An = Np, Pu) complexes using the temperature dependent paramagnetic NMR shifts. (ongoing manuscript).

7. The authors. NMR study of paramagnetic actinide(IV)-DOTA complexes in aqueous solution. (ongoing manuscript).

Bibliography

[1] Cotton, S. *Lanthanide and actinide chemistry*; John Wiley & Sons, 2013.

[2] Neidig, M. L.; Clark, D. L.; Martin, R. L. Covalency in f-element complexes. *Coord. Chem. Rev.* **2013**, *257*, 394–406.

[3] Minasian, S. G.; Keith, J. M.; Batista, E. R.; Boland, K. S.; Clark, D. L.; Kozimor, S. A.; Martin, R. L.; Shuh, D. K.; Tyliszczak, T. New evidence for 5f covalency in actinocenes determined from carbon K-edge XAS and electronic structure theory. *Chem. Sci.* **2014**, *5*, 351–359.

[4] Solomon, E. I.; Hedman, B.; Hodgson, K. O.; Dey, A.; Szilagyi, R. K. Ligand K-edge X-ray absorption spectroscopy: covalency of ligand–metal bonds. *Coord. Chem. Rev.* **2005**, *249*, 97–129.

[5] Cary, S. K.; Vasiliu, M.; Baumbach, R. E.; Stritzinger, J. T.; Green, T. D.; Diefenbach, K.; Cross, J. N.; Knappenberger, K. L.; Liu, G.; Silver, M. A., et al. Emergence of californium as the second transitional element in the actinide series. *Nat. Commun.* **2015**, *6*, 1–8.

[6] Magnani, N. Spectroscopic and magnetic investigations of actinide-based nanomagnets. *Int. J. Quantum Chem.* **2014**, *114*, 755–759.

[7] Magnani, N.; Colineau, E.; Griveau, J.-C.; Apostolidis, C.; Walter, O.; Caciuffo, R. A plutonium-based single-molecule magnet. *Chem. Commun.* **2014**, *50*, 8171–8173.

[8] Clark, D. L.; Hobart, D. E.; Neu, M. P. Actinide carbonte complexes and their importance in actinide environmental chemistry. *Chem. Rev.* **1995**, *95*, 25–48.

[9] Gendron, F.; Sharkas, K.; Autschbach, J. Calculating NMR chemical shifts for paramagnetic metal complexes from first-principles. *J. Phys. Chem. Lett.* **2015**, *6*, 2183–2188.

[10] Gendron, F.; Autschbach, J. Ligand NMR chemical shift calculations for paramagnetic metal complexes: 5f1 vs 5f2 actinides. *J. Chem. Theory Comput.* **2016**, *12*, 5309–5321.

[11] Autillo, M.; Islam, M. A.; Héron, J.; Guérin, L.; Acher, E.; Tamain, C.; Illy, M.-C.; Moisy, P.; Colineau, E.; Griveau, J.-C., et al. Temperature Dependence of 1H Paramagnetic Chemical Shifts in Actinide Complexes, Beyond Bleaney's Theory: The AnVIO22+–Dipicolinic Acid Complexes (An= Np, Pu) as an Example. *Chem.Eur. J.* **2021**, *27*, 7138–7153.

[12] Hinckley, C. C. Paramagnetic shifts in solutions of cholesterol and the dipyridine adduct of trisdipivalomethanatoeuropium(III). A shift reagent. *J. Am. Chem. Soc.* **1969**, *91*, 5160–5162.

[13] Cockerill, A. F.; Davies, G. L.; Harden, R. C.; Rackham, D. M. Lanthanide shift reagents for nuclear magnetic resonance spectroscopy. *Chem. Rev.* **1973**, *73*, 553–588.

[14] Sievers, R., Ed. *Nuclear magnetic resonance shift reagents*; Elsevier, 2012.

[15] McConnell, H. M.; Robertson, R. E. Isotropic nuclear resonance shifts. *J. Chem. Phys.* **1958**, *29*, 1361–1365.

[16] Kurland, R. J.; McGarvey, B. R. Isotropic NMR shifts in transition metal complexes: the calculation of the Fermi contact and pseudocontact terms. *J. Magn. Reson.* **1970**, *2*, 286–301.

[17] Bleaney, B. Nuclear magnetic resonance shifts in solution due to lanthanide ions. *J. Magn. Reson.* **1972**, *8*, 91–100.

[18] Bleaney, B.; Dobson, C.; Levine, B.; Martin, R.; Williams, R.; Xavier, A. Origin of lanthanide nuclear magnetic resonance shifts and their uses. *J. Chem. Soc., Chem. Commun.* **1972**, 791b–793.

[19] Golding, R.; Halton, M. P. A theoretical study of the 14N and 17O NMR shifts in lanthanide complexes. *Aust. J. Chem.* **1972**, *25*, 2577–2581.

[20] Hill, H. A. O.; Williams, D.; Zarb-Adami, N. Origin of isotropic shifts in lanthanide complexes: a study of the temperature dependence of the 1H nmr spectra of the tetrakis-N, N-diethyldithiocarbamatolanthanate (III) anions. *J. Chem. Soc., Faraday Trans. 2* **1976**, *72*, 1494–1502.

[21] Stout Jr, E.; Gutowsky, H. On the temperature dependence of lanthanide-induced NMR shifts. *J. Magn. Reson.* **1976**, *24*, 389–398.

[22] Desreux, J. F.; Reilley, C. N. Evaluation of contact and dipolar contributions to proton and carbon-13 paramagnetic NMR shifts in axially symmetric lanthanide chelates. *J. Am. Chem. Soc.* **1976**, *98*, 2105–2109.

[23] Autillo, M.; Islam, M. A.; Jung, J.; Pilmé, J.; Galland, N.; Guerin, L.; Moisy, P.; Berthon, C.; Tamain, C.; Bolvin, H. Crystallographic structure and crystal field parameters in the [An IV (DPA) 3] 2- series, An= Th, U, Np, Pu. *Physical Chemistry Chemical Physics* **2020**, *22*, 14293–14308.

[24] Reilley, C. N.; Good, B. W.; Desreux, J. F. Structure-independent method for dissecting contact and dipolar NMR shifts in lanthanide complexes and its use in structure determination. *Anal. Chem.* **1975**, *47*, 2110–2116.

[25] Reilley, C. N.; Good, B. W.; Allendoerfer, R. D. Separation of contact and dipolar lanthanide induced nuclear magnetic resonance shifts: evaluation and application of some structure independent methods. *Anal. Chem.* **1976**, *48*, 1446–1458.

[26] Autillo, M.; Guerin, L.; Dumas, T.; Grigoriev, M. S.; Fedoseev, A. M.; Cammelli, S.; Solari, P. L.; Guillaumont, D.; Guilbaud, P.; Moisy, P., et al. Insight of the Metal-Ligand Interaction in f-Element Complexes by Paramagnetic NMR Spectroscopy. *Chem. Eur. J.* **2019**, *25*, 4435–4451.

[27] Bertini, I.; Luchinat, C.; Parigi, G. Magnetic susceptibility in paramagnetic NMR. *Prog. Nucl. Magn. Reson. Spectrosc.* **2002**, *40*, 249.

[28] Pennanen, T. O.; Vaara, J. Nuclear magnetic resonance chemical shift in an arbitrary electronic spin state. *Phys. Rev. Lett.* **2008**, *100*, 133002.

[29] Van den Heuvel, W.; Soncini, A. NMR chemical shift as analytical derivative of the Helmholtz free energy. *J. Chem. Phys.* **2013**, *138*, 054113.

[30] Martin, B.; Autschbach, J. Temperature dependence of contact and dipolar NMR chemical shifts in paramagnetic molecules. *J. Chem. Phys.* **2015**, *142*, 054108.

[31] Desreux, J. F. Nuclear magnetic resonance spectroscopy of lanthanide complexes with a tetraacetic tetraaza macrocycle. Unusual conformation properties. *Inorg. Chem.* **1980**, *19*, 1319–1324.

[32] Di Bari, L.; Salvadori, P. Solution structure of chiral lanthanide complexes. *Coord. Chem. Rev.* **2005**, *249*, 2854–2879.

[33] Piguet, C.; Geraldes, C. F. *Handbook on the physics and chemistry of rare earths*; Elsevier, 2003; Vol. 33; pp 353–463.

[34] Platas-Iglesias, C. The solution structure and dynamics of MRI probes based on lanthanide (III) DOTA as investigated by DFT and NMR spectroscopy. *Eur. J. Inorg. Chem.* **2012**, *2012*, 2023–2033.

[35] Wybourne, B. *Spectroscopic Properties of Rare Earths*; Wiley, New York, 1965.

[36] Abragam, A.; Bleaney, B. *Electron paramagnetic resonance of transition ions*; OUP Oxford, 2012.

[37] William. DeW. Horrocks Jr., I., James P. Sipe; Sudnick, D. In *Nuclear magnetic Resonance Shift Reagents*; Sievers, R. E., Ed.; Academic Press, New York, 1973; Chapter 3, pp 53–86.

[38] Golding, R.; Pyykkö, P. On the theory of pseudocontact NMR shifts due to lanthanide complexes. *Mol. Phys.* **1973**, *26*, 1389–1396.

[39] Jung, J.; Islam, M. A.; Pecoraro, V. L.; Mallah, T.; Berthon, C.; Bolvin, H. Derivation of Lanthanide Series Crystal Field Parameters From First Principles. *Chem.Eur. J.* **2019**, *25*, 15112–15122.

[40] Lévy-Leblond, J.-M. Nonrelativistic particles and wave equations. *Commun. Math. Phys.* **1967**, *6*, 286–311.

[41] Kutzelnigg, W. Origin and meaning of the Fermi contact interaction. *Theor. Chim. Acta* **1988**, *73*, 173–200.

[42] van Lenthe, E.; Van Der Avoird, A.; Wormer, P. E. Density functional calculations of molecular hyperfine interactions in the zero order regular approximation for relativistic effects. *J. Chem. Phys.* **1998**, *108*, 4783–4796.

[43] Sharkas, K.; Pritchard, B.; Autschbach, J. Effects from Spin–Orbit Coupling on Electron–Nucleus Hyperfine Coupling Calculated at the Restricted Active Space Level for Kramers Doublets. *J. Chem. Theory Comput.* **2015**, *11*, 538–549.

[44] Autschbach, J. Relativistic Effects on Electron-Nucleus Hyperfine Coupling Studied with an Exact 2-Component (X2C) Hamiltonian. *J. Chem. Theory Comput.* **2017**, *13*, 710–718.

[45] Neese, F. In *High Resolution EPR: Applications to Metalloenzymes and Metals in Medicine*; Hanson, G. R., Berliner, L. J., Eds.; Springer, 2009; Chapter 5, pp 175–229.

[46] Pell, A. J.; Pintacuda, G.; Grey, C. P. Paramagnetic NMR in solution and the solid state. *Prog. Nucl. Magn. Reson. Spectrosc.* **2019**, *111*, 1–271.

[47] Ramsey, N. F. Magnetic shielding of nuclei in molecules. *Phys. Rev.* **1950**, *78*, 699.

[48] Dolg, M., Ed. *Computational Methods in Lanthanide and Actinide Chemistry*; John Wiley & Sons, 2015.

[49] Szabo, A.; Ostlund, N. S. *Modern quantum chemistry: introduction to advanced electronic structure theory*; Courier Corporation, 2012.

[50] Roos, B. O.; Taylor, P. R.; Sigbahn, P. E. A complete active space SCF method (CASSCF) using a density matrix formulated super-CI approach. *Chem. Phys.* **1980**, *48*, 157–173.

[51] Veryazov, V.; Malmqvist, P. Å.; Roos, B. O. How to select active space for multi-configurational quantum chemistry? *Int. J. Quantum Chem.* **2011**, *111*, 3329–3338.

[52] Angeli, C.; Cimiraglia, R.; Evangelisti, S.; Leininger, T.; Malrieu, J.-P. Introduction of n-electron valence states for multireference perturbation theory. *J. Chem. Phys.* **2001**, *114*, 10252–10264.

[53] Nakajima, T.; Hirao, K. The Douglas-Kroll-Hess Approach. *Chem. Rev.* **2012**, *112*, 385–402.

[54] Andersson, K.; Malmqvist, P. A.; Roos, B. O.; Sadlej, A. J.; Wolinski, K. Second-order perturbation theory with a CASSCF reference function. *J. Phys. Chem.* **1990**, *94*, 5483–5488.

[55] Hohenberg, P.; Kohn, W. *Phys. Rev.* **1964**, *136*, B 864.

[56] Kohn, W.; Sham, L. J. *Phys. Rev* **1965**, *140*, A1133.

[57] Mardirossian, N.; Head-Gordon, M. Thirty years of density functional theory in computational chemistry: an overview and extensive assessment of 200 density functionals. *Mol. Phys.* **2017**, *115*, 2315–2372.

[58] Jensen, F. *Introduction to computational chemistry*, 2nd ed.; John wiley & sons, 2017.

[59] Heß, B. A.; Marian, C. M.; Wahlgren, U.; Gropen, O. A mean-field spin-orbit method applicable to correlated wavefunctions. *Chem. Phys. Lett.* **1996**, *251*, 365–371.

[60] Malkina, O.; Schimmelpfennig, B.; Kaupp, M.; Hess, B.; Chandra, P.; Wahlgren, U.; Malkin, V. Spin-orbit corrections to NMR shielding constants from density functional theory. How important are the two-electron terms? *Chem. Phys. Lett.* **1998**, *296*, 93–104.

[61] Van Vleck, J. H. *The theory of electric and magnetic susceptibilities*; Oxford University Press, 1965.

[62] Moon, S.; Patchkovskii, S. In *Calculation of NMR and EPR parameters: theory and applications*; Kaupp, M., Buhl, M., Malkin, V. G., Eds.; Wiley Online Library, 2004; Chapter 20, pp 325–338.

[63] Soncini, A.; Van den Heuvel, W. Communication: Paramagnetic NMR chemical shift in a spin state subject to zero-field splitting. *J Chem Phys* **2013**, *138*, 021103.

[64] Suturina, E. A.; Mason, K.; Geraldes, C. F.; Kuprov, I.; Parker, D. Beyond Bleaney's Theory: Experimental and Theoretical Analysis of Periodic Trends in Lanthanide-Induced Chemical Shift. *Angew. Chem. Int. Ed.* **2017**, *129*, 12383–12386.

[65] McConnell, H. M. Indirect hyperfine interactions in the paramagnetic resonance spectra of aromatic free radicals. *J. Chem. Phys.* **1956**, *24*, 764–766.

[66] Denning, R. G. Electronic structure and bonding in actinyl ions and their analogs. *J. Phys. Chem. A* **2007**, *111*, 4125–4143.

[67] Notter, F.-P.; Dubillard, S.; Bolvin, H. A theoretical study of the excited states of AmO2n+, n= 1, 2, 3. *J. Chem. Phys.* **2008**, *128*, 164315.

[68] Schnaars, D. D.; Wilson, R. E. Structural and Vibrational Properties of U(VI)O2Cl42- and Pu(VI)O2Cl42- Complexes. *Inorg. Chem.* **2013**, *52*, 14138–14147.

[69] Mizuoka, K.; Grenthe, I.; Ikeda, Y. Structural and kinetic studies on uranyl (V) carbonate complex using 13C NMR spectroscopy. *Inorg. Chem.* **2005**, *44*, 4472–4474.

[70] Odoh, S. O.; Schreckenbach, G. Theoretical study of the structural properties of plutonium (IV) and (VI) complexes. *J. Phys. Chem. A* **2011**, *115*, 14110–14119.

[71] Hu, S.-X.; Li, W.-L.; Dong, L.; Gibson, J. K.; Li, J. Crown ether complexes of actinyls: a computational assessment of AnO 2 (15-crown-5) 2+(An= U, Np, Pu, Am, Cm). *Dalton Trans.* **2017**, *46*, 12354–12363.

[72] Vasiliu, M.; Jian, T.; Gibson, J. K.; Peterson, K. A.; Dixon, D. A. A Computational Assessment of Actinide Dioxide Cations AnO22+ for An= U to Lr: The Limited Stability Range of the Hexavalent Actinyl Moiety, [O= An= O]2+. *Inorg. Chem.* **2020**, *59*, 4554–4566.

[73] Gendron, F.; Páez-Hernández, D.; Notter, F.-P.; Pritchard, B.; Bolvin, H.; Autschbach, J. Magnetic Properties and Electronic Structure of Neptunyl (VI) Complexes: Wavefunctions, Orbitals, and Crystal-Field Models. *Chem. Eur. J.* **2014**, *20*, 7994–8011.

[74] Gendron, F.; Pritchard, B.; Bolvin, H.; Autschbach, J. Magnetic resonance properties of actinyl carbonate complexes and plutonyl (VI)-tris-nitrate. *Inorg. Chem.* **2014**, *53*, 8577–8592.

[75] Eisenstein, J. C.; Pryce, M. H. L. The electronic structure and magnetic properties of uranyl-like ions I. Uranyl and neptunyl. *Proceedings of the Royal Society of London. Series A. Mathematical and Physical Sciences* **1955**, *229*, 20–38.

[76] Koprowiak, F. Étude théorique de l'anisotropie magnétique dans les dimères d'éléments f. Ph.D. thesis, Ecole Doctorale Sciences de la Matiére, Université Toulouse III - Paul Sabatier, 2017.

[77] Yusov, A. B.; Mishkevich, V. I.; Fedoseev, A. M.; Grigor'ev, M. Complexation of An(VI) (An= U, Np, Pu, Am) with 2, 6-pyridinedicarboxylic acid in aqueous solutions. Synthesis and structures of new crystalline compounds of U(VI), Np(VI), and Pu(VI). *Radiochemistry* **2013**, *55*, 269–278.

[78] Evans, D. The determination of the paramagnetic susceptibility of substances in solution by nuclear magnetic resonance. *J. Chem. Soc.* **1959**, 2003–2005.

[79] Vonci, M.; Mason, K.; Suturina, E. A.; Frawley, A. T.; Worswick, S. G.; Kuprov, I.; Parker, D.; McInnes, E. J.; Chilton, N. F. Rationalization of Anomalous Pseudocontact Shifts and Their Solvent Dependence in a Series of C3-Symmetric Lanthanide Complexes. *J. Am. Chem. Soc.* **2017**, *139*, 14166–14172.

[80] Parker, D.; Suturina, E. A.; Kuprov, I.; Chilton, N. F. How the ligand field in lanthanide coordination complexes determines magnetic susceptibility anisotropy, paramagnetic NMR shift, and relaxation behavior. *Acc. Chem. Res.* **2020**, *53*, 1520–1534.

[81] Esteban-Gómez, D.; Blas, A. d.; Rodríguez-Blas, T.; Helm, L.; Platas-Iglesias, C. Hyperfine coupling constants on inner-sphere water molecules of GdIII-based MRI contrast agents. *ChemPhysChem* **2012**, *13*, 3640–3650.

[82] Castro, G.; Regueiro-Figueroa, M.; Esteban-Gómez, D.; Pérez-Lourido, P.; Platas-Iglesias, C.; Valencia, L. Magnetic anisotropies in rhombic lanthanide(III) complexes do not conform to Bleaney's theory. *Inorg. Chem.* **2016**, *55*, 3490–3497.

[83] Adamo, C.; Barone, V.; Subra, R. The mechanism of spin polarization in aromatic free radicals. *Theor. Chem. Acc.* **2000**, *104*, 207–209.

[84] Schindler, M.; Kutzelnigg, W. Theory of magnetic susceptibilities and NMR chemical shifts in terms of localized quantities. II. Application to some simple molecules. *J. Chem. Phys.* **1982**, *76*, 1919–1933.

[85] Barone, V. Inclusion of Hartree–Fock exchange in density functional methods. Hyperfine structure of second row atoms and hydrides. *J. Chem. Phys.* **1994**, *101*, 6834–6838.

[86] Wang, X.; Jin, T.; Comblin, V.; Lopez-Mut, A.; Merciny, E.; Desreux, J. F. A kinetic investigation of the lanthanide DOTA chelates. Stability and rates of formation and of dissociation of a macrocyclic gadolinium(III) polyaza polycarboxylic MRI contrast agent. *Inorg. Chem.* **1992**, *31*, 1095–1099.

[87] Stasiuk, G. J.; Long, N. J. The ubiquitous DOTA and its derivatives: the impact of 1, 4, 7, 10-tetraazacyclododecane-1, 4, 7, 10-tetraacetic acid on biomedical imaging. *Chem. Commun.* **2013**, *49*, 2732–2746.

[88] Spirlet, M. R.; Rebizant, J.; Desreux, J. F.; Loncin, M. F. Crystal and molecular structure of sodium aqua (1, 4, 7, 10-tetraazacyclododecane-1, 4, 7, 10-tetraacetato) europate (III) tetrahydrate Na+ (EuDOTA. H2O)-. 4H2O, and its relevance to NMR studies of the conformational behavior of the lanthanide complexes formed by the macrocyclic ligand DOTA. *Inorg. Chem.* **1984**, *23*, 359–363.

[89] Aime, S.; Barge, A.; Botta, M.; Fasano, M.; Ayala, J. D.; Bombieri, G. Crystal structure and solution dynamics of the lutetium(III) chelate of DOTA. *Inorganica chimica acta* **1996**, *246*, 423–429.

[90] Rodríguez-Rodríguez, A.; Arnosa-Prieto, A.; Brandariz, I.; Esteban-Gomez, D.; Platas-Iglesias, C. Axial Ligation in Ytterbium(III) DOTAM Complexes Rationalized with Multireference and Ligand-Field ab Initio Calculations. *J. Phys. Chem. A* **2020**, *124*, 1362–1371.

[91] Maron, S.; Dantelle, G.; Gacoin, T.; Devreux, F. NMR and ESR relaxation in Nd and Gd-doped LaPO4: towards the accurate determination of the doping concentration. *Phys. Chem. Chem. Phys.* **2014**, *16*, 18788–18798.

[92] Martel, L.; Rakhmatullin, A.; Baldoví, J. J.; Perfetti, M.; Popa, K.; Deschamps, M.; Gouder, T.; Colineau, E.; Kovács, A.; Griveau, J.-C. Local structure and magnetism of LaxEu1-xPO4 solid solutions. *Phys. Rev. B* **2019**, *100*, 054412.

[93] Ni, Y.; Hughes, J. M.; Mariano, A. N. Crystal chemistry of the monazite and xenotime structures. *Am. Mineral.* **1995**, *80*, 21–26.

[94] Gagliardi, L.; Lindh, R.; Karlström, G. Local properties of quantum chemical systems: The LoProp approach. *J. Chem. Phys.* **2004**, *121*, 4494–4500.

[95] Jung, J.; Atanasov, M.; Neese, F. Ab initio ligand-field theory analysis and covalency trends in actinide and lanthanide free ions and octahedral complexes. *Inorg. Chem.* **2017**, *56*, 8802–8816.

[96] Carnall, W. T. A systematic analysis of the spectra of trivalent actinide chlorides in D 3 h site symmetry. *J. Chem. Phys.* **1992**, *96*, 8713–8726.

[97] Gofryk, K.; Kaczorowski, D.; Griveau, J.; Magnani, N.; Jardin, R.; Colineau, E.; Rebizant, J.; Wastin, F.; Caciuffo, R. Extensive studies of antiferromagnetic PuPd2Sn. *Phys. Rev. B* **2008**, *77*, 014431.

[98] Jones Jr, E.; Hendricks, M.; Stone, J.; Karraker, D. Magnetic properties of the trichlorides, tribromides, and triiodides of U(III), Np (III), and Pu(III). *J. Chem. Phys.* **1974**, *60*, 2088–2094.

[99] Gaggioli, C. A.; Gagliardi, L. Theoretical investigation of plutonium-based single-molecule magnets. *Inorg. Chem.* **2018**, *57*, 8098–8105.

[100] Bethe, H. *Ann. Physik* **1929**, *3*, 133.

[101] Van Vleck, J. The group relation between the Mulliken and Slater-Pauling theories of valence. *J. Chem. Phys.* **1935**, *3*, 803–806.

[102] Van Vleck, J. Valence strength and the magnetism of complex salts. *J. Chem. Phys.* **1935**, *3*, 807–813.

[103] Atanasov, M.; Daul, C.; Rauzy, C. New insights into the effects of covalency on the ligand field parameters: a DFT study. *Chem. Phys. Lett.* **2003**, *367*, 737–746.

[104] Atanasov, M.; Daul, C.; Rauzy, C. A DFT based ligand field theory. *Structure & Bonding* **2004**, 97–125.

[105] Atanasov, M.; Zadrozny, J. M.; Long, J. R.; Neese, F. A theoretical analysis of chemical bonding, vibronic coupling, and magnetic anisotropy in linear iron (II) complexes with single-molecule magnet behavior. *Chem. Sci.* **2013**, *4*, 139–156.

[106] Buckmaster, H.; Shing, Y. A survey of the EPR spectra of Gd3+ in single crystals. *Phys. status solidi A* **1972**, *12*, 325–361.

[107] Sessoli, R.; Powell, A. K. Strategies towards single molecule magnets based on lanthanide ions. *Coord. Chem. Rev.* **2009**, *253*, 2328–2341.

[108] Pointillart, F.; Cador, O.; Le Guennic, B.; Ouahab, L. Uncommon lanthanide ions in purely 4f Single Molecule Magnets. *Coord. Chem. Rev.* **2017**, *346*, 150–175.

[109] Clemente-Juan, J. M.; Coronado, E.; Gaita-Ariño, A. In *Lanthanides and Actinides in Molecular Magnetism*; Layfield, R. A., Murugesu, M., Eds.; Wiley-VCH Verlag & Co. KGaA: Boschstr, 2015; Vol. 12; Chapter 2, pp 27–59.

[110] Duan, C.-K.; Tanner, P. A. What use are crystal field parameters? A chemist's viewpoint. *J. Phys. Chem. A* **2010**, *114*, 6055–6062.

[111] Ishikawa, N.; Sugita, M.; Okubo, T.; Tanaka, N.; Iino, T.; Kaizu, Y. Determination of ligand-field parameters and f-electronic structures of double-decker bis (phthalocyaninato) lanthanide complexes. *Inorg. Chem.* **2003**, *42*, 2440–2446.

[112] Chang, N.; Gruber, J. B.; Leavitt, R. P.; Morrison, C. A. Optical spectra, energy levels, and crystal-field analysis of tripositive rare earth ions in Y2O3. I. Kramers ions in C 2 sites. *J. Chem. Phys.* **1982**, *76*, 3877–3889.

[113] Ungur, L.; Chibotaru, L. F. Ab initio crystal field for lanthanides. *Chem.Eur. J.* **2017**, *23*, 3708–3718.

[114] Rinehart, J. D.; Long, J. R. Exploiting single-ion anisotropy in the design of f-element single-molecule magnets. *Chem. Sci.* **2011**, *2*, 2078–2085.

[115] Alessandri, R.; Zulfikri, H.; Autschbach, J.; Bolvin, H. Crystal Field in Rare-Earth Complexes: From Electrostatics to Bonding. *Chem.–Eur. J.* **2018**, *24*, 5538–5550.

[116] Jørgensen, C. K. The interelectronic repulsion and partly covalent bonding in transition-group complexes. *Discuss. Faraday Soc.* **1958**, *26*, 110–115.

[117] Bolvin, H. d-> d Spectrum and High-Spin/Low-Spin Competition in d6 Octahedral Coordination Compounds: ab Initio Study of Potential Energy Curves. *J. Phys. Chem. A* **1998**, *102*, 7525–7534.

[118] Kaltsoyannis, N. Does covalency increase or decrease across the actinide series? Implications for minor actinide partitioning. *Inorg. Chem.* **2013**, *52*, 3407–3413.

[119] Lu, E.; Sajjad, S.; Berryman, V. E.; Wooles, A. J.; Kaltsoyannis, N.; Liddle, S. T. Emergence of the structure-directing role of f-orbital overlap-driven covalency. *Nat. Commun.* **2019**, *10*, 1–10.

[120] Bolvin, H.; Wahlgren, U.; Gropen, O.; Marsden, C. Ab initio study of the two isoelectronic molecules NpO4-and UO42. *J. Phys. Chem. A* **2001**, *105*, 10570–10576.

[121] Aquilante, F.; De Vico, L.; Ferré, N.; Ghigo, G.; Malmqvist, P.-å.; Neogrády, P.; Pedersen, T. B.; Pitoňák, M.; Reiher, M.; Roos, B. O., et al. MOLCAS 7: the next generation. *J. Comput. Chem.* **2010**, *31*, 224–247.

[122] Hess, B. A. Relativistic electronic-structure calculations employing a two-component no-pair formalism with external-field projection operators. *Phys. Rev. A* **1986**, *33*, 3742.

[123] Sharkas, K.; Pritchard, B.; Autschbach, J. Effects from Spin-Orbit Coupling on Electron-Nucleus Hyperfine Coupling Calculated at the Restricted Active Space Level for Kramers Doublets. *J. Chem. Theory Comput.* **2015**, *11*, 538–549.

[124] Sauri, V.; Serrano-Andrés, L.; Shahi, A. R. M.; Gagliardi, L.; Vancoillie, S.; Pierloot, K. Multiconfigurational second-order perturbation theory restricted active space (RASPT2) method for electronic excited states: A benchmark study. *J. Chem. Theory Comput.* **2011**, *7*, 153–168.

[125] Malmqvist, P. Å.; Roos, B. O.; Schimmelpfennig, B. The restricted active space (RAS) state interaction approach with spin–orbit coupling. *Chem. Phys. Lett.* **2002**, *357*, 230–240.

[126] Heß, B. A.; Marian, C. M.; Wahlgren, U.; Gropen, O. A mean-field spin-orbit method applicable to correlated wavefunctions. *Chem. Phys. Lett.* **1996**, *251*, 365–371.

[127] Roos, B. O.; Lindh, R.; Malmqvist, P.-Å.; Veryazov, V.; Widmark, P.-O. New relativistic ANO basis sets for actinide atoms. *Chem. Phys. Lett.* **2005**, *409*, 295–299.

[128] Roos, B. O.; Lindh, R.; Malmqvist, P.-Å.; Veryazov, V.; Widmark, P.-O. Main group atoms and dimers studied with a new relativistic ANO basis set. *J. Phys. Chem. A* **2004**, *108*, 2851–2858.

[129] Bolvin, H. An Alternative Approach to the g-Matrix: Theory and Applications. *ChemPhysChem* **2006**, *7*, 1575–1589.

[130] Lenthe, E. v.; Baerends, E.-J.; Snijders, J. G. Relativistic regular two-component Hamiltonians. *J. Chem. Phys.* **1993**, *99*, 4597–4610.

[131] Ernzerhof, M.; Scuseria, G. E. Assessment of the Perdew-Burke-Ernzerhof exchange-correlation functional. *J. Chem. Phys.* **1999**, *110*, 5029–5036.

[132] Van Lenthe, E.; Baerends, E. J. Optimized Slater-type basis sets for the elements 1-118. *J. Comput. Chem.* **2003**, *24*, 1142–1156.

[133] Moncho, S.; Autschbach, J. Relativistic Zeroth-Order Regular Approximation Combined with Nonhybrid and Hybrid Density Functional Theory: Performance for NMR Indirect Nuclear Spin-Spin Coupling in Heavy Metal Compounds. *J. Chem. Theory Comput.* **2010**, *6*, 223–234.

[134] van Lenthe, E.; Wormer, P. E.; van der Avoird, A. Density functional calculations of molecular g-tensors in the zero-order regular approximation for relativistic effects. *J. Chem. Phys.* **1997**, *107*, 2488–2498.

[135] Jensen, F. Polarization consistent basis sets. II. Estimating the Kohn–Sham basis set limit. *J. Chem. Phys.* **2002**, *116*, 7372–7379.

[136] Jensen, F. The basis set convergence of spin-spin coupling constants calculated by density functional methods. *J. Chem. Theory Comput.* **2006**, *2*, 1360–1369.

[137] Jensen, F. The optimum contraction of basis sets for calculating spin–spin coupling constants. *Theor. Chem. Acc.* **2010**, *126*, 371–382.

[138] Komorovsky, S.; Repisky, M.; Ruud, K.; Malkina, O. L.; Malkin, V. G. Four-component relativistic density functional theory calculations of NMR shielding tensors for paramagnetic systems. *J. Phys. Chem. A* **2013**, *117*, 14209–14219.

[139] Chemcraft - graphical software for visualization of quantum chemistry computations. https://www.chemcraftprog.com.

[140] Zhao, Y.; Truhlar, D. G. The M06 suite of density functionals for main group thermochemistry, thermochemical kinetics, noncovalent interactions, excited states, and transition elements: two new functionals and systematic testing of four M06-class functionals and 12 other functionals. *Theor. Chem. Acc.* **2008**, *120*, 215–241.

[141] Zhao, Y.; Truhlar, D. G. A new local density functional for main-group thermochemistry, transition metal bonding, thermochemical kinetics, and noncovalent interactions. *J. Chem. Phys.* **2006**, *125*, 194101.

[142] Hay, P. J.; Wadt, W. R. Ab initio effective core potentials for molecular calculations. Potentials for K to Au including the outermost core orbitals. *J. Chem. Phys.* **1985**, *82*, 299–310.

[143] Neese, F. Software update: the ORCA program system, version 4.0. *Wiley Interdisciplinary Reviews: Computational Molecular Science* **2018**, *8*, e1327.

[144] Reiher, M. Douglas-Kroll-Hess Theory: a relativistic electrons-only theory for chemistry. *Theor. Chem. Acc.* **2006**, *116*, 241–252.

[145] Neese, F. Efficient and accurate approximations to the molecular spin-orbit coupling operator and their use in molecular g-tensor calculations. *J. Chem. Phys.* **2005**, *122*, 034107.

[146] Aravena, D.; Neese, F.; Pantazis, D. A. Improved segmented all-electron relativistically contracted basis sets for the lanthanides. *J. Chem. Theory Comput.* **2016**, *12*, 1148–1156.

[147] Weigend, F.; Furche, F.; Ahlrichs, R. Gaussian basis sets of quadruple zeta valence quality for atoms H-Kr. *J. Chem. Phys.* **2003**, *119*, 12753–12762.

[148] Weigend, F.; Ahlrichs, R. Balanced basis sets of split valence, triple zeta valence and quadruple zeta valence quality for H to Rn: Design and assessment of accuracy. *Phys. Chem. Chem. Phys.* **2005**, *7*, 3297–3305.

[149] Stoychev, G. L.; Auer, A. A.; Neese, F. Automatic generation of auxiliary basis sets. *J. Chem. Theory Comput.* **2017**, *13*, 554–562.

[150] Neese, F. An improvement of the resolution of the identity approximation for the formation of the Coulomb matrix. *J. Comput. Chem.* **2003**, *24*, 1740–1747.

[151] Pantazis, D. A.; Neese, F. All-electron scalar relativistic basis sets for the actinides. *J. Chem. Theory Comput.* **2011**, *7*, 677–684.

Abstract

Paramagnetic NMR (pNMR) shifts are the extra induced chemical shifts in a paramagnetic complex compared to its diamagnetic counterpart. The pNMR shift of a nucleus can be divided into two terms: the pseudocontact shift which is a 'through-space magnetic dipole-dipole interaction and originates from the anisotropic magnetic properties of the metal center, and the contact shift which arises from the presence of spin density at the nuclear position, a phenomenon due to the spin delocalization. In the 1970s, Bleaney had proposed a simple model based on crystal field theory (CFT) which permits the separation of the two terms based on their temperature dependency in the axially symmetric lanthanide complexes. According to his theory, the contact and the pseudocontact shifts behave as functions of T^{-1} and T^{-2} , respectively. Furthermore, his theory relates the magnetic anisotropy responsible for the pNMR shifts with only one crystal field parameter (CFP) B_0^2: an effective parameter that can be extracted from the experimental pNMR shifts, helps to model the zero field splitting and molecular magnetism.

In this thesis, we have shown that Bleaney's model fails to describe pNMR shifts in axially symmetric actinide complexes, neither their magnetic anisotropy can be modeled with only one CFP nor the shifts follow the temperature dependency as proposed for lanthanides. This is shown by detailed studies performed in axially symmetric actinide complexes with DPA^{2-} , $DOTA^{4-}$, TEDGA ligands. Actinides show variable oxidation numbers (+III, +IV, +VI) compared to the Ln (mostly stable in +III) and the electronic structure is more complicated. In the +VI oxidation state, the earlier actinides (U, Np, Pu) form linear actinyl cations AnO_2^{2+}, which cannot be described with the ligand field theory. We have shown that Bleaney's theory completely fails to describe the temperature dependency of the pNMR shifts in these complexes. Ab initio calculations suggest that two low-lying Kramers doublets are responsible for the pNMR shifts in the $5f^1$ actinyl complexes, whereas a well-isolated ground non-Kramers doublet dictates the magnetic properties in the $5f^2$ complexes. In the axially symmetric An(IV) DPA chelates, the pseudocontact shifts are small compared to the contact shifts, temperature dependency of the contact shifts mostly follow T^{-1} relationship whereas the pseudocontact shifts require T^{-3} term in addition to the T^{-2} to properly fit the experimental data.

Spin density distributions on the ligands are estimated from the contact shifts; DFT-based evaluation plays an important role in support of the observed patterns. The survey is completed by analyzing the trends of the CFPs in the Ln(III) and An(IV) DPA complexes. CFT parametrically describe the interaction of the f electrons with the ligands and the CFPS effectively include various effects as the electron-electron repulsion, J-J coupling, covalency etc. Our analysis leads to the following conclusions- the overall magnitude of the CFPs decreases along both the Ln(III) and An(IV) DPA series, these declining trends are attributed to the decrease of covalency that includes all the effects beyond the electrostatic picture, the decrease was much larger in the An(IV) series due to large J-J coupling. The fourth and sixth orders axial CFPs (B_0^4, B_0^6) are larger than the second-order order B_0^2which implies that the modeling of the pNMR shifts in the axially symmetric Ln or An complexes according to Bleaney's theory effectively includes the higher-order effects in B_0^2 and denotes a limitation to this theory.

Résumé

Les déplacements chimiques RMN paramagnétiques sont les déplacements induits par un centre paramagnétique par comparaison à un équivalent diamagnétique. Ils comprennent deux termes: i) le terme de pseudocontact correspond à l'interaction dipôle-dipôle et provient des propritétés magnétiques anisotropes du centre paramagnétique, ii) le terme de contact qui provient de la densité de spin au noyau actif en NMR, induite par la délocalisation de spin du centre paramagnétique. Pour exploiter les résultats de pNMR, il est nécessaire de séparer ces deux termes. Le modèle de Bleaney, élaboré dans les années 1970 pour les complexes de Ln(III) de symétrie axiale, est fondé sur la théorie du champ cristallin, et permet cette séparation à partir de la dépendance en température: les termes de contact et de pseudocontact ont des dépendances respectives en T^{-1} et en T^{-2}. De plus, l'anisotropie magnétique s'exprime à l'aide d'un unique paramètre de champ cristallin B_0^2 , paramètre effectif qui peut être déduit déduire des déplacements chimiques expérimentaux.

Lors de cette thèse, nous avons montré que le modèle de Bleaney n'est pas valable dans les complexes d'actinide de symétrie axiale; en effet, l'anisotropie magnétique ne peut pas être décrite par un seul paramètre de champ cristallin, et la dépendance en température n'est pas celle des lanthanides. Ceci a été montré sur des complexes d'actinide de symétrie axiale formés avec les ligands DPA^{2-} , $DOTA^{4-}$, TEDGA. Leur synthèse et leur caractérisation spectroscopique a été effectuée au CEA Marcoule par l'équipe de Claude Berthon. Les complexes d'actinide montrent différents degrés d'oxydation (+III, +IV, +VI) par comparaison avec les lanthanides (généralement stables sous la forme +III) et leur structure électronique est plus complexe. Au dégré d'oxydation +VI, les actinides du début de la série (U, Np, Pu) forment des cations actinyles linéaires AnO_2^{2+}, qui ne peuvent pas être décrits par la théorie du champ des ligands. Nous avons montré que la théorie de Bleaney échoue totalement à décrire la dépendance en température des déplacements pNMR dans ces complexes. Les calculs ab initio suggèrent que ce sont les deux doublets de Kramers de basse énergie qui induisent la pNMR dans les complexes actinyles $5f^1$. Par ailleurs, un doublet non Kramers bien séparé dicte les propriétés magnétiques dans les complexes $5f^2$. Dans les chelates An(IV), les déplacements de pseudocontact sont faibles par rapport aux termes de contact. Le terme de pseudocontact est en T^{-1} et on doit ajouter un terme en T^{-3} au terme T^{-2} pour bien reproduire les données expérimentales.

Les densités de spin sur les ligands peuvent être estimées des déplacements de contact; des calculs DFT permettent de rationaliser les schémas observés. Cette étude est complétée en analysant les tendances des paramètres de champs cristallins (CFP) dans les complexes Ln(III) et An(IV) DPA. Ces paramètres jouent un rôle essentiel pour la chimie des lanthanides et des actinides. Ils décrivent l'interaction des électrons de la couche f avec les ligands et peuvent inclure de façon effective la répulsion électron-électron, le couplage J-J, et la covalence. Notre analyse a mené aux conclusions suivantes: les CFPs décroissent globalement le long de la série des Ln(III) et An(IV) DPA, effet attribué à la diminution de la covalence qui inclue tous les effets au délà de la théorie électrostatique. L'effet est plus important dans la série des An(IV) due à un large couplage J-J. Les CFPs axiaux d'ordre 4 et 6 (B_0^4, B_0^6) sont plus importants que ceux d'ordre deux B_0^4 dans les actinides. Ceci implique que la modélisation des déplacements pNMR dans les lanthanides et actinides de symétrie axiale par la théorie de Bleaney inclue defaçon effective les effets d'ordres supérieurs. Et montre la limitation de cette théorie.